

Measurement and Analysis of Uranium and Cerium Depositions from
LiCl-KCl Eutectic

A Dissertation

Presented in Partial Fulfillment of the Requirements for the
Degree of Doctorate of Philosophy

with a

Major in Materials Science and Engineering

in the

College of Graduate Studies

University of Idaho

by

Ken C. Marsden

December 2015

Major Professor: Supathorn Phongikaroon, Ph.D.

Committee Members: Indrajit Charit, Ph.D.; Michael Simpson, Ph.D.; Darryl Butt, Ph.D.

Department Administrator: D. Eric Aston, Ph.D.

AUTHORIZATION TO SUBMIT DISSERTATION

This dissertation of Ken C. Marsden, submitted for the degree of Doctorate of Philosophy with a Major in Materials Science and Engineering, and titled "Measurement and Analysis of Uranium and Cerium Depositions from LiCl-KCl Eutectic," has been reviewed in final form. Permission, as indicated by the signatures and dates below, is now granted to submit final copies to the College of Graduate Studies for approval.

Major Professor:

Supathorn Phongikaroon, Ph.D.

Date

Committee Members:

Indrajit Charit, Ph.D.

Date

Michael Simpson, Ph.D.

Date

Darryl Butt, Ph.D.

Date

Department Administrator:

D. Eric Aston, Ph.D.

Date

ABSTRACT

Molten salt electrorefining of uranium is an important recycling technique for recovery of reusable materials from used nuclear fuel. The purity of the recovered uranium product is one of many important considerations which can impact the value of such recycling. Two primary groups of contaminants are often the most widely considered: actinoid species, such as plutonium and neptunium, and lanthanoid species, such as cerium and lanthanum. The present study investigated fundamental and applied factors important to this subject.

A detailed literature survey of the primary electrochemical properties of the actinoid and lanthanoid species was performed. Detailed electrochemical studies of cerium in LiCl-KCl eutectic were performed, including measurement of apparent standard potential, diffusion coefficient, nucleation mode, and exchange current density.

The purity of uranium dendrites produced in an engineering-scale electrorefiner in the presence of fission and transmutation products was investigated, and this information was compared against purities of final uranium products. The results indicate that the intrinsic purity of the uranium crystals is very high, and most impurities in final uranium products are very likely introduced during following process operations.

Uranium dendrites were also produced under laboratory conditions with six UCl_3 and UCl_3 - CeCl_3 mixtures at 773 K in the LiCl-KCl eutectic. No clear link was found between cerium contamination of the uranium and the deposition overpotential. However, the cerium contamination was found to rise significantly at all deposition potentials in uranium dendrites produced from electrolytes of low uranium activity. The morphology of uranium crystals created at electrochemical overpotentials of 25, 150, and 450 mV relative to the uranium equilibrium potential in LiCl-KCl eutectic at 773 K was studied by microscopy. The resulting morphology was observed to be significantly influenced by deposition potential. Deposition at larger electrochemical overpotentials created fibrous deposits with limited evidence of porosity. However, significant microscopic cavities were observed in uranium crystals grown at low overpotential.

ACKNOWLEDGEMENTS

This work was partially supported by the U.S. Department of Energy, Office of Nuclear Energy, under DOE-NE Idaho Operations Office Contract DE-AC07-05ID14517. This manuscript was approved for release through STIMS review number INL/EXT-15-36896.

There are many individuals and organizations to thank for essential contributions to this work:

- First, and foremost, my wife and children for their support and encouragement during a very long process;
- Dr. Supathorn Phongikaroon for his advice and support to see this effort through;
- My committee: Drs. Indrajit Charit, Michael Simpson, and Darryl Butt for taking the time to review this work and provide invaluable input and suggestions;
- Mr. Bernard Cowan, for many hours of assistance ensuring this effort did not result in a safety statistic;
- Tom O'Holleran and Natalie Gese for their hours sitting at an SEM with me;
- The team of dedicated scientists and technicians at the Materials and Fuels Complex Analytical Laboratory, for expert assistance with chemical analyses and patience with thousands of questions; most notably Jeff Giglio, Joey Charboneau, Dan Cummings, Martin Kearns, Mike Rodriguez, and Jeff Berg; and
- Fellow investigators at INL for many hours of discussion and debate, including Brian Westphal, Steve Herrmann, Dee Vaden, and Shelly Li.

TABLE OF CONTENTS

AUTHORIZATION TO SUBMIT.....	ii
ABSTRACT	iii
ACKNOWLEDGEMENTS.....	iv
TABLE OF CONTENTS.....	v
LIST OF FIGURES	ix
LIST OF TABLES	xiii
 CHAPTER 1. INTRODUCTION	 1
1.1 Electrometallurgical Recycling of Used Nuclear Fuel.....	1
1.2 Purpose	3
1.3 Motivation.....	3
1.4 Approach	4
1.5 Organization of Dissertation	4
 CHAPTER 2. REVIEW OF PRINCIPLES	 6
2.1 Conventions.....	6
2.2 Concentration Scales	6
2.3 Activity Scales.....	6
2.4 Reference Electrode Systems.....	7
2.5 Electrochemical Methods	8
2.6 Reversibility	9
2.7 Stable Oxidation States	11
2.7.1 Oxidation States by Voltammetry	11
2.7.2 Oxidation States by Chronopotentiometry.....	12
2.8 Diffusion Coefficients	13
2.8.1 Diffusion Coefficients by Voltammetry	13

2.8.2	Diffusion Coefficients by Chronopotentiometry	14
2.9	Equilibrium Potential.....	14
2.9.1	Equilibrium Potential by Voltammetry.....	14
2.9.2	Equilibrium Potential by Chronopotentiometry.....	15
2.10	Exchange Current Density.....	16
2.10.1	Exchange Current Density by Tafel Method	16
2.10.2	Exchange Current Density by Linear Polarization Method	17
2.11	Nucleation Mode	19
2.11.1	Nucleation Mode by Simple Theoretical Method.....	19
2.11.2	Nucleation Mode by Scharifker and Hills Dimensionless Method.....	20
CHAPTER 3. LITERATURE REVIEW.....		23
3.1	The Ag^+/Ag^0 Reference Electrode	23
3.2	Thermodynamic Databases for Gibbs Free Energy of Formation	26
3.3	Crucible Materials and Purification.....	26
3.4	Molten Salt Complexes.....	27
3.5	Exchange Current Density in Fused Salt Systems	30
3.6	Cerium Electrochemistry in Fused LiCl-KCl Eutectic.....	31
3.7	Actinoid Electrochemistry Investigations in Fused LiCl-KCl Eutectic	32
3.8	Purity of Molten Salt Electrorefining Products	33
3.9	Survey of Lanthanoid and Actinoid Properties in Molten LiCl-KCl.....	35
3.9.1	Oxidation States of Lanthanoid and Actinoid Species.....	35
3.9.2	Diffusion Behavior of Lanthanoid and Actinoid Species.....	40
3.9.3	Apparent Standard Potential of Lanthanoid and Actinoid Species	40
3.9.4	Nucleation Behavior of Lanthanoid and Actinoid Species	46
3.10	Uranium Crystallography	47

CHAPTER 4. EXPERIMENTAL APPROACH	50
4.1 Experiments for Electrochemistry of Cerium	50
4.1.1 Apparatus	50
4.1.2 Electrodes	52
4.1.3 Reagents	53
4.1.4 Experiment Preparation	53
4.2 Experiments for Electrochemistry with Uranium and Cerium	54
4.2.1 Apparatus	55
4.2.2 Electrodes	57
4.2.3 Reagents	58
4.2.4 Sampling	60
4.2.5 Experiment Preparation	64
4.3 Process Sampling in the Fuel Conditioning Facility	65
4.3.1 Electrorefiner Salt Samples	66
4.3.2 Dendrite Samples	68
CHAPTER 5. RESULTS AND ANALYSIS – ELECTROCHEMISTRY OF CERIUM	71
5.1 Cyclic Voltammetry	71
5.2 Number of Electrons	75
5.3 Diffusion Coefficients from Cyclic Voltammetry	76
5.4 Diffusion Coefficients from Chronopotentiometry	76
5.5 Equilibrium Potential	79
5.6 Gibbs Free Energy and Activation Coefficient	80
5.7 Nucleation Characteristics	82
5.8 Exchange Current Density	85
5.9 Summary of Ce Electrochemistry	88

CHAPTER 6. PROCESS SAMPLES FROM ELECTROMETALLURGICAL TREATMENT	89
6.1 Process Sample Overview	89
6.2 Process Sample Results.....	93
6.3 Discussion of Process Samples.....	102
CHAPTER 7. RESULTS AND ANALYSIS OF URANIUM AND URANIUM-CERIUM ELECTROCHEMISTRY	104
7.1 Electrochemical Studies.....	104
7.2 Microscopy	113
7.2.1 Uranium Deposit from 450 mV Overpotential.....	113
7.2.2 Uranium Deposit from 150 mV Overpotential.....	125
7.2.3 Uranium Deposit from 25 mV Overpotential	134
7.2.4 Discussion of Electrochemistry of Uranium	145
7.3 Uranium Dendrite Samples in the Presence of Cerium.....	146
7.3.1 Overview of Sampling and Analysis	146
7.3.2 Results and Discussion	148
7.3.3 Summary.....	157
CHAPTER 8. SUMMARY AND FUTURE WORK.....	158
REFERENCES.....	166
APPENDIX A. RAW ANALYTICAL DATA FROM U-CE DENDRITE SAMPLES	179

LIST OF FIGURES

Figure 1.1:	The Mk-IV electrorefiner and a typical uranium product.....	2
Figure 1.2:	The cathode processor with products.....	2
Figure 2.1:	An example of nucleation curves.....	20
Figure 2.2:	Theoretical nucleation behavior as predicted by Sharifker and Hills.....	21
Figure 3.1:	Estimations of E_{AgCl}	25
Figure 3.2:	Orthorhombic α -uranium structure in a 2x2x2 supercell.....	48
Figure 3.3:	Pictorial of the (310) crystal plane as defined by Miller indices.....	48
Figure 3.4:	The uranium-cerium phase diagram	49
Figure 4.1:	Argon-atmosphere glovebox for performance of LiCl-KCl-CeCl ₃ experiments.....	51
Figure 4.2:	Experimental cell for electrochemistry of cerium.....	51
Figure 4.3:	Molybdenum basket for cerium counter electrode	52
Figure 4.4:	Typical sheathed electrode assembly for LiCl-KCl-CeCl ₃ experiments.....	52
Figure 4.5:	A typical setup for LiCl-KCl-CeCl ₃	54
Figure 4.6:	Prepared crucible for experiments with LiCl-KCl-UCl ₃ -CeCl ₃	56
Figure 4.7:	Measuring electrode length	56
Figure 4.8:	“Window” electrode for collection of uranium deposits	57
Figure 4.9:	Two uranium rods used in experiments	58
Figure 4.10:	LiCl-KCl-CeCl ₃ -UCl ₃ salt samples.....	61
Figure 4.11:	Harvesting a dendrite sample in the glovebox	62
Figure 4.12:	Typical uranium dendrite experiments ready for sample harvest	63
Figure 4.13:	Uranium dendrite sample grown at 25 mV overpotential.....	64
Figure 4.14:	Experiment control cabinet	65
Figure 4.15:	Tantalum salt sampling device.....	67
Figure 4.16:	Impact mortar used to crush dendrite samples.....	69
Figure 4.17:	Crushed dendrite sample from the Mk-IV ER	69
Figure 5.1:	Cyclic voltammogram of LiCl-KCl eutectic.....	72
Figure 5.2:	Cyclic voltammogram of CeCl ₃ in LiCl-KCl eutectic.....	73

Figure 5.3:	The effect of scan rate upon reduction of CeCl_3	74
Figure 5.4:	Peak cathodic current as a function of the square root of scan rate.....	74
Figure 5.5:	Net-current square wave voltammogram for CeCl_3	75
Figure 5.6:	Chronopotentiograms for CeCl_3	77
Figure 5.7:	Relation between i and $\tau^{-1/2}$ from chronopotentiograms.....	77
Figure 5.8:	Variation of diffusion coefficient of CeCl_3 with temperature in LiCl-KCl eutectic... 79	
Figure 5.9:	Variation of the Standard Potential of Ce.....	80
Figure 5.10:	Nucleation transients of 1.0 mol% CeCl_3 in LiCl-KCl.....	83
Figure 5.11:	Plots of current versus time ^{1/2}	84
Figure 5.12:	Comparison of the theoretical models for nucleation	84
Figure 5.13:	Tafel-type plot for Ce(III)/Ce(0) in LiCl-KCl eutectic.....	86
Figure 5.14:	Plots of current density versus potential.....	87
Figure 6.1:	Photographs of uranium dendrite products.....	90
Figure 6.2:	Photographs of washed crushed dendrite material	91
Figure 6.3:	Photographs of washed crushed/pulverized dendrite material.....	92
Figure 6.4:	Relative stability of major chloride species in pyroprocessing	93
Figure 7.1:	Cyclic voltammetry of LiCl-KCl.....	104
Figure 7.2:	Cyclic voltammetry of UCl_3 in LiCl-KCl.....	105
Figure 7.3:	The effect of scan rate upon reduction of UCl_3	105
Figure 7.4:	Peak cathodic current as a function of scan rate	106
Figure 7.4a:	Cyclic voltammogram of 1.0 mol% UCl_3 and 1 mol% CeCl_3	107
Figure 7.4b:	The effect of scan rate in 1.0 mol% UCl_3 and 1 mol% CeCl_3	108
Figure 7.4c:	Peak cathodic current as a function of the square root of scan rate.....	109
Figure 7.4d:	Cyclic voltammogram of 0.33 mol% UCl_3 and 6.0 mol% CeCl_3	109
Figure 7.5:	Tafel-type plot for U(III)/U(0) in LiCl-KCl at 773 K.....	111
Figure 7.6:	Plots of current density versus potential.....	112
Figure 7.6a:	Comparison of i_0	113
Figure 7.7:	Dendrite mass produced at 450 mV overpotential.....	115
Figure 7.8:	Overview of 450 mV dendrite mass on SEM mount.....	115

Figure 7.9: SE overview image of uranium dendrite cluster.....	116
Figure 7.10: SE image of area (a) from Figure 7.9.....	116
Figure 7.11: BSE image of area (a) from Figure 7.9.....	117
Figure 7.12: BSE image of area (b) from Figure 7.9.....	117
Figure 7.13: SE image of area (c) from Figure 7.9.....	118
Figure 7.14: SE image of area (c1) from Figure 7.13.....	118
Figure 7.15: BSE image of area (d) from Figure 7.9.....	119
Figure 7.16: Chlorine overlay of BSE image of area (d) from Figure 7.9.....	120
Figure 7.17: Oxygen overlay of BSE image of area (d) from Figure 7.9.....	120
Figure 7.18: SE image of area (e) from Figure 7.9.....	121
Figure 7.19: SE image of area (e1) from Figure 7.18.....	122
Figure 7.20: SE image of area (e1-a) from Figure 7.19.....	122
Figure 7.21: SE image of area (e2) from Figure 7.18.....	123
Figure 7.22: SE image of dendrite with regular side branches.....	124
Figure 7.23: SE image of area (f1) from Figure 7.2.....	124
Figure 7.24: Oxidized mass of very fine fibers.....	125
Figure 7.25: SE image of a cluster of fiber-like dendrites.....	126
Figure 7.26: BSE image of area (a) from Figure 7.25.....	127
Figure 7.27: EDS spectra from Figure 7.26.....	127
Figure 7.28: BSE image of area (b) from Figure 7.25.....	128
Figure 7.29: SE image of area (c) from Figure 7.25.....	129
Figure 7.30: EDS spectra from Figure 7.29.....	129
Figure 7.31: SE image of area (c1) from Figure 7.29.....	130
Figure 7.32: BSE image of area 9d) from Figure 7.25 showing regularly-branched dendrite.	131
Figure 7.33: BSE image of area (e) from Figure 7.25.....	132
Figure 7.34: SE image of area (e1) from Figure 7.33 showing regularly-branched dendrite...	132
Figure 7.35: BSE image of area (e1) from Figure 7.33.....	133
Figure 7.36: SE image of area (f) from Figure 7.25.....	133
Figure 7.37: Low resolution overview of uranium dendrites from 25 mV overpotential.....	135

Figure 7.38: SE image of area (a) from Figure 7.37.....	135
Figure 7.39: SE image of area (b) from Figure 7.37.....	136
Figure 7.40: BSE image of area (b) from Figure 7.39.....	136
Figure 7.41: EDS spectra of points from Figure 7.40.....	137
Figure 7.42: SE image of area (b1) from Figure 7.39 of uranium dendrite.....	137
Figure 7.43: SE image of area (b1-a) from Figure 7.42.....	138
Figure 7.44: SE image of area (c) from Figure 7.37.....	139
Figure 7.45: SE image of area (c1) from Figure 7.44.....	139
Figure 7.46: SE image of area (c1-a) from Figure 7.45.....	140
Figure 7.47: EDS spectrum of points from Figure 7.46.....	140
Figure 7.48: SE image of area (d) from Figure 7.37.....	141
Figure 7.49: SE image of 25 mV uranium dendrites.....	142
Figure 7.50: SE image of area (e) from Figure 7.49.....	142
Figure 7.51: BSE image of area (e) from Figure 7.50.....	143
Figure 7.52: SE image of 25 mV uranium dendrites and key to areas (f) and (g).....	143
Figure 7.53: SE image of area (f) from Figure 7.52.....	144
Figure 7.54: SE image of area (g) from Figure 7.52.....	144
Figure 7.55: Photographs of uranium dendrite samples.....	147
Figure 7.56: Observed currents during uranium dendrite growth.....	149
Figure 7.57: Residual cerium content in samples from 0.33 mol% U and 1.0 mol% Ce.....	154
Figure 7.58: Residual cerium content in samples from 0.33 mol% U and 6.0 mol% Ce.....	155
Figure 7.59: Residual cerium content in samples from 1.0 mol% U and 1.0 mol% Ce.....	155
Figure 7.60: Residual cerium content in samples from 6.0 mol% U and 1.0 mol% Ce.....	156
Figure 7.61: Residual cerium content in samples from 6.0 mol% U and 6.0 mol% Ce.....	156

LIST OF TABLES

Table 3.1:	Survey of stable oxidation states of light lanthanoid elements	37
Table 3.2:	Survey of stable oxidation states of scandium and heavy lanthanoid elements.....	38
Table 3.3:	Survey of stable oxidation states of actinoid elements	38
Table 3.4:	Survey of light lanthanoid diffusion coefficients	42
Table 3.5:	Survey of Sc, Y, and heavy lanthanoid diffusion coefficients	43
Table 3.6:	Survey of actinoid diffusion coefficients	43
Table 3.7:	Survey of apparent standard potential of the light lanthanoids	44
Table 3.8:	Survey of apparent standard potential of heavy lanthanoids	45
Table 3.9:	Survey of apparent standard potential	45
Table 3.10:	Summary of nucleation characteristics	46
Table 3.11:	Allotropic transformations and melting temperature of uranium.....	47
Table 3.12:	Crystallographic data for uranium.....	47
Table 4.1:	Experimental data set for dendrite samples.....	55
Table 4.2:	Analysis of LiCl-KCl feedstock.....	59
Table 4.3:	Composition LiCl-KCl-UCl ₃ feedstock	60
Table 4.4:	Composition of cast uranium rod.....	60
Table 4.5:	Planned dendrite samples from electrometallurgical processing.....	66
Table 4.6:	Sample preparation for Mk-IV salt	68
Table 4.7:	Sample preparation for Mk-IV uranium dendrites	70
Table 5.1:	Values of α_n computed from cyclic voltammetry.....	76
Table 5.2:	Diffusion coefficients of Ce(III) in LiCl-KCl eutectic at [1.0 mol%]	79
Table 5.3:	Experimental data for equilibrium potentials of Ce(III)/Ce(0)	80
Table 5.4:	Comparison of predicted E_0 and ΔG_0 for CeCl ₃ in LiCl-KCl eutectic.....	81
Table 5.5:	Activity coefficient for CeCl ₃ in LiCl-KCl eutectic.....	82
Table 5.6:	Estimates of i_0 utilizing a thin Ce coating on a W wire at 1 mol% CeCl ₃	88
Table 6.1:	Dendrite samples obtained for this study.....	89
Table 6.2:	Apparent standard potentials in LiCl-KCl eutectic.....	93

Table 6.3:	Received analytical results from washed dendrite samples.....	95
Table 6.4:	Re-scaled analytical results from washed dendrite samples.....	96
Table 6.5:	Electrorefiner salt samples.....	97
Table 6.6:	Calculated residual contaminant content of uranium dendrites.....	98
Table 6.7:	Composition of casting samples.....	100
Table 6.8:	Calculated residual salt content of uranium dendrites.....	101
Table 7.1:	Estimates of i_0 from metallic uranium rods.....	110
Table 7.2:	EDS summary from scan of image in Figure 7.8.....	115
Table 7.3:	Dendrite samples obtained for this study.....	146
Table 7.4:	Target test conditions, in mol% and wt%.....	148
Table 7.5:	Average observed current during dendrite growth.....	148
Table 7.6:	Measured composition of electrolyte samples.....	150
Table 7.7:	Summary of Ce/Li ratio from dendrite water washes.....	150
Table 7.8:	Summary of potassium/lithium ratio from dendrite water washes.....	151
Table 7.9:	Total cerium content in dendrite samples.....	152
Table 7.10:	Salt-based cerium content in dendrite samples.....	152
Table 7.11:	Average fraction of salt-based cerium.....	152
Table 7.12:	Estimated mass of occluded salt in dendrites.....	152
Table 7.13:	Final estimated cerium content in dendrite samples.....	153
Table 7.14:	Average cerium content for each electrolyte test condition.....	154
Table 7.15:	Summary of potassium/lithium ratios from dendrites.....	157
Table 7.16:	Solubility of LiCl and KCl in water, units of g/100g H ₂ O.....	157

CHAPTER 1. INTRODUCTION

1.1 Electrometallurgical Recycling of Used Nuclear Fuel

Used nuclear fuel (UNF) can be reprocessed to reclaim useful elements and remove those with long-term radiotoxicity, reducing requirements for mined uranium and the environmental burden of the nuclear fuel cycle. Various separation methods have been investigated and deployed for the recycling of UNF. Electrometallurgical processing, also known as ‘electrochemical recycling’ or ‘pyroprocessing,’ is a separation method that utilizes a molten halide salt as an electrolyte for the dissolution of UNF and the partition of constituents based on their electrochemical potentials. The molten ionic electrolyte is immune to thermal or radiation damage. In addition, it does not contain hydrogen, which acts as an undesirable neutron moderator. These favorable characteristics allow for the reprocessing of very briefly cooled UNF—even that of high fissile content—in compact and remotely operated processes (1, 2).

For the above reasons, this recycling method is often considered ideal for certain closed fuel cycles, especially those utilizing metallic-fueled fast reactors. Of the possible molten electrolytes, the primary focus has been on LiCl-KCl eutectic. Focused research and development programs are underway in the European Union (3-5), China (6-8), Japan (9-11), South Korea (12-14), India (15-17), and the United States (18-22).

Engineering-scale electrometallurgical processing of used metallic fuel from the Experimental Breeder Reactor II (EBR-II) and Fast Flux Test Facility (FFTF) commenced in 1996 at Idaho National Laboratory (INL). Here, UNF is processed in the Mk-IV electrorefiner (ER), and a dendritic uranium product is recovered, as shown in Figure 1.1. To perform the electrorefining, UNF is chopped and placed into stainless steel anode baskets with perforated walls. Impure uranium contained in the anode basket is electrochemically dissolved, and purified uranium deposited as a highly dendritic mass on the cathode. Transuranium elements, lanthanoids, and other fission products accumulate in the LiCl-KCl electrolyte. The cathode of purified uranium is removed from the ER and mechanically removed from the stainless steel cathode mandrel. The harvested dendrites are placed in a crucible, which is loaded into the

upper section of a furnace described as the Cathode Processor (see Figure 1.2). The ER salts are separated from the metal by vacuum distillation, and the uranium product is consolidated into ingots by melting. The evaporated salt is condensed and collected into a receiver crucible in the lower section.

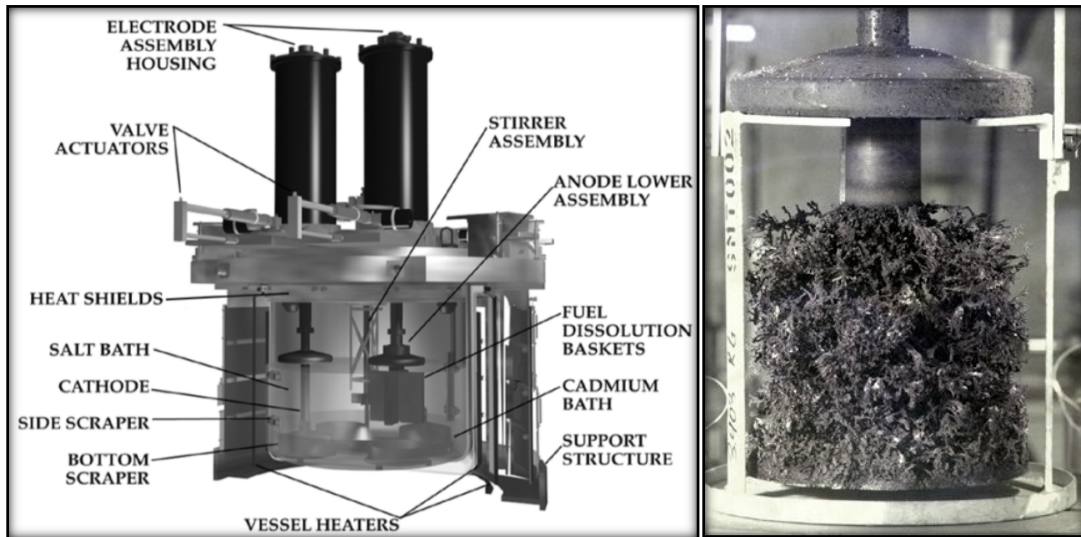


Figure 1.1: The Mk-IV electrorefiner and a typical ~10 kg uranium product (20).

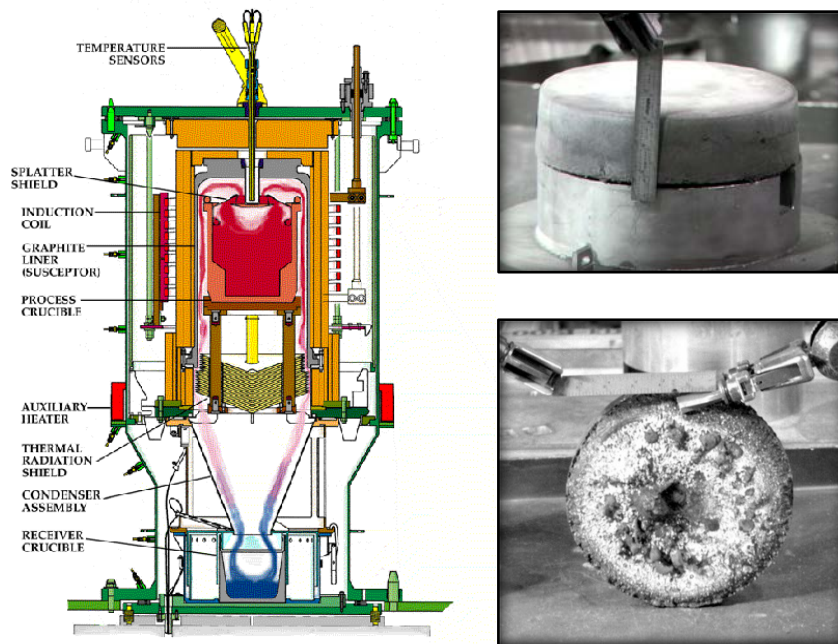


Figure 1.2: The Cathode Processor with a consolidated uranium product (top right) and condensed electrorefiner salt (bottom right).

1.2 Purpose

The purpose of this dissertation is to study and determine factors affecting impurity content of an electrorefined uranium product as a part of a nuclear fuel cycle. To elucidate issues associated with impurities in electrochemically deposited uranium, two major areas have been investigated. The first area is an investigation at the INL Fuel Conditioning Facility to acquire and analyze 10 uranium dendrite samples from the electrorefining of UNF. The dendrite analyses are evaluated to understand dendrite impurity contents. The second area is a study of unirradiated uranium electrorefined in the presence of cerium salts. This component begins with electrochemical studies of cerium and uranium individually and transitions to a mixed system. This study provides an experimental matrix with a range of constituent concentrations and deposition potentials. Dendrite samples are obtained and analyzed for cerium to describe the relationships between the extent of cerium contamination, salt concentrations and deposition potentials.

1.3 Motivation

Ideally, electrorefined uranium deposits would be pure uranium, without any contaminants. However, practice has shown that uranium recovered from UNF via electrochemical processes does include a variety of undesirable contaminants. Some contaminant species, such as Pu even when present at very low levels, preclude re-use of the recovered uranium in fuel for commercial nuclear energy plants due to licensing restrictions by the U.S. Nuclear Regulatory Commission (23). Other contaminants, such as the lanthanoid elements, contribute to residual radioactivity, which complicates the handling and re-use of the recovered uranium. The sources of, and solutions to, the contamination problem have not been clearly established. These aforementioned issues provide motivation for this study to improve the fundamental understanding and determine important mechanisms of the contamination of electrorefined uranium deposits.

1.4 Approach

The approach for this work was to first perform an in-depth literature survey of electrochemical behaviors of actinoid and lanthanoid elements in the LiCl-KCl eutectic and of product purities achieved in similar molten salt process industries. Dendrite samples were obtained from engineering-scale electrorefining operations, washed to remove adhering salt deposits, and analyzed for impurity content via inductively coupled plasma mass spectroscopy (ICP-MS). The electrochemical behavior of cerium, a representative contaminant, was explored in detail in molten LiCl-KCl in an argon-atmosphere environment. The electrochemical behavior of uranium was then similarly explored. Uranium dendrites were grown to explore how deposition potential impacts the morphology of the uranium deposits. These deposits were cleaned of adhering salt and inspected by scanning electron microscopy (SEM). It may be that contamination mechanisms are impacted by deposit morphology, and little information is available in this area. Experiments then investigated the behavior of uranium and cerium together, including the electrorefining of uranium at small scale in the presence of cerium chloride. Uranium dendrite samples were grown at a range of electrochemical potentials and concentrations of constituents. Salt concentrations were determined through separation of salt and metal fractions by water washing and ICP-MS. The uranium dendrites were sampled and analyzed to determine the contamination of the metal dendrites by cerium under the tested conditions.

1.5 Organization of Dissertation

Chapter 2 reviews the important electrochemical principles which are used throughout this work. Chapter 3 provides a literature review of relevant topics, including a general overview of important electrochemical behaviors in molten LiCl-KCl, a review of the electrochemical properties of uranium and cerium, and a review of product purities achieved in other electrorefining industries. A discussion of the experimental program is provided in Chapter 4. This chapter is divided into three sections to appropriately address the three primary research activities and includes presentation of the materials, experimental systems, and techniques utilized. Chapter 5 presents the results and analyses of CeCl_3 in LiCl-KCl eutectic. Then, Chapter

6 will provide results and discussion on experimental investigations of the purity of electrorefined uranium product from the Fuel Conditioning Facility. Investigation of uranium electrochemistry and cerium contamination of uranium dendrites during electrochemical processes in fused LiCl-KCl eutectic salt is given in Chapter 7. The collective results of these studies are also discussed in context of the overall purpose of this work. Chapter 8 summarizes the findings of the overall dissertation and proposes future investigations which could provide additional benefits toward the motivations of this dissertation.

CHAPTER 2. REVIEW OF PRINCIPLES

2.1 Conventions

In the present work, the recommendations and conventions of the International Union of Pure and Applied Chemistry (24, 25) are generally followed unless noted.

2.2 Concentration Scales

A variety of concentration scales are found in the literature. Although knowledge of the concentration scale is critical information to allow other researchers to utilize data, a description of the concentration scale employed is often overlooked. The most common concentration scales in electrochemistry are molality (m), molarity (M), and mole fraction (X). Mole fraction is arguably the most common in modern high-temperature electrochemistry and is the concentration scale utilized in this study. Mole fraction is defined as the moles of solute divided by the total moles. Molality is defined as the moles of solute per 1000 grams of solvent. The conversion between mole fraction and molality for dilute solutions can be obtained by

$$X = m \cdot W_{\text{solvent}}/1000, \quad [2.1]$$

where W_{solvent} is the molar mass of the solvent. For example, W_{solvent} is 55.83 g/mol for the LiCl-KCl eutectic. Molarity is defined as the moles of solute per 1000 mL of solvent. It is occasionally used in high-temperature electrochemistry; however, it has the disadvantage of varying with temperature due to thermal expansion of the solvent. The conversion between mole fraction and molarity for dilute solutions can be obtained by

$$X = M \cdot V_{\text{solvent}}/1000, \quad [2.2]$$

where V_{solvent} is the molar volume of the solvent. For the LiCl-KCl eutectic at 500 °C, V_{solvent} is 1.62 g/cm³ (26).

2.3 Activity Scales

Two different activity scales can be used with the mole fraction concentration scale. One is based on a theoretical standard state in which the activity approaches the concentration as the concentration approaches infinite dilution. This case is based on Henrian behavior of dilute

solutions, and the activity coefficient approaches unity at infinite dilution. The second activity scale is based on the standard state in which the activity approaches the concentration as the concentration approaches unity. Thus, both the activity and activity coefficient approach unity with the concentration. This scale is often described as Raoultian behavior. In either case, the activity coefficient of component i is defined by

$$\gamma_i \equiv a_i/X_i, \quad [2.3]$$

where a_i is the activity of component i , and X_i is the mole fraction of component i .

Electrorefining and other pyrochemical activities in molten salts with the lanthanoids and actinoids are generally performed at concentrations below 5-6 mol% and often much lower. In this region, these species are observed to have low activity coefficients and are generally considered to follow Henrian behavior.

2.4 Reference Electrode Systems

To measure the potential of an electrode, a reference point must be used. Sometimes this reference point is the opposing electrode in an anodic and cathodic pair. In this case, the measured potential is described as the *cell* potential. This situation, however, does not provide specific information about either electrode. For example, it is impossible to determine the electrode polarization, which is critical information to understand which species are contributing to electrode current.

To determine the potential of an electrode, an unvarying electrode reaction is needed as a reference point. This is typically done by the use of a reference reaction at an electrode, or a reference electrode. To be useful, the potential at the reference electrode must remain stable; thus, it must be reversible and in equilibrium. In aqueous electrochemistry, the reference used is often the standard hydrogen electrode. In chloride molten salts, the chlorine electrode, Eq. [2.4], is generally considered the most fundamental reference with the following reaction



However, the chlorine gas required for the chlorine electrode is not often convenient to use. Thus, more simple electrodes, such as those based on silver and silver chloride are often used:



In this case, the electrode is constructed of a silver wire, immersed in a ceramic or glass tube conductive to ions and containing a small amount of LiCl-KCl-AgCl of a known composition. The tube is immersed into the experiment bath and thus maintained at electrode operating temperature. Ionic conductivity is provided by the presence of Na⁺ ions in the glass-containing membrane, with which Li⁺ can substitute. The reaction is maintained at equilibrium conditions by very high impedance on the reference electrode signal wire. The cell formula may be written as



The measured potentials relative to the reference electrode are generally converted to potentials relative to the Cl₂/Cl⁻ couple in order to more easily compare data between experimenters and to compute thermodynamic data. In the case of the common Ag⁺/Ag electrode system, its relationship relative to Cl₂/Cl⁻ is commonly based on the works of Yang and Hudson (27, 28), although the data of Laitinen (29), Salstrom (30, 31), or Takahashi (32) are occasionally cited.

2.5 Electrochemical Methods

Voltammetry is a method in which current is measured as it responds to changes under an applied potential. Cyclic voltammetry (CV) is often the first technique used in an electrochemical examination. In this method, the electrode current is measured as it responds to electrode potential which changes at a selected constant rate. Scans are often repeated across a variety of scan rates and vertex potentials to gain an understanding of the reactions. In addition to this general comprehension, data can be obtained regarding reaction reversibility, species valence and diffusion constants, and the formal standard equilibrium potential. Methods used in this work are described in the following sections.

Square wave voltammetry utilizes a square wave superimposed on a staircase potential and has been extensively developed by the Osteryoungs (33). For reversible processes, the peak potentials are equal to the half potentials ($E_{1/2}$) of the reaction. In this method, currents are

sampled at the end of every half wave and differentiated. Sampling at the end allows data to be obtained without the inaccuracies of capacitive and residual currents. The peaks are Gaussian, and peak height is proportional to concentration of the active species. The peak width is dependent upon temperature and the number of electrons in the reaction. For soluble-insoluble reactions with significant nucleation overpotential, the peak may be asymmetric. In this case, the Gaussian cathodic side is reflected to compute the peak width.

Chronopotentiometry (CP) is the study of changes in electrode potential as a constant electrode current is applied. An electrode current is provided by the lowest energy reaction available, and the electrode necessarily acquires this potential. As this reactant is depleted at the electrode surface, current is then primarily provided by the next lowest energy reaction. This technique can be utilized to provide information about reaction rates within multi-step electrode reactions but is most often utilized as a route to acquire diffusion coefficient.

2.6 Reversibility

The linked concepts of reversibility, quasi-reversibility, and irreversibility can be used in different contexts relating to the discussion on chemical, thermodynamic, and electrochemical properties. A reaction may be described as chemically reversible if it can occur in both directions, while a reaction may be described as thermodynamically reversible if a reversal of driving force has a corresponding effect on the reaction rates. A reaction is considered to be electrochemically reversible, or *Nernstian*, in the range in which the system remains essentially in equilibrium. This is the range for which the *Nernst* equation still applies (34-36), which is

$$E = E^0 + RT/nF \ln(a_{ox}/a_{red}), \quad [2.7]$$

where E^0 is the standard potential, R is the universal gas constant, T is the absolute temperature, n is the number of electrons, F is Faraday's constant, a_{ox} is the activity of the oxidizing species, and a_{red} is the activity of the reduced species. Since activity coefficients of the species are often unknown, the Nernst equation is often rewritten using apparent standard potential, E^* , which accommodates the effect of activity coefficients,

$$E = E^* + RT/nF \ln(X_{ox}/X_{red}), \quad [2.8]$$

where X_{ox} is the mole fraction of the oxidizing species and X_{red} is the mole fraction of the reducing species.

Reversibility depends on the speed of electrode processes, as well as the ability of diffusion and convection to maintain concentrations sufficiently near equilibrium. At sufficiently high overpotentials or scanning rates, a reversible reaction will become quasi-reversible and then irreversible, due to the limitation of mass transfer. A reaction may also be irreversible if chemical reactions occur with either the oxidant or reductant, altering or preventing equilibrium concentrations at the electrode surface.

In a qualitative aspect, a determination of the range of reversibility for a reaction indicates the range where simplified calculations based on the Nernst equation are applicable; it is something relatively easy to determine for a set range of experimental conditions. For this work, if the range of reversibility changes with the alteration of a condition, such as modification of the electrolyte, this is a qualitative indication that electrode processes have been affected. Thus, care must be taken to distinguish between effects caused by changes to diffusion or convection and those from genuine alteration of electrode processes.

During voltammetric scans, Nernstian reactions will follow the Randles-Sevcik equation

$$i_p = kn^{3/2}SD^{1/2}C_{ox}v^{1/2}, \quad [2.9]$$

where i_p is the peak current, k is a constant, n is the number of electrons, S is the electrode surface area, D is the diffusion coefficient, C_{ox} is the concentration of the oxidant species, and v is the scanning speed or scan rate. If parameters are held constant for a series of voltammetric scans across a range of scanning speeds, it can be seen that

$$i_p \propto v^{1/2}. \quad [2.10]$$

Thus, the peak current can be plotted against the square root of scanning speed, and the reaction remains Nernstian for the range which is linear; this line passes through the origin.

In addition, if the reaction is reversible, the peak potential is not altered by the scan rate, while irreversible reactions display increasing cathodic and anodic peak separation as scan rate increases.

2.7 Stable Oxidation States

2.7.1 Oxidation States by Voltammetry

Theoretical expressions have been developed which allow estimation of the number of electrons involved in electrochemical reactions (34-37). The form of the relationship varies depending on the nature of the reaction and reactants.

For a simple case in a reversible soluble-soluble system, the cathodic and anodic peak potentials can be described by

$$E_{p,c} = E_C^{0'} - 1.109 RT/nF - RT/2nF \ln(D_{ox}^{1/2}/D_{red}^{1/2}) \quad [2.11]$$

$$E_{p,a} = E_C^{0'} - 1.109 RT/nF - RT/2nF \ln(D_{ox}^{1/2}/D_{red}^{1/2}), \quad [2.12]$$

where D_{ox} and D_{red} are the diffusion coefficient of the oxidant and reductant species, respectively. If the diffusion coefficients are similar, the relationship can be simplified to

$$E_{p,c} - E_{p,a} = 2.22 RT/nF . \quad [2.13]$$

For an irreversible reaction with a soluble reactant and soluble product, the relationships are

$$E_{p,c} - E_{1/2,c} = - 1.109 RT/nF, \text{ and} \quad [2.14]$$

$$E_{p,a} - E_{1/2,a} = + 1.109 RT/nF . \quad [2.15]$$

As $E_{1/2}$ is located very near midway between E_p and $E_{p/2}$, the above can be rewritten as

$$|E_{p,c} - E_{p/2,c}| = 2.22 RT/nF . \quad [2.16]$$

For an irreversible reaction with insoluble product, the quantity αn for a cathodic peak can be approximated from the expression

$$E_{p,c} - E_{1/2,c} = - 1.857 RT/\alpha nF . \quad [2.17]$$

This equation can then be used with a reasonable estimate of the transfer coefficient, α , to estimate the number of electrons transferred.

Similarly, for soluble-insoluble reactions in reversible systems, the Delahay relationship can be used to calculate the number of electrons transferred (38):

$$E_{p/2} - E_p = 0.7725 (RT + nF) \quad [2.17b]$$

where E_p is the peak potential and $E_{p/2}$ is the potential when the current is half of the peak current.

Square wave voltammetry may also be used to estimate the number of participating electrons for reversible systems (33, 39-41). The peak width is dependent upon temperature and the number of electrons in the reaction. A good estimate of the number of electrons can be obtained from the half-peak width for reversible soluble-soluble reactions from the relationship

$$W_{1/2} = 3.52 RT/nF, \quad [2.18]$$

where $W_{1/2}$ is the half-peak width. Square wave voltammetry can also be used for reversible soluble-insoluble reaction and yields most accurate results for reaction regions where the current density of the peak is linear with the square root of scanning frequency (42). This is quite often the case at lower frequencies, such as a few tens of hertz. In the case of soluble-insoluble reactions, sometimes the peaks are not fully symmetric, and this is generally due to a delayed deposition from nucleation overpotential. This effect can be minimized by reflecting the diminishing side of the peak, and using the new computed peak width with Eq. [2.18].

2.7.2 Oxidation States by Chronopotentiometry

The number of electrons involved in the reaction can also be determined with a CP method. For a reversible soluble-soluble reaction where the Sand equation is valid for the current density of interest, the transition time, τ , of the cathodic deposition, may be examined according to the equation (34, 43-45)

$$E = E^0 + \frac{RT}{nF} \ln \left(\frac{D_{red}}{D_{ox}} \right)^{1/2} + \frac{RT}{nF} \ln \left(\frac{\gamma_{ox}}{\gamma_{red}} \right) + \frac{RT}{nF} \ln \left(\frac{\tau^{1/2} - t^{1/2}}{t^{1/2}} \right). \quad [2.19]$$

However, in practice, this can be approximated by an equation of the form

$$E = a + b \ln \left(\frac{\tau^{1/2} - t^{1/2}}{t^{1/2}} \right) \quad [2.20]$$

or

$$E = \frac{2.3RT}{nF} \log \left(\frac{\tau^{1/2} - t^{1/2}}{t^{1/2}} \right), \quad [2.21]$$

and the number of electrons can be computed from the slope of the plotted line of potential, E versus $\log \left[\left(\tau^{1/2} - t^{1/2} \right) / t^{1/2} \right]$.

A different approach works better for irreversible conditions (34, 44-46) and has been found to work in some cases for the deposition of metals from molten salt systems (43, 47, 48). It is based on evaluation of concentration in a thin film by means of Laplace transform methods relating to the distance l between an electrode and parallel inert surface. That is, for situations when the transition time is sufficiently long such that $l^2 < \tau \cdot D$, the Laplace transform can be applied, and the transition time becomes [45]

$$\tau = \frac{nFAIC_{ox}^0}{i} - \frac{l^2}{3D}. \quad [2.22]$$

For a system that is Nernstian, at relatively substantial values of t , the potential versus time is

$$E = E^0 + \frac{RT}{nF} \ln \left(\frac{\tau - t}{t + \frac{l^2}{3D}} \right), \quad [2.23]$$

where the term $l^2/3D$ can be considered extremely small in comparison to t ; that is, $l^2/3D \ll t$.

Thus, Eq. [2.23] can be simplified to

$$E = \frac{2.3RT}{nF} \log \left(\frac{\tau - t}{t} \right). \quad [2.24]$$

In practice, E is plotted versus $\log \left[\left(\tau - t \right) / t \right]$, and n is determined from the slope of the resulting line.

2.8 Diffusion Coefficients

2.8.1 Diffusion Coefficients by Voltammetry

Diffusion coefficients may be determined through voltammetric methods by using one of several modifications of the Randles-Sevcik equation (Eq. [2.9]) (34, 44). For reversible soluble-soluble processes, the rate constant can be expanded to yield

$$i_p = 0.4463 nFSC (nFvD/RT)^{1/2}. \quad [2.25]$$

For reversible, soluble-insoluble processes, the Randles-Sevcik equation takes the form

$$i_p = 0.611 nFSC (nFvD/RT)^{1/2}. \quad [2.26]$$

Lastly, for soluble-insoluble reactions under conditions of complete irreversibility, the Nernstian boundary conditions are replaced and the equation developed along the same lines to yield

$$i_p = 0.496 FSC (\alpha FvD/RT)^{1/2}. \quad [2.27]$$

2.8.2 Diffusion Coefficients by Chronopotentiometry

Diffusion coefficients can be obtained from chronopotentiometric methods using the Sand equation (34, 49)

$$i\tau^{1/2} = \frac{nFSC_0(\pi D)^{1/2}}{2}. \quad [2.28]$$

The Sand equation only applies to relatively uncomplicated electrode reactions, and prior to use, it must be demonstrated that the transition time constant, $i\tau^{1/2}/C_0$, is not dependent upon the current or bulk concentration, if appropriate. In practice, i is plotted versus $\tau^{-1/2}$, for a series of chronopotentiometric runs at constant concentration and electrode area. If the resulting plot is linear, then the Sand equation may be applied, and the diffusion coefficient is obtained from the slope.

2.9 Equilibrium Potential

2.9.1 Equilibrium Potential by Voltammetry

The equilibrium potential may be estimated using a number of voltammetric methods (34, 36, 38, 44). One approach is to extrapolate the slope of the anodic peak back to zero current. Use of the anodic peak is generally more accurate than the cathodic peak due to the inherent sensitivities of nucleation processes, which can shift the onset of cathodic deposition.

Equilibrium potential can also be found by a very slow linear sweep in the anodic direction, as is done when obtaining a Tafel plot. The sweep in the anodic direction eliminates inaccuracies associated with nucleation. It is performed at a very slow sweep rate, on the order

of 1 mV/s, to ensure that the system is very near equilibrium. For a reversible system with a soluble reactant and product, the formal equilibrium potential can be calculated from combining Eqs. [2.14] and [2.15] to yield

$$E_{1/2} = (E_{p,c} + E_{p,a})/2. \quad [2.29]$$

At low concentrations, the Nernst equation simplifies to

$$E^* = E^0 + \frac{RT}{nF} \ln \left(\frac{\gamma_{ox}}{\gamma_{red}} \right). \quad [2.30]$$

And the half wave potential is

$$E_{1/2} = E^0 + \frac{RT}{nF} \ln \left(\frac{D_{red}}{D_{ox}} \right)^{1/2} + \frac{RT}{nF} \ln \left(\frac{\gamma_{ox}}{\gamma_{red}} \right). \quad [2.31]$$

Substitution of Eqs. [2.21] and [2.22] into [2.23] yields

$$E^* = \frac{(E_{p,c} + E_{p,a})}{2} - \frac{RT}{nF} \ln \left(\frac{D_{red}}{D_{ox}} \right)^{1/2}. \quad [2.32]$$

For a reversible soluble-insoluble system, the cathodic peak potential is described by

$$E_{p,c} = E^0 + \frac{RT}{nF} \ln \left(\frac{a_{ox}}{a_{red}} \right) - 0.854 \frac{RT}{nF}. \quad [2.33]$$

And the relationship between apparent standard potential and standard potential now has the form:

$$E^* = E^0 + \frac{RT}{nF} \ln(\gamma_{ox}). \quad [2.34]$$

When these are combined, the equation to find the apparent standard potential using voltammetry is

$$E_{p,c} = E^* + \frac{RT}{nF} \ln(X_{ox}) - 0.854 \frac{RT}{nF}. \quad [2.35]$$

2.9.2 Equilibrium Potential by Chronopotentiometry

The equilibrium potential may also be determined by chronopotentiometric methods for soluble-insoluble couples. The potential of a mass of metal at relevant concentration conditions is measured relative to a reference electrode. This so-called open circuit potential of the metal of interest should be monitored for a period of time to ensure transient effects have been minimized.

2.10 Exchange Current Density

A reduction-oxidation reaction held at the equilibrium potential is not static; electron transfer reactions are occurring simultaneously in both directions at an equivalent rate. This equilibrium rate for both the anodic and cathodic reactions is known as the exchange current density, i_0 . The exchange current density is closely related to nucleation and deposition processes, as well as the resulting morphology of the deposits. An understanding of i_0 and knowledge of the parameters which influence its value are important in order to gain insight into deposition and morphology.

2.10.1 Exchange Current Density by Tafel Method

Here, the Butler-Volmer equation is used to describe the relationship of net current to the applied potential and generally takes the form

$$i = i_c - i_a = i_0 \left\{ \exp \left[\frac{\alpha n F}{RT} (E_{eq} - E) \right] - \exp \left[-\frac{(1-\alpha) n F}{RT} (E_{eq} - E) \right] \right\}, \quad [2.36]$$

where the symmetry factor α and $(1-\alpha)$ are the fractions of the overpotential which contribute to the cathodic and anodic reactions, respectively. In situations of relatively high cathodic current density, the term on the right-hand side corresponding to i_a is very small and can be neglected, and the equation can be simplified to

$$i = i_c = i_0 \left\{ \exp \left[\frac{\alpha n F}{RT} (E_{eq} - E) \right] \right\}. \quad [2.37]$$

This can be rearranged in the form

$$(E_{eq} - E) = \frac{2.3RT}{\alpha n F} \log \frac{i_c}{i_0}. \quad [2.38]$$

The quantity $(E_{eq} - E)$ is the cathodic overpotential, often written as η_c and Eq. [2.38] may be rewritten as

$$\eta_c = \frac{2.3RT}{\alpha n F} \log i_0 - \frac{2.3RT}{\alpha n F} \log i_c, \quad [2.39]$$

where η_c is the cathodic overpotential. This matches the empirical form originally described by Tafel; that is,

$$\eta_c = a + b \log i_c. \quad [2.40]$$

It also commonly takes the form

$$\eta_c = \beta_c \log \frac{i_c}{i_0}, \text{ where} \quad [2.41]$$

$$\beta_c = \frac{2.3RT}{\alpha nF}. \quad [2.42]$$

For each reaction, the Tafel equation is used twice to describe both the cathodic and anodic half reactions. Thus, there is a parallel equation to [2.36] for the anodic side, which is

$$\eta_a = \beta_a \log \frac{i_a}{i_0}, \quad [2.43]$$

where $\eta_a = -\eta_c$. [2.44]

In practice, experimental data are obtained and the slope of the line is used to compute α . The intercept at $\eta = 0$ yields i_0 .

2.10.2 Exchange Current Density by Linear Polarization Method

A linear relationship between $\log(i)$ and overpotential is often considered an indication of a reaction region where the reaction is controlled by charge transfer. For processes with low activation energy such as some high temperature systems, it can be difficult to determine the linear region of a Tafel plot, or one may not exist at all. In other cases, rapid surface area change, or the formation of electrode films may complicate the evaluation. In these cases, it may be possible to instead utilize the linear polarization method to determine exchange current density (50-52). This method is most commonly employed to study corrosion current density but applies equally well to the determination of exchange current density of a metal surface in molten salt.

The method also begins with the Butler-Volmer equation (Eq. [2.36]). When the overpotential, equivalent to $(E_{eq} - E)$, is low, the term

$$\left[\frac{\alpha nF}{RT} (E_{eq} - E) \right] \quad [2.45]$$

will be $\ll 1$, allowing the exponential terms in the Butler-Volmer equation to be expanded by the power series method. Returning to Eqs. [2.41] and [2.43], we can rewrite them as

$$\frac{\eta_c}{\beta_c} = \log \frac{i_c}{i_0} \quad [2.46]$$

or

$$10^{\eta_c/\beta_c} = \frac{i_c}{i_0}. \quad [2.47]$$

This is similar for the anodic component as well. The powers series expansion is given by

$$10^x = 1 + 2.3x + \left[\frac{(2.3x)^2}{2!} \right] + \dots \quad [2.48]$$

When x is very small, Eq. [2.48] can be approximated by using only the first two terms on the right. Therefore, Eq. [2.47] can be approximated by

$$10^{\eta_c/\beta_c} \cong 1 + 2.3 \frac{\eta_c}{\beta_c}. \quad [2.49]$$

Placing Eq. [2.49] back into [2.47] yields

$$i_c = i_0 \left(1 + 2.3 \frac{\eta_c}{\beta_c} \right). \quad [2.50]$$

By remembering the definition of net current, which is $i = i_c - i_a$, and that $\eta_a = -\eta_c$ (see Eq. [2.39]), Eq. [2.36] can be expressed as

$$i = i_0 \left\{ \left(1 + 2.3 \frac{\eta_c}{\beta_c} \right) - \left(1 - 2.3 \frac{\eta_c}{\beta_a} \right) \right\}. \quad [2.51]$$

This can then be manipulated in two steps:

$$i = 2.3 \cdot i_0 \left\{ \frac{\eta_c \beta_a}{\beta_c \beta_a} + \frac{\eta_c \beta_c}{\beta_a \beta_c} \right\}, \text{ and} \quad [2.52]$$

$$i = 2.3 \cdot i_0 \cdot \eta_c \left\{ \frac{\beta_a + \beta_c}{\beta_a \beta_c} \right\}. \quad [2.53]$$

Previously for the Tafel method, relationships for β were established in Eqs. [2.42] and [2.43].

Therefore, Eq. [2.53] can then be reduced to the simple relationship

$$i = i_0 \cdot \eta_c \left[\frac{nF}{RT} \right] \quad [2.54]$$

In practice, current is plotted at very low overpotentials near the equilibrium potential ($\sim \pm 10$ mV) and i_0 is obtained from the slope.

2.11 Nucleation Mode

When a material is nucleated on a foreign substrate, chronoamperometry can be used to learn about the characteristics of the initial nuclei. A short range of potentials exists, within a few tens of millivolts above the equilibrium potential, where a nucleation peak can often be seen. When a constant potential is applied, charging of the double layer typically generates an initial spike in current, following which the current dips as the first nuclei are created. The current then rises as the crystals grow and reaches a maximum value as the individual diffusion zones overlap. The peak position shifts earlier and the height of the peak increases as the applied overpotential increases, and eventually the peak merges into the capacitive current. This is due to the much broader coverage of the surface with nuclei and the generally higher currents caused by the greater overpotential (53-56). These processes can be seen in Figure 2.1.

In progressive nucleation, new nuclei are constantly being generated, even on the surface of existing crystals. However, in the case of instantaneous nucleation, all nuclei are created at the beginning of the electrochemical pulse. Deposition of metals from high temperature molten salts usually involves instantaneous nucleation, and this mode promotes the formation of dendrites. If conditions or parameters can be found where the nucleation shifts to progressive mode, dense deposition may be more easily achieved.

2.11.1 Nucleation Mode by Simple Theoretical Method

For the rising portion of the nucleation curve, the relationship between the current rise and time can be described by an equation of the form (53, 57-59)

$$i \propto t^x \quad [2.55]$$

where x varies according to the type of nucleation. In Eq. [2.55], x equals 1/2 in the case of instantaneous nucleation and 3/2 in the case of progressive nucleation. It is typical to plot the

values of i versus t^x for the range of nucleation curves and determine by observation which value of x provides the most accurate fit.

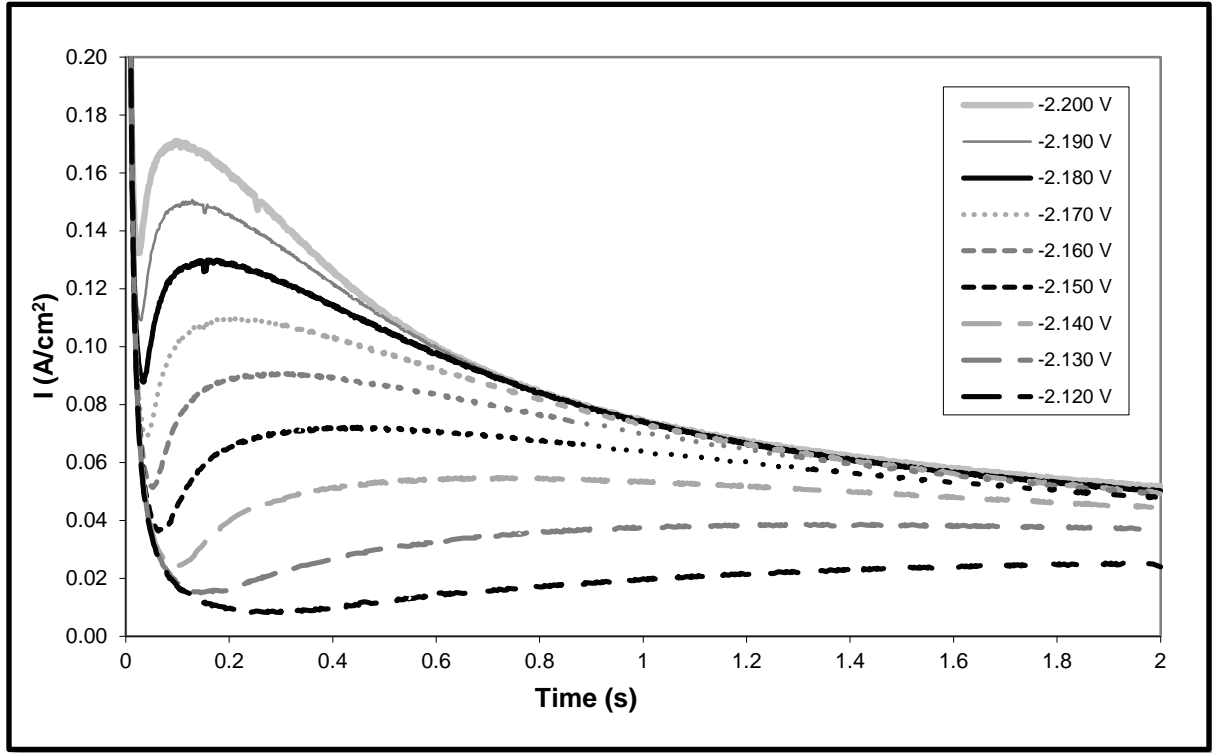


Figure 2.1: An example of nucleation curves; yttrium in LiCl-KCl at 653 K on tungsten electrode.

2.11.2 Nucleation Mode by Scharifker and Hills Dimensionless Method

Scharifker and Hills (53) also developed dimensionless theoretical models describing the peak current for instantaneous and progressive nucleation. In the case of instantaneous nucleation, the model takes the form

$$\left(\frac{I}{I_m}\right)^2 = \frac{1.9542}{(t/t_m)} \cdot [1 - \exp\{-1.2564(t/t_m)\}]^2 \quad [2.56]$$

where

$$t_m = \frac{1.2564}{N_0 \pi k D}, \quad [2.57]$$

$$k = \left(\frac{8\pi C_0 M}{\rho}\right)^{1/2}, \quad [2.58]$$

$$I_m = -0.6382nFD C_0 S (kN_0)^{1/2}, \text{ and} \quad [2.59]$$

$$I_m^2 t_m = 0.1629(nFSC_o)^2 D \quad [2.60]$$

Here, N_0 is the initial number of crystallites, M is the molecular weight of the deposited species and ρ is its density.

For progressive nucleation, the equations are

$$\left(\frac{I}{I_m}\right)^2 = \frac{1.2254}{(t/t_m)} \cdot [1 - \exp\{-2.3367(t/t_m)\}]^2 \quad [2.61]$$

where

$$t_m = \frac{4.6733^{1/2}}{AN_0 \pi k' D}, \quad [2.62]$$

$$k' = \frac{4}{3} \left(\frac{8\pi C_0 M}{\rho} \right), \quad [2.63]$$

$$I_m = -0.4615nFD^{3/4}C_oS(k'AN_0)^{1/4}, \text{ and} \quad [2.64]$$

$$I_m^2 t_m = 0.2598(nFSC_o)^2 D \quad [2.65]$$

In practice, the value I/I_m^2 is plotted versus t/t_m for the model predictions along with the actual data at various nucleation overpotentials. The data typically will clearly follow one or the other relationship. The theoretical relationship can be seen in Figure 2.2. In addition, Eqs. [2.56] and [2.61] can also be used as a chronoamperometric method to compute D .

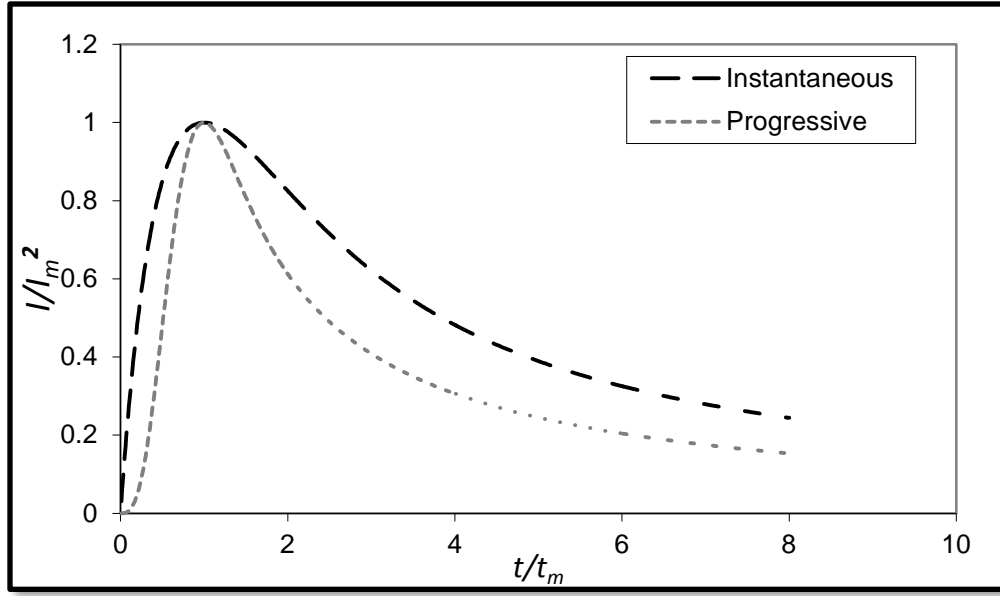


Figure 2.2: Theoretical nucleation behavior as predicted by Sharifker and Hills (53).

CHAPTER 3. LITERATURE REVIEW

This chapter is organized to include initial topics of critical importance to molten salt studies in fused LiCl-KCl. These include how reference electrodes are used by different research groups to measure electrochemical potentials (Section 3.1); the importance of thermodynamic databases when comparing computed data (Section 3.2); the impacts of crucible material selection upon valid and reproducible data (Section 3.3); and the nature and importance of complexes (Section 3.4) and exchange current density (Section 3.5) within molten salt electrochemistry. The following sections review the range of electrochemical data available in published studies for cerium (Section 3.6) and the actinoid elements (Section 3.7). Section 3.8 provides a review of product purity achieved in various studies of molten salt electrorefining. The final section provides a survey of electrochemical properties for actinoid and lanthanoid species in fused LiCl-KCl eutectic.

3.1 The Ag^+/Ag^0 Reference Electrode

Different research groups often perform and present research studies in slightly different ways, such as through the use of different types of reference electrodes or use of different concentrations within a reference electrode system. Potentials relative to the reference electrode are often converted to potentials relative to the Cl_2/Cl^- couple, in order to compute thermodynamic data. In the case of the common Ag^+/Ag electrode system, its relationship relative to Cl_2/Cl^- is commonly based on the works of Yang and Hudson (27, 28), although the data of Laitinen and Liu (29), Salstrom (30, 31), and Takahashi and Amada (32) have been occasionally cited. Unfortunately, the Yang and Hudson Ag^+/Ag data were obtained at concentrations and temperatures greater than those typically used in reference electrode systems of most researchers today. Furthermore, the data sets show a reversal of temperature dependence at the lowest concentration tested, displaying clearly a non-Nernstian behavior. This is most likely caused by variation in Ag^+ activity coefficient, which is known to vary modestly with concentration (60). In each case, the predicted apparent standard potential E^* depends on the exact details of the extrapolation, and the accuracy is also a function of how far the reference electrode $[\text{Ag}^+]$ lies from that measured in the original Ag^+/Ag data. These are

generally presented in the form of predicted potential, E , convenient for that experiment set, and these relationships have been converted to apparent standard potential, E^* , through Eq. [2.8] to enable more clear comparison. At least five independent extrapolations of $E_{Ag^+/Ag}^*$, all derived from Yang and Hudson data, are found in the literature including: Roy and co-workers (61)

$$E_{Ag^+/Ag}^* = -1.0432 + 0.000374 T (K); \quad [3.1]$$

Kuznetsov and colleagues (43) found

$$E_{Ag^+/Ag} = -1.0651 - 0.0001805 T (K) \quad [3.2]$$

Looking back at Eq. [2.8]

$$E = E^* + RT/nF \ln(X_{ox}/X_{red}), \quad [2.8]$$

and entering the concentration of AgCl used in their system, the relationship can be converted to terms of $E_{Ag^+/Ag}^*$,

$$E_{Ag^+/Ag}^* = -1.0659 + 0.0002974 T (K); \quad [3.3]$$

Marsden and Pesic (18) reported the $CeCl_3$ electrochemical behavior by converting into terms of $E_{Ag^+/Ag}^*$

$$E_{Ag^+/Ag}^* = -0.9716 + 0.0001280 T (K); \quad [3.4]$$

Caravaca and co-workers (62) use an expression from Mottot (63) for their gadolinium study in molten LiCl-KCl, and when converted to mole fraction is

$$E_{Ag^+/Ag}^* = -1.224 + 0.000292 T (K); \quad [3.5]$$

and Roy et al. (64) and Fusselman et al. (65) utilize the expression given below

$$E_{Ag^+/Ag}^* = -1.0910 + 0.0002924 T (K). \quad [3.6]$$

The predictions of $E_{Ag^+/Ag}^*$ can be seen in Figure 3.1. Three of these are parallel lines due an assumption of Nernstian behavior, while two of them attempt to account for the variation with temperature seen in the data of Yang and Hudson. These results indicate that the differences can be quite significant, despite being derived from the same data set. The equation of Roy and

Fusselman is very nearly identical to that predicted from thermodynamic data (66) for an activity coefficient of unity.

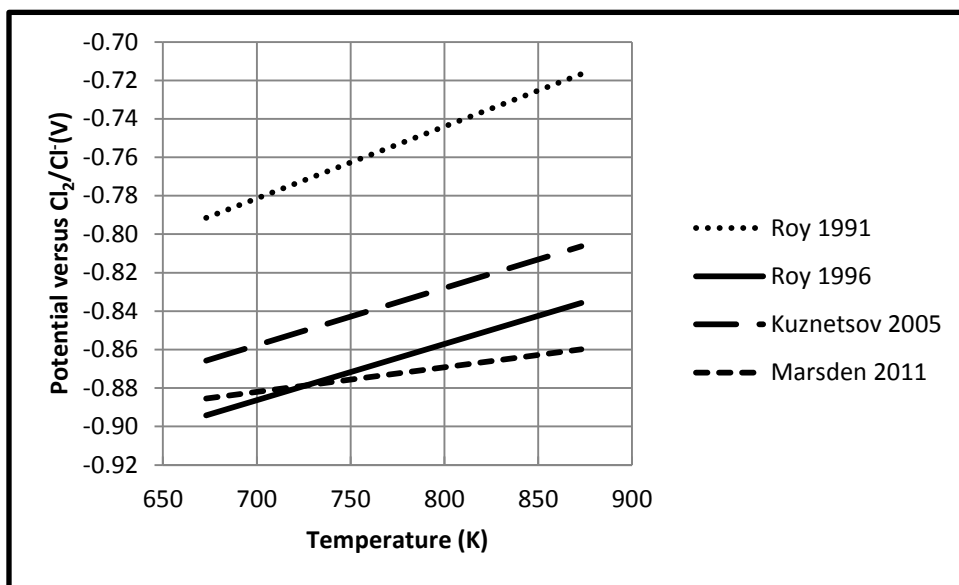


Figure 3.1: Estimations of E_{AgCl}^* from Roy (61), Roy (64), Kuznetsov (43), and Marsden (18) from the data of Yang and Hudson (28).

Many other studies do not publish the relationship utilized to convert voltages versus the Ag^+/Ag reference to Cl_2/Cl^- . Of the listed equations, Eq. [3.6] used by Roy et al. [58] and Fusselman et al. [59], is arguably the most common and has been adopted by several research groups. For this reason, it is selected as the common reference for this work.

Some investigators have reported data in the molality scale and some in the mole fraction scale, which generally creates a difference of approximately 0.060 V versus the Cl_2/Cl^- electrode for a three electron transfer (29). The present work has selected the mole fraction scale, and data are converted to this basis for comparison. However, published studies do not always state in which scale the electrochemical potential data are presented. Furthermore, it is not unusual to find authors unknowingly comparing data from different concentration scales. This issue is likely a contributing factor in the scatter values listed in property summary tables.

Further elucidation of the Ag^+/Ag couple would be extremely valuable, specifically near 723-773 K and between 1 wt% and 0.75 mol·kg⁻¹ AgCl (0.0039 and 0.0419 mole fraction, respectively), as these conditions are most often utilized. Some literature data presented in this

work for apparent standard potential of the lanthanoids, obtained at various $[Ag^+]$, were converted using the Nernst equation,

$$E = E_{M^n}^* + \frac{RT}{nF} \ln X_{M^n} + \frac{RT}{nF} \ln \gamma_{M^n} - E_{Ag^+/Ag}^* - \frac{RT}{F} \ln X_{Ag^+} \quad [3.7]$$

with $E_{Ag^+/Ag}^*$ obtained from Eq. [3.5].

3.2 Thermodynamic Databases for Gibbs Free Energy of Formation

Another point of difference between published studies is the thermochemical database used to obtain data. To estimate activity coefficients and the energy of solvation, the experimental data of the metal dissolved in LiCl-KCl eutectic must be compared with data for Gibbs free energy of formation, ΔG_f , from the reaction of the metal, M . To compute ΔG_f , the reaction is



Several thermodynamic databases (67-71) are utilized in the literature, adding one more point of discrepancy between various published studies. Thermodynamic values differ between the databases by only a few percent. However, these minor differences in the thermochemical databases can be magnified during computations of activity coefficient. The present work utilizes both the thermochemical database edited by Pankratz (67) and the more recent database by Barin (68).

3.3 Crucible Materials and Purification

It should be recognized that both lithium chloride in the LiCl-KCl eutectic and the lanthanoid and actinoid chlorides are very hygroscopic, and most researchers utilize commercially available high-purity anhydrous salts whenever available rather than purify their own. Beads of LiCl-KCl eutectic are available with less than ~ 50 ppm moisture content, as determined by Karl Fischer titration. Moisture has considerable solubility in LiCl-KCl eutectic (72) and is very difficult to remove by vacuum drying. If extreme care is not taken, hydrolysis may occur during heating, producing soluble hydroxides. The purge of dry chlorine (73) or HCl (74) through the fused electrolyte, followed by a flush with bubbled argon, has been found effective to eliminate hydroxides. In addition, some experimenters purify their melts by

sustained pre-electrolysis at potentials slightly more positive than the equilibrium potential of the most noble electrolyte constituent (75-78). The electrodes used to remove the contaminants are then immediately removed from the electrolyte.

Lanthanoid and actinoid metals and chlorides are very reactive toward ceramic oxide crucibles or instrumentation sheaths (18, 79-82). New species, most probably oxychlorides of the salt and/or container cations, appear on cyclic voltammetry scans (80), and an electrically conductive film can form on ceramic surfaces (18). As a consequence, when in contact with oxide ceramics, the concentration of the rare earth chloride may change as a function of time and temperature. Oxygen-free containment materials such as glassy carbon or metals avoids this issue, but oxide crucibles can be utilized with careful pre-purification of the salt, short duration at temperature, and closely coupled sampling, such as the methods employed by Castrillejo and coworkers. (83).

Salt samples should be taken while the bulk salt is molten, as the zone refining effect may create heterogeneity during the freezing process (84). The potential for the presence of metal particulate in the salt sample should also be considered. Salts which are expected to remain anhydrous should be stored and handled under high-purity inert atmosphere. It is a reasonable practice to perform cyclic voltammetry scans of the LiCl-KCl electrolyte to verify the absence of contaminant peaks and a background current of 1 mA/cm² or less, depending on the nature of the studies to be performed. Another technique to identify the presence of impurities is inconsistency in repeated voltammetric scans, particularly the observation of a progressive change in peak amplitude on multiple scans.

3.4 Molten Salt Complexes

In a solid form, the actinoid and lanthanoid elements take crystal structures with coordination numbers ranging from 6 to 9 (85) and form compounds of the type A₃MCl₆ (86), where M is the metal of interest and A is an alkali metal such as Na, K, or Cs. The existence of compounds—more frequently described as complexes due to their dynamic, transient nature—of this type in high-temperature molten salt systems has long been proposed due to observations from a number of physicochemical properties (87). The effect of complexation can

be indirectly deduced by several means, including differences between apparent standard and standard potential, examination of expected versus actual conductivity or viscosity changes for incremental substitution, association of diffusion properties (88) with ionic radius, and observation of changes in entropy upon melting.

A difference between apparent standard and standard potentials arises when chemical activity is less than unity, and this difference indicates a possible chemical engagement in the melt. A minimum in conductivity or maximum in viscosity (87) may indicate the complexation of ions into larger units, reducing effective ion mobility. Kovalevskii and Shishalov (89) studied the electrical conductivity of rare earth chlorides in LiCl-KCl eutectic and concluded that the formation of complexes reduces the conductivity of the mixture. The reduction was observed to be a function of ionic radius, and it was concluded that the smaller radius was associated with stronger complexes. Akdeniz and Tosi (90) observed an abnormally low entropy change in trihalides upon melting, and this was interpreted as an evidence of strong remnants of order within the melt.

Essentially all modern studies concur with the existence of complexes of the rare earths in LiCl-KCl eutectic. Complexes have been studied by Raman spectroscopy (86, 91, 92), electronic absorption spectra (93, 94), x-ray (95), neutron diffraction (96, 97), and ionic modeling (98). The solid crystal structure of the heavy rare earths (having smaller ionic radii), including Y and Dy through Lu, is an octahedral structure with 6-fold coordination. The studies agree that these elements retain this octahedral MCl_6^{3-} structure upon melting. However, there are disagreements regarding the molten structure of the light rare earths, La through Gd. Some Raman (86, 92, 99, 100), diffraction (101), and electronic (93) studies conclude that the octahedral MCl_6^{3-} is the dominant species common to Y and all of the lanthanoids. Other diffraction studies (95, 96, 102-104) find evidence that the light lanthanoid elements have an average coordination number greater than 6, possibly dominated by a distorted octahedral with 7-fold coordination, MCl_7^{4-} . This position is also supported by polarizable ion simulation models (105, 106). Recent detailed diffraction work (107) shows that both positions are likely correct, as the average coordination number for $LaCl_3$ changes as a function of the alkali

metal(s) and concentration with which it is diluted. In the case of 0.01 mole fraction LaCl_3 in LiCl-KCl eutectic, it was found that LaCl_3 existed in mixture of 6- and 7-coordinated species, MCl_6^{3-} and MCl_7^{4-} . This was similar to conclusions made regarding UCl_3 in LiCl-KCl eutectic, which has similar ionic radius (108-110).

Scandium chloride has a small ionic radius, similar to AlCl_3 , and these two have similar physicochemical properties. It is coordinated to approximately 5 Cl⁻ ions in a complicated melt structure, for which octahedral MCl_6^{3-} appears to be one of several species present (98, 104, 111, 112). This observation further supports the importance of ionic radius in the complex ion.

A clear picture of the structure of the divalent lanthanoids in LiCl-KCl eutectic is yet to emerge. In NaCl-KCl melts, the diffusion coefficient of Eu was found to approximately double as the oxidation state is reduced from Eu(III) to Eu(II) (113, 114). This increase is consistent with correlations of diffusion coefficients versus the oxidation state of the central cation (115), and increased diffusion would be expected for lower-strength complexes of Eu(II). Raman spectroscopy of EuCl_2 in NaCl suggested that complex species were possibly not formed at all (116). However, studies of Eu (117) and Yb (118) in LiCl-KCl eutectic found the diffusion coefficients of the tri- and bivalent species to be essentially identical, suggesting complexes of similar stability. Studies of divalent alkaline earth chlorides with similar ionic radii to the divalent rare earths show localized structure with average cation-anion coordination number in the range of 5-7 (97, 119), which is similar to trivalent lanthanoid chlorides. It is difficult to reconcile these apparent differences without further information about the characteristics of divalent lanthanoid chlorides.

Examination of trends with the molten salt complexes also provides information about other properties. Two detailed studies of the enthalpy of mixing of Eu chlorides conducted by Kuznetsov and co-workers (120, 121) show that the stability of the molten salt complexes, as measured by enthalpy of mixing, increases for larger alkali metal cation size in the electrolyte. It can then be expected that the activity coefficient will decrease as larger alkali metal cations, $\text{Li}^+ \rightarrow \text{Na}^+ \rightarrow \text{K}^+ \rightarrow \text{Cs}^+$, are substituted in the dilutant. The increase in stability of the complexes is accompanied by a corresponding decrease in diffusion coefficients as larger alkali

metal cations join the complex. This conclusion was confirmed by the work of Papatheodorou and Ostvold (122) with lanthanum chloride-alkali chloride mixtures.

In addition to larger alkali cations stabilizing the complex, smaller central cations appear to provide similar effect. Raman spectroscopy studies (99) show increasing network cohesion from LaCl_3 to YCl_3 , indicating a more rigid network with longer MCl_y^{X-} lifetime. The movement of the smaller cations is increasingly inhibited, in contradiction with Stokes' law, and this observation has also been made in limited studies of lanthanoid diffusion coefficients (123-125). The increasing strength of rare earth complexes as the ionic radius decreases also manifests in other ways, such as increased energy of solution and smaller activity coefficients (125, 126), and the ionization energy of metal cations from their complexes (127).

3.5 Exchange Current Density in Fused Salt Systems

Morphology of an electro-crystallized product is partially a function of i_0 at different deposition conditions. Thus, it is important to understand i_0 of the element of interest relative to other elements present. Information on i_0 of cerium or other lanthanoids is sparse. Moreover, many of the data that have been published for other metals in LiCl-KCl are highly inconsistent, with data varying by 3 orders of magnitude between investigators, with the discrepancy appearing to be largely dependent upon different electroanalytical techniques (128-131). This was largely explained by Settle and Nagy (132), who reviewed the data of the literature and performed a comparative error analysis showing that classic techniques must be used for the fast molten salt reactions only with great care, lest grossly erroneous measurements result. They found that a systematic error can occur if the reaction rate is much faster than the diffusion rate. In the present work, this potential issue is circumvented by use of the linear polarization method.

There are several studies for uranium in fused LiCl-KCl eutectic. Choi and coworkers (133) measured i_0 of uranium coated on a tungsten wire in LiCl-KCl at 773 K with the linear polarization technique. They found it to be in the range of 0.02-0.06 A/cm² for a melt of 3.27 wt% UCl_3 (~0.006 mole fraction) at 773 K. Gosh et al. (134) performed anodic dissolution

experiments to obtain anodic and cathodic Tafel constants for uranium. They estimate i_0 of 0.006-0.07 A/cm² at 773 K. Rose, Williamson and Willit performed similar studies with a uranium rod of 6-mm diameter (135). They found the relationship for i_0 can be expressed by

$$i_0 = 20396e^{-\frac{4143}{T(K)}} \left(\frac{A}{cm^2} \right), \quad [3.9]$$

corresponding to approximately 0.096 A/cm² at 773 K. Cumberland and Yim (136) performed a computational meta-analysis of CV obtained from literature data sets and estimated the standard exchange current density, i_0^0 , of uranium to follow the expression:

$$i_0^0 = 13281e^{-\frac{60362}{RT(K)}} \left(\frac{A}{cm^2} \right), \text{ where} \quad [3.10]$$

$$i_{0,X} = i_0^0 \cdot X. \quad [3.10a]$$

The value for i_0^0 corresponds to a value of ~ 1.1 A/cm² at 773 K. Values of i_0 for other actinoids have not been reported in the literature.

3.6 Cerium Electrochemistry in Fused LiCl-KCl Eutectic

In addition to its general industrial importance as a light lanthanoid, cerium may potentially be useful as a surrogate for the behavior of actinoids in molten salt. The use of a non-radioactive surrogate offers significant advantages during the initial phases of technology development. Cerium has similar ionic size and an electrochemical potential that is nearer to uranium and plutonium than most lanthanoids (18).

Several prior investigations have been conducted on the electrochemistry of cerium in molten LiCl-KCl eutectic. Betancourt and Nattland (137) investigated the trivalent cerium chloride system using Raman spectroscopy and found it exists as an octahedral LnCl_6^{3-} species. Castrillejo et al. (138, 139) studied the electrochemical behavior of Ce(III) at 723 K. They found the system to be a quasi-reversible, three-electron reaction and determined the apparent standard potential and diffusion coefficient. Iizuka (123) utilized chronopotentiometry to determine the diffusion coefficient from 673 to 873 K. Fusselman et al. (65) measured the apparent standard potential between 673 and 773 K, while Lantelme et al. (125) measured it

between 650 and 880 K. A recent study by Yoon and Phongikaroon (140) provided thermodynamic and electrochemical properties at a range of CeCl_3 concentrations (0.5 – 4 wt%) and temperatures (698 to 798 K) via both CV and electrochemical impedance spectroscopy.

Nucleation characteristics of Ce from solutions of LiCl-KCl- CeCl_3 are not found in the literature prior to the present work (18). Values of i_0 were published recently by Yoon and Phongikaroon (140) and found to be $\sim 0.146 \text{ A/cm}^2$ at 773 K for a concentration near 1 mol%. Summary tables for oxidation states, diffusion coefficients, and apparent standard potentials of cerium and other lanthanoid elements in LiCl-KCl eutectic are presented in Section 3.9.

3.7 Actinoid Electrochemistry Investigations in Fused LiCl-KCl Eutectic

Due to interest in pyrochemical reprocessing, uranium electrochemistry in fused LiCl-KCl eutectic has been explored by a range of investigators (6, 16, 43, 64, 134-136, 141-145). Most authors report the U(IV)/U(III) couple (see Figure 7.4a) to be diffusion controlled at low scan rates with a transition to mixed control above 200–300 mV/s scan rates (6, 142), and the U(III)/U(0) reduction to be a three-electron reaction with similar transition of reversibility (6, 16, 43, 142). Many investigators also report an adsorption pre-peak preceding the reduction to uranium metal (16, 43, 142, 145). These studies provide diffusion coefficients and standard potentials across 723–823 K at a range of concentrations. Modeling and x-ray diffraction studies indicate that dilute UCl_3 in LiCl-KCl eutectic exists as a mixture of six- and seven-coordinated species, MCl_6^{3-} and MCl_7^{4-} (108-110), identical to lanthanoid elements of similar ionic radii. However, Polovov and coworkers found that UCl_4 in 3LiCl-2KCl melt led to formation of UCl_6^{2-} (146).

Neptunium displays electrochemical characteristics similar to that of uranium. Fully chlorinated neptunium chloride is reduced to metal via two transitions, Np(IV)/Np(III) and Np(III)/Np(0) (147). Both reactions were found to be reversible below a scan rate of approximately 200-300 mV/s at 773 K. A pre-adsorption peak is observed at low concentrations prior to the Np(III)/Np(0) reduction (147). Diffusion coefficients and apparent standard potentials have been measured between 723 and 823 K (64, 141, 143, 146, 147).

Plutonium is found to reduce to metal in a single-step, three-electron transfer and is purely diffusion-limited below 200–300 mV/s scan rates (142, 148). A pre-adsorption peak is reported for the Pu(III)/Pu(0) reduction (142, 148). Apparent standard potentials and diffusion coefficients have been measured between 723 and 823 K (64, 141, 143, 148). Studies of the nature of Pu(III) complexes in LiCl-KCl are not found in the literature.

Summary tables for uranium, plutonium, and neptunium properties are provided in Section 3.9.

3.8 Purity of Molten Salt Electrorefining Products

The electrorefining of metals in molten salts has been performed for many years. The most well-known process is arguably that developed by Hall and Héroult for aluminum in the late 1800s. Aluminum is now produced world-wide by electrorefining processes with a typical product purity of 99.6–99.85%. If further purification is required, a secondary electrorefining process is sometimes performed to increase the purity to approximately 99.99% (149, 150).

Kononov et al. (151) presents a summary of electrorefining purity for tantalum, hafnium and scandium. The level of purification from different impurity species is highly dependent upon proximity of electrochemical potential. For example, the electrorefining of tantalum results in a reduction of niobium impurities by approximately a factor of 10. While details of the niobium concentration in the salt are not provided, it is reasonable to assume the salt of a commercial electrorefining operation is maintained in a relatively pure state.

Nagai and co-workers (152) studied the purity of gadolinium by molten salt electrorefining, and concluded that the purity of the product was strongly dependent upon the purity of the salt. Their experimental results revealed that concentrations of aluminum were reduced from ~70 ppm in the anode to ~20 ppm in the cathode. However, pre- and post-test magnesium concentrations, near 10–20 ppm, were essentially unchanged.

Sharma and Mukherjee (153) investigated electrorefining of silicon in molten electrolyte and found that product purities could approach 99.99%. The electrolytes used were quite pure. Lai et al. (154) reported a very specific molten salt electrorefining apparatus to produce high

purity silicon with respect to boron and phosphorus contaminants. Their device was claimed to reduce boron concentrations from ~12 to 3 ppm and phosphorus from ~100 to ~5 ppm but did not clearly evaluate levels of other impurities.

Lei and coworkers (155)(156) studied the production of vanadium in a two-step molten salt electrorefining operation with vanadium carbide as the initial anode material. The first step yielded vanadium of 99% purity and the second step 99.9% purity. They observed a decrease in purity as vanadium was depleted and impurities became increasingly concentrated at the anode. Tripathy et al. (157) later studied the electrorefining of vanadium with a different feedstock and molten bath. The main objective of these studies was to increase the vanadium purity, especially relative to carbon contamination. Results showed that it was possible to achieve vanadium of 99.85% purity with a single stage of electrorefining.

McCawley (158) described a molten salt electrorefining process for molybdenum, which was capable to produce molybdenum of 99.94% purity when charged with clean electrolyte.

Mullins and Leary (159) provided a summary of electrorefining of plutonium at an intermediate scale of 40 kilograms per month from molten salts. Here, products were generally of 99.98% purity. Specifically, this electrorefining process was able to reduce americium concentration from 100–200 ppm to about 20–30 ppm.

Marzano and Noland (160) studied the purity of uranium electrorefining at a laboratory scale and found that the impurity quantities of silicon and manganese were reduced by a factor of 10–100, with magnesium and nickel reduced by at least that same factor. They also found that the purification was a function of temperature with lower temperature operation yielding purer product. However, they did not study the effect of impurity concentration in the electrolyte but note that it would be expected to negatively affect product purity.

3.9 Survey of Lanthanoid and Actinoid Properties in Molten LiCl-KCl

3.9.1 Oxidation States of Lanthanoid and Actinoid Species

Table 3.1 and Table 3.2 list the reported oxidation states of the lanthanoid elements in LiCl-KCl eutectic, as observed in the listed studies. Table 3.3 lists the stable oxidation states of the actinoids. The oxidation states are determined by a number of methods in the various investigations. The two most common methods are (1) through determination of the slope of an isothermal Nernst plot and (2) by square wave voltammetry. In the case of the Nernst plot, for a varying concentration, the quantity

$$E - (RT/nF) \ln X \quad [3.11]$$

is plotted.

While the square wave voltammetry method is intended for soluble-soluble reactions in a reversible region, the half-peak width described by Eq. [2.18] can be applied to soluble-insoluble reactions. Researchers also often use the Delahay relationship, Eq. [2.17b], for peak potential for an insoluble product to calculate the number of electrons transferred (38). In addition to these electroanalytical techniques, one study utilized UV-visible spectroscopy to identify species in situ (13), and the early work of Johnson and Mackenzie (79) used careful observation of potentials to draw conclusions regarding oxidation state.

As seen in Table 3.1 and Table 3.2, investigators agree that the stable oxidation states in LiCl-KCl eutectic for Sc, Y, La, Ce, Pr, Gd, Tb, Ho, and Er are three (III) and zero (0). Only one investigation of Lu is available, but it is of high quality and also indicates (III) and (0) oxidation states. Investigators also agree upon stable oxidation states of (III) and two (II) for Sm, Eu, and Yb. If these metals are immersed in LiCl-KCl eutectic, they exothermically react to produce free lithium, according to the reaction



The metals Nd, Dy, and Tm are more complicated and display stable trivalent, divalent, and fully reduced species, (III), (II), and (0), within the electrolyte window. Conclusions regarding Nd have been inconsistent until the last decade, with the challenge being that the Nd(III)/Nd(II)

transition occurs very near the peak for full reduction to Nd(0). These two transitions can appear merged into a single peak on voltammetric scans, and the Nernst (Eq. [3.8]) and Delahay (Eq. [2.17b]) methods fail to distinguish the separate transitions. However, upon application of square wave voltammetry, as performed in the works of Pernel et al. (161) and Yamana et al. (162), the two peaks are clearly visible.

A discussion of stable oxidation states would not be complete without noting that elements without directly observed divalent species may still possess them at low concentration in the presence of their metal, M , according to the reaction



$$K = [M(II)]^3/[M(III)]^2, \quad [3.14]$$

where K is the equilibrium constant and is a small value. Bronstein (163) and then Roy and coworkers (61) found evidence of divalent species of these rare earth elements in LiCl-KCl eutectic using an electrochemical titration technique. Panchenko and colleagues (164) concluded that their polarograms of lanthanum were greatly complicated by disproportionation reactions which formed lower valence species. In studies of electrical conductivity of Ln-LnCl₃ systems, an observed rise in conductivity is believed due to electron exchange between Ln(III) and Ln(II) species. Specifically, this effect was observed for La, Ce, and Pr (82, 165-167), three lanthanoids for which the divalent state is not observed by electroanalytical methods. In the case of Nd, its trichloride reacts with Nd metal to create a solution of only Nd(II). This is confirmed by observation of the solubility of Nd in its chloride at 33.3 (168) or 32.9 (169) mol%, showing that reaction [3.13] proceeds to completion. Kvam (81) showed that solubility of actual metal, Nd(0), in LiCl-KCl eutectic is negligible, and this was confirmed by Wu (170). There is no clear research to indicate to what extent this phenomenon applies to actinoids.

Table 3.1: Survey of stable oxidation states of light lanthanoid elements.

Element	Temperature (K)	Stable Oxidation States	Reference
La	823	(III)/(0)	(171)
	775-820	(III)/(0)	(27)
	673-723	(III)/(0)	(65)
	723	(III)/(0)	(172)
	683-773	(III)/(0)	(7)
	723-823	(III)/(0)	(61)
	650-870	(III)/(0)	(124)
	723-873	(III)/(0)	(173)
Ce	773	(III)/(0)	(174)
	673	(III)/(0)	(18)
	673-723	(III)/(0)	(65)
	723	(III)/(0)	(172)
	673-723	(III)/(0)	(61)
	723	(III)/(0)	(139)
	650-880	(III)/(0)	(125)
	773	(III)/(0)	(174)
Pr	698-798	(III)/(0)	(140)
	673-773	(III)/(0)	(65)
	723	(III)/(0)	(172)
	673-700	(III)/(0)	(61)
	650-880	(III)/(0)	(125)
	723	(III)/(0)	(175)
Nd	723	(III)/(0)	(176)
	775-820	(III)/(0)	(27)
	723	(III)/(II)/(0)	(172)
	700-723	(III)/(0)	(61)
	670-870	(III)/(0)	(170)
	723	(III)/(0)	(177)
	733	(III)/(II)/(0)	(161)
	723-823	(III)/(II)/(0)	(162)
	773	(III)/(II)/(0)	(178)
Sm	773	(III)/(II)/(0)	(174)
	723	(III)/(II)	(179)
	723	(III)/(II)	(13)
Eu	723	(III)/(II)	(79)
	673-823	(III)/(II)	(180)
	673-823	(III)/(II)	(117)
Gd	760-820	(III)/(0)	(27)
	673-773	(III)/(0)	(65)
	673-723	(III)/(0)	(61)
	650-870	(III)/(0)	(124)
	673-823	(III)/(0)	(181)
	723-823	(III)/(0)	(62)

Table 3.2: Survey of stable oxidation states of scandium and heavy lanthanoid elements.

Element	Temperature (K)	Stable Oxidation States	Reference
Sc	650-875	(III)/(0)	(182)
Y	723	(III)/(0)	(171)
	770-825	(III)/(0)	(27)
	723-800	(III)/(0)	(183)
	673-723	(III)/(0)	(65)
	673-700	(III)/(0)	(61)
	650-880	(III)/(0)	(125)
Tb	673-823	(III)/(0)	(184)
Dy	673-773	(III)/(0)	(185)
	Not reported	(III)/(II)/(0)	(186)
	Not reported	(III)/(II)/(0)	(187)
	723	(III)/(II)/(0)	(188)
Ho	773	(III)/(0)	(174)
	723	(III)/(0)	(177)
Er	673-823	(III)/(0)	(189)
	653-823	(III)/(0)	(190)
Tm	873	(III)/(0)	(75)
	673	(III)/(II)/(0)	(83)
Yb	723	(III)/(II)	(13)
	723	(III)/(II)	(79)
	673-823	(III)/(II)	(180)
	723	(III)/(II)	(191)
	773	(III)/(II)	(192)
	723	(III)/(II)	(118)
Lu	673-823	(III)/(0)	(42)

Table 3.3: Survey of stable oxidation states of actinoid elements.

Element	Temperature (K)	Stable Oxidation States	Reference
U	728	(IV)/(III)/(0)	(6)
	723-823	(IV)/(III)/(0)	(43)
	660-780	(IV)/(III)/(0)	(16)
	733	(IV)/(III)/(0)	(141)
	773	(IV)/(III)/(0)	(145)
	773	(IV)/(III)/(0)	(174)
	773	(IV)/(III)/(0)	(134)
Np	673-823	(IV)(III)/(0)	(147)
	723-773	(IV)(III)/(0)	(193)
	733	(IV)(III)/(0)	(141)
Pu	733-833	(III)/(0)	(148)
	733	(III)/(0)	(141)
Am	733-823	(III)/(II)/(0)	(141)
	723	(III)/(II)/(0)	(143)
	733	(III)/(II)/(0)	(4)

Using electrochemical techniques, Smirnov et al. (194) were able to estimate $E_{Ce(III)/Ce(II)}^*$, Vnuckkova et al. (195) that for $E_{Pr(III)/Pr(II)}^*$, and Usov and Bel'skaya (196) that of $E_{Gd(III)/(II)}^*$. The potentials lie between $E_{M(III)/M(0)}^*$ and the lithium reduction potential. Furthermore,

Lebedev (197, 198) developed a methodology to correlate the values of $E_{M(III)/M(II)}^*$ observed in aqueous solutions to chloride melt systems and benchmarks the approach with the well-known $E_{Eu(III)/Eu(II)}^*$. Here, Sc and Y were not being considered; however, for La, Ce, Pr, Gd, Tb, and Ho, results indicated that the values of $E_{M(III)/M(II)}^*$ were approximately between $E_{M(III)/M(0)}^*$ and the lithium reduction potential.

A related issue, also known as *metal fog* or *black fog*, was observed upon the immersion of a lanthanoid metal in solutions containing its trichloride. It has long been recognized that the electrolytic yield of lanthanoid metal is reduced due to the production of finely dispersed metal particles in the electrolyte (162, 199, 200). It is also observed that the current efficiency of deposition is inversely proportional to the extent of metal solubility (200). Several researchers reported their studies on Nd-NdCl₃ systems (81, 168, 169) showing three distinctive colors: (i) the starting solution of pure NdCl₃ is red-purple, (ii) systems in transition are black, and (iii) completely reacted NdCl₂ is green. Some authors have constructed transparent electrochemical cells and observed black fog spreading from the lanthanoid metal into the bulk electrolyte, even when the lanthanoid was cathodically polarized at potentials more negative than $E_{M(III)/M(0)}^*$ (161, 200, 201). These behaviors are the consequence of a reaction given by Eq. [3.13].

It has been observed that SmCl₃, EuCl₃, and YbCl₃ spontaneously reduce to their dichloride to a certain extent in LiCl-KCl eutectic, even in the absence of their metal to produce their dichloride (82, 202) with a chlorine gas generation according to the following reaction:



However, when EuCl₂ alone is dissolved into LiCl-KCl eutectic, it does not observably oxidize to EuCl₃ (202).

None of the rare earths takes an oxidation state higher than (III) within normal operating conditions of the LiCl-KCl eutectic. Of the rare earths, cerium has the most stable (IV) oxidation state in other chemistries and can exist as Ce(IV) in solid chloride complexes at lower temperature. However, Ce(IV) does not persist above the melting temperature of LiCl-KCl

eutectic except in the presence of a powerful oxidizing agent, such as Cl₂ gas at atmospheric pressure (165, 203).

3.9.2 Diffusion Behavior of Lanthanoid and Actinoid Species

Diffusion coefficient can provide information about the nature of the cations in the solution. It is an important factor for modeling of behaviors. Table 3.4 and Table 3.5 present a survey of diffusion coefficients and activation energy for diffusion found in the literature for lanthanoid chlorides in LiCl-KCl eutectic at 723 K. All of the lanthanoid species have been studied at least once except Sc(III) and Nd(II). While some scatter is present, the measured diffusion coefficients are generally near $1 \times 10^{-5} \text{ cm}^2 \text{ s}^{-1}$ at 723 K. Table 3.6 presents a similar survey of diffusion coefficients for actinoid species.

3.9.3 Apparent Standard Potential of Lanthanoid and Actinoid Species

The free energy of a reaction is given by thermodynamics

$$\Delta G = \Delta G^0 + RT \ln \frac{a_{red}}{a_{ox}}, \quad [3.16]$$

where

$$\Delta G = -nFE, \text{ and} \quad [3.17]$$

$$\Delta G^0 = -nFE^0. \quad [3.18]$$

The potential of a reaction is then a function of the *standard reduction potential*, E^0 , and activities; that is,

$$E = E^0 + \frac{RT}{nF} \ln \frac{a_{ox}}{a_{red}}, \text{ and} \quad [3.19]$$

$$E = E^0 + \frac{RT}{nF} \ln \frac{\gamma_{ox} X_{ox}}{\gamma_{red} X_{red}}. \quad [3.20]$$

However, it can be difficult to use standard reduction potential in practice due to the effect of activity coefficients, which are generally not known. Therefore, an *apparent standard potential*, also called *formal potential*, is being considered, and this incorporates the effect of activity coefficient. The electrode potential can then be defined as

$$E = E^* + \frac{RT}{nF} \ln \frac{X_{ox}}{X_{red}}, \text{ where} \quad [3.21]$$

$$E^* = E^0 + \frac{RT}{nF} \ln \frac{\gamma_{ox}}{\gamma_{red}}. \quad [3.22]$$

In fact, the difference between E^* and E^0 can be used to determine the activity coefficients for a particular concentration range. Table 3.7, Table 3.8, and Table 3.9 provide a survey of values of apparent standard potential from the literature. The fourth column of both tables notes the reference electrode systems used to collect the data in the studies and the method by which the authors converted their data to the standard Cl_2/Cl^- reference. As previously noted, this work uses the conversion Eq. [3.5] developed by Roy et al. (64). Literature data points were converted to this equation if not already utilized by the source author. Literature data presented in the molality concentration scale by the source author were converted to the mole fraction concentration scale. In some cases, the concentration scale in which the work was performed was not provided by the source author. It is seen in Table 3.7 and Table 3.8 that measured values of E^* may differ by about 60 millivolts. While on absolute terms, this variance may not seem unreasonable. However, it is sufficient to prevent the discrimination of some lanthanoids and actinoid elements from each other.

Table 3.4: Survey of light lanthanoid diffusion coefficients.

Species	[X]	D (cm ² /s) at 723 K	E _a (kJ/mol)	Reference
La(III)	0.002-0.015	1.47 x 10 ⁻⁵	-30.0	(124, 125)
	0.0028	1.14 x 10 ⁻⁵	-32.86	(171)
	0.011	0.72 x 10 ⁻⁵		(172)
	0.0027	0.67 x 10 ⁻⁵		(7)
	0.001-0.003	0.73 x 10 ⁻⁵	-32.2	(204)
	unkwn	0.76 x 10 ⁻⁵		(141, 205)
	0.0023	0.88 x 10 ⁻⁵		(206)
	0.0034	1.83 x 10 ⁻⁵	-29.3	(207)
	0.0033-0.0049	1.04 x 10 ⁻⁵		(161)
0.0026	1.04 x 10 ⁻⁵		(208)	
Ce(III)	0.01	1.03 x 10 ⁻⁵	-35.8	(18)
	0.002-0.015	1.29 x 10 ⁻⁵	-29.7	(125)
	0.0054	0.58 x 10 ⁻⁵		(172)
	unkwn	1.01 x 10 ⁻⁵		(138)
	0.0036	1.03 x 10 ⁻⁵	-34.6	(139)
	0.0005-0.0018	1.00 x 10 ⁻⁵		(123)
	0.0008	0.55 x 10 ⁻⁵	-30.7	(140)
	0.003	0.55 x 10 ⁻⁵	-31.6	(140)
0.006	0.54 x 10 ⁻⁵	-33.4	(140)	
Pr(III)	0.002-0.0015	1.24 x 10 ⁻⁵	-30.1	(125)
	0.0039	0.68 x 10 ⁻⁵		(172)
	0.004-0.005	1.11 x 10 ⁻⁵	-32.0	(175)
Nd(III)	0.0047	0.97 x 10 ⁻⁵		(172)
	unkwn	1.08 x 10 ⁻⁵		(141, 205)
	unkwn	1.16 x 10 ⁻⁵	-30.5	(207)
	0.0023-0.0032	1.01 x 10 ⁻⁵		(161)
Nd(II)				No data
Sm(III)	0.0009-0.0043	1.01 x 10 ⁻⁵		(179)
Eu(III)	0.0035	0.58 x 10 ⁻⁵	-32.1	(117)
Eu(II)	0.0035	0.57 x 10 ⁻⁵		(117)
Gd(III)	0.002-0.015	0.735 x 10 ⁻⁵	-33.0	(124, 125)
	0.0004-0.0021	0.81 x 10 ⁻⁵	-32.0	(123)
	0.0041	0.90 x 10 ⁻⁵	-32.5	(62)
	0.0036	0.77 x 10 ⁻⁵	-32.2	(181)

Table 3.5: Survey of Sc, Y, and heavy lanthanoid diffusion coefficients.

Species	[X]	D (cm ² /s) at 723 K	E _a (kJ/mol)	Reference
Sc(III)				No data
Y(III)	0.002-0.015	0.527 x 10 ⁻⁵	-35.1	(125)
	unkwn	0.915 x 10 ⁻⁵	-31.94	(171)
Tb(III)	0.0037	0.63 x 10 ⁻⁵	-33.4	(184)
Dy(III)	0.0043	1.04 x 10 ⁻⁵	-32.6	(188)
Ho(III)	unkwn	2.14 x 10 ⁻⁵		(177)
	0.0035	0.68 x 10 ⁻⁵	-31.5	(189)
Er(III)	0.0035	0.77 x 10 ⁻⁵	-32.5	(190)
Tm(III)	0.004	0.74 x 10 ⁻⁵	-29.8	(83)
Tm(II)	0.004	0.74 x 10 ⁻⁵		(83)
Yb(III)	unkwn	1.00 x 10 ⁻⁵		(191, 209)
	0.004	0.76 x 10 ⁻⁵		(118)
Yb(II)	0.004	0.75 x 10 ⁻⁵		(118)
Lu(III)	0.004	0.72 x 10 ⁻⁵	-31.5	(42)

Table 3.6: Survey of actinoid diffusion coefficients.

Species	[X]	D (cm ² /s) at 723 K	E _a (kJ/mol)	Reference
U(III)	0.0003	8.1 x 10 ⁻⁵		(6)
	unkwn	1.02 x 10 ⁻⁵	-32.6	(43)
	unkwn	0.55 x 10 ⁻⁵	-66.4	(16)
	unkwn	2.7 x 10 ⁻⁵		(141)
	0.0016-0.016	1.04 x 10 ⁻⁵ ††		(145)
U(IV)	0.00097	0.84 x 10 ⁻⁵	-37.5	(43)
	unkwn	2.1 x 10 ⁻⁵		(141)
	0.0016-0.016	0.67 x 10 ⁻⁵ ††		(145)
Np(III)	unkwn	1.7 x 10 ⁻⁵		(141)
	0.00087	1.86 x 10 ⁻⁵	-23.6	(147)
	0.0012	1.5 x 10 ⁻⁵	-33.9	(193)
Np(IV)	0.00043	1.91 x 10 ⁻⁵	-14.1	(147)
Pu(III)	0.0004-0.003	1.6 x 10 ⁻⁵ †		(148)
	unkwn	1.6 x 10 ⁻⁵		(141)
	0.00075-0.0014	6.0 x 10 ⁻⁵		(210)
Am(III)	unkwn	2.5 x 10 ⁻⁵ †		(141)
	0.0013	2.4 x 10 ⁻⁵ †		(4)
Am(II)	unkwn	1.1 x 10 ⁻⁵		(141)
	0.0013	1.15 x 10 ⁻⁵ †		(4)

Unkwn Concentration for derivation of diffusion coefficient not clearly noted

† 733 K

†† 773 K

Table 3.7: Survey of apparent standard potential of the light lanthanoids versus Cl_2/Cl^- .

Reaction	Log k_0 ($\text{cm}\cdot\text{s}^{-1}$)	α	Reference Electrode	E^* (723 K)	Source
La(III)/La(0)			2	-3.146	(65)
			1	-3.129	(125)
			2	-3.124	(126)
			1	-3.139	(27)
			2	-3.143	(143)
			3	-3.105	(63)
			3	-3.100	(172)
			2	-3.116	(7)
			2	-3.124	(141, 205)
			3	-3.159	(206)
			1	-3.116	(124)
4	-3.099	(173)			
2	-3.152	(208)			
Ce(III)/Ce(0)	-3.6	0.4	2	-3.106	(18)
			2	-3.098	(65)
			1	-3.085	(125)
			2	-3.092	(126)
			3	-3.090	(63)
			3	-3.095	(172)
			2	-3.088	(139)
			1	-3.075	(194)
3	-3.130	(140)			
Pr(III)/Pr(0)	-3.7	0.4	2	-3.085	(65)
			1	-3.070	(125)
			2	-3.097	(126)
			3	-3.086	(63)
			3	-3.090	(172)
			3	-3.15 or -3.09	(176)
Nd(III)/Nd(0)			1	-3.034	(27)
			2	-3.087	(143)
			3	-3.054	(63)
			3	-3.056	(172)
Nd(III)/Nd(II)			3	3.098	(63)
			5	-3.082	(178)
			2	-3.140	(162)
			2	-3.071	(205)
Nd(II)-Nd(0)			2	-3.089	(126)
			3	-3.121	(63)
			3	-3.123	(172)
			2	-3.112	(205)
			5	-3.179	(178)
Sm(III)/Sm(II)			2	-3.206	(126)
			4	-2.035	(79)
Eu(III)/Eu(II)	-2.47	0.5	2	-2.067	(179)
			4	-0.860	(79)
Gd(III)/Gd(0)			2	-0.898	(117)
			2	-3.065	(65)
			1	-3.040	(125)
			1	-3.050	(27)
			1	-3.031	(124)
6	-3.040	(62)			

1-7, see key, Table 3.9

Table 3.8: Survey of apparent standard potential of Sc, Y, and heavy lanthanoids versus Cl₂/Cl⁻.

Reaction	Log k ⁰ (cm·s ⁻¹)	α	Reference Electrode	E* (723 K)	Source
Sc(III)/Sc(0)			7	-2.801	(182)
			4	-2.804	(211)
Y(III)/Y(0)			2	-3.124	(65)
			1	-3.114	(125)
			2	-3.108	(126)
			1	-3.121	(27)
			4	-3.082	(212)
Tb(III)/Tb(0)			2	-3.038	(184)
Dy(III)/Dy(II)			2	-3.103	(213)
			2	-3.143	(214)
			2	-3.243	(188)
Dy(II)/Dy(0)			2	-3.164	(188)
Ho(III)/Ho(0)			2	-2.951	(177)
Er(III)/Er(0)				No data	
Tm(III)/Tm(II)	-2.21	0.5	2	-2.860	(83)
Yb(III)/Yb(II)			4	-1.681	(79)
			1	-1.662	(191, 209, 215, 216)
			7	-1.659	(180)
			2	-1.715	(118)
Lu(III)/Lu(0)	-2.25	0.5		No data	

1-7, see key, Table 3.9

Table 3.9: Survey of apparent standard potential of actinoids versus Cl₂/Cl⁻.

Reaction	Log k ⁰ (cm·s ⁻¹)	α	Reference Electrode	E* (723 K)	Source
U(IV)/U(III)	-1.80		3	-1.530	(43)
			3	-1.459	(141)
			3	-1.448	(145)
U(III)/U(0)	-3.74		3	-2.51	(6)
			3	-2.541	(43)
			3	-2.563	(141)
			2	-2.498	(64)
Np(IV)/Np(III)			3	-0.77	(147)
Np(III)/Np(0)			3	-2.73	(147)
			3	-2.68	(193)
			2	-2.698	(64)
Pu(III)/Pu(0)			2	-2.796 †	(148)
			3	-2.802	(141)
			2	-2.808	(64)
			3	-2.748	(210)
Am(III)/Am(II)			3	-2.703	(141)
			2	-2.700	(4)
Am(II)/Am(0)			3	-2.915	(141)
			2	-2.843	(64)
			2	-2.916	(4)

Reference electrodes:

- 1 Cl₂/Cl⁻ reference electrode
 - 2 Ag⁺/Ag reference electrode, converted to Cl₂/Cl⁻ by equation [3.5] by source author
 - 3 Ag⁺/Ag reference, converted to Cl₂/Cl⁻ by source author, but equation different or not given
 - 4 Pt quasi-reference electrode, converted to Cl₂/Cl⁻ with data from Laitinen (29) by source or present author
 - 5 Ag⁺/Ag reference electrode, converted to Cl₂/Cl⁻ reference by a Cl₂/Cl⁻ calibration
 - 6 Ag⁺/Ag reference electrode, converted to Cl₂/Cl⁻ by equation [3.4] by source author
 - 7 Different or unknown reference electrode and conversion to Cl₂/Cl⁻ used by source author
- † 733K

3.9.4 Nucleation Behavior of Lanthanoid and Actinoid Species

The type of nucleation displayed by a metal on a foreign substrate offers information about the nature of chemical and electrochemical processes and plays a strong role in deposition morphology. One possible nucleation mode is instantaneous, where all of the nuclei are created at the beginning of electrolysis and further deposition occurs only by growth of these crystals. The second type is progressive nucleation, where additional nuclei continue to be generated throughout the deposition process. It is sometimes possible to alter the nucleation mode by changes in temperature, substrate, and electrolyte chemistry. In general, the lanthanoid elements deposit by instantaneous nucleation (18, 171, 181, 184, 188-190), which tends to promote highly dendritic deposits. However, the heaviest lanthanoids show progressive nucleation behavior at a limited, lower-temperature range (42, 83). The identification of conditions or development of modified electrolytes altering these behaviors would be a valuable contribution toward the achievement of dense and coherent lanthanoid deposits. Serrano and Taxil (217) studied the nucleation behavior of uranium at 953 K in fused NaCl-KCl on a vitreous carbon substrate and observed instantaneous 3-D nucleation. No other studies of nucleation behavior for actinoid species are available. Table 3.10 provides a summary of available information for nucleation characteristics.

Table 3.10: Summary of nucleation characteristics.

Element	Substrate	Temperature (K)	Nucleation Mode	Reference
Y	Tungsten	673-823	Instant. 3-D	(171)
La	Tungsten	673-823	Instant. 3-D	(171)
Ce	No data			
Gd	Tungsten	673-823	Instant. 3-D	(181)
Tb	Tungsten	673-823	Instant. 3-D	(184)
Dy	Tungsten	673-823	Instant. 3-D	(188)
Ho	Tungsten	673-773	Instant. 3-D	(189)
Er	Tungsten	653-823	Instant. 3-D	(190)
Tm	Tungsten	673-698 723-823	Transitional- Instant. 3-D	(83)
Lu	Tungsten	673-748 773 823	Progressive -Transitional- Instant. 3-D	(42)
U	Vit. Carbon †	943 †	Instant. 3-D †	(217) †
Np	No data			
Pu	No data			
Am	No data			

† Fused NaCl-KCl

3.10 Uranium Crystallography

Room temperature uranium has the orthorhombic crystal structure, described as the α phase. Uranium is expected to form as the α phase during depositions at 773 K, but would be expected to begin to deposit as or convert to the tetragonal β phase at 941 K (218). Additional allotropic information and crystallographic information are presented in Tables 3.11 and 3.12, respectively. Figure 3.2 provides a visual depiction of a $2 \times 2 \times 2$ block of α -uranium crystal cells. This structure is anisotropic, with strongly differing thermal and mechanical properties between crystal directions.

Prior investigations have reported rhomboidal uranium crystals growing with the longer dimension of the crystal pointed away from the cathode surface (219). Marzano and Noland (160) report on neutron diffraction studies of a long uranium crystal which was found to be growing in the $[310]$ direction. Figure 3.3 provides a reference showing the (310) plane. Marzano and Noland do not report the conditions for which the crystal was produced, but the physical description is similar to those observed in this study to result from depositions at the lowest overpotential, 25 mV.

Portions of this study examine depositions of uranium in the presence of cerium, and Figure 3.4 shows the binary uranium-cerium phase diagram. No U-Ce intermetallics are observed, and the solubility of cerium in α -uranium is very low (218, 220).

Table 3.11: Allotropic transformations and melting temperature for uranium (218).

Phase	Characteristics	Transition (K)
α	Orthorhombic	941
β	Tetragonal	1049
γ	Body-centered cubic	1408
Liquid	Liquid	

Table 3.12: Crystallographic data for α uranium at 297 K (221).

Cell Parameter	Dimension
a	0.2854 nm
b	0.5870 nm
c	0.4956 nm
α	90°
β	90°
γ	90°

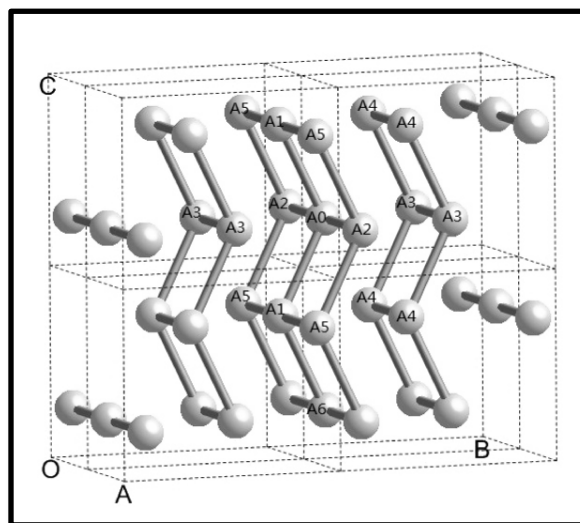
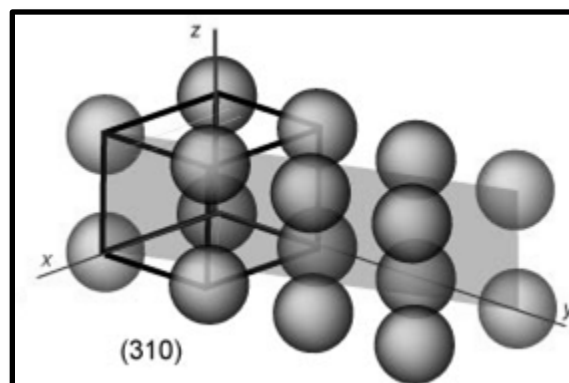
Figure 3.2: Orthorhombic α -uranium structure in a 2x2x2 supercell (222).

Figure 3.3: Pictorial of the (310) crystal plane as defined by Miller indices (223).

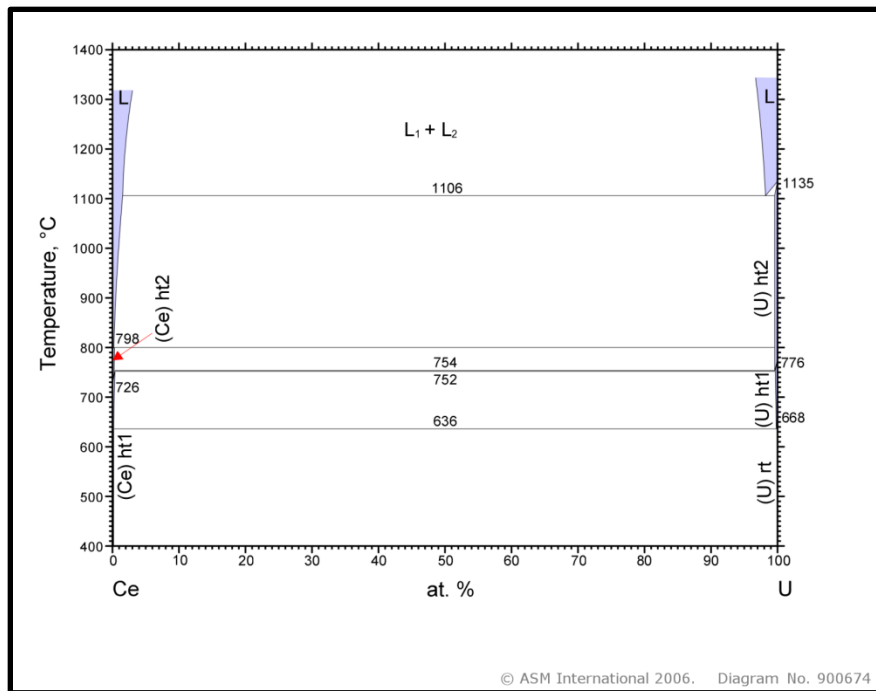


Figure 3.4: The uranium-cerium phase diagram (218, 220).

CHAPTER 4. EXPERIMENTAL APPROACH

4.1 Experiments for Electrochemistry of Cerium

4.1.1 Apparatus

Electrochemical experiments with LiCl-KCl-CeCl_3 were performed inside a small custom-fabricated stainless steel, argon-atmosphere glovebox, as shown in Figure 4.1. The glovebox was maintained at a slight positive pressure by a constant purge of laboratory-grade argon (Air Liquide) containing less than 5 ppm O_2 and 20 ppm N_2 , with constant monitoring of oxygen concentration. The glovebox contained a stainless steel furnace well attached to the floor plate, as shown in Figure 4.2. The furnace well was heated by an external-resistance heater, and an external water cooling coil protected the O-ring seal at the interface of the furnace well to the glovebox floor. A straight-wall, 55-mL nickel crucible (Metal Technology) was used for the containment of the reagents and was held in position by an alumina-silica support inside a large secondary stainless steel crucible. The larger stainless steel crucible was insulated from electrical contact with the furnace walls by an aluminum silicate spacer and cover. The electrodes and thermocouple were held by a metal positioning plug in the furnace cover and hung through a series of thin metal heat shields into the nickel crucible. The temperature of the bath was monitored by a calibrated, stainless steel-sheathed, chromel-alumel thermocouple (Omega Engineering) immersed directly in the molten electrolyte. The electrodes and thermocouple were electrically insulated from the positioning plug and heat shields by ceramic tubes.



Figure 4.1: Argon-atmosphere glovebox for performance of LiCl-KCl-CeCl₃ experiments.

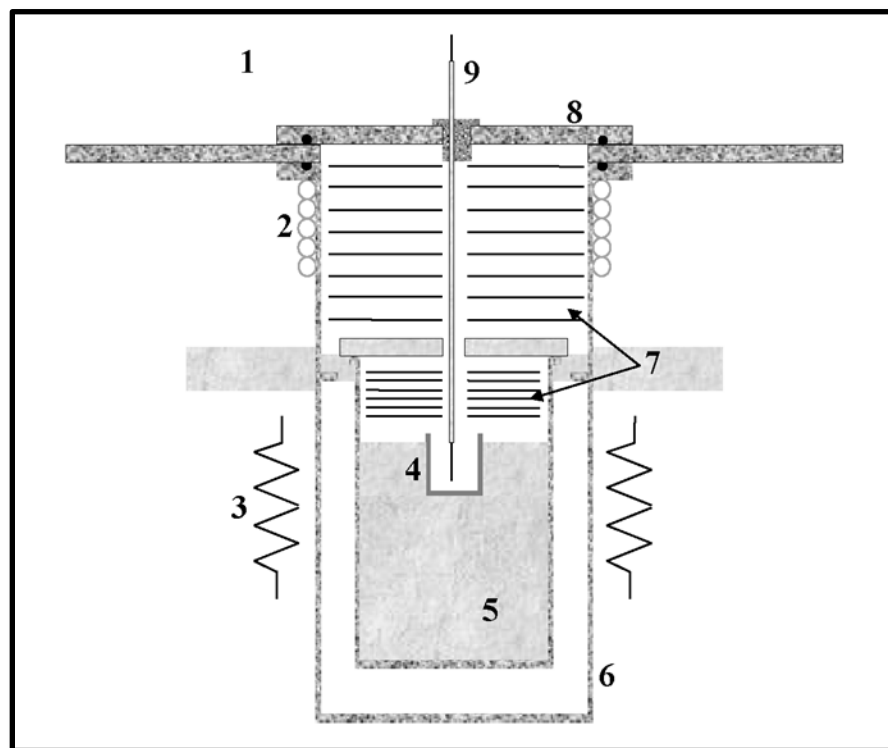


Figure 4.2: Experimental cell for electrochemistry of cerium: (1) argon glovebox; (2) external water cooling jacket; (3) resistance heater; (4) 55-mL nickel crucible; (5) alumina-silica centering plates inside stainless steel crucible; (6) stainless-steel furnace well; (7) metal heat shields; (8) stainless-steel cover plate with electrode centering plug; (9) electrodes.

4.1.2 Electrodes

Annealed 0.5 or 1.0-mm tungsten wire (Alfa Aesar 99.95%) was used as the working electrode. The counter electrode was a 1 to 2-gram piece of cerium metal enmeshed by a basket of molybdenum wire cloth (99.9+%, Cleveland wire cloth) as shown in Figure 4.3. The active area of the cerium counter electrode was a factor of 20 or greater than the working electrode, before including the molybdenum mesh. The reference electrode was the Ag/AgCl type (28, 224) constructed of 1-mm silver wire (Alfa Aesar, 99.999%) in contact with LiCl-KCl-AgCl of weight fraction 44.35:54.65:1 (Aldrich APL, 99.99%) inside a 6.25-mm-diameter, glass-bonded mullite tube (Omega Engineering) with a 0.78-mm wall. These electrodes were fabricated inside the argon glovebox and the open end sealed with epoxy. A typical electrode assembly can be seen in Figure 4.4. Electrodes and the thermocouple sheath were electrically insulated with alumina tubes (Omega Engineering). The alumina sheaths for electrical insulation do not extend into the molten salt.

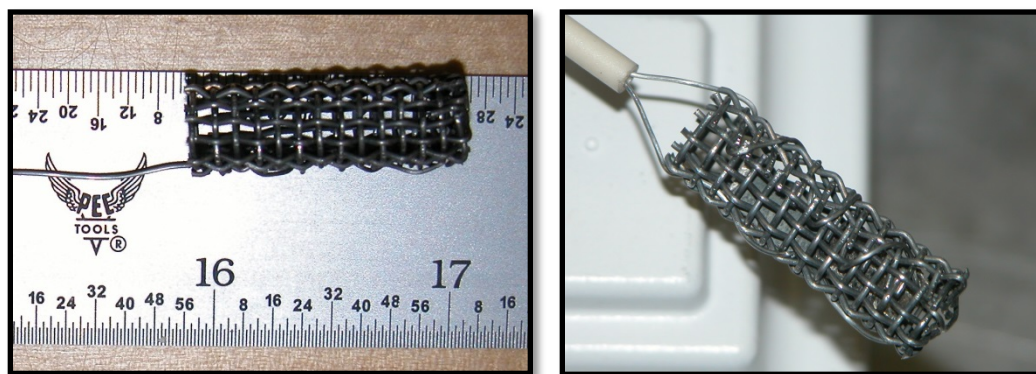


Figure 4.3: Molybdenum basket for cerium counter electrode.

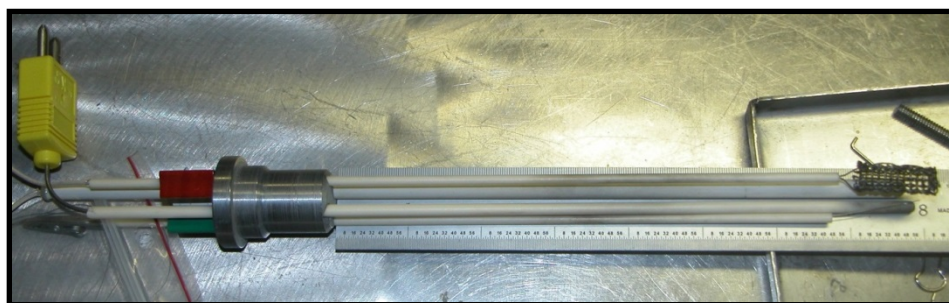


Figure 4.4: Typical sheathed electrode assembly for LiCl-KCl-CeCl₃ experiments inside the argon glovebox.

4.1.3 Reagents

Anhydrous lithium chloride-potassium chloride eutectic (Sigma-Aldrich 99.99%) received in sealed glass ampoules under argon was used as the electrolyte. Anhydrous cerium chloride (Sigma-Aldrich 99.99+%) received in sealed glass ampoules under argon was used as the active component in the salt. Cerium metal was cut from a 6-mm diameter rod packaged in Mylar under argon (Alfa Aesar 99.9%). Surface oxide layers were removed from the cerium inside the glovebox using a stainless steel knife blade.

4.1.4 Experiment Preparation

To eliminate the possibility of adsorbed moisture being released from the furnace internal structure, the experimental assembly was thoroughly out-gassed by heating to 1073 K for 6 hours prior to an experiment campaign. Working and counter electrode wires and the mullite tube of the reference electrode were cleaned with methanol prior to use. Chemicals received from the manufacturer were opened inside the glovebox and stored thereafter inside the glovebox in sealed glass or metal containers. Appropriate mixtures of CeCl_3 and LiCl-KCl salts, corresponding to approximately 40 mL of electrolyte containing 0.01 mole fraction CeCl_3 , were weighed on a calibrated balance and transferred into a nickel crucible, as seen in Figure 4.. The crucible was loaded into the molten salt furnace, along with the molybdenum counter electrode basket containing 1–2 grams of cerium metal, and heated to 773 K for 14 hours prior to use. No oxide materials, including the reference electrode sheath, were in contact with the melt during this soak. Such an approach yielded reproducible data with low background current.

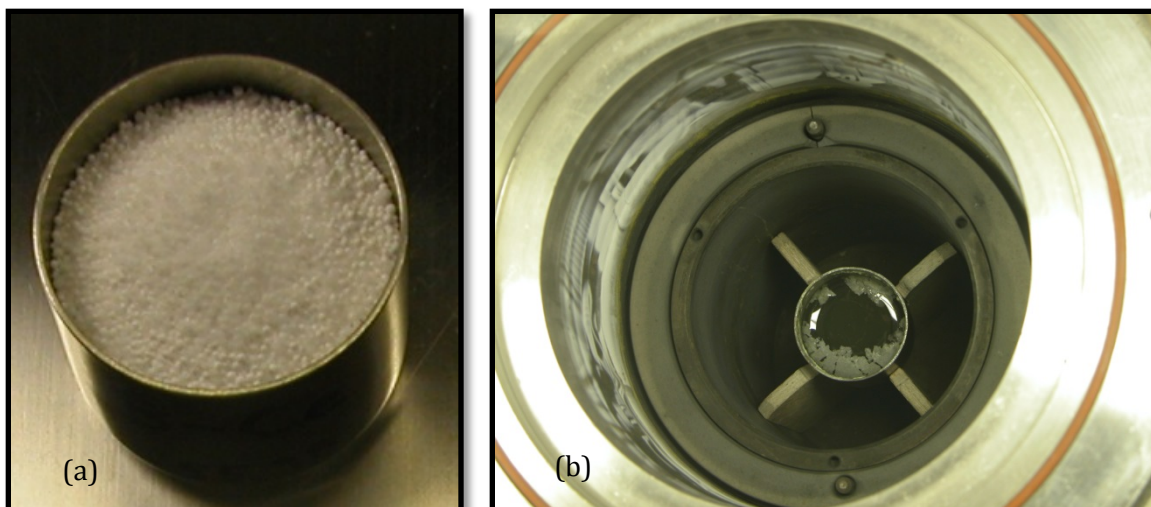


Figure 4.5: A typical setup with (a) a prepared 55-mL nickel crucible with LiCl-KCl-CeCl_3 and (b) a crucible cooling in the furnace well after a long experimental set.

The area of the working electrode was established by pulling wire through the alumina sheath to a prescribed electrode length, followed by determination/ confirmation of immersion depth by a rapid insertion and removal for observation of the salt line. The alumina sheaths did not extend into the salt. Reference electrode sheaths were found to be more reliable when heated slowly by holding above the melt pool to minimize thermal shock.

The working electrode was anodically cleaned following each experiment by stripping at a potential of 0.0 V versus the Ag/AgCl reference electrode for 60 seconds, followed by at least a 60-second pause to ensure relaxation of concentration gradients or electrode polarization. Prior to each test series, a cyclic voltammogram was repeated for 10 cycles to confirm reliable and consistent system behavior, and a similar cyclic voltammogram was repeated periodically throughout testing to confirm reproducible electrolyte behavior. It was found that this procedure screened problematic test preparations and generated a repeatable data set. All electrochemical measurements for CeCl_3 electrochemistry were performed using an EG&G PAR 273A potentiostat/galvanostat controlled with Corrware software (Scribner Associates).

4.2 Experiments for Electrochemistry with Uranium and Cerium

This portion of the study was directed toward acquisition of knowledge data regarding the intrinsic purity of electrorefined uranium dendrites produced under laboratory conditions. The

investigation included cerium as a representative contaminant. It was planned to acquire dendrite samples produced from a suite of uranium and cerium concentrations to evaluate important factors relative to dendrite purity. Table 4.1 depicts the planned samples for cathode products. The results of these efforts are described in Chapter 7.

Table 4.1: Experimental data set for dendrite samples.

Uranium Concentration (X)	Deposition overpotential, η ¹ (vs $E^*_{U(III)/U}$)	Cerium Concentration (X)	
		0.01	0.06
0.0033	-25 mV	○	○
	-150 mV	○	○
	-300 mV	○	○
	-450 mV	○	○
	-525 mV	○	○
0.01	-25 mV		○
	-150 mV	○	○
	-300 mV	○	○
	-450 mV	○	○
	-525 mV	○	○
0.06	-25 mV	○	○
	-150 mV	○	○
	-300 mV	○	○
	-450 mV	○	○
	-525 mV	○	○

¹ Apparent Standard Potential of U is -2.514 vs Cl_2/Cl^- . The apparent standard potential of Ce is -3.08 vs Cl_2/Cl^- .

4.2.1 Apparatus

Electrochemical experiments with $LiCl-KCl-UCl_3-CeCl_3$ were performed in a radiological facility in an argon-atmosphere glovebox. The glovebox was maintained at a slight negative pressure and with constant monitoring of oxygen content. The glovebox was constantly purged with laboratory-grade argon (Air Liquide) containing less than 1 ppm H_2O , 5 ppm O_2 , and 20 ppm N_2 . The glovebox contained a stainless steel furnace well attached to the floor plate, very similar to that described in Section 4.1.1 and depicted in Figure 4.1, with the only difference being this furnace was approximately 5 cm deeper than that used for non-radiological tests. For these tests, straight-wall, 55-mL tantalum crucibles (99.9%, Metal Technology Inc.) were used

for the containment of the reagents, with a dense zirconia crucible used as a secondary cup. In other respects, the experiment setup was identical. A typical experiment setup and the glovebox can be seen in Figure 4.6 and Figure 4.7, respectively.



Figure 4.6: Prepared crucible for experiments with $\text{LiCl-KCl-UCl}_3\text{-CeCl}_3$.



Figure 4.7: Measuring electrode length in the radiological glovebox for experiments with $\text{LiCl-KCl-UCl}_3\text{-CeCl}_3$.

4.2.2 Electrodes

Annealed 1.0-mm tungsten wire (Alfa Aesar 99.95%) was used as the working electrode for electrochemical experiments such as cyclic voltammetry. It was adjusted to a prescribed length, and the wetted depth was verified by measurement following a rapid immersion and withdrawal. For collection of dendrite deposits, it was observed that the ability to bend the wire into a hook or U shape was very beneficial to collect an adherent deposit, but the tungsten wire tended to fracture when bent. For this reason, an annealed 1.0-mm tantalum wire (Alfa Aesar 99.95%) was used to collect uranium deposits. Successful extraction of the hot dendrite samples through the heat shield still proved challenging, and a protective alumina tube or sleeve (99.8%, Omega Engineering) was added around the electrode. A “window” was cut into the bottom of the alumina tube to allow dendrite growth onto the Ta wire, but with protection for the deposit from being dislodged during extraction from the furnace system. This window electrode setup is shown in Figure 4.8.

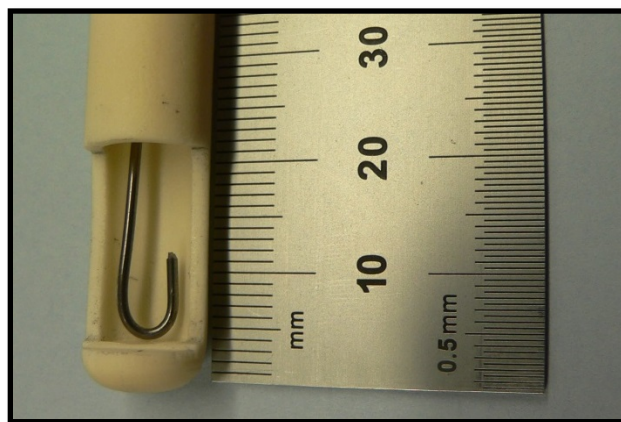


Figure 4.8: “Window” electrode for collection of uranium deposits.

The counter electrodes for cyclic voltammetry and anodes for dendrite experiments were a series of approximately 5-mm diameter uranium rods (Figure 4.9). Electrical connection and mechanical position were accomplished by multiple wraps of 1.0-mm tantalum wire near the top of the rod. When used as a counter electrode for certain electrochemical experiments such as cyclic voltammetry, the uranium rods were lowered to rest on the bottom of the tantalum crucible to provide a very large counter electrode area. During use of the uranium rods for dendrite collection experiments, obvious mass loss occurred. The uranium rods were

occasionally replaced when necessary due to physical degradation or certain changes of salt chemistry.

When a uranium rod was prepared for first use, the diameter was measured at six places along the planned wetted height to obtain a good estimate of surface area. The electrode was then adjusted to a prescribed length, and the wetted depth was verified by measurement following a rapid immersion and withdrawal. For these experiments, the immersion depth of the uranium rod was chosen to ensure the tantalum wire attachment point remained above the pool. Before any other use, each uranium rod was used to perform linear polarization resistance experiments to obtain a measurement of exchange current density. For these experiments where the uranium rod was used as the working electrode, the counter electrode was a tungsten wire allowed to be electrically connected to the tantalum crucible.

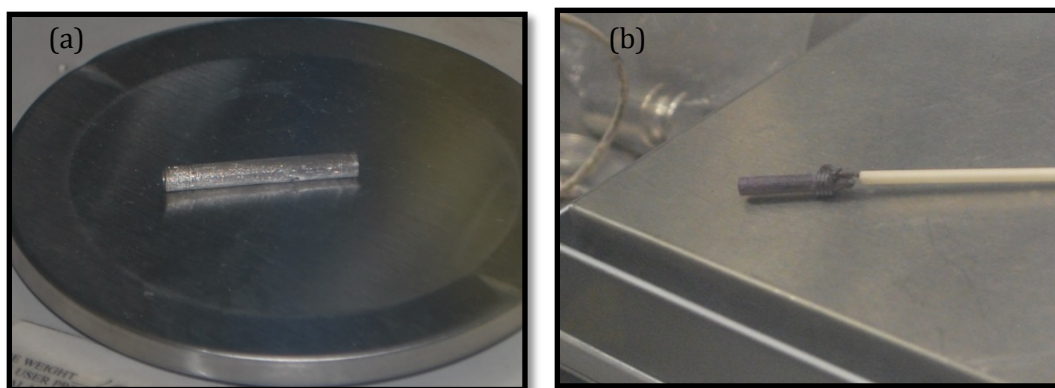


Figure 4.9: Two uranium rods used in experiments, (a) first uranium rod cleaned and prepared for construction of an electrode, (b) second uranium rod following use for linear polarization experiments in 6 mol% UCl_3 and 1 mol% CeCl_3 .

The reference electrodes were identical to those described in Section 4.1.2. Electrodes were held in place with a metal plug and electrically insulated with alumina tubes similar to the description in Section 4.1.2 and depicted in Figure 4.4. Electrode lengths for these experiments were slightly longer to accommodate the 5-cm-deeper furnace well in the radiological glovebox.

4.2.3 Reagents

Anhydrous lithium chloride-potassium chloride eutectic (Sigma-Aldrich 99.99%) received in sealed glass ampoules under argon was used as the electrolyte. An independent analysis was

performed to evaluate the purity of the LiCl-KCl electrolyte from this vendor and is provided in Table 4.2. The analysis for this batch shows impurities of approximately 400 $\mu\text{g/g}$, or a purity of approximately 99.96%.

Table 4.2: Analysis of LiCl-KCl feedstock (Analytical Log No. 96974).

Element	$\mu\text{g/g}$	2σ
ICP-OES		
Al	<810	
Ba	<26	
Ca	<18	
Cd	<52	
Co	<31	
Cr	<67	
Cu	<36	
Fe	229	$\pm 10\%$
Mg	54	$\pm 5\%$
Mn	<5.4	
Mo	<270	
Na	154	$\pm 30\%$
Ni	<53	
Ta	<260	
Ti	<69	
U	<1600	
W	<610	
Zr	<180	

Anhydrous cerium chloride (Sigma-Aldrich 99.99+%) received in sealed glass ampoules under argon was used. Uranium trichloride used was from a nominally LiCl-KCl-73 wt% UCl_3 ternary synthesized by reaction of uranium metal with CdCl_2 at another laboratory site. Analysis of this feedstock can be seen in Table 4.3. No major contaminants are seen, and the measured content of uranium corresponds to a mixture of 72.3 w% UCl_3 in the ternary feedstock. Uranium rods were depleted uranium metal cast in the laboratory as a part of other investigations, and analysis is provided in Table 4.4. The analysis shows uranium purity on the order of 99.7%. The majority of these contaminants (Fe, Ni) were electrochemically noble species that should not participate in the electrochemistry and may have been contamination from the sampling tool. Prior to use, any surface oxide layer was removed from the uranium rod by washing in nitric acid, followed by light scraping with a clean surface of a diamond jewelry file inside the glovebox.

Table 4.3: Composition LiCl-KCl-UCl₃ feedstock (Analytical Log No. 96980).

Element	$\mu\text{g/g}$	2σ
ICP-OES		
Al	<1900	
Ba	<72	
Ca	<200	
Cd	<120	
Cr	<340	
Cu	<160	
Fe	<340	
Mg	<170	
Mn	<40	
Mo	<620	
Na	<600	
Ni	<300	
Ta	<600	
Ti	<160	
U	501,000	$\pm 5\%$
W	<1410	
Zr	<420	

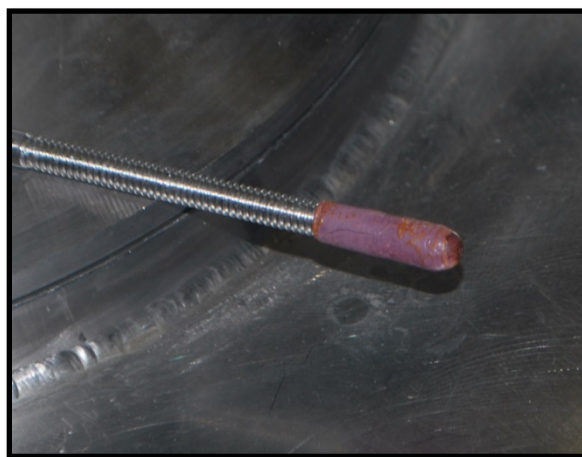
Table 4.4: Composition of cast uranium rod (Analytical Log No. 96978).

Element	$\mu\text{g/g}$	2σ
ICP-OES		
Al	<3300	
Ba	<110	
Ca	<350	
Cd	<210	
Cr	<580	
Cu	<280	
Fe	1060	$\pm 5\%$
Mg	254	$\pm 5\%$
Mn	<69	
Mo	<1100	
Na	<1100	
Ni	1580	$\pm 10\%$
Ta	<1100	
Ti	<280	
U	675000	$\pm 5\%$
W	<2500	
Zr	<720	

4.2.4 Sampling

Salt samples from each test condition were obtained to confirm expected compositions. Samples were obtained by the rapid immersion of a clean, room-temperature stainless steel threaded rod into the electrolyte with immediate removal, as shown in Figure 4.10. The salt

samples could be easily removed from the threaded rod by light tapping of a clean metal spatula. Salt samples were sealed in glass vials and analyzed following the procedure described in Section 4.3.1. Samples of the metallic uranium rods were obtained by cutting a small piece from the rod with a clean diamond jewelry file.



(a)



(b)

Figure 4.10: LiCl-KCl-CeCl₃-UCl₃ salt samples (a) on a stainless-steel threaded rod and (b) being weighed and packaged for analysis.

Dendrite samples were obtained by using clean tweezers or fine-tipped, needle-nose pliers to pull dendrite from the tantalum wire in the window electrode while the electrolyte remained molten. The bulk of the sample was harvested rapidly, as samples were much more difficult to obtain when the primary mass had cooled below the salt freezing temperature. Samples were fully stripped from the wire to avoid mixing of dendrites produced at different conditions.

Figure 4.11 shows a sample collection in the glovebox, and Figure 4.12 shows a close view of several dendrite experiments prior to sample harvest.

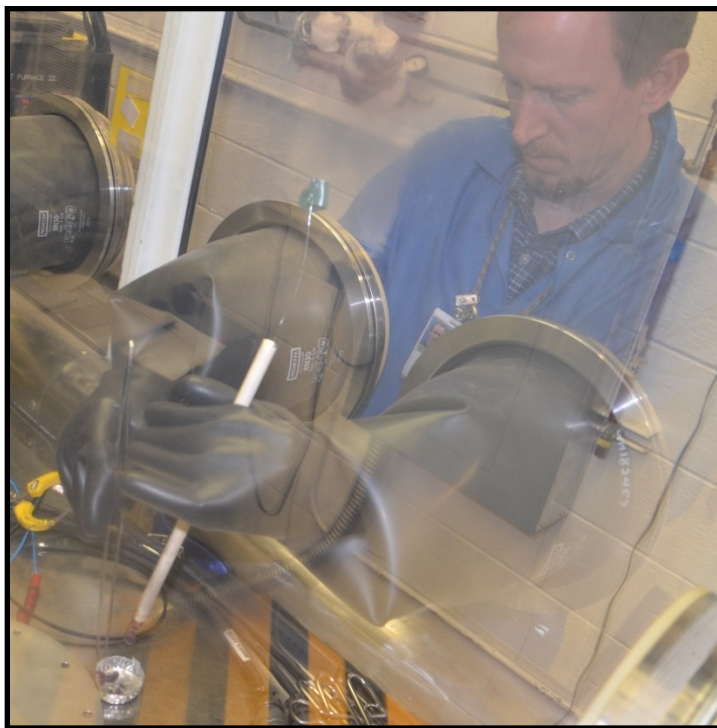


Figure 4.1: Harvesting a dendrite sample in the glovebox.

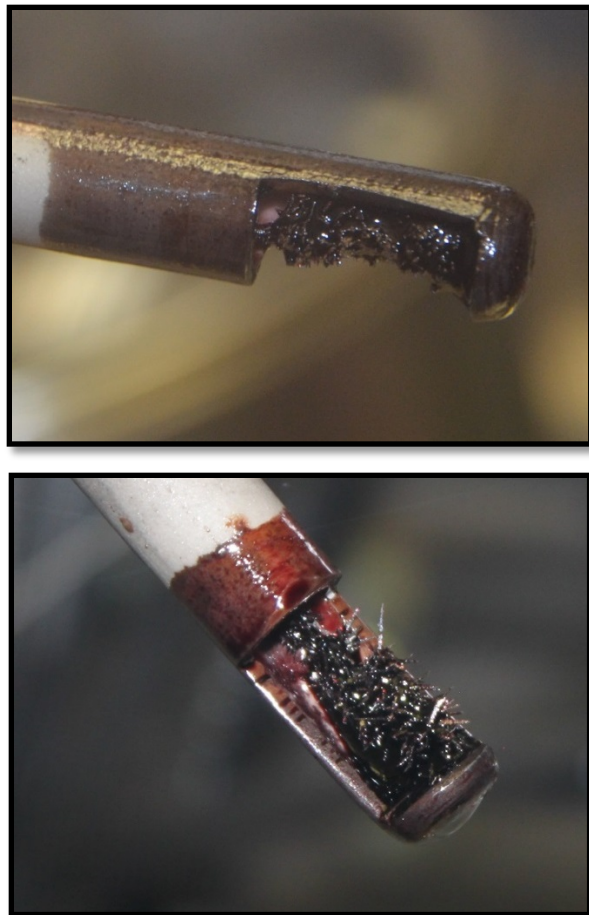


Figure 4.12: Typical uranium dendrite experiments ready for sample harvest.

Several uranium dendrite samples were grown under different conditions and inspected via SEM. These samples were harvested using the technique described above, followed by a 10- to 15-minute duration gentle washing in 30 mL of deionized water or by direct immersion of the window electrode itself in deionized water. For this case, the wet window electrode was discarded. Figure 4.13 shows the process with uranium crystals grown at a very low overpotential. A small sample was then collected on filter paper in the glovebox and carefully transferred onto a carbon sticky dot attached to a metallurgical mount. It was attempted to rapidly transfer samples into the SEM vacuum chamber to limit surface oxidation of the metal dendrites. High magnification secondary electron and back scatter electron images of the samples were obtained on a JEOL 7600 FE scanning electron microscope, as well as compositional spectra from energy dispersive spectroscopy.

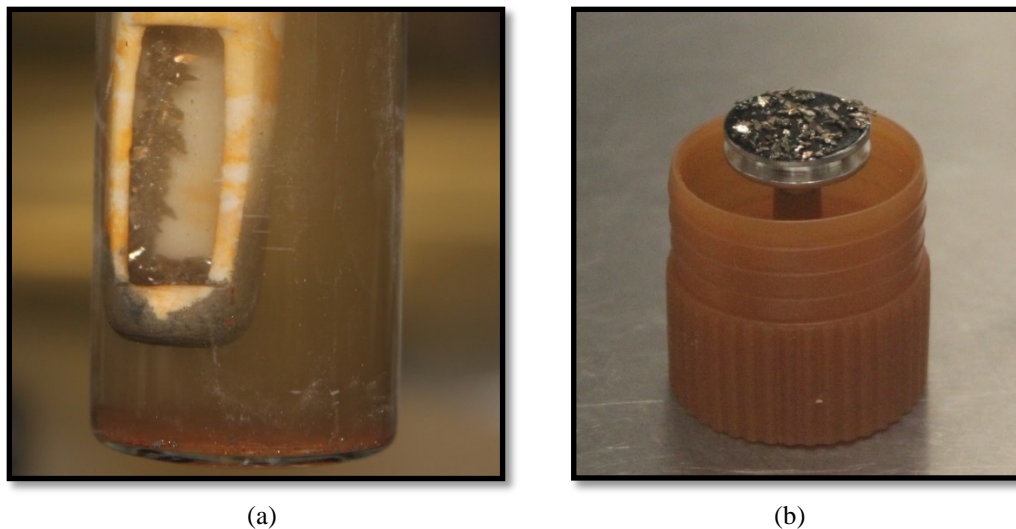


Figure 4.13: Uranium dendrite sample grown at 25 mV overpotential being prepared in the glovebox for inspection by SEM; (a) salt removal by washing in deionized water and (b) sample on metallurgical mount.

4.2.5 Experiment Preparation

To eliminate the possibility of adsorbed moisture being released from the furnace internal structure, the experiment assembly was thoroughly out-gassed by heating to 1073 K for 6 hours prior to an experiment campaign. Chemicals received from the manufacturer were opened inside the glovebox and stored thereafter inside the glovebox in sealed glass or metal containers. Appropriate mixtures of CeCl_3 , LiCl-KCl , and LiCl-KCl-UCl_3 salts were weighed on a calibrated balance and transferred into a tantalum crucible (Figure 4.6). The crucible was placed into the furnace, heated, and held at a stable setting of 773 ± 1 K. The melting temperature of the salt is expected to be near 623 K. The experiment routine followed for these experiments was similar to that described in Section 4.1.4.

The alumina tubes, tantalum wires, and tungsten wires were rinsed by a methanol wash and dried prior to use. Immersed wires and tubes were replaced between experiment sets to eliminate the potential for cross contamination.

Electrochemical measurements were performed using a Solartron 1287 potentiostat/galvanostat controlled with Corrware software (Scribner Associates) (Figure 4.14).



Figure 4.14: Experiment control cabinet with laptop for Corware (top), furnace power and temperature monitoring (center), and Solartron 1287 potentiostat (bottom).

4.3 Process Sampling in the Fuel Conditioning Facility

Samples were obtained from the Mk-IV ER (refer to Figure 1.1) in the Fuel Conditioning Facility of the Materials and Fuels Complex of INL. The Fuel Conditioning Facility is an argon-atmosphere hot cell for processing of highly radioactive materials. Electrometallurgical processing equipment for the treatment of used EBR-II fuel is operated inside the hot cell through the use of automation and tele-manipulators.

The Mk-IV ER contains a pool of approximately 41 cm depth of molten LiCl-KCl eutectic. The salt pool also contains fission and transmutation products from the processing of several metric tons of used EBR-II fuel. During electrometallurgical processing operations, chopped irradiated sodium-bonded metallic fuel is electrochemically dissolved with collection of purified uranium on a carbon steel cathode rod. These dendrite masses can reach approximately 10 kg in mass

and grow up to approximately 25 cm diameter and height (Figure 1.1). When an electrorefining operation has reached terminal conditions, the cathode deposit is vertically raised into the heated gas space above the molten pool and held for approximately 10 minutes to allow excess salt to drain. The steel rod and deposit are then removed from the electrorefiner and transferred to a device where the uranium deposit is mechanically sheared into a zirconia-lined graphite crucible. The crucible is transferred into a vacuum furnace where the salt is vacuum distilled and the uranium melted into a consolidated ingot.

This portion of the study was directed toward acquisition of data regarding the intrinsic purity of electrorefined uranium dendrites from the electrometallurgical processing of used nuclear fuel. The investigation included major transuranium elements and major lanthanoid contaminants which may serve as indicators or follow similar trends to transuranium contaminants. It was planned to acquire samples from at least three uranium products and analyze for characteristic rare earth and actinide contaminants. Table 4.5 depicts the planned samples for cathode products. The results of these efforts are described in Chapter 6.

Table 4.5: Planned dendrite samples from electrometallurgical processing.

Sample Form	Source	La	Pr	Np	Pu
Top, crushed	Cathode 5	○	○	○	○
Bottom, crushed	Cathode 5	○	○	○	○
Top, crushed	Cathode 6	○	○	○	○
Bottom, crushed	Cathode 6	○	○	○	○
Crushed	Cathode 9	○	○	○	○
Crushed	Cathode 10	○	○	○	○
Crushed	Cathode 11	○	○	○	○
Uncrushed	Cathode 9	○	○	○	○
Uncrushed	Cathode 10	○	○	○	○
Uncrushed	Cathode 11	○	○	○	○

4.3.1 Electrorefiner Salt Samples

Salt samples from the electrorefiner are periodically obtained for process observation and mass accountancy purposes. These salt samples are important to this work, as they indicate the quantity of background contaminants which are present in the electrolyte itself. These samples

are manually obtained by dipping a small tantalum tube through an open port into the molten salt. The tantalum tube has a tantalum frit pressed into the bottom end which is intended to filter potential particulate larger than several tens of microns. A small section of the tube is cut from above the frit, and this serves as the sample. The salt sampling device is shown in Figure 4.15.

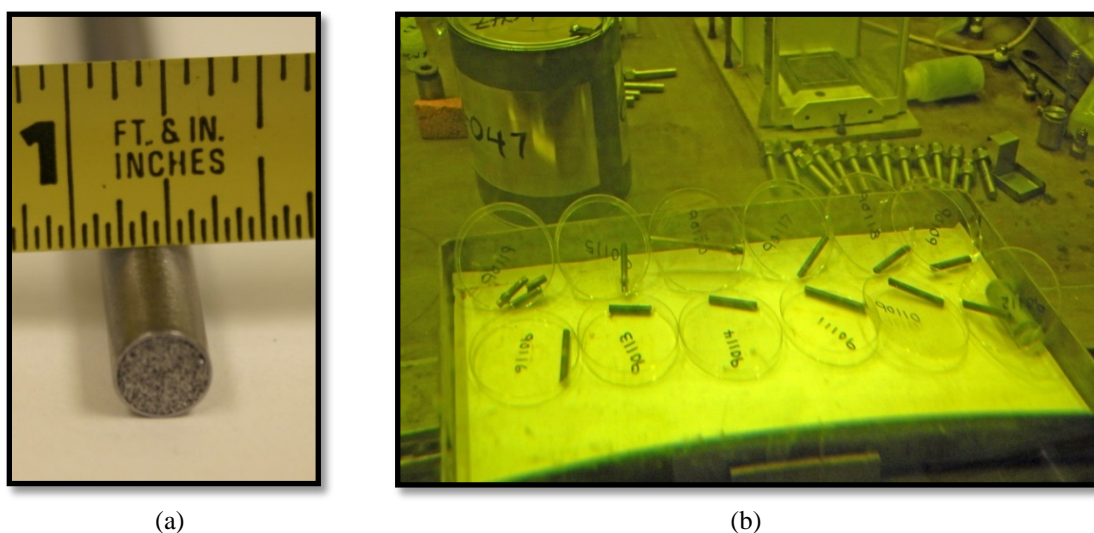


Figure 4.15: Tantalum salt sampling device used in the Mk-IV electrorefiner in the Fuel Conditioning Facility; (a) new device and (b) salt samples being prepared for analysis.

Radioactive process samples from the Fuel Conditioning Facility are packaged in sealed metal containers and pneumatically transferred via underground tubing to the INL Analytical Laboratory (AL). The AL hot cells have air atmosphere, and oxygen or moisture-sensitive samples are gradually affected if not processed quickly. When samples are received, they are weighed and dissolved as soon as possible to limit changes to sample mass from reaction with oxygen or moisture. Samples for the present study were analyzed by ICP-MS or inductively coupled plasma optical emission spectroscopy (ICP-OES). Analysis error for these methods at the two standard deviations (2σ) level varies depending on details of the dilutions and content, and the error may be as low as $\pm 5\%$. Table 4.6 provides a summary of the analytical procedures for the analysis of salt samples.

Table 4.6: Sample preparation for Mk-IV salt.

1)	Sample container is opened. Sample is weighed and placed in a glass beaker.
2)	Sample is covered with 25mL of nano-pure water.
3)	Beaker is gently heated on a hotplate for ~1 hour.
4)	Following visual verification, that salt is fully removed from the tube, and the tantalum tube section is removed from the beaker with tweezers.
5)	25mL of 8M nitric acid and 2 drops of 24M hydrofluoric acid are added to the beaker sequentially.
6)	Solution and any residual solids are allowed to react at room temperature for several minutes.
7)	If necessary, beaker is heated to $\leq 50^{\circ}\text{C}$ on a hot plate until all solids are dissolved.
8)	Dissolved sample solutions are quantitatively transferred to a polyethylene dissolver bottle and allowed to cool.
9)	Dissolver bottle is weighed, and aliquots for analysis are drawn as needed.

4.3.2 Dendrite Samples

Samples of these dendrite masses reported in the present study were obtained manually in the Fuel Conditioning Facility by physically breaking a piece of dendrite from the primary cathode mass with the fingers of a tele-manipulator. Some of the dendrite samples were manually crushed in order to explore the possibility for reduction of physically occluded salt within the dendrite. Pulverization was accomplished using an impact-type mortar and pestle constructed of tool steel and tungsten carbide, shown in Figure 4.16, which was operated manually by tele-manipulators through the cell wall. Figure 4.17 shows a crushed dendrite sample being prepared for analysis in AL.

Samples were weighed, packaged in sealed metal containers, and pneumatically transferred via underground tubing to the analysis facility. In some cases, each dendrite sample is divided into two different analyses. One is the *water wash* solution which contains salt adhered to the outside of the dendrites. The second is the sample of the dissolved dendrite pieces after the external salt has been removed by the water wash. Once received in the AL, the procedure presented in Table 4.7 was followed for sample preparation.

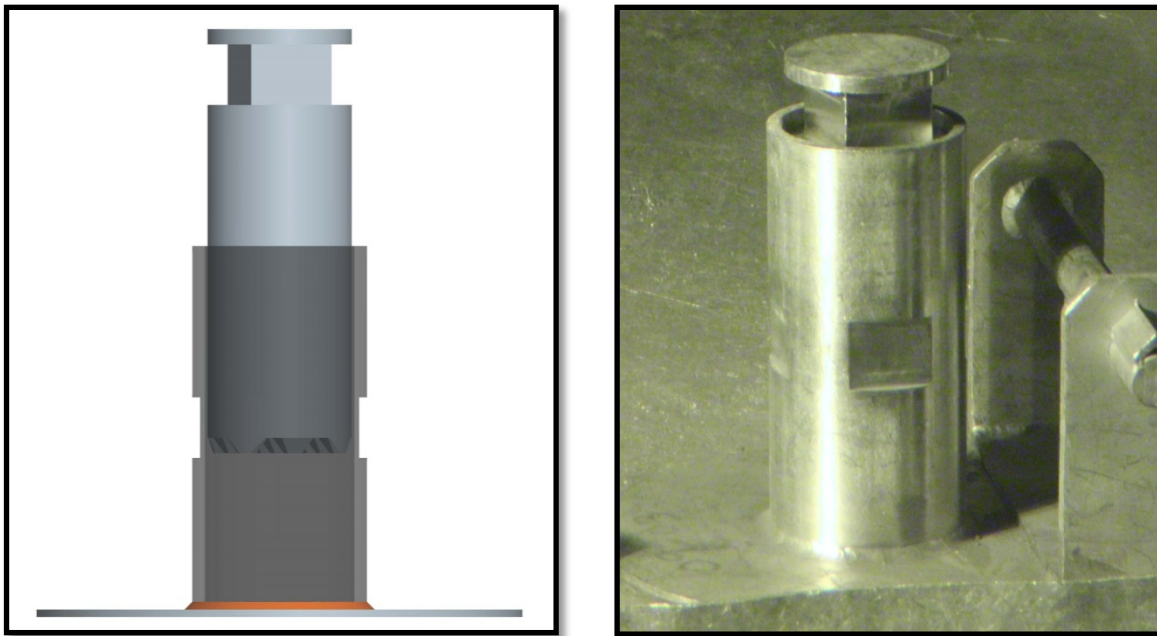


Figure 4.16: Impact mortar used to crush dendrite samples in the Fuel Conditioning Facility.

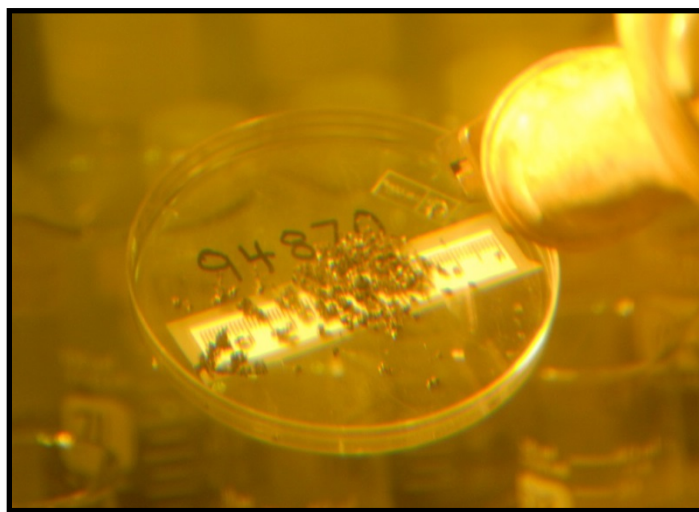


Figure 4.17: Crushed dendrite sample from the Mk-IV ER being prepared for analysis in the AL hot cell.

Table 4.7: Sample preparation for Mk-IV uranium dendrites.

1)	The received dendrite sample is photographed.
2)	The dendrite sample is weighed and placed in a glass beaker.
3)	Sample is covered with 25mL of nano-pure water.
4)	Beaker is gradually heated on a hotplate for ~1 hour.
5)	The beaker is allowed to cool, and beaker contents are filtered to remove insoluble material such as dendrite pieces.
6)	1 mL of 16M nitric acid is added to the filtered solution to ensure analytes remain dissolved.
7)	Filtered solution is quantitatively transferred into a dissolver bottle, and a solution weight is obtained.
8)	Aliquots for analysis are drawn as needed from the dissolver bottle for the water-wash solution.
9)	Filter, filter backing, and captured solids (metal dendrite pieces) are placed into another beaker.
10)	A small amount of nano-pure water is used to rinse the filter/backing, but the filter/backing remains in the beaker.
11)	25 mL of 8M nitric acid and two drops of 24M hydrofluoric acid are added to the beaker sequentially.
12)	The solution is allowed to react at room temperature for several minutes.
13)	Beaker is heated to $\leq 50^{\circ}\text{C}$ on a hot plate until all solids are dissolved. Solution volume is maintained by adding 8M nitric acid as necessary.
14)	12M hydrochloric acid is added to the beaker if insoluble material persists.
15)	To ensure no solids remain on the filter, the filter/backing is removed and rinsed with 1M nitric acid. The rinse acid is added to the dissolver solution.
16)	Solution is quantitatively transferred to a polyethylene dissolver bottle and allowed to cool.
17)	The dissolver bottle is weighted, and aliquots for analysis are drawn as needed for the dendrite sample.

CHAPTER 5. RESULTS AND ANALYSIS – ELECTROCHEMISTRY OF CERIUM

Investigation of cerium began with cyclic voltammetry to establish the nature of the system and the reversibility of observed reactions. Square wave voltammetry was performed to establish the number of electrons transferred, and this allowed the estimation of diffusion coefficients from the cyclic voltammogram peaks. Diffusion coefficients were also measured using chronopotentiometry as a means to increase confidence in the measurement results. The equilibrium potential of the cerium reaction was measured by open circuit chronopotentiometry and used to compute the Gibbs free energy, enthalpy, and entropy. The experimental Gibbs free energy and that obtained from reaction of the elements in their sub-cooled state were then used to estimate the activity coefficient of CeCl_3 in LiCl-KCl eutectic. Nucleation characteristics of cerium were investigated by chronoamperometry to establish whether nucleation of cerium nuclei was “instantaneous,” near the onset of the electric potential, or continued “progressively” throughout the deposition. Finally, exchange current density was estimated using the linear polarization technique with data obtained at very slow scan rates.

5.1 Cyclic Voltammetry

Figure 5.1 shows a voltammogram of the pure LiCl-KCl eutectic system. The residual current is less than 2 mA between -1.0 V and initiation of the Li reduction summit at approximately -2.40 V versus the Ag/AgCl reference electrode. The absence of any other peaks in this region showed a melt free of oxides, hydroxides, or other impurities which would complicate the signal of the intended active component.

Figure 5.2 shows a characteristic voltammogram of CeCl_3 in a LiCl-KCl eutectic melt. Residual current between 0.0 V and cerium deposition (-1.8 V) is very low, less than 3–4 mA. The reduction (R1) occurs in a single sharp peak with a gradual decay, characteristic of deposition of an insoluble phase limited by diffusion. Deposition begins at a more positive potential than the beginning of the oxidation peak (Ox1), which shows that the required nucleation overpotential for deposition of cerium is limited. The reverse anodic scan shows an oxidation peak (Ox1) of much higher amplitude than the reduction peak due to the availability

of deposited metal for the oxidation. The peak abruptly drops, corresponding to depletion of the deposited metal. The positive side of the peak shows a plateau (P1) often seen at high current densities in molten salts, possibly caused by the formation of a transient solid film. A sharp, even rise in anodic current is seen at 1.3 V which does not have a corresponding cathodic peak on the reverse scan. This is characteristic of gas evolution from electrolyte decomposition.

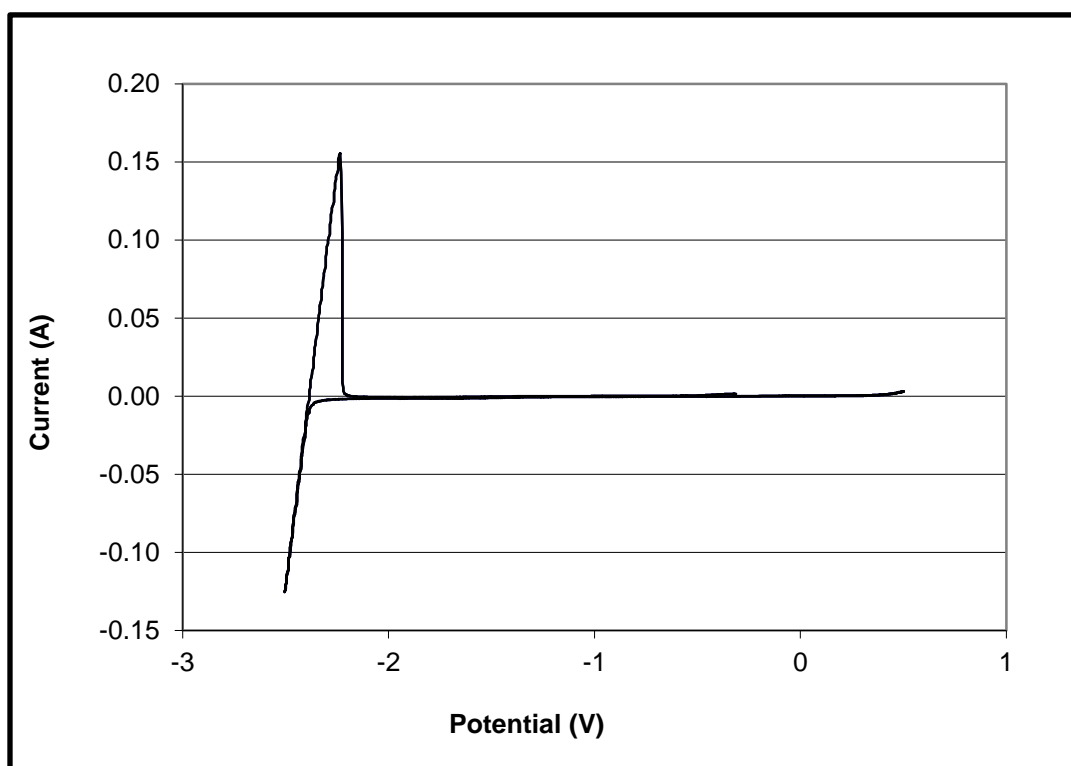


Figure 5.1: Cyclic voltammogram of LiCl-KCl eutectic at 773 K. Tungsten working electrode of 0.22 cm²; molybdenum mesh counter electrode; Ag/AgCl reference electrode. Scan rate 0.2 V/s.

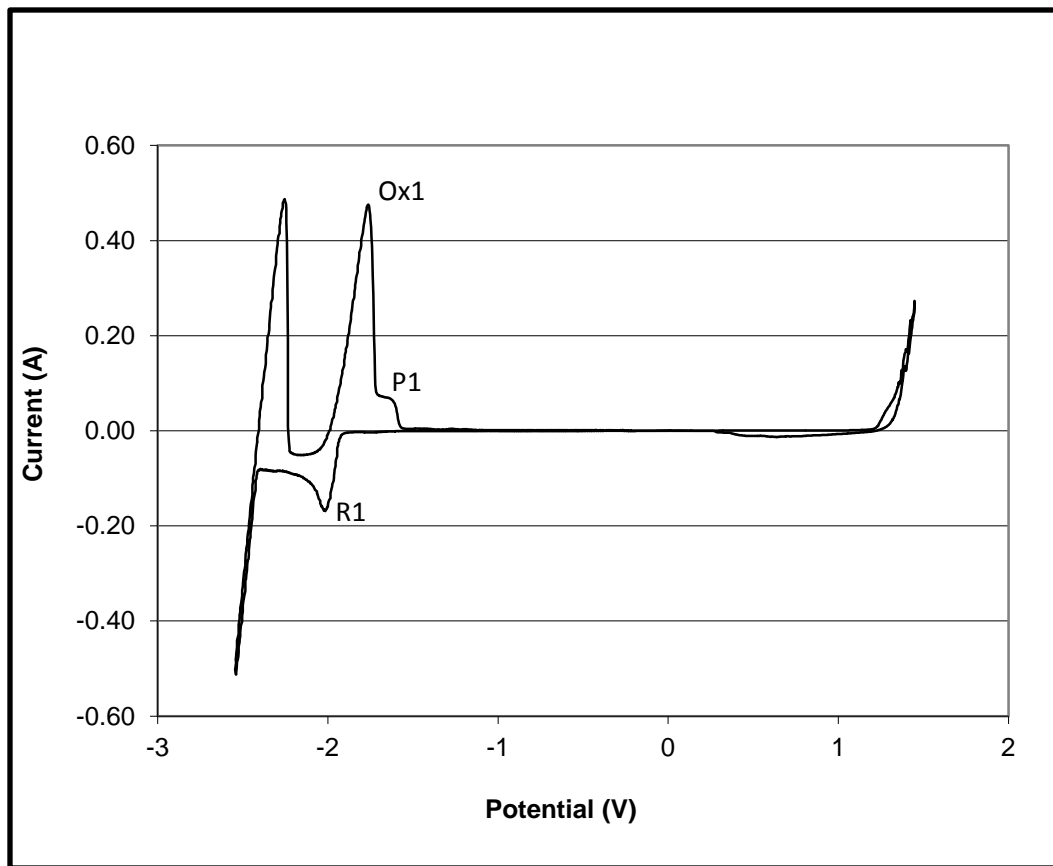


Figure 5.2: Cyclic voltammogram of CeCl_3 in LiCl-KCl eutectic at 773 K and 1.0 mol% CeCl_3 . Working electrode of 0.46 cm^2 ; Ce in Mo mesh counter electrode; Ag/AgCl reference electrode. Scan rate 0.2 V/s.

The reversibility of the reaction was evaluated at 653 and 773 K with similar results. The effect of scan rate upon deposition and dissolution of CeCl_3 is seen in Figure 5.3. Above a scan rate of approximately 0.2 V/s, the peak potential clearly shifts toward more negative potentials as scan rate is increased. This is characteristic of a reaction limited by electron transfer. Furthermore, Figure 5.4 shows that when the cathodic peak current is plotted versus the square root of scan rate, the data are bound by two lines from the origin, with an intermediate transition. The behaviors seen in Figure 5.3 and Figure 5.4 are characteristic of a quasi-reversible system where the system displays Nernstian behavior at low scan rates but transitions to irreversibility at high scan rates.

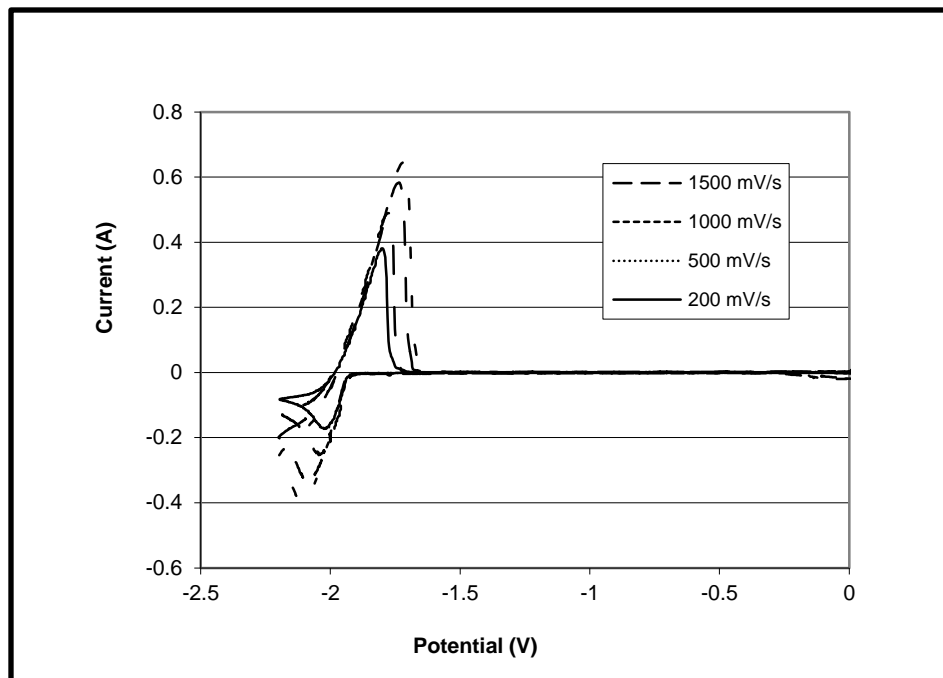


Figure 5.3: The effect of scan rate upon reduction of CeCl_3 in LiCl-KCl eutectic at 773 K and 1.0 mol% CeCl_3 . Tungsten working electrode of 0.46 cm^2 ; cerium in molybdenum mesh counter electrode; Ag/AgCl reference electrode.

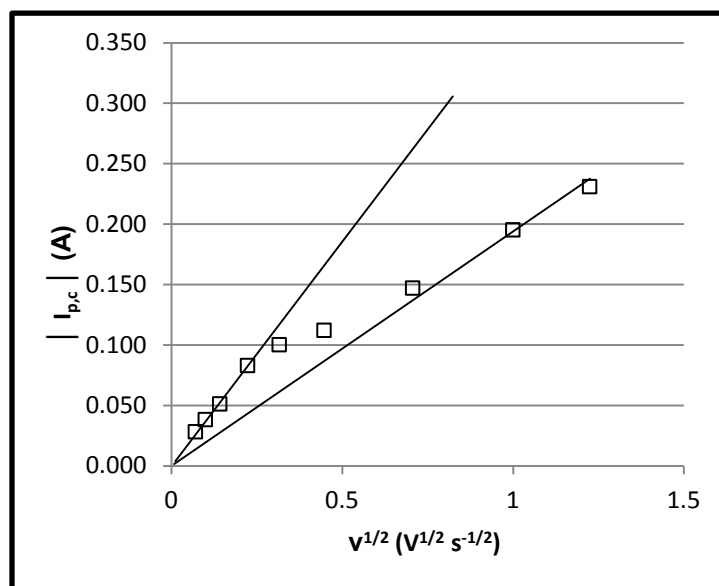


Figure 5.4: Peak cathodic current as a function of the square root of scan rate. CeCl_3 in LiCl-KCl eutectic at 653 K and 1.0 mol% CeCl_3 . Tungsten working electrode of 0.46 cm^2 ; cerium in molybdenum mesh counter electrode; Ag/AgCl reference electrode.

5.2 Number of Electrons

The diffusion coefficient of the cerium species can later be obtained from the slope of the line in Figure 5.4, provided the number of electrons transferred is known. This can be obtained with square wave voltammetry using the principles described in Section 2.7.2 and specifically Eq. [2.18]. Figure 5.5 shows a square wave voltammogram for CeCl_3 at 673 K, obtained at a step potential of 1 mV and 20 Hz, which places the reaction in the reversible range. In the case of an insoluble product in molten salts, it is sometimes found that the wave is very asymmetric due to a delay in the rise of the wave from a required nucleation overpotential (47, 190, 225). However, as observed via cyclic voltammetry (Figure 5.2), the nucleation overpotential is limited, and the wave for cerium is relatively symmetric. The computed value of n is 3.14, close to three electrons. A similar observation was made by Castrillejo and coworkers (139) and Yoon and Phongikaroon (140).

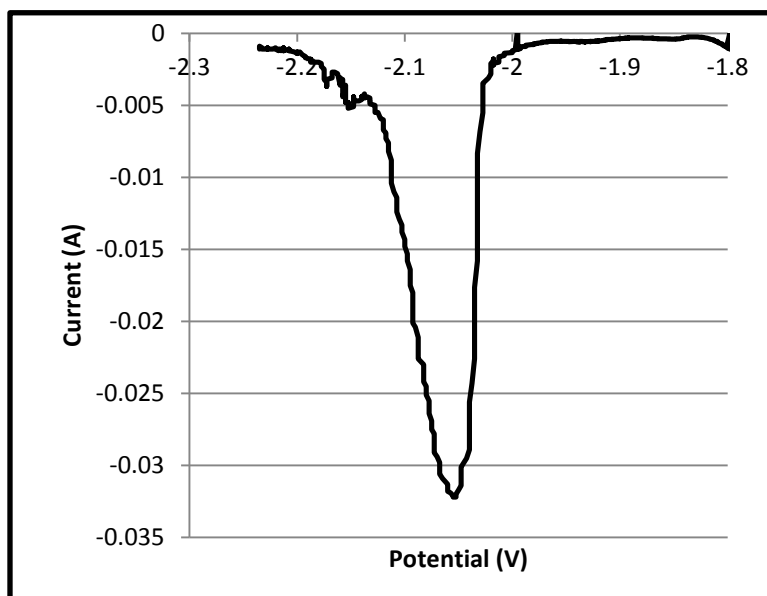


Figure 5.5: Net-current square wave voltammogram for CeCl_3 in LiCl-KCl eutectic at 673 K at 1.0 mol% CeCl_3 . Working electrode of 0.24 cm^2 ; cerium in molybdenum mesh counter electrode; Ag/AgCl reference electrode; pulse height 25 mV; potential step 1 mV; frequency 20 Hz.

5.3 Diffusion Coefficients from Cyclic Voltammetry

With the number of electrons known, the Randles-Sevcik equation (Eq. [2.9]) described in Section 2.6 can be used to determine the diffusion coefficient. For reversible, soluble-insoluble processes, Berzins and Delahay relation (Eq. [2.26] from Section 2.8) can be used with the data obtained from cyclic voltammograms at slow, reversible scan rates.

Alternatively, Eq. [2.27] is appropriate for conditions of irreversibility. For this case, data from the irreversible portion of the curve at higher scan rates is utilized. To utilize Eq. [2.27], the quantity αn_α must be obtained. It was estimated using Eq. [2.17] as described in Section 2.7, with the data obtained from cyclic voltammetry such as those depicted in Figure 5.3. Table 5.1 summarizes results for αn_α obtained at different temperatures.

Table 5.1: Values of αn_α computed from cyclic voltammetry.

Temperature (K)	αn_α (1 V/s)
653	1.45
773	1.36
973	1.66

5.4 Diffusion Coefficients from Chronopotentiometry

The diffusion coefficient can also be determined by chronopotentiometry, via the Sand equation, Eq. [2.28]. The Sand equation was developed for the assumption of linear diffusion, but under the experimental conditions, the corrections for cylindrical geometry are minor and can be neglected (226-228). Some investigators utilize an experimental technique that modifies the surface area instead of the applied current, on the assumption that this may reduce errors due to interfacial wetting. However, in the present set of experiments it was observed that wetting is a function of time and immersion history, and altering the immersion depth without consideration of these factors may introduce more error than that obtained with the traditional approach of successive chronopotentiometric tests with a constant surface area. In the present work, the traditional approach of successive tests at a consistent surface area was utilized, with the electrode anodically stripped between tests. Figure 5.6 shows a group of potentiograms for CeCl_3 in LiCl-KCl eutectic. Prior to use, it must be demonstrated that i and $\tau^{-1/2}$ have a linear

relationship and pass through the origin. Figure 5.7 shows i plotted versus $\tau^{-1/2}$, for a series of chronopotentiometric runs at constant concentrations and electrode area. It is seen that the Sand equation is upheld, and the diffusion coefficient may be obtained from the slope.

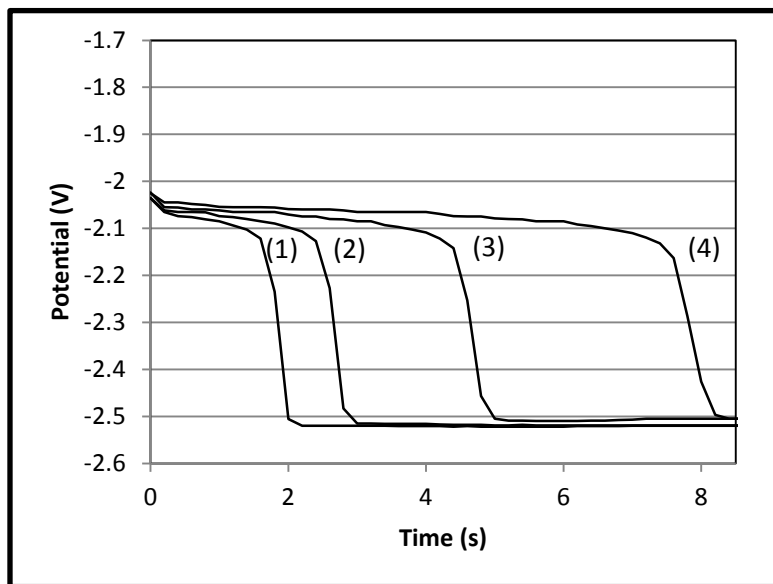


Figure 5.6: Chronopotentiograms for CeCl_3 in LiCl-KCl eutectic at 653 K (1.0 mol% CeCl_3); (1) - 60 mA; (2) -50 mA; (3) -40 mA; (4) -30 mA. Tungsten working electrode of 0.42 cm^2 ; cerium in molybdenum mesh counter electrode; Ag/AgCl reference electrode.

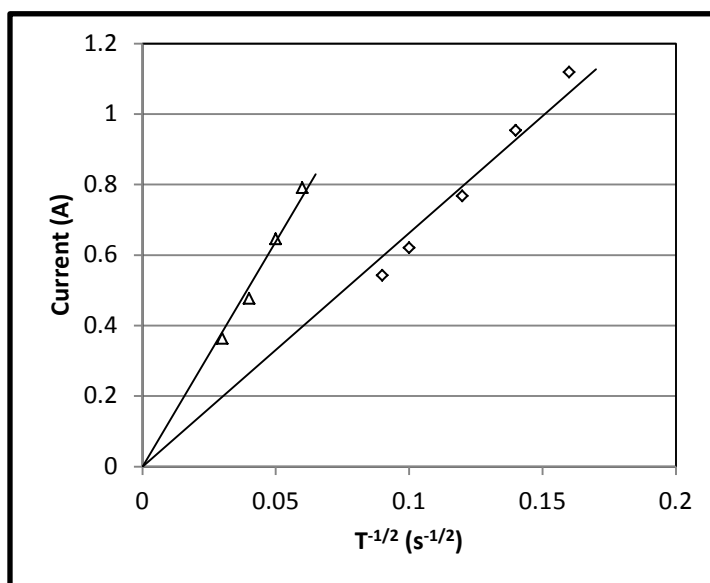


Figure 5.7: Relation between i and $\tau^{-1/2}$ from chronopotentiograms for CeCl_3 in LiCl-KCl eutectic at (Δ) 653 and (\diamond) 773 K. Tungsten working electrode of 0.42 and 0.44 cm^2 , respectively; cerium in molybdenum mesh counter electrode; Ag/AgCl reference electrode.

Table 5.2 contains the values of diffusion coefficients for Ce(III) obtained by the three methods employed (Eqs. [2.26], [2.27], and [2.28]). These values are similar to those observed by Iizuka (123), Castrillejo and coworkers (139), and Lantelme and coworkers (125), but these values are modestly higher than those measured by Yoon and Phongikaroon (140). Figure 5.8 compares the D values obtained in the present work with those obtained at the narrower testing temperatures of prior studies. The relationship is linear with temperature on a log plot, confirming the Arrhenius law. No phenomena are observed to complicate the diffusion behavior across this temperature range. A summary diffusion coefficient of Ce(III) in molten LiCl-KCl can be obtained from this aggregate data. The trend shown in Figure 5.8 is described by

$$\log D_{Ce(III)} = -2.43 - 1952/T \quad (D_{Ce(III)}: cm^2s^{-1}), \quad [5.1]$$

or in exponential form

$$D_{Ce(III)} = 0.003965 \exp(-4305/T) \quad (cm^2s^{-1}). \quad [5.2]$$

The second expression is of the form

$$D_{Ce(III)} = D_{Ce(III)}^0 \exp(-E_a / RT) \quad (cm^2s^{-1}), \quad [5.3]$$

where $D_{Ce(III)}^0$ is the pre-exponential factor and E_a is the activation energy ($kJ mol^{-1}$). The calculated activation energy for diffusion of Ce(III) was computed to be $-35.8 kJ mol^{-1}$. This is slightly higher than the values obtained by Lantelme and coworkers (125) and by Yoon and Phongikaroon (140) who found E_a to be $-29.7 kJ mol^{-1}$ and -30.7 to $-33.4 kJ mol^{-1}$, respectively.

Table 5.2: Diffusion coefficients of Ce(III) in LiCl-KCl eutectic at [1.0 mol%].

Temperature (K)	$D_{Ce(III)} 10^5 (cm^2s^{-1})$		
	CV - Eq. [2.26]	CV - Eq. [2.27]	CP
653	0.47 ± 0.03	0.39 ± 0.02	0.53 ± 0.3
773	0.99 ± 0.07	1.49 ± 0.09	1.96 ± 0.12
973	2.76 ± 0.17	5.06 ± 0.31	-

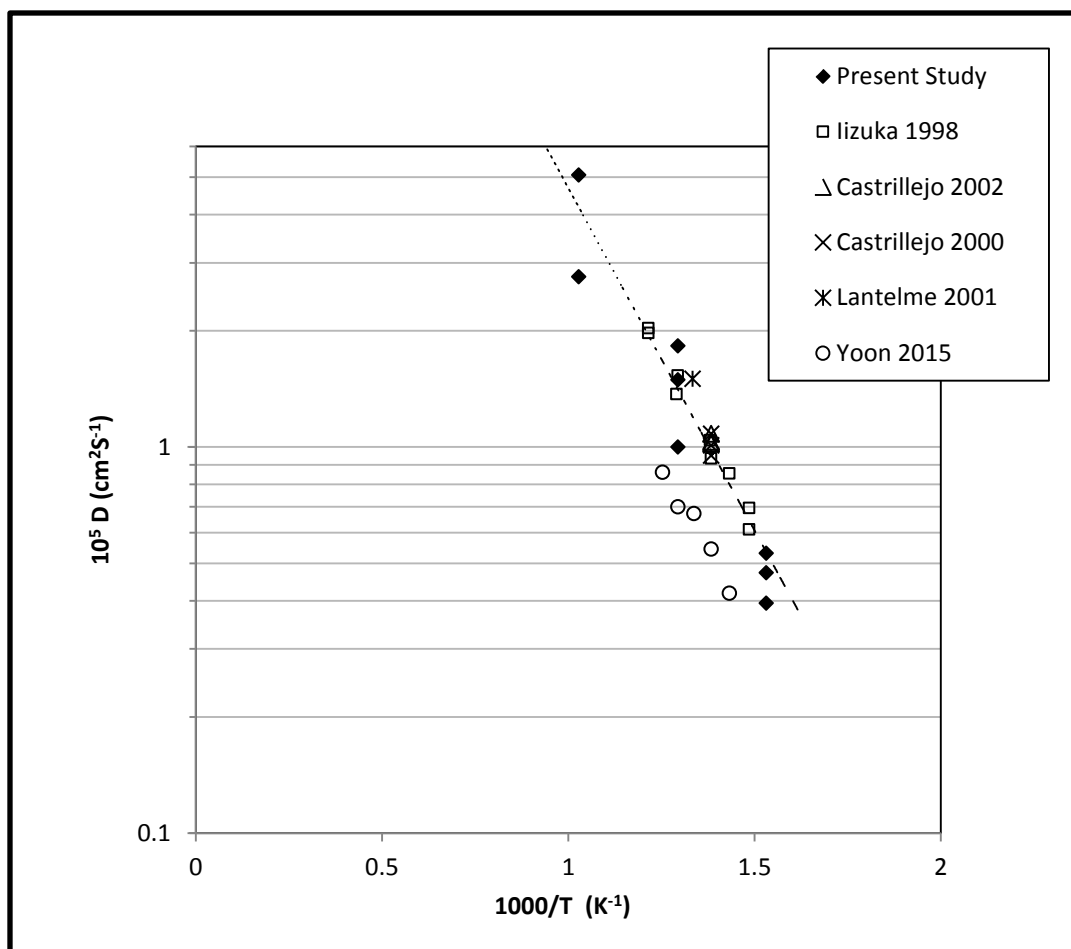


Figure 5.8: Variation of diffusion coefficient of CeCl_3 with temperature in LiCl-KCl eutectic.

5.5 Equilibrium Potential

The measured potential for a metal in equilibrium with its metal chloride, in this case the Ce(III)/Ce(0) couple, is determined by the Nernst relationship Eq. [2.7]. This work utilized chronopotentiometric evaluations to measure equilibrium potential of cerium. The open circuit potential of a cerium rod or cerium deposited on a tungsten wire was measured on multiple occasions across a range of temperatures, and these measurements are summarized in Table 5.3. Figure 5.9 shows the apparent standard potentials computed from the experimental data of Table 5.3, as well as literature data from several other studies. The experimental data of the present study (shown by the line of Figure 5.9) can be described by

$$E_{\text{CeCl}_3}^* = -3.5338 + 5.923 \times 10^{-4} T \text{ (V)}. \quad [5.4]$$

Table 5.3: Experimental data for equilibrium potentials of Ce(III)/Ce(0) in LiCl-KCl eutectic.

Temperature (K)	E (V) vs. Ag/AgCl	E* (V) vs. Cl ₂ /Cl ⁻
653	-2.024	-3.138
672	-2.015	-3.133
673	-2.015	-3.133
673	-2.018	-3.136
773	-1.934	-3.074
773	-1.945	-3.085
774	-1.945	-3.085
774	-1.935	-3.075
775	-1.945	-3.086
778	-1.935	-3.076
785	-1.915	-3.058
966	-1.773	-2.955
973	-1.773	-2.957

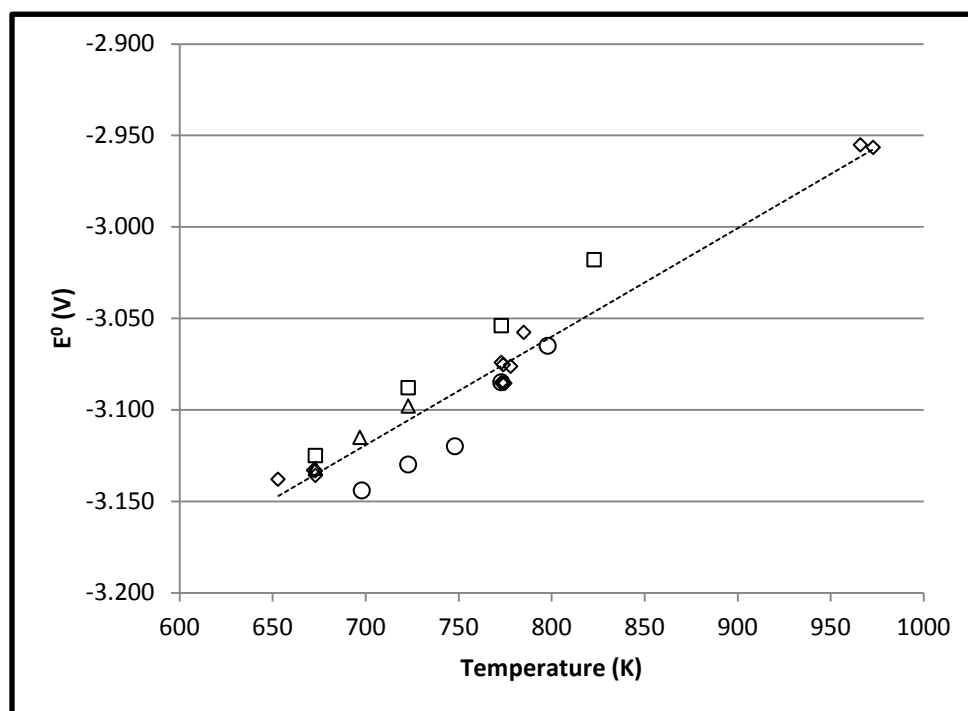


Figure 5.9: Variation of the apparent standard potential of Ce(III)/Ce(0) with temperature in LiCl-KCl. (◇) Experimental results of present work, (□) Castrillejo (139), (Δ) Fusselman (65), (○) Yoon and Phongikaroon (140).

5.6 Gibbs Free Energy and Activation Coefficient

The standard potential relationship of Eq. [5.4] can be used to compute the Gibbs free energy of formation and subsequent dissolution of the reaction



according to the relationship

$$\Delta G_{CeCl_3}^* = -nFE_{CeCl_3}^* \text{ (kJ mol}^{-1}\text{)} \quad [5.6]$$

where $\Delta G_{CeCl_3}^*$ is the Gibbs free energy of the dissolved metal chloride, calculated from the experimentally determined standard potential, $E_{CeCl_3}^*$. Gibbs free energy is also a function of temperature, following the form

$$\Delta G_{CeCl_3}^0 = \Delta H_{CeCl_3}^0 - T\Delta S_{CeCl_3}^0 \text{ (kJ mol}^{-1}\text{)} \quad [5.7]$$

from which the enthalpy ($\Delta H_{CeCl_3}^0$) and entropy ($\Delta S_{CeCl_3}^0$) may be obtained. The values of $\Delta G_{CeCl_3}^*$ from the present study were plotted versus temperature, and the equation of this form was found to be

$$\Delta G_{CeCl_3}^* = -1023 + 0.1715T \text{ (kJ mol}^{-1}\text{)}. \quad [5.8]$$

A comparison of ΔG^* and E^* values from the present study and the literature is provided in Table 5.4. The values of E^* determined in this work are very similar but slightly more negative than those previously reported. This may be partially due to the challenging experiment environment and partially a function of small differences in extrapolation of the data reported by Yang and Hudson (28) for Ag/AgCl reference electrodes as described in Section 3.1.

Table 5.4: Comparison of predicted E^* and ΔG^* for $CeCl_3$ in LiCl-KCl eutectic.

Temp (K)	E^* (V)				$\Delta G_{CeCl_3}^*$ (kJ/mol)		
	Present Work	Castrillejo (139)	Fusselman (65)	Yoon (140)	Present Work	Castrillejo (139)	Fusselman (65)
673	-3.135	-3.125	-3.132		-907.6	-904.7	-906.7
723	-3.106	-3.088	-3.098	-3.132	-899.0	-894.0	-896.9
773	-3.076	-3.054		-3.085	-890.4	-884.2	
823	-3.046	-3.018			-881.9	-873.8	
873	-3.017				-873.3		
923	-2.987				-864.7		
973	-2.957				-856.1		

The activity coefficient for $CeCl_3$ in LiCl-KCl eutectic can be obtained from the relationship

$$RT \ln \gamma_{CeCl_3} = \Delta G_{CeCl_3}^* - \Delta G_{CeCl_3(sc)}^0 \quad [5.9]$$

where $\Delta G_{CeCl_3(sc)}^0$ is the Gibbs energy of formation from reaction of the pure compounds in the supercooled state (67). The results are summarized in Table 5.5. The computed activity coefficients are modestly lower than those calculated with the $\Delta G_{CeCl_3}^*$ data from Castrillejo and coworkers (139). The difference is the result of relatively modest differences in determined E^* and the literature values of $\Delta G_{CeCl_3(sc)}^0$ utilized by the different works. Due to this sensitivity to E_{AgCl} or E_{AgCl}^* extrapolations and the source of $\Delta G_{CeCl_3(sc)}^0$ data, activity coefficients determined by different investigators must be compared cautiously.

Table 5.5: Activity coefficient for $CeCl_3$ in LiCl-KCl eutectic.

Temperature (K)	γ
673	1.90E-02
723	1.46E-02
773	1.18E-02
823	9.78E-03
873	8.50E-03
923	7.59E-03
973	6.93E-03

5.7 Nucleation Characteristics

The electrochemical nucleation of cerium was investigated at 673 K to establish whether the nucleation mechanism is progressive or instantaneous on a tungsten electrode by the methods described in Section 2.11. Figure 5.10 shows a group of transients obtained at a range of overpotentials on a polished tungsten wire.

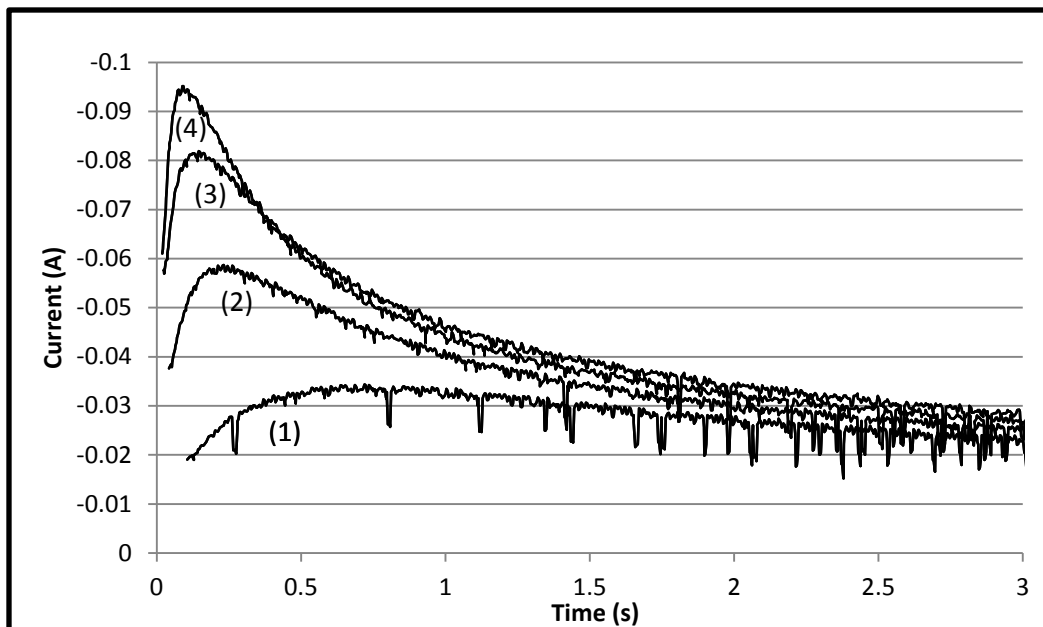


Figure 5.10: Nucleation transients of 1.0 mol% CeCl_3 in LiCl-KCl eutectic at various overpotentials [(1) -2.060 V; (2) -2.080 V; (3) -2.090 V; (4) -2.100 V versus Ag/AgCl] at 673 K. Tungsten working electrode; cerium in molybdenum mesh counter electrode; Ag/AgCl reference electrode.

Figure 5.11 presents plots of the rising portion of the nucleation transients, and these show a linear relationship between i and $t^{1/2}$. The work of Allongue and Souteyrand show the value $\alpha = 1/2$ corresponds to an instantaneous nucleation mode, with three-dimensional nuclei whose growth is controlled by hemispherical or planar diffusion.

Alternatively, the Scharifker and Hills method (see Section 2.11) analyzes the entire transient curve in a non-dimensional method. The nucleation transients previously shown in Figure 5.10 are re-plotted in Figure 5.12 along with the theoretical relationships shown in Figure 2.2. It is seen that the transients follow the model of instantaneous nucleation at all overpotentials. This confirms the conclusion that nucleation of cerium at 673 K was instantaneous.

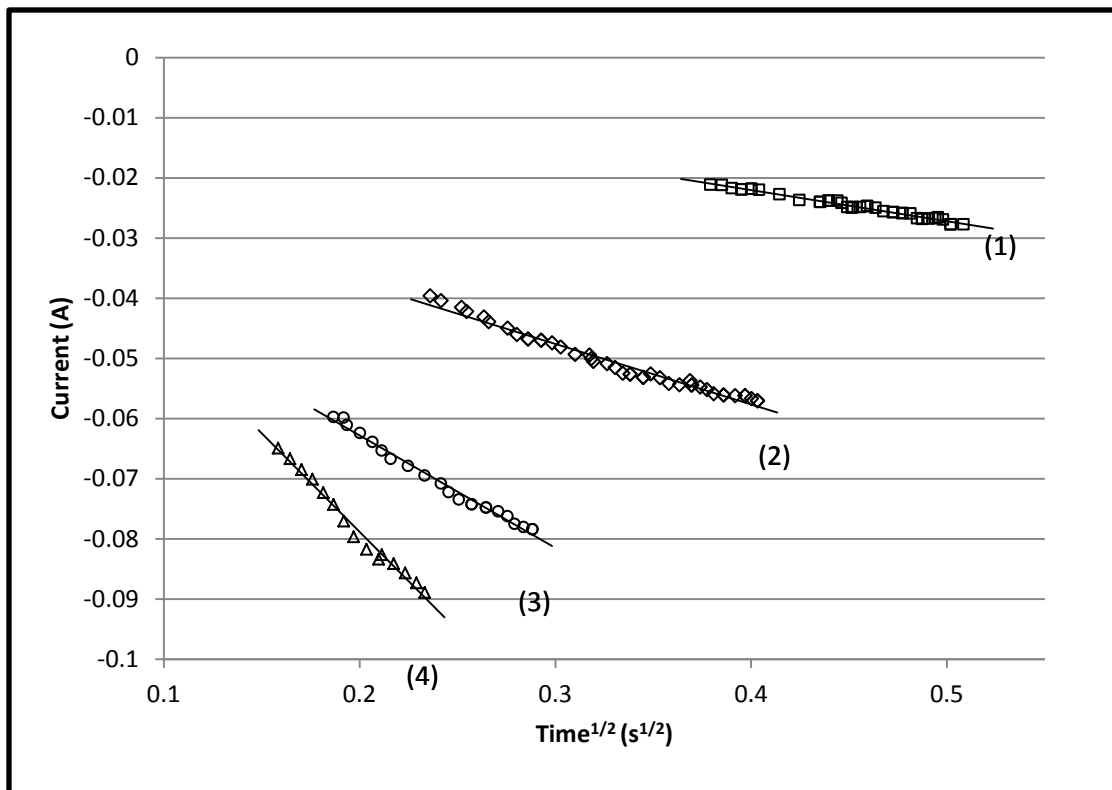


Figure 5.11: Plots of current versus $\text{time}^{1/2}$ from the rising portion of the nucleation transients shown in Figure 5.10 [(1) -2.060 V; (2) -2.080 V; (3) -2.090 V; (4) -2.100] at 673 K at 1.0 mol% CeCl_3 .

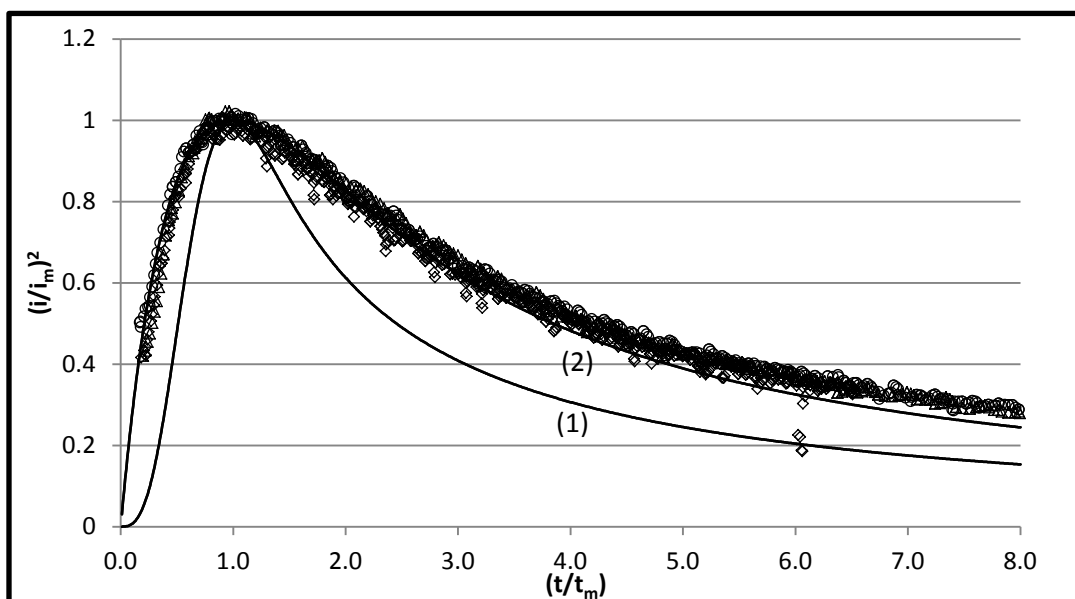


Figure 5.12: Comparison of the theoretical model for progressive (1) and instantaneous (2) nucleation with experimental nucleation transients shown in Figure 5.11 (\diamond) -2.080 V; (\circ) -2.090 V; (\square) -2.100 V.

5.8 Exchange Current Density

Exchange current density, i_0 , is the quantity of cathodic and anodic current that are exactly balanced when the electrochemical cell is held at the equilibrium potential. Generally, i_0 is a function of kinetic reaction parameters and is linked to reaction reversibility. It is also linked to nucleation characteristics and deposit morphology. For these reasons, it was desired to quantify the order of magnitude of exchange current density of the Ce(III)/Ce(0) couple in LiCl-KCl eutectic. These methods were described in Section 2.10 and are derived from the Butler-Volmer equation (Eq. [2.36]).

Cerium was deposited onto a tungsten wire to obtain Tafel-type plots at low scan rates at 653, 773, and 973 K, with a typical plot shown in Figure 5.13. Experiments showed that the tungsten wire was fully coated, and a visual examination under a microscope showed the surface area of the deposit to be approximately twice that of the tungsten substrate. In Figure 5.13, it can be seen that the indicated exchange current densities at the tested concentrations and temperatures are in the region between 0.01 and 0.1 A/cm². However, it was difficult to establish specific values due to the lack of well-defined linear regions in the Tafel plots.

To avoid the challenges posed by the Tafel approach, the linear polarization method was employed. This approach utilized data at very low overpotentials, where the cerium coating on the wire remained at nearly constant surface area. The data from Figure 5.13 at very low overpotentials was re-plotted in Figure 5.14, and a very linear region was seen at all temperatures. Assuming the surface area of the coating is approximately twice that of the underlying wire, the slope of the lines in Figure 5.14 may be utilized to estimate i_0 . The resulting estimates are shown in Table 5.6. The listed range is based on a potential surface area error of $\pm 100\%$. The surface of the tungsten was fully coated, and thus the area of the base substrate is a reasonable minimum. If the surface area was actually greater than twice that of the tungsten substrate, the estimated i_0 would be correspondingly reduced. The order of magnitude of these results is similar to the lowest exchange current densities reported for mono and divalent elements in molten LiCl-KCl (128-132). The reversibility at only the slowest scan rates and low

activity coefficient of CeCl_3 supports a conclusion that significant molecular complexation occurs, and this may explain the observation of a low i_0 .

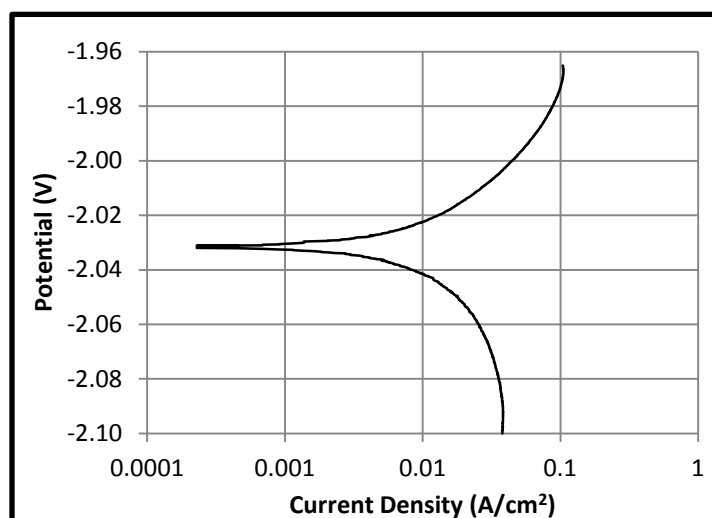


Figure 5.13: Tafel-type plot for Ce(III)/Ce(0) in LiCl-KCl eutectic at 653 K, 1 mV/s at 1.0 mol% CeCl_3 . W working electrode of 0.44 cm²; Ce in Mo mesh counter electrode; Ag/AgCl reference electrode.

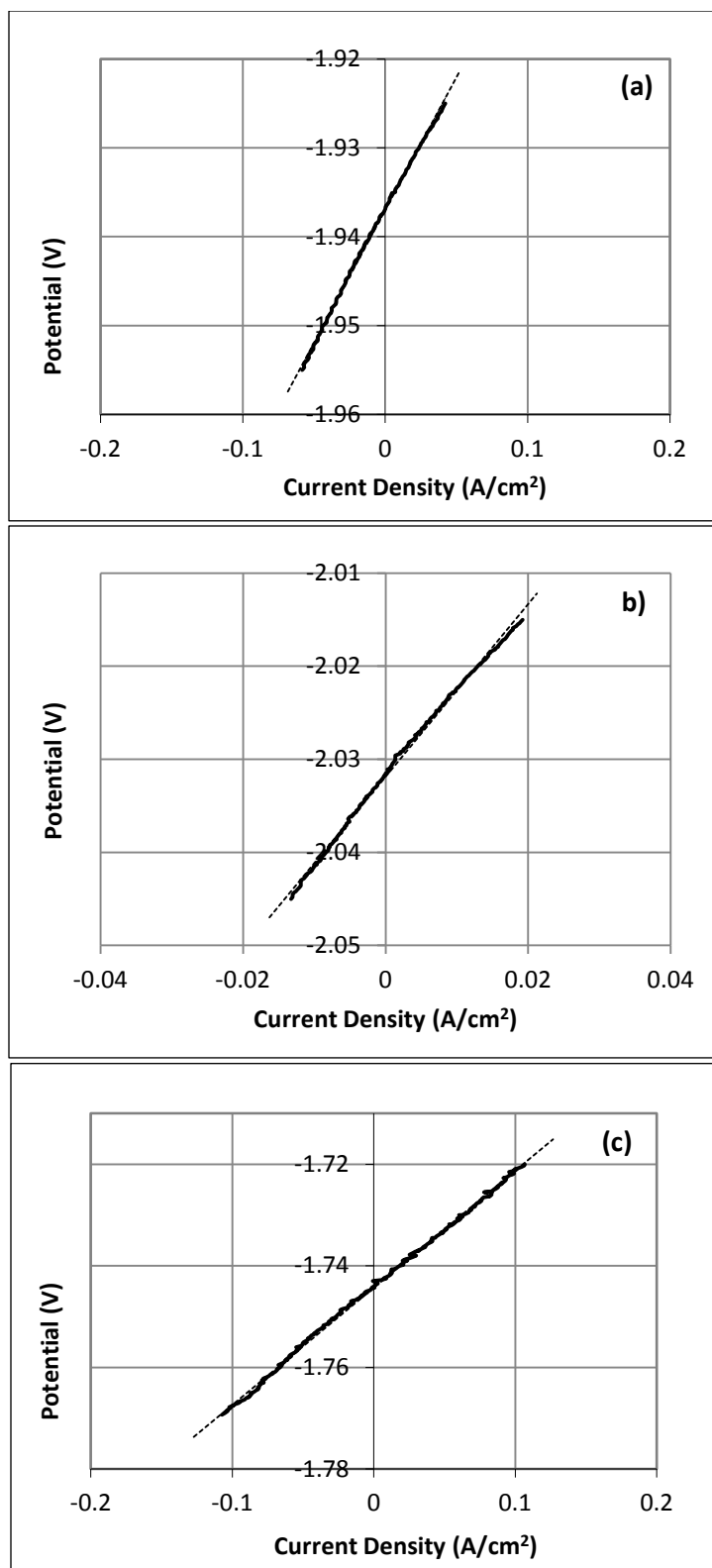


Figure 5.14: Plots of current density versus potential in the region near zero current for Ce(III)/Ce(0) in LiCl-KCl eutectic at (a) 653, (b) 773, and (c) 973K at 1.0 mol% CeCl₃. Tungsten working electrode of 0.44, 0.44, and 0.47 cm², respectively; cerium in Mo mesh counter electrode; Ag/AgCl reference electrode.

Table 5.6: Estimates of i_0 utilizing a thin Ce coating on a W wire at 1 mol% CeCl₃.

Temperature (K)	i_0 (A/cm ²)
653	0.01 – 0.03
773	0.04 – 0.1
973	0.06 – 0.2

The exchange current density of cerium was measured by Yoon and Phongikaroon (140) using electrochemical impedance spectroscopy and found to be 0.146 A/cm² at 773 K for a concentration near 1 mol%. In addition, i_0 of uranium in LiCl-KCl has been estimated by Choi and coworkers (133) and found to be in the region of 0.02 to 0.06 A/cm² for a melt of 3.27 wt% UCl₃ (~0.006 mole fraction) at 773 K. When extrapolated to similar molar concentration as this work (near 0.01 mole fraction), Choi's estimates overlap the estimates of the present work with cerium. Considering the 3 order of magnitude range of i_0 values published for specific elements, these results appear very similar.

5.9 Summary of Ce Electrochemistry

The electrochemical deposition of Ce(III) was observed to be a relatively uncomplicated three-electron reaction with quasi-reversible characteristics. The diffusion coefficient of Ce(III) was calculated by both CV and CP methods between 653 and 973 K. The data showed a temperature dependence consistent with Arrhenius law and indicated no phenomena that significantly complicated the diffusion behavior at the expanded temperature range. The equilibrium potential was measured between 653 and 973 K by CP technique and was used to calculate the Gibbs free energy and activity coefficient of Ce(III). The nucleation characteristics of cerium had not previously been reported and were explored using two chronoamperometric techniques. Both techniques consistently indicated that cerium nuclei were formed “instantaneously” with application of the initial potential step at 673 K, with continued three-dimensional growth of the initial nuclei. The exchange current density of Ce(III)/Ce(0) on a cerium-coated W wire had not previously been reported and was determined using the linear polarization method.

CHAPTER 6. PROCESS SAMPLES FROM ELECTROMETALLURGICAL TREATMENT

6.1 Process Sample Overview

Dendrite deposits are grown in the Mk-IV ER in a current-controlled mode at currents up to several hundred amperes. Cathode deposits can grow up to 25 cm in diameter and height. Dendrite samples are not routinely obtained, with more conclusive process samples instead obtained during a casting process following the separation of salt and metal via high-temperature vacuum distillation. However, a total of 10 dendrite samples from five uranium cathodes were obtained for this study to gain an understanding to the practical applications; these are summarized in Table 6.1. Figure 6.1 shows photographs of the uranium cathodes from which samples were obtained. These deposits are presumed to be comprised of α -phase uranium. Two dendrite samples were manually plucked from each of the dendrite products shown. It has previously been shown by Totemeier and Mariani (219) that under some conditions, salt can be microscopically occluded in cavities within the dendrites. To expose any occluded salt such that it could be removed during a water wash, most samples from each of these dendrites were manually crushed for a period of approximately 2 minutes in the hot cell using the device shown in Figure 4.7. The crushed or uncrushed dendrite samples were individually placed into metal sample containers and transferred to the AL for analysis.

Table 6.1: Dendrite samples obtained for this study.

	Production Date	Sample Description	AL Sample #
Cathode 5	January 2011	Top elevation, outer diameter, crushed	94870
		Lower elevation, outer diameter, crushed	94871
Cathode 6	February 2011	Top elevation, outer diameter, crushed	94872
		Lower elevation, outer diameter, crushed	94873
Cathode 9	April 2011	Lower elevation, outer diameter, crushed	93676
		Lower elevation, outer diameter	93677
Cathode 10	April 2011	Lower elevation, outer diameter, crushed	93678
		Lower elevation, outer diameter,	93679
Cathode 11	May 2011	Lower elevation, outer diameter, crushed	93680
		Lower elevation, outer diameter	93681

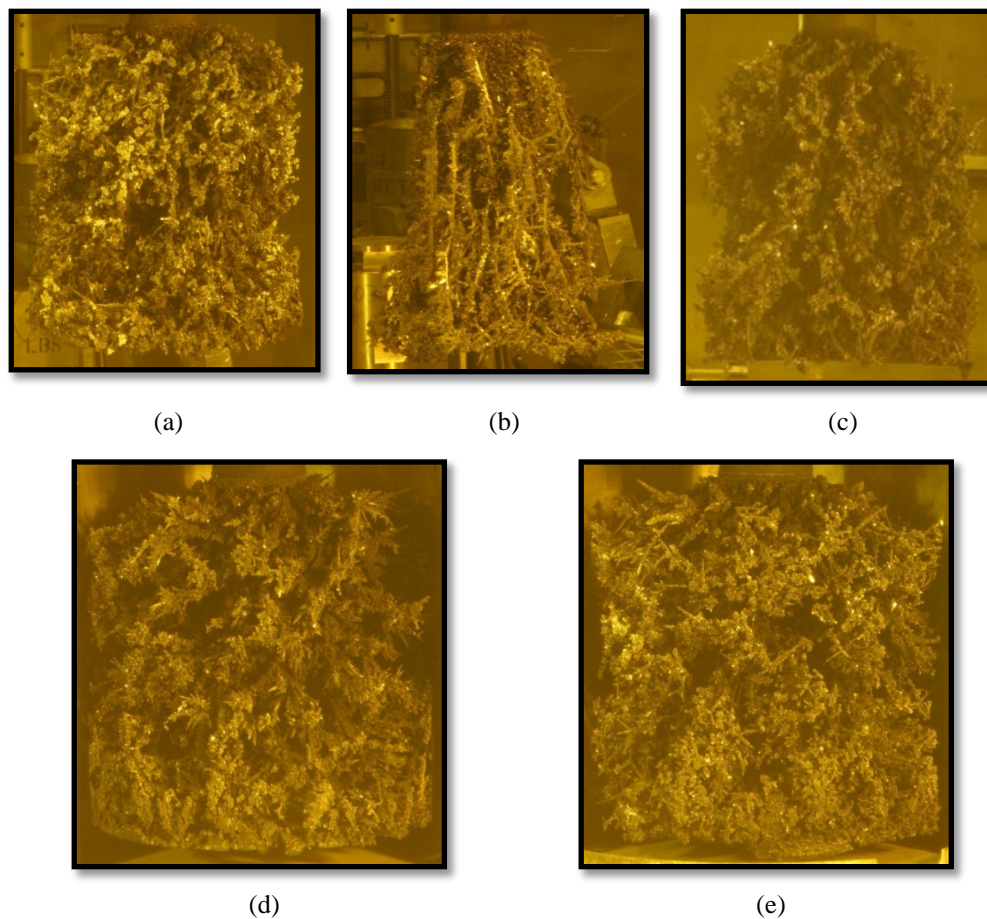


Figure 6.1: Photographs of uranium dendrite products from which dendrite samples were obtained for this work: (a) Cathode 5, (b) Cathode 6, (c) Cathode 9, (d) Cathode 10, and (e) Cathode 11.

Figure 6.2 shows photographs of the dendrite samples from Cathodes 5 and 6 during preparations for analysis in the AL. These photographs were obtained following salt removal by the water washing procedure described in Chapter 4. It was observed that some samples were much more pulverized than others. Specifically, metal pieces seen in Figure 6.2(a) are millimeter-sized granules, whereas metal remaining in (d) appears to be sub-millimeter powder. Figure 6.3 shows the crushed material from Cathodes 9, 10, and 11 in the AL following washing. The metal particles of these samples were observed to be pulverized into sub-millimeter powder.

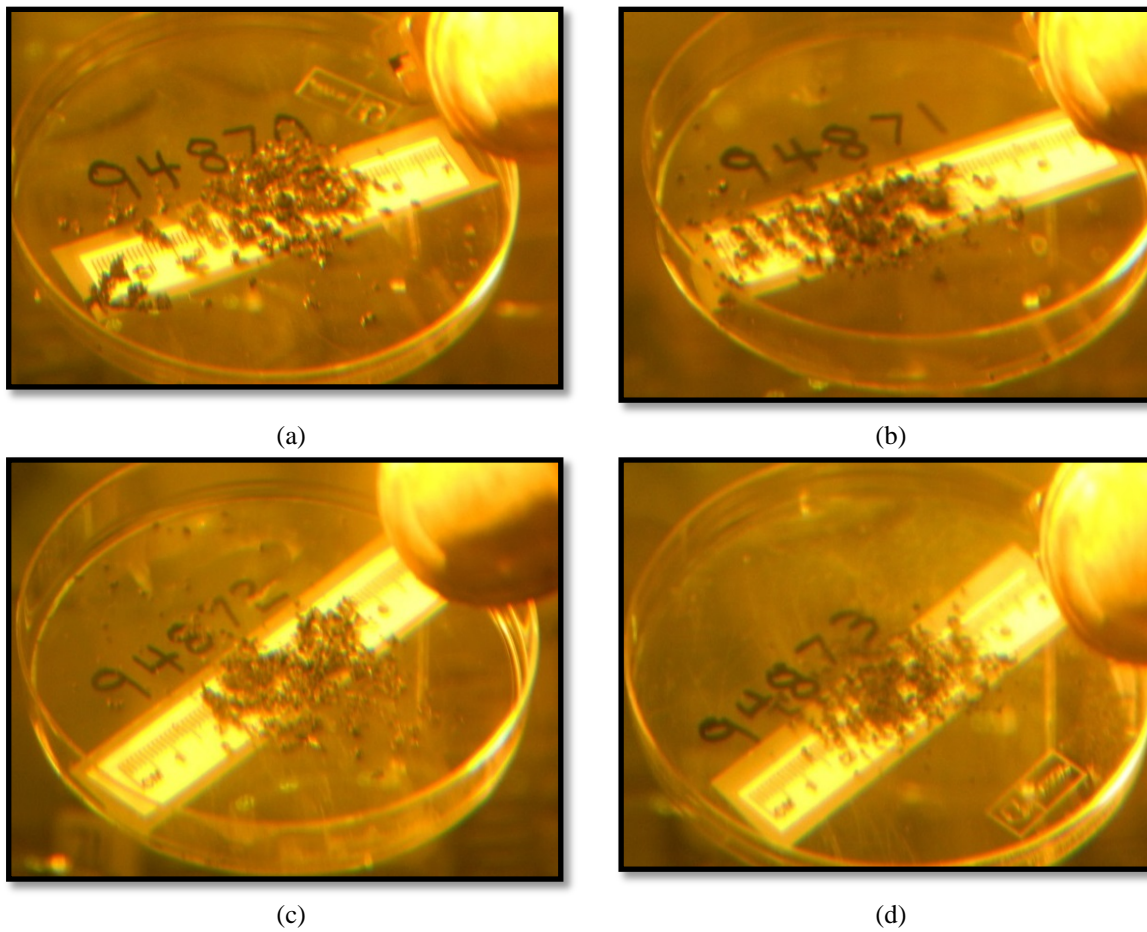


Figure 6.2: Photographs of washed crushed dendrite material: (a) Sample 94870 from the top of Cathode 5, (b) Sample 94871 from the bottom of Cathode 5 (c) Sample 94872 from the top of Cathode 6, and (d) Sample 94873 from the bottom of Cathode 6.

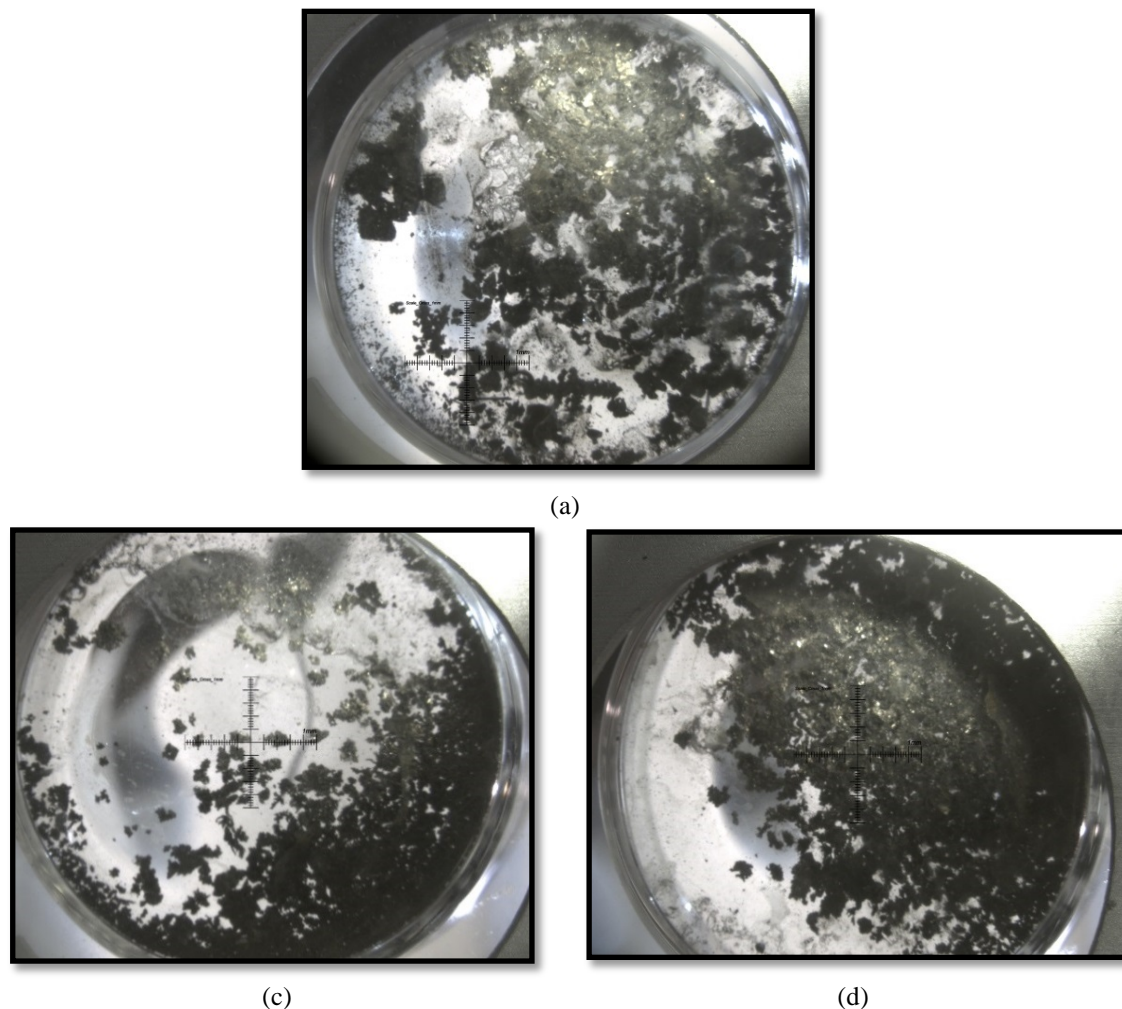


Figure 6.3: Photographs of washed crushed/pulverized dendrite material: (a) Sample 93676 from Cathode 9, (b) Sample 93678 from Cathode 10, and (c) Sample 93680 from Cathode 11.

Samples were analyzed following the procedures described in Chapter 4. Unfortunately, analysis of Ce was not performed due to fission product isotope interferences with with the isotopic distribution of fission-derived cerium isotopes. Based on the relative electrochemical stabilities, seen in Figure 6.4 and Table 6.2, it is expected that Pr, La, and Ce will follow similar behavior and trends. Priorities of the supporting project necessitated samples from Cathode Products 9 through 11 to be analyzed for a more streamlined suite of contaminants.

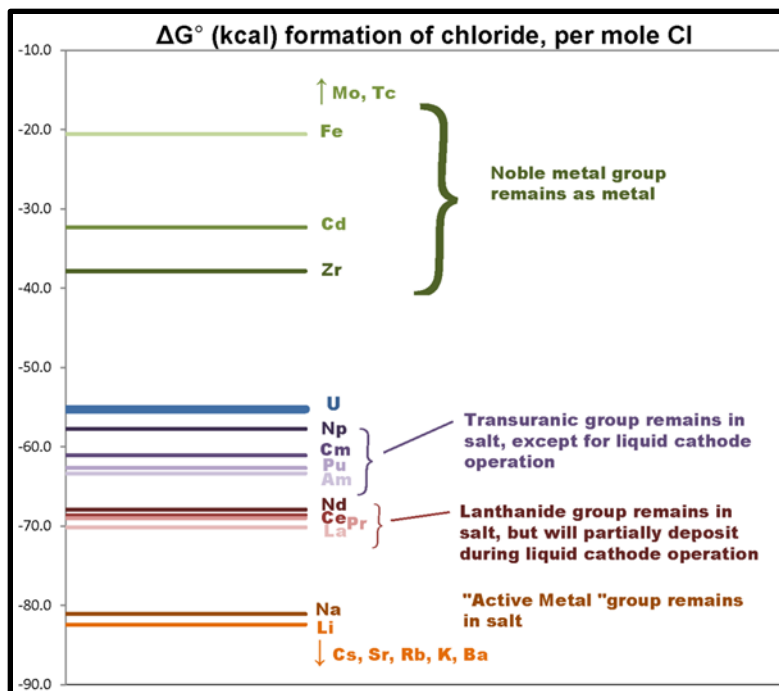


Figure 6.4: Relative stability of major chloride species in pyroprocessing.

Table 6.2: Apparent standard potentials in LiCl-KCl eutectic for lanthanoid and actinoid species.

Element	Apparent Standard Potential (vs Cl ₂ /Cl ⁻ at 723 K)
U	-2.498 (64)
Np	-2.698 (64)
Pu	-2.808 (64)
Pr	-3.085 (65)
Ce	-3.098 (65)
La	-3.146 (65)

6.2 Process Sample Results

Table 6.3 summarizes raw analytical results. It is important to note that these concentrations are reported based on the received sample mass. In some cases, a large fraction of the received sample is salt which is removed by the water wash. This work is primarily interested in the actinoid and lanthanoid analyses, but other available data are included to facilitate broader evaluation of dendrite contaminants. Several hundred ppm of iron is observed in the first four samples; the crushing operation may be responsible for introducing some iron into the dendrite samples. It is also seen that the uranium fraction of the received samples range from approximately 49 wt% to approximately 93 wt%. The mass measurement following

washing has an element of error due to the potential for samples to experience partial oxidation or incomplete drying. However, this measurement is still more representative than the mass obtained at sample receipt.

In Table 6.4 the relevant data are re-scaled to the washed sample mass to obtain contaminant content relative to the metal mass. It is seen that the total uranium content is still below, but much closer to 100 wt%. The remaining decrement is likely due to unquantifiable oxidation and residual moisture.

The contaminant data values provided in Table 6.3 and Table 6.4 include the contribution from occluded salt trapped within the metal dendrite structures. The presence of extremely stable salt species, such as Li, K, Ba, and Cs, is evidence of this. The electrolyte is highly impure, so a significant fraction of the contaminant species measured is actually present from the residual salt and is not from metal species deposited with the dendrite. In order to understand the contribution of contaminants present from occluded salt, analyses from ER salt samples are presented in Table 6.5. These salt samples were obtained as described in Chapter 4. It is seen that the concentration of contaminant species, such as the lanthanoids and transuranium actinoids, slowly rise as additional used fuel is processed. Some minor contaminant species, notably Fe, Mn, and Zr, are noticeably higher in the salt samples following Cathode 11. A cadmium chloride addition was made to the ER between Cathode 11 and Salt Samples 93805 and 93806. Although the measured cadmium is not obviously elevated, it is possible that these species were elevated by the operation and had not returned to equilibrium values.

It should be noted that lithium is the most abundant salt species with high analysis confidence. Thus, Li is selected as the most accurate indication of all residual salt contents. The quantity of contaminants is estimated based on their content in the bounding salt samples presented in Table 6.5.

Table 6.6 presents the calculated residual composition of the metal dendrite once the salt contribution (estimated by ICP-OES measured residual lithium) has been removed. The error column has been computed by considering the error introduced by the dendrite analysis value for the contaminant, lithium species, and the salt analyses.

Table 6.3: Received analytical results from washed dendrite samples, units of $\mu\text{g/g}$ with 2σ at $\pm 5\%$ unless noted.

	Cathode 5		Cathode 6		Cathode 9		Cathode 10		Cathode 11	
Sample ID	94870	94871	94872	94873	93676	93677	93678	93679	93680	93681
Detail	Top, crushed	Bottom, crushed	Top, crushed	Bottom, crushed	Bottom, crushed	Bottom	Bottom, crushed	Bottom	Bottom, crushed	Bottom
ICP MS										
133 Cs	4.61 [†]	3.91 [†]	5.39	4.91	n/a					
135 Cs	4.34	3.68	5.04	4.79						
136 Ba	<0.3	<0.5	<0.5	<0.6						
138 Ba	4.94	3.62 [†]	4.62 [†]	5.85						
139 La	5.68	5.15	5.19	6.53 [†]	13.5	19.5	4.05	4.38	5.14	8.25
141 Pr	5.83	5.1	5.02	6.28	11.8	20.7	3.46	3.77	4.25	7.34
237 Np	3.35	4.41	3.77 [†]	4.41	4.72	10.9	2.69	3.28	3.48	3.82
239 Pu	47.7	40.8	34.6	42.5	60	199	20.1	22.4	25.1	35.8
240 Pu	<0.05	0.636 ^{††}	0.511	0.786 ^{†††}	1.12	4.31	0.233	<0.259	0.318	0.536
Li	73.1	58.9	69	77.5	n/a					
U tot	900000	837000	817000	488000	927000	803000	680000	906000	843000	821000
ICP OES										
Cd	16700	1570	481	609	n/a					
Cr	89 ^{††}	<11	63	55						
Fe	370 ^{††}	99	359	235						
K	265 ^{†††}	209 ^{†††}	236 ^{††}	281	<970	<1500	<1370	<1800	<920	<1700
Li	64.2	55.7	64.7	73.6	174	261 [†]	85 ^{††}	107 [†]	92.2	147 [†]
Mn	11.5 [†]	7.3	11.9	6.7	n/a					
Zr	573	856	2310	589						
Recvd Sample Mass	4.237 g	2.758 g	2.565 g	2.273 g	5.695 g	3.729 g	4.095 g	3.286 g	6.301 g	3.348 g
Washed Sample Mass	3.934 g	2.283 g	2.159 g	1.135 g	5.381 g	3.612 g	3.118 g	2.999 g	5.845 g	3.184 g

[†] 2σ at $\pm 10\%$

^{††} 2σ at $\pm 15\%$

^{†††} 2σ at $\pm 20\%$

n/a = not analyzed

Table 6.4: Re-scaled analytical results from washed dendrite samples, units of $\mu\text{g/g}$ with 2σ at $\pm 5\%$ unless noted.

	Cathode 5		Cathode 6		Cathode 9		Cathode 10		Cathode 11	
Sample ID	94870	94871	94872	94873	93676	93677	93678	93679	93680	93681
Detail	Top, crushed	Bottom, crushed	Top, crushed	Bottom, crushed	Bottom, crushed	Bottom	Bottom, crushed	Bottom	Bottom, crushed	Bottom
ICP MS										
133 Cs	4.97	4.72	6.40	9.83	n/a					
135 Cs	4.67	4.45	5.99	9.59						
136 Ba	<0.3	<0.6	<0.6	<1.2						
138 Ba	5.32	4.37	5.49	11.72						
139 La	6.12	6.22	6.17	5.96	14.3	20.1	5.32	4.80	5.54	8.68
141 Pr	6.28	6.16	5.96	12.58	12.5	21.4	4.54	4.13	4.58	7.72
237 Np	3.61	5.33	4.48	8.83	5.00	11.3	3.53	3.59	3.75	4.02
239 Pu	51.4	49.3	41.1	85.1	63.5	205	26.4	24.5	27.1	37.6
240 Pu	<0.05	0.77	0.61	1.57	1.18	1.19	0.306	<0.28	0.343	0.564
Li	78.7	71.2	82.0	155.2	n/a					
U tot	969319	1011146	970637	977290	981094	829011	893072	992703	908767	863288
ICP OES										
Cd	17,986	1897	572	1220	n/a					
Cr	96	<13	75	110						
Fe	398	120	427	471						
K	285	252	280	563	<1027	<1549	<1799	<1972	<992	<1788
Li	69.1	67.3	76.9	147.4	184	269	112	117	99	154
Mn	12.4	8.8	14.1	13.4	n/a					
Zr	617	1034	2744	1180						
Sample Mass Scaling	1.077	1.208	1.188	2.003	1.058	1.032	1.313	1.096	1.078	1.052

n/a = not analyzed

Table 6.5: Electrorefiner salt samples, units of $\mu\text{g/g}$ with 2σ at $\pm 5\%$ unless noted.

Sample ID	Prior to Cathode 5		Following Cathode 6	Prior to Cathode 9	Following Cathode 11	
	93423	93424	93501	93586	93805	93806
ICP MS & OES						
133 Cs	3890	3850	3950	3420	3710	3700
135 Cs	3680	3660	3740	3330	3600	3610
139 La	3320	3370	3630	3470	3630	3640
141 Pr	2970	3020	3170	3250	3520	3520
237 Np	379	376	420	406	453	452
239 Pu	8970	8870	10000	9870	11100	11100
240 Pu	184	181	215	217	254	255
Li	52200	51900	51600	49300	51600	51800
Cd	129 [†]	152	80	67	190	200
Cr	72	75	210	29	180	200
Fe	180	180	23	168	410	440
K	197000	197000	19700	189000	194000	194000
Mn	15	15	17	23	90	97
Zr	110	120	140	40	642	659

[†] 2σ at $\pm 10\%$

Table 6.6: Calculated residual contaminant content of uranium dendrites, units of $\mu\text{g/g}$.

	Cathode 5		Cathode 6		Cathode 9		Cathode 10		Cathode 11		Avg. $\pm 2\sigma$
Sample ID	94870	94871	94872	94873	93676	93677	93678	93679	93680	93681	
Detail	Top, crushed	Bottom, crushed	Top, crushed	Bottom, crushed	Bottom, crushed	Bottom	Bottom, crushed	Bottom	Bottom, crushed	Bottom	
133 Cs	0.0	-0.1	0.9	-0.8	n/a						0.0 \pm 0.6
135 Cs	-0.1	-0.2	0.7	-0.6							-0.1 \pm 0.5
139 La	1.5	1.7	1.0	3.2	1.3	1.2	-2.5	-3.4	-1.5	-2.2	0.0 \pm 0.8
141 Pr	2.0	2.0	1.2	3.5	0.1	3.3	-2.9	-3.7	-2.1	-2.6	0.1 \pm 0.7
237 Np	3.3	5.1	4.2	8.3	4.1	10.0	3.0	3.0	3.3	3.3	4.8 \pm 0.5
239 Pu	39	37	27	58	25	150	3	0.0	6	6	35 \pm 5.3
240 Pu	-0.22	0.50	0.30	0.99	0.33	3.2	-0.22	-0.26	-0.12	-0.16	0.4 \pm 0.1
Cd	18000	1897	571	1219	n/a						5400 \pm 470
Cr	96	13	75	110							73 \pm 6
Fe	398	119	426	470							350 \pm 31
K	22.1	-3.8	-12.4	1.4							1.8 \pm 30
Mn	12	9	14	13							12 \pm 1
Zr	617	1034	2744	1179							1400 \pm 120
Total Impts.	19200	3100	3900	3100	31	167	1	-4	6	4	

The concentrations of lanthanoids estimated to be present as metal in the uranium dendrites is essentially zero. The average concentrations of Np and Pu are estimated at 4.8 ± 0.5 and 35 ± 5.3 $\mu\text{g/g}$, respectively. Notable concentrations of Cd, Zr, and Fe are also observed. For comparison, Table 6.7 provides the composition of casting samples at the end of the process. The enriched uranium is diluted with depleted uranium to facilitate storage as low-enriched uranium; so the data presented in the table have been corrected to reflect impurities present in the uranium product assuming that the dilutant is absolutely pure uranium. It is seen that the concentration of Np and Pu species have risen to an average of 30.9 ± 19.3 and 133.2 ± 32.7 $\mu\text{g/g}$, respectively, which is considerably higher than the estimation in the dendrite samples. Lanthanoid species are detected but only at low concentrations (below 1 $\mu\text{g/g}$). Cadmium is no longer detected, and this would be expected during vacuum distillation, given its high vapor pressure. Zirconium content appears to increase from an average of 1400 ± 120 to 2480 ± 4550 $\mu\text{g/g}$. This may be an artifact of wide scatter in zirconium content from cathode to cathode or may be a function of the high-temperature vacuum distillation operation being performed inside a zirconium dioxide crucible. Depending on the end use of electrorefined uranium, residual zirconium content may be irrelevant and possibly beneficial. Iron content is seen to be similar to that observed in dendrite samples, which was unexpected. Iron is a relatively electrochemically noble species compared to other species of discussion. The ER vessel is constructed from an iron alloy containing minor amounts of Cr and Mn. It may be possible that very fine corrosion-derived iron oxide particles are resident in the ER. Finally, it is seen that the purity of the uranium product before dilution is approximately 99.7%, or 99.95% if zirconium is excluded (or greater, if some fraction of the contaminant species are introduced with the dilutant uranium).

Table 6.7: Composition of casting samples, units $\mu\text{g/g}$, with 2σ error at $\pm 10\%$ unless noted.

	Casting FF02	Casting FF04	Casting FF06	Casting FF07	Avg ± 2 std dev
Sample ID	93507	93592	94233	94230	
	Includes Cathode 5	Includes Cathode 6	Includes Cathodes 9, 10	Includes Cathode 11	
Dilution Correction	1.98	2.01	1.60	2.03	
139 La			0.592	0.609	
141 Pr			0.064	0.1218	
237 Np	17.4	30.6	37.3	38.4	30.9 \pm 19.3
239 Pu	146.9	109.9	134.1	141.7	133.2 \pm 32.7
240 Pu	3.11	2.39	3.50	3.59	3.15 \pm 1.09
Li	<40	<18	<10	<18	
Cd	<9	<7	<6	<12	
Cr	53.5	<22	<18	<32	
Fe	378	366	69	217	257 \pm 291
K	<1030	<850	<780	<1480	
Mn	32.9	30.6	17.4	82.4	40.8 \pm 57.1
Zr	919	840	2450	5700	2480 \pm 4550
Total Impurities	1550	1380	2710	6190	2960 \pm 4470
Impurities Excluding Zr	630	540	260	480	480 \pm 310

Other information can also be obtained from these analyses, such as salt content. Table 6.8 provides a summary of these data values. The final row of the table shows the fraction of the dendrite mass which is occluded salt. Although only a few uncrushed samples were examined in this study, the average mass fraction of occluded salt is 0.21 ± 0.17 wt% for crushed samples and 0.34 ± 0.34 wt% for uncrushed samples. Crushing may provide some benefit to reduce occluded salt, but additional study will be required.

Table 6.8: Calculated residual salt content of uranium dendrites, units of wt%.

	Cathode 5		Cathode 6		Cathode 9		Cathode 10		Cathode 11		Avg. ± 2sdv
Sample ID	94870	94871	94872	94873	93676	93677	93678	93679	93680	93681	
Detail	Top, crushed	Bottom, crushed	Top, crushed	Bottom, crushed	Bottom, crushed	Bottom	Bottom, crushed	Bottom	Bottom, crushed	Bottom	
Fraction of total sample which was salt	7.2	17.2	15.8	50.1	5.8	3.7	24	8.9	7.4	5.2	15 ±28
Fraction of cathode which was salt*	16-19 [†]	16-19 [†]	16-19 [†]	16-19 [†]	20	20	20	20	22.6	22.6	20.9 ± 2.7
Fraction of salt that was occluded	1.9	0.7	0.8	0.3	5.8	14	0.53	2.2	2.2	5.2	3.4 ±8.4
Fraction of dendrite which was occluded salt	0.15	0.13	0.16	0.3	0.35	0.53	0.17	0.21	0.18	0.28	0.25 ± 0.25

* From mass balances following salt removal from cathode via high-temperature vacuum distillation

† More precise value not known due to merging of cathodes for salt removal

Based on the results presented in Tables 6.5, 6.7, and 6.8, one can estimate whether plutonium present in the occluded salt could be the dominant source of plutonium appearing in the final cast uranium product. Based on the average value of occluded salt measured in the water wash samples (0.25 ± 0.25 wt%) following water washing and the concentration of plutonium in the electrorefiner salt at that time (near 1 wt%), the occluded salt could only account for ~20% of the observed plutonium contamination. Approximately 5% of the plutonium borne by the overall salt transferred would account for the plutonium observed in the final uranium product. However, it is possible that the dendrite samples broken from the outer diameter of the deposit do not accurately reflect the whole. One specific potential is the case of 'macroscopic' encapsulation where clusters of dendrites at the interior of a deposit have grown sufficiently close together that salt deposits are trapped between and around them. The hot water wash may also be more effective to remove salt from crevices than is achieved in the cathode processor. Either of these possibilities would result in the quantity of 'occluded' salt being underestimated in Table 6.8.

6.3 Discussion of Process Samples

The intrinsic purity of uranium dendrites produced from processing of UNF in the Mk-IV ER was estimated from 10 dendrite samples with temporally corresponding ER salt samples. The estimated intrinsic purity was compared to uranium product samples obtained from the casting operation at the end of processing. It was found that neptunium and plutonium contaminants are present as metals in the dendrites at the order of tens of ppm. These same species are present in the casting samples at a level of hundreds of $\mu\text{g/g}$. It appears that two separate phenomena introduce transuranium contaminants into the uranium product. If it is desired to substantially reduce neptunium and plutonium contamination of the final uranium products, additional studies are needed of thermochemical and metallurgical behaviors in other process operations. An average of approximately 0.25 wt% of the dendrite was measured to be salt resistant to removal by washing and likely to be present as occlusions inside cavities of the metal dendrite. If the plutonium borne by this quantity of occluded salt was all later introduced into the product, it would introduce approximately 25 ppm of additional contaminants. This is

still a minority of final contaminants observed in the uranium products. Pulverization of dendrites may reduce the observed fraction of occluded salt, but further investigation is needed.

CHAPTER 7. RESULTS AND ANALYSIS OF URANIUM-CERIUM ELECTROCHEMISTRY

7.1 Electrochemical Studies

A limited study of the electrochemical behavior of uranium was performed. Initially, cyclic voltammograms were performed to confirm the batch of LiCl-KCl eutectic received from the vendor was of adequate purity; the result is shown in Figure 7.1 indicating residual currents are below a few millivolts. A typical cyclic voltammogram for a LiCl-KCl solution with 1.0 mol% UCl_3 is presented in Figure 7.2. Here, the reaction pair R1/Ox1 are described as the U(III)/U(0) couple, the R2/Ox2 pair as the U(IV)/U(III) couple, and the R3/Ox3 pair as monolayer absorption and desorption peaks (15, 16, 43, 145). The effect of scan rate upon deposition and dissolution of UCl_3 is plotted in Figure 7.3. At more rapid scan rates, the peak potential for R1 begins to shift toward more negative potentials as scan rate increases. This is characteristic of an irreversible reaction limited by electron transfer.

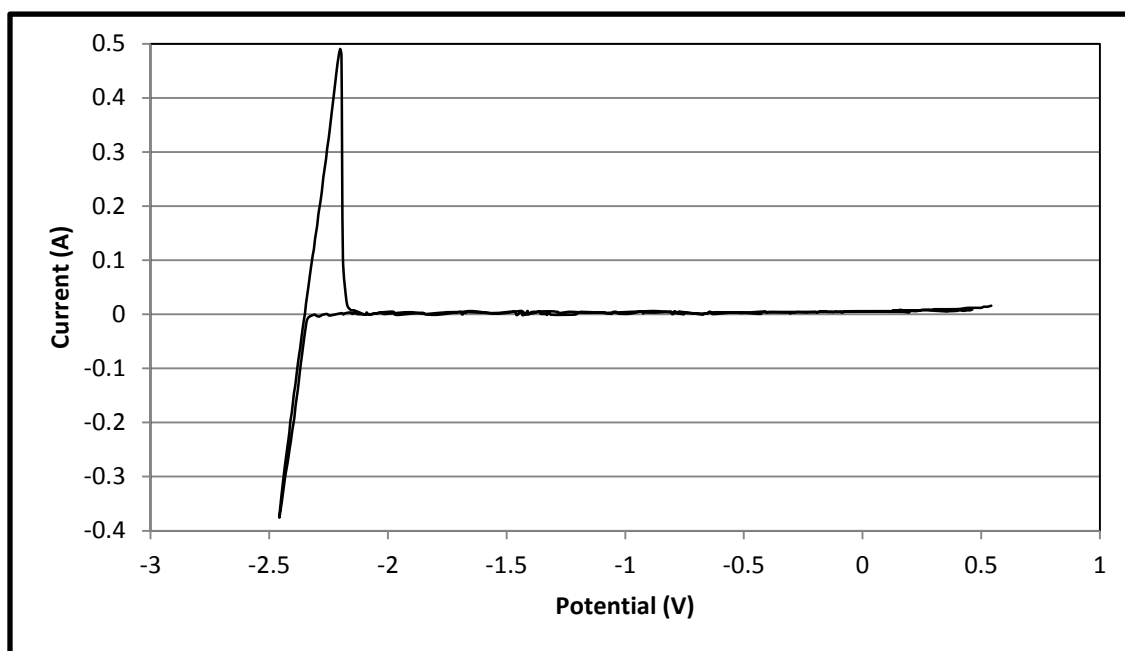


Figure 7.1: Cyclic voltammogram of LiCl-KCl eutectic at 773 K. W working electrode of 0.45 cm^2 ; molybdenum mesh counter electrode; Ag/AgCl reference electrode. Scan rate 0.05 V/s .

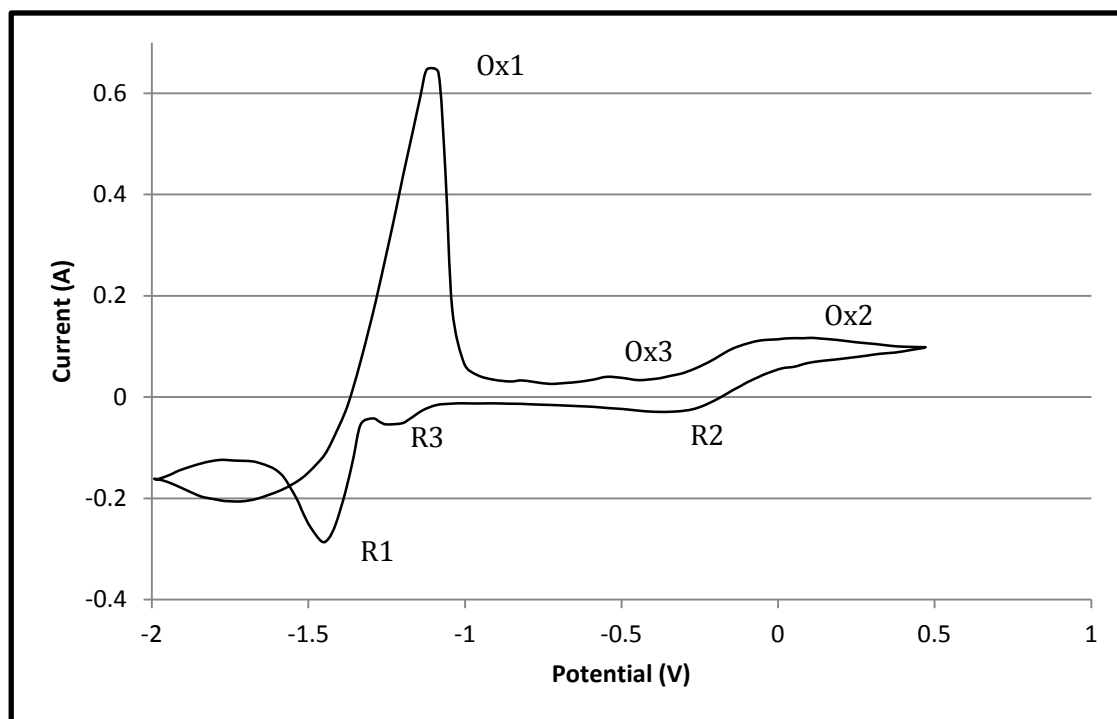


Figure 7.2: Cyclic voltammogram of UCl_3 in LiCl-KCl at 773 K and 1.0 mol% UCl_3 . W working electrode of 0.45 cm^2 ; U rod counter electrode; Ag/AgCl reference electrode. Scan rate 0.2 V/s.

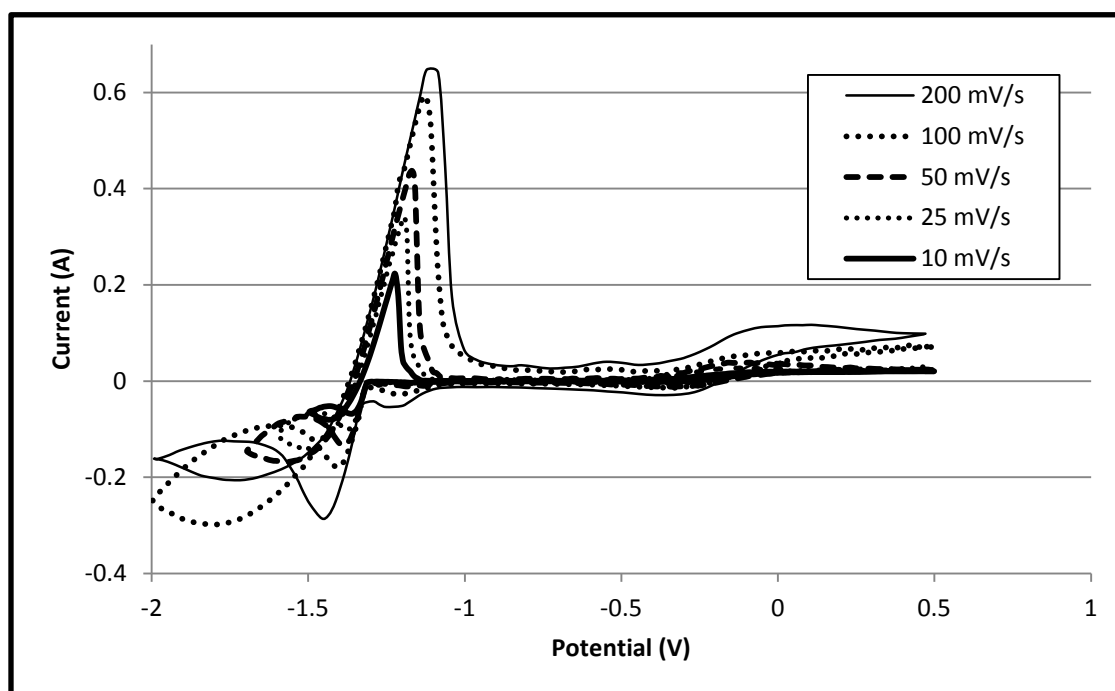


Figure 7.3: The effect of scan rate upon reduction of UCl_3 in LiCl-KCl eutectic at 773 K and 1.0 mol% UCl_3 . Tungsten working electrode of 0.45 cm^2 ; Uranium rod counter electrode; Ag/AgCl reference electrode.

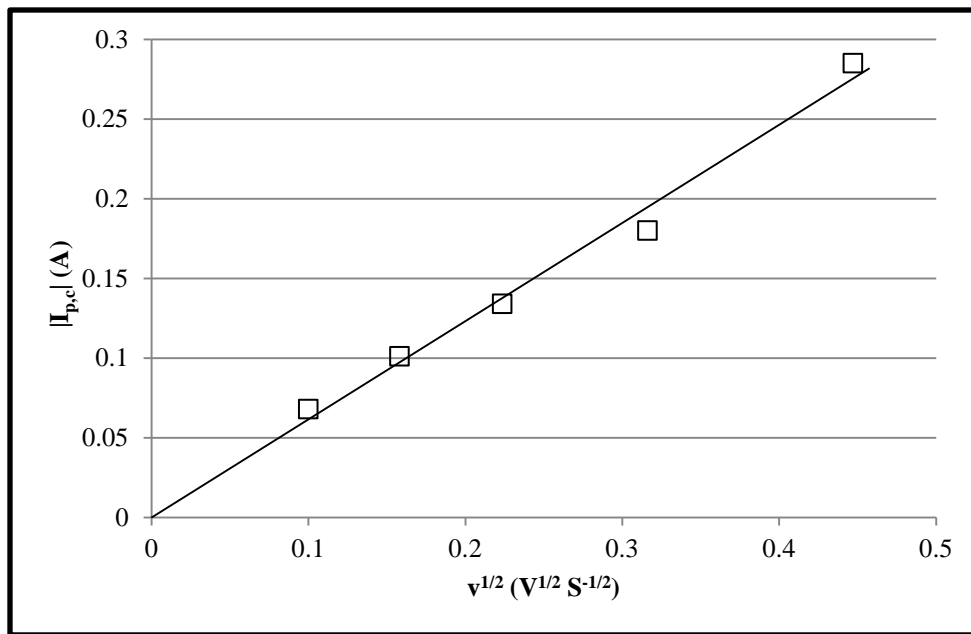


Figure 7.4: Peak cathodic current as a function of the square root of scan rate, obtained from cyclic voltammogram of Figure 7.3.

One method to estimate diffusion coefficient is to utilize the slope of a plot of peak cathodic current as a function of the square root of scan rate (see Figure 7.4). From this data, with an assumption of reversible conditions, the diffusion coefficient of uranium at 773 K was estimated through Eq. [2.26] to be near $1.6 \times 10^{-5} \text{ cm}^2/\text{s}$. For an assumption of irreversible conditions, the diffusion coefficient was estimated through Eq. [2.27] to be near $5.0 \times 10^{-5} \text{ cm}^2/\text{s}$. Given the relatively slow scan rates evaluated (10 mV/s – 200 mV/s), the former assumption is reasonable and is similar to values estimated from other studies (145, 229).

Figure 7.4a shows a cyclic voltammogram for an electrolyte containing 1 mol% UCl_3 and 1 mol% CeCl_3 at a scan rate of 200 mV/s. Compared with Figure 7.2, additional peaks R4 and Ox4 can be seen for the reduction and oxidation of cerium metal, respectively. In CVs with significant combined UCl_3 and CeCl_3 electrolytes with appreciable UCl_3 content, the Ce deposition peak R4 is often obscured by a continually rising current which is likely a consequence of increasing electrode surface area from U deposition.

Figure 7.4b shows the effect of scan rate upon reduction of UCl_3 in 1.0 mol% UCl_3 and 1.0 mol% CeCl_3 in LiCl-KCl eutectic. The peaks are again seen to shift in the more negative direction as scan rate increases. Figure 7.4c shows a plot of peak cathodic current as a function of scan

rate. From this data, with an assumption of reversible conditions, the diffusion coefficient of uranium at 773K was estimated through Eq. [2.26] to be near $0.68 \times 10^{-5} \text{ cm}^2/\text{s}$. For an assumption of irreversible conditions, the diffusion coefficient was estimated through Eq. [2.27] to be near $1.5 \times 10^{-5} \text{ cm}^2/\text{s}$. These values are close to those reported for uranium by other studies, but lower than those estimated earlier with the data presented within Figure 7.3 and Figure 7.4. It may be possible that the presence of CeCl_3 complexes in the salt has an impact on the mobility of UCl_3 complexes. However, a more thorough study of diffusion coefficient with both CP and CV methods would be valuable to clearly investigate this issue.

CVs were attempted for 6.0 mol% UCl_3 electrolytes, but the electrode area changes too rapidly to obtain useful information. Figure 7.4d shows a typical CV for the condition of 0.33 mol% UCl_3 and 6 mol% CeCl_3 . A clear peak for cerium reduction can be discerned due to the lower concentration of uranium in this test condition. Unfortunately, these latter experiment setups were focused on dendrite collection, and detailed CVs were not obtained.

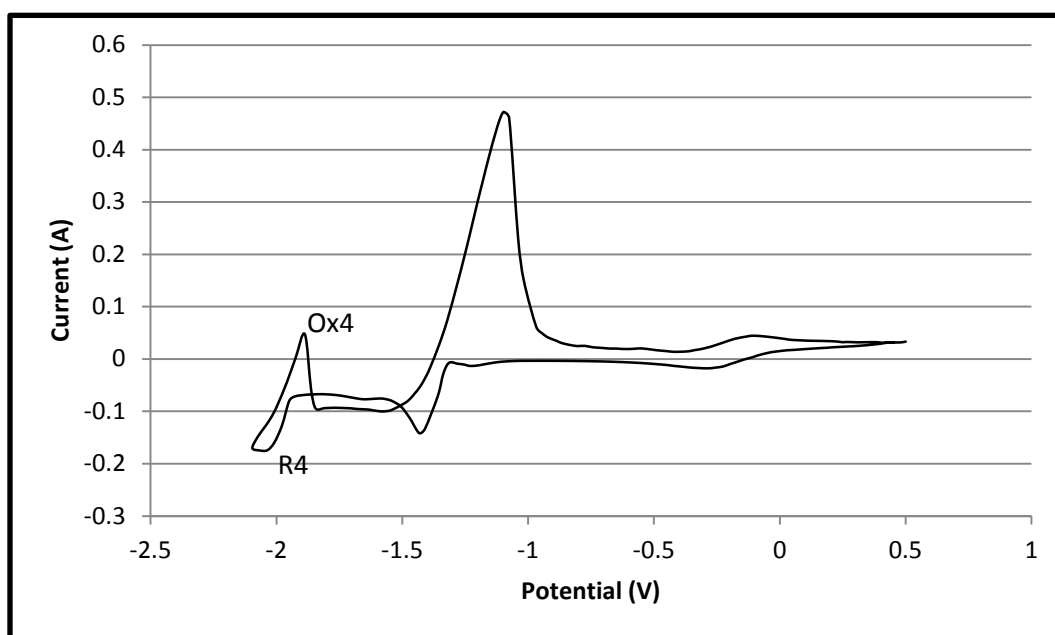


Figure 7.4a: Cyclic voltammogram of 1.0 mol% UCl_3 and 1 mol% CeCl_3 in LiCl-KCl at 773 K. Working electrode of 0.38 cm^2 ; U counter and Ag/AgCl reference electrodes. Scan rate 0.2 V/s.

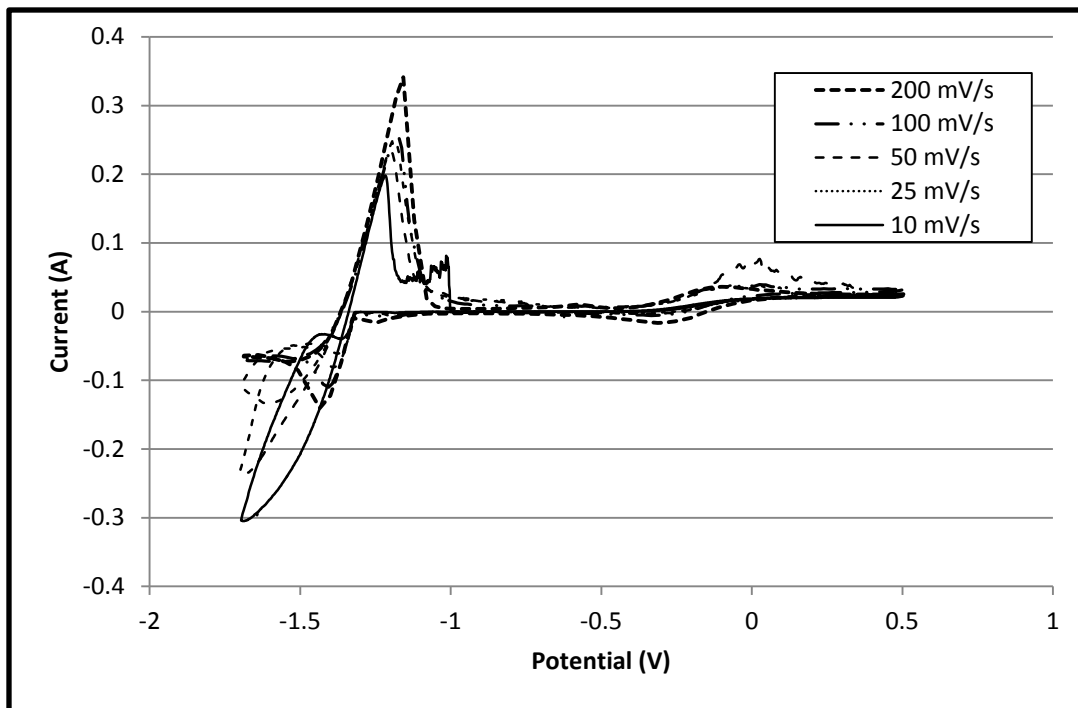


Figure 7.4b: The effect of scan rate in 1.0 mol% UCl_3 and 1 mol% CeCl_3 in LiCl-KCl eutectic at 773 K. W working electrode of 0.38 cm^2 ; U rod counter electrode; Ag/AgCl reference electrode.

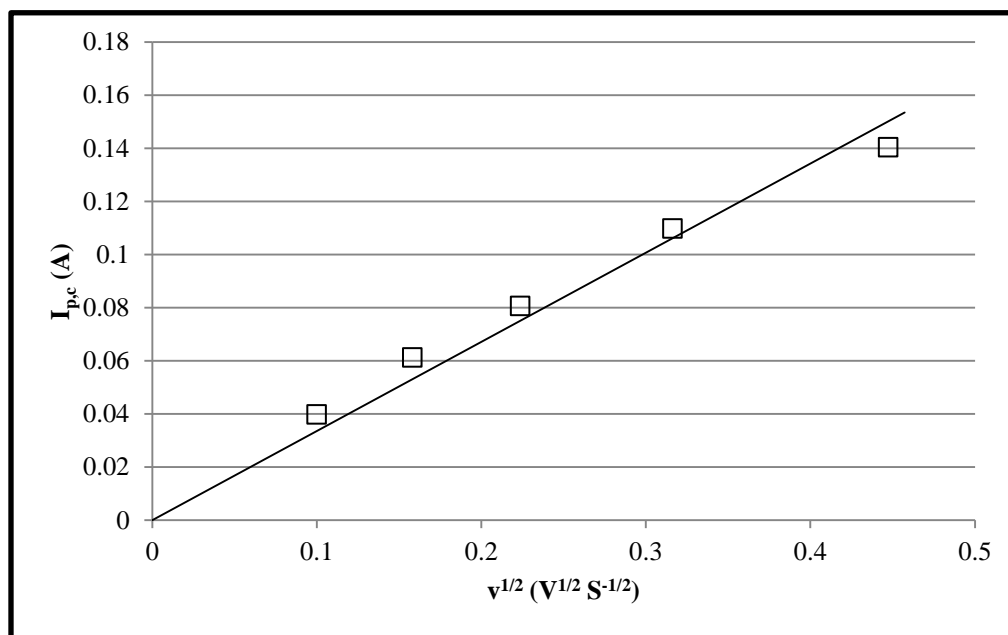


Figure 7.4c: Peak cathodic current as a function of the square root of scan rate, obtained from cyclic voltammogram of Figure 7.4b.

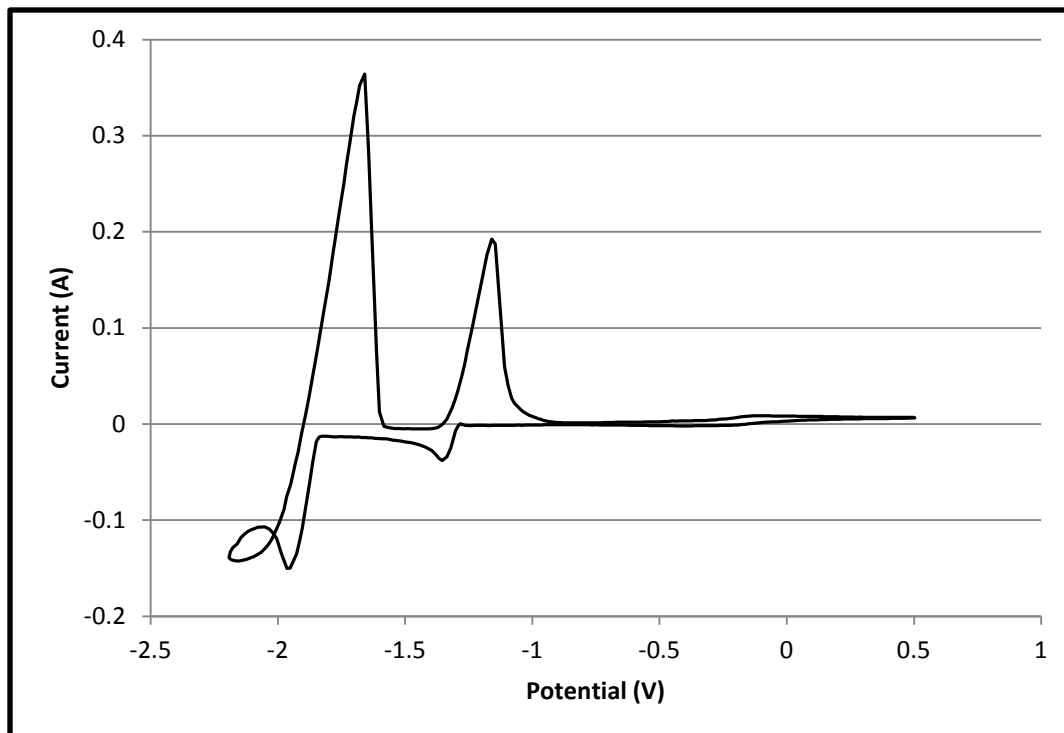


Figure 7.4d: Cyclic voltammogram of 0.33 mol% UCl_3 and 6.0 mol% CeCl_3 in LiCl-KCl at 773 K. Working electrode of 0.22 cm^2 ; U counter and Ag/AgCl reference electrodes. Scan rate 0.1 V/s .

Exchange current density is also linked to nucleation characteristics and deposit morphology. In addition, it is an important parameter for accurate electrochemical modeling. For these reasons, it was desired to quantify the order of magnitude of exchange current density of the U(III)/U(0) couple in LiCl-KCl eutectic. These methods were described in Section 2.10, and are derived from the Butler-Volmer equation (Eqs. 2.36)].

Tafel-type plots at low scan rates were obtained using four uranium rods in four different solutions at 773 K. Typical plots are shown in Figure 7.4, and i_0 values at the tested concentrations and temperatures can be visually estimated in the realm of 0.01 A/cm^2 . However, it was difficult to establish specific values due to the lack of well-defined linear regions in the Tafel plots.

To avoid the challenges posed by the Tafel approach, the linear polarization method was employed. This approach utilized data at very low overpotentials, where the surface area of the uranium remained nearly constant. The data from Figure 7.5 at very low overpotentials was re-plotted in Figure 7.6, and a very linear region was seen. The slope of the lines in Figure 7.6 may

be utilized to estimate i_0 , and the resulting estimates are provided in Table 7.1. The maximum listed range is based on the surface area from dimensional measurements, with the lower limit provided to account for error introduced by the roughness of a real surface.

Table 7.1: Estimates of i_0 from metallic uranium rods at 773 K.

Rod	Salt constituents	i_0 (A/cm ²)
Solid uranium A, S= 2.13 cm ²	0.33 mol% UCl ₃ and 1 mol% CeCl ₃	0.002 – 0.004
Annular uranium, S= 3.09 cm ²	1 mol% UCl ₃	0.009 – 0.017
Solid uranium B, S= 1.81 cm ²	1 mol% UCl ₃ and 6 mol% CeCl ₃	0.009 – 0.017
Solid uranium C, S= 1.71 cm ²	6 mol% UCl ₃ and 1 mol% CeCl ₃	0.022 – 0.043

Very similar i_0 was found for 1 mol% UCl₃, with and without a significant concentration of CeCl₃. This seems reasonable, assuming that the cerium concentration is not so great as to make significant changes to the electrolyte or complexation of U³⁺. The i_0 value appears to increase nearly linearly with UCl₃ concentration. Additional studies of concentration effects would be a valuable contribution to the literature.

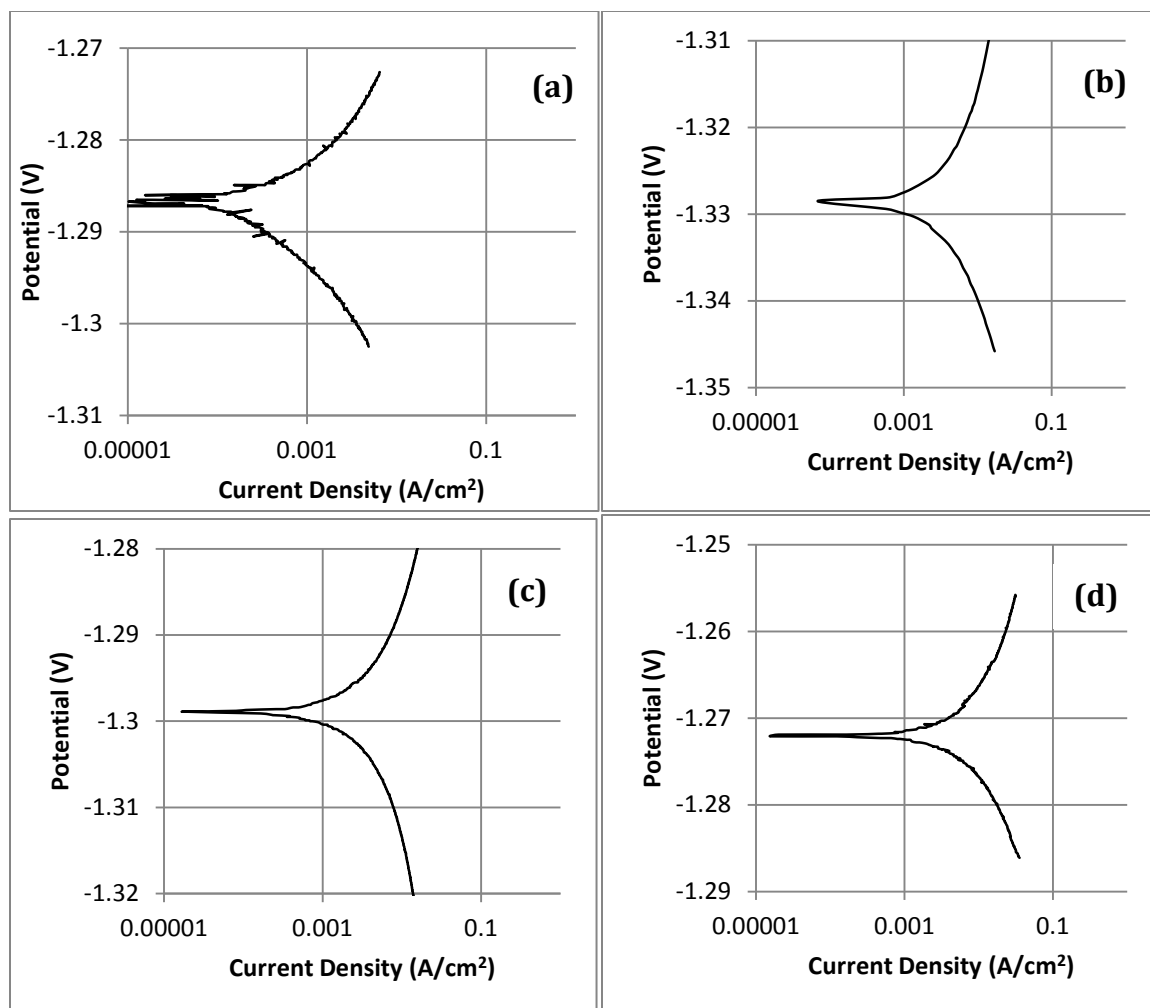


Figure 7.5: Tafel-type plot for U(III)/U(0) in LiCl-KCl eutectic at 773K, in (a) 1 mol% CeCl₃ and 0.33 mol% UCl₃ (b) 1 mol% UCl₃, (c) 6 mol% CeCl₃ and 1 mol% UCl₃, and (d) 1 mol% CeCl₃ and 6 mol% UCl₃, respectively; Ta crucible counter electrode; Ag/AgCl reference electrode.

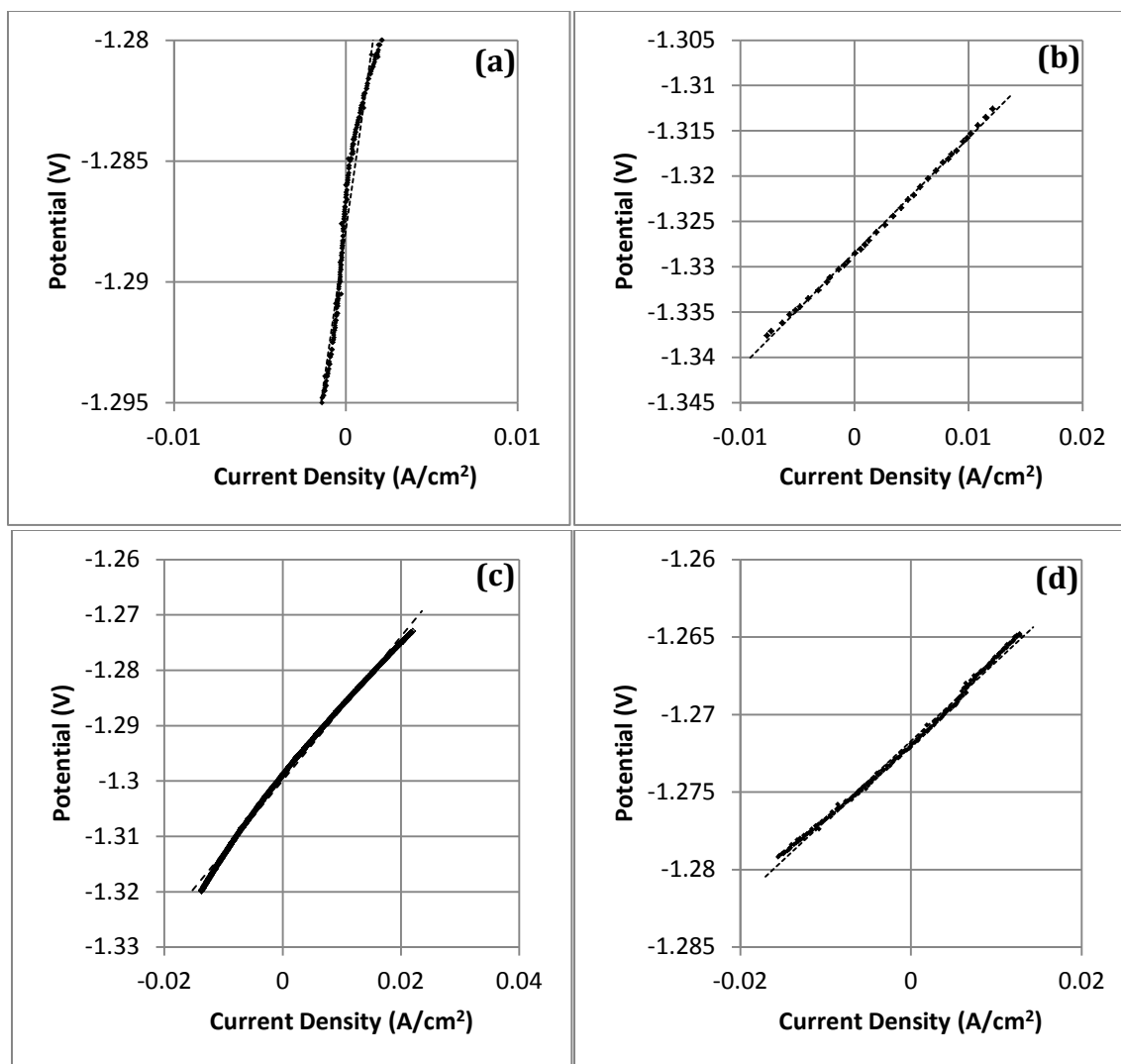


Figure 7.6: Plots of current density versus potential in the region near zero current for U(III)/U(0) at 773K in (a) 1 mol% CeCl₃ and 0.33 mol% UCl₃ (b) 1 mol% UCl₃, (c) 6 mol% CeCl₃ and 1 mol% UCl₃, and (d) 1 mol% CeCl₃ and 6 mol% UCl₃, respectively; Ta crucible counter electrode; Ag/AgCl reference electrode.

The exchange current density of uranium in LiCl-KCl has been estimated by Choi and coworkers (133) and found to be in the region of 0.02 to 0.06 A/cm² for a melt of 3.27wt% UCl₃ (~0.006 mole fraction) at 773 K, which is modestly higher than this study. Ghosh and coworkers (15) published i_0 for uranium of 0.006-0.026 A/cm² although the functional concentration of UCl₃ was not provided. Rose and coworkers (135) have very recently published values for exchange current density also using the Tafel method, and estimate an i_0 of ~.096 A/cm². They predict an i_0 greater than the current density actually measured during their experimental routine. Cumberland and Yim (136) published predictions for uranium exchange

current density based on cyclic voltammetry reported in literature; they predict a standard exchange current density of approximately 1.1 A/cm^2 at 773 K . This yields values of 3.6, 11, and 66 mA/cm^2 at 0.33, 1, and 6 mol%, respectively. Figure 7.6a provides a visual summary of i_0 measured by the several investigations.

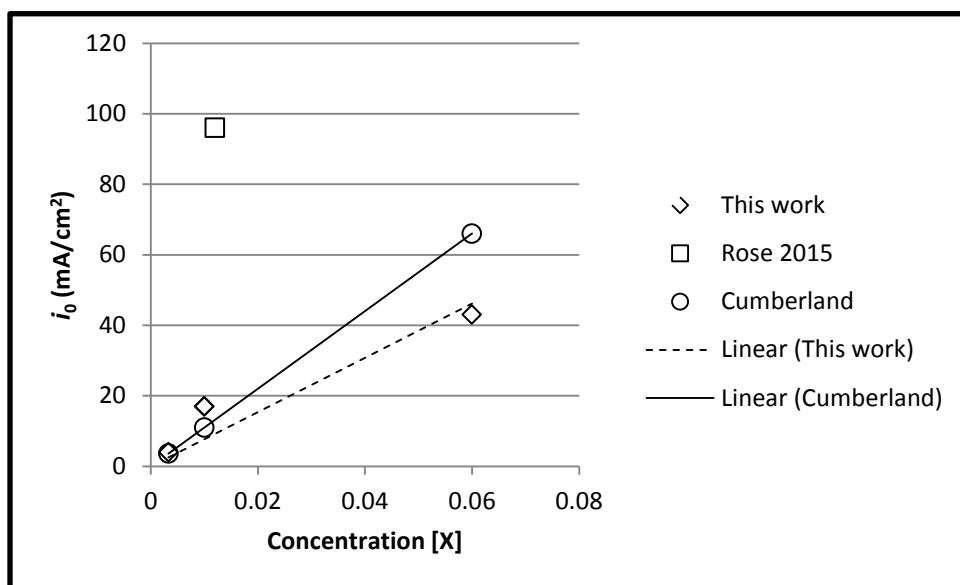


Figure 7.6a: Comparison of i_0 measured by this work, Rose and coworkers (135), and Cumberland and Yim (136).

7.2 Microscopy

Microscopy was performed on uranium crystals produced under electrochemical potentials to improve understanding of morphology, with specific interest regarding cavities or voids formed in the crystals. All samples of uranium dendrites were produced from a solution of 1 mol% UCl_3 in LiCl-KCl eutectic at 773 K , onto a 1 mm Ta wire. These samples are presumed to be α -phase uranium. Three deposits were produced at overpotentials of 450, 150, and 25 mV relative to the open circuit potential of a uranium rod. Two photos of the harvesting and mounting of these uranium crystals are shown in Figure 4.13, and the preparation procedure was previously described in Chapter 4.

7.2.1 Microscopy of Uranium Deposit from 450 mV Overpotential

The first dendrites to be inspected were produced at an overpotential of 450 mV (see Figure 7.7). Figure 7.8 is a secondary-electron (SE) image of cluster of uranium whiskers and/or fibers

during washing with deionized water to remove salt. The cluster was attached to a carbon sticky dot on a metallurgical mount, and held in the glovebox for several weeks prior to SEM inspection. Figure 7.8 provides an overview of the cluster on the SEM. It can be seen that the majority of the uranium is in the form of long fibers with lengths up to several millimeters and diameters in the 30-50 μm range. Analysis by energy dispersive spectroscopy (EDS) was performed on the entire visible image of Figure 7.8. The only species identified in the spectrum were ~ 0.75 wt% Cl, ~ 10 wt% O with balance uranium, shown in Table 7.2. Figure 7.9 provides a closer view and a key for later images. Figure 7.10 shows a closer image of a dendrite comprised of triangular platelets from area (a) from Figure 7.9. The growth direction expected to be toward bottom left corner of image. It is seen that the uranium seems to be coated in fuzzy layer. EDS analysis was performed on 5 spots in this image, ranging across the smooth surface and what appear to be particles on the surface. The estimated oxygen content ranged from 6 wt% to 20 wt% for the large particle near the left elbow of the platelet. Minor quantities of Cl were also detected in each. It appeared that significant oxidation had occurred during the several-week pause prior to SEM analysis. Figure 7.11 is a similar image except capture from back-scatter electrons (BSE). Figure 7.12 shows a back-scatter electron image of area (b) containing several platelets, a slender fiber of approximately 30 μm diameter, and underlying irregular dendritic structures. The growth direction of the platelet is expected to be toward the left-hand side of the image. Figure 7.13 shows an image of area (c) while Figure 7.14 displays the SE image of area (c1). Here, EDS spectra were obtained from six points, with results 0.5 wt% - 2 wt% chlorine, 5-14% oxygen and balance uranium. Some of the debris between the oxidized uranium platelets was high in chlorine content.



Figure 7.7: Dendrite mass produced at 450 mV condition during washing in DI water.



Figure 7.8: Overview of dendrite mass on SEM mount, produced at 450 mV condition.

Table. 7.2: EDS summary from EDS scan of image in Figure 7.8.

Spectrum	In Stats.	Cl	U	O	Total
Spectrum 1	Yes	10.18	0.74	89.07	100.00

Notes: Results in weight%. All elements analyzed.

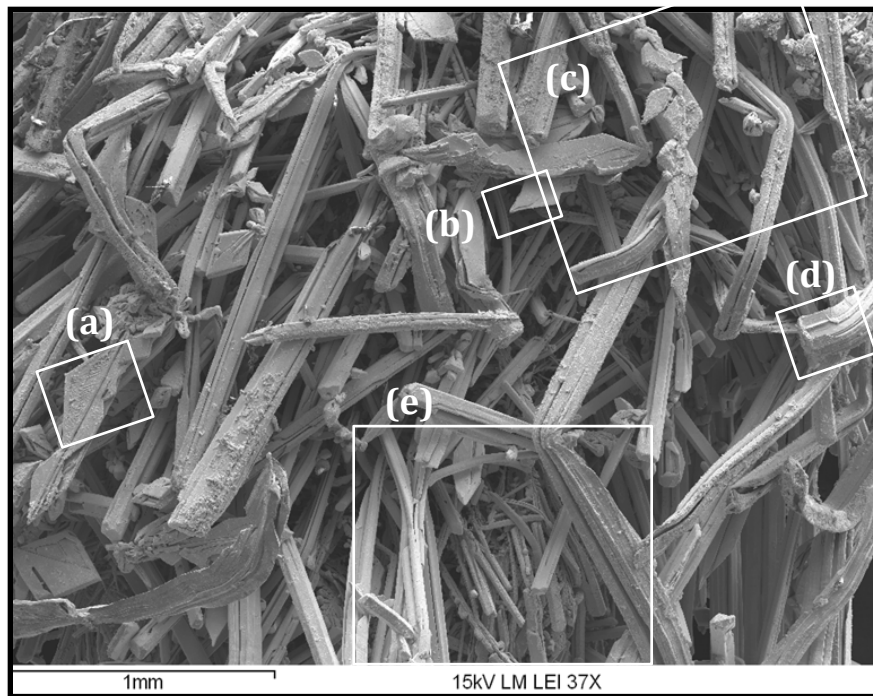


Figure 7.9: SE overview image of uranium dendrite cluster produced at 450 mV.

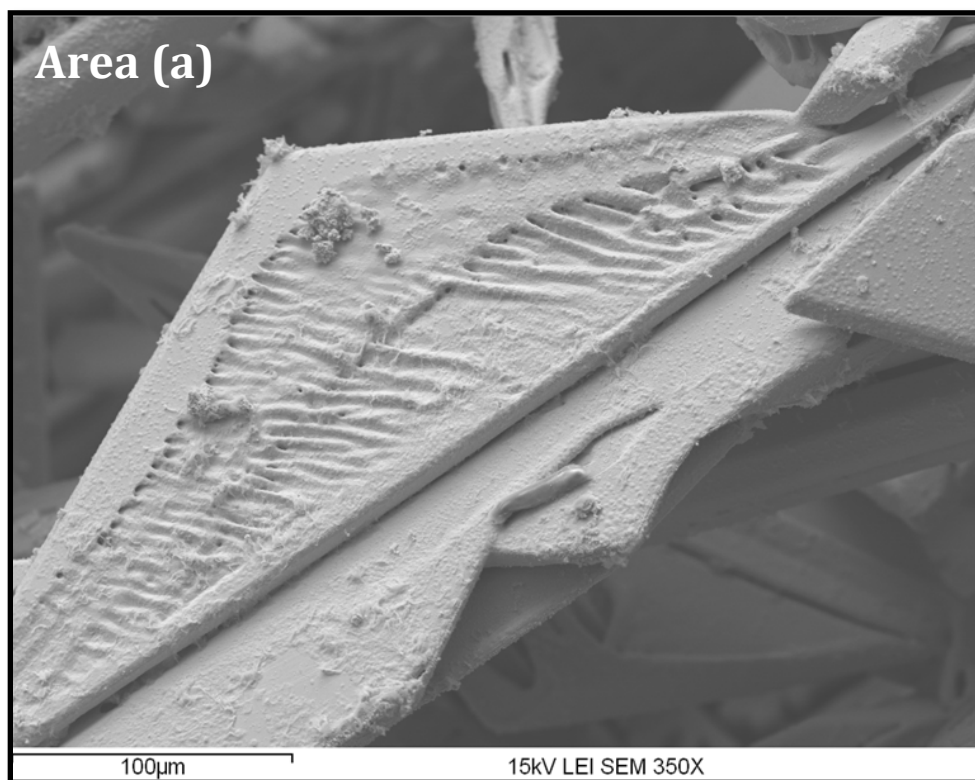


Figure 7.10: SE image of area (a) from Figure 7.9. The growth direction expected to be toward bottom left corner of image.

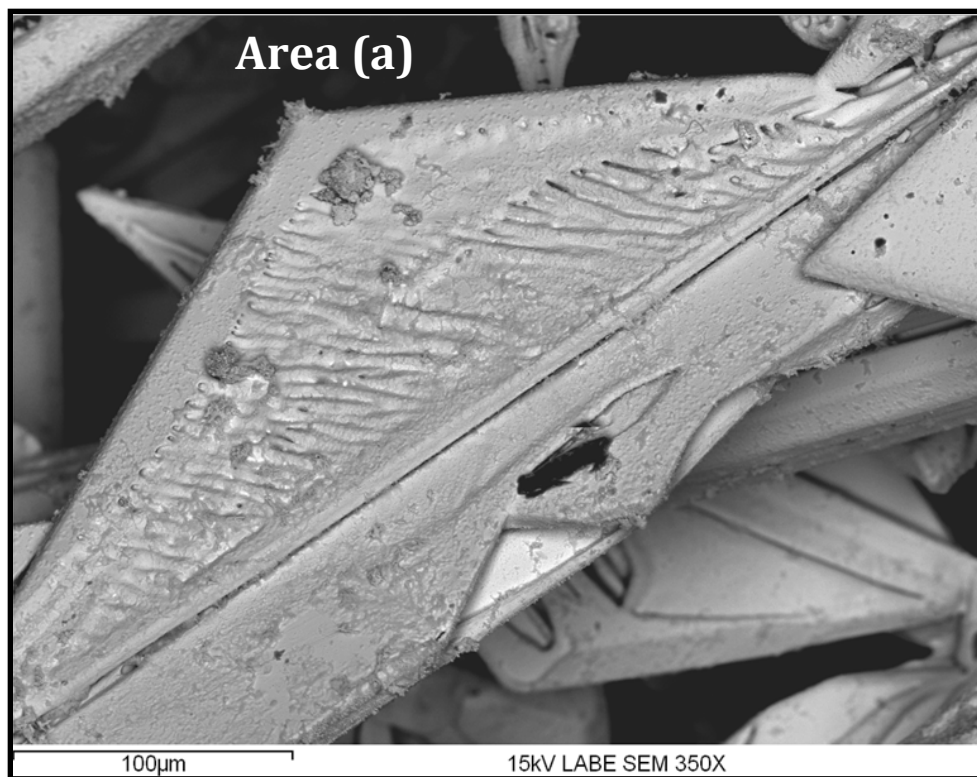


Figure 7.11: BSE image of area (a) from Figure 7.9.

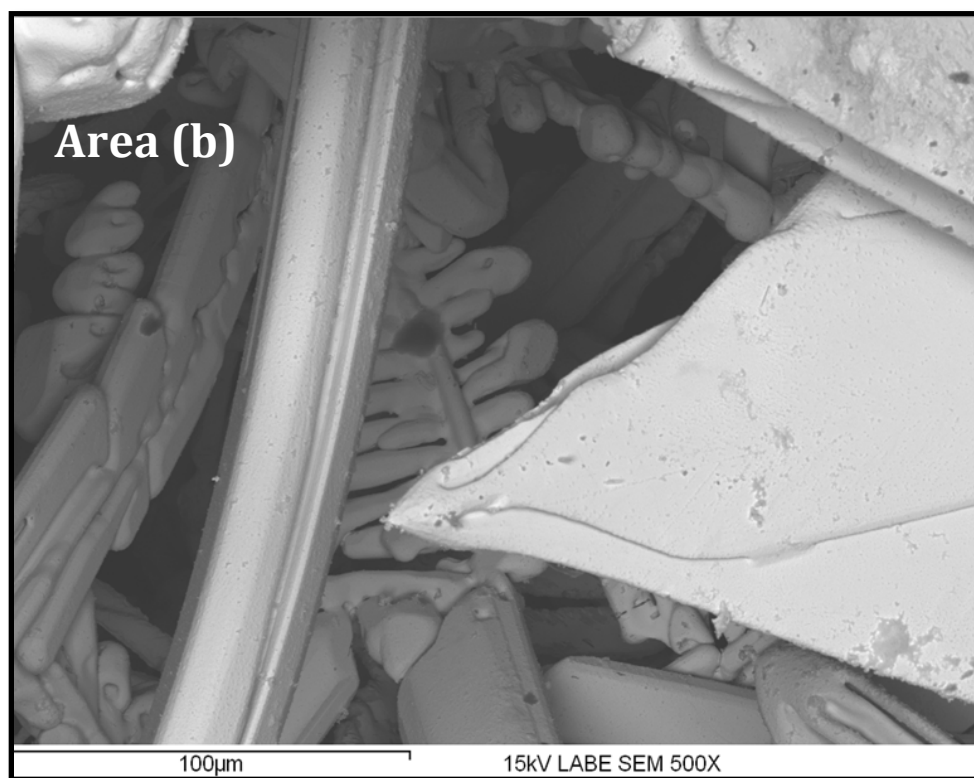


Figure 7.12: BSE image of area (b) from Figure 7.9. The platelet growth direction is to the left.

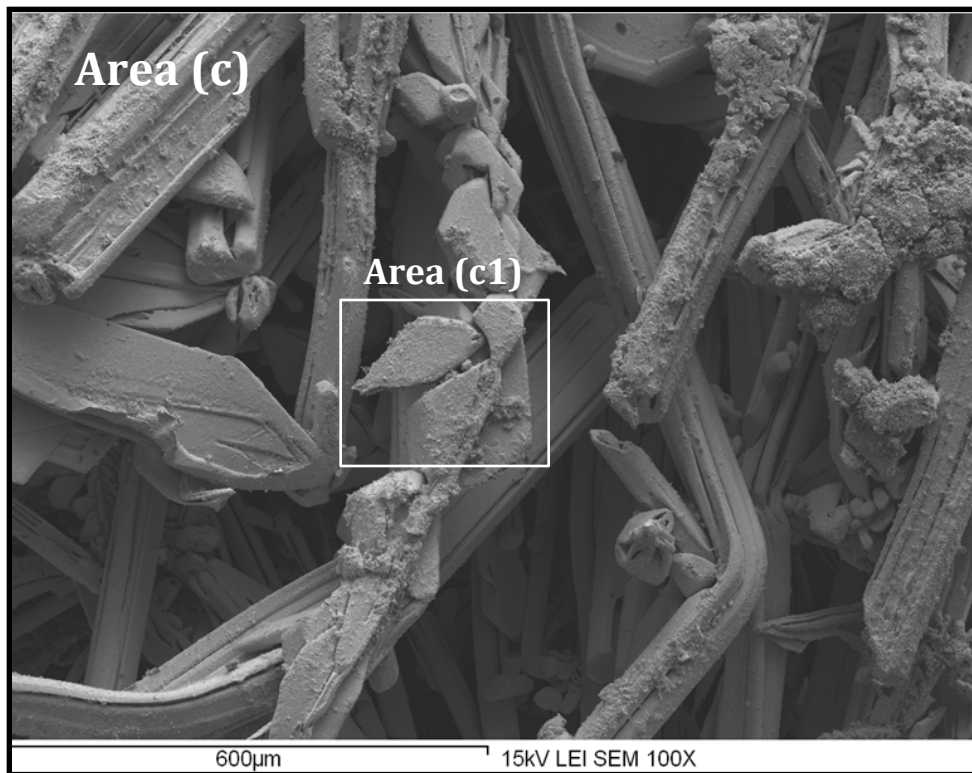


Figure 7.13: SE image of area (c) from Figure 7.9.

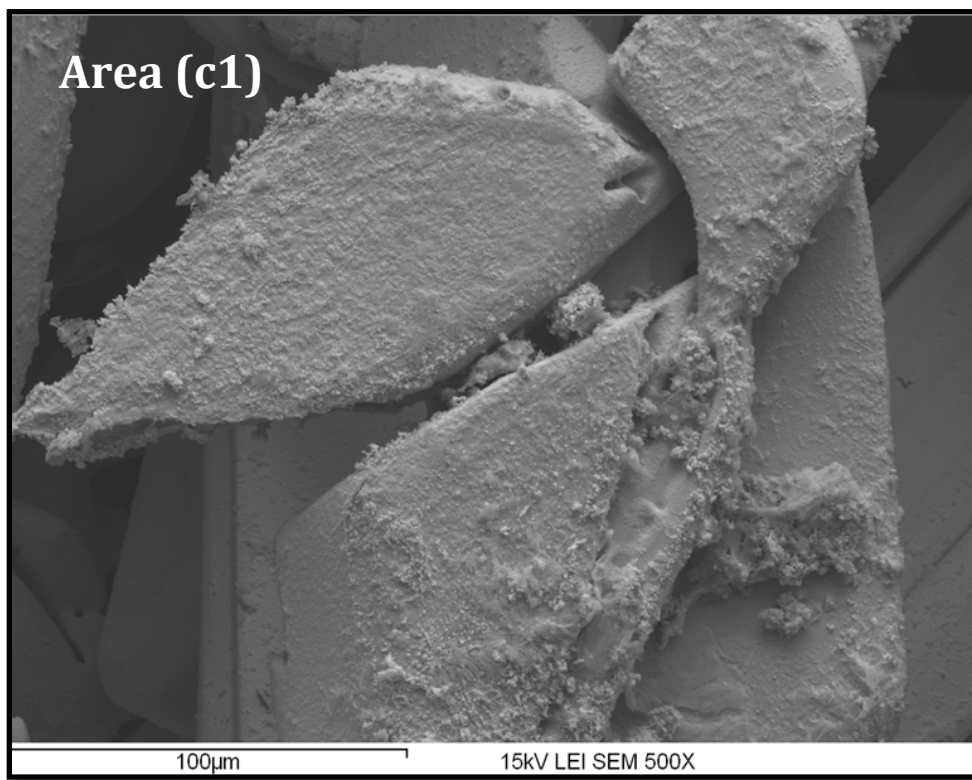


Figure 7.14: SE image of area (c1) from Figure 7.13.

Figure 7.15 provides a BSE image of area (d) from Figure 7.9. This image is focused on a fiber comprised of several filaments, with a combined diameter near 150 μm . Dark spots of foreign material of low atomic mass can be seen. The darkest of these may be carbon residue from the adhesive carbon mounting. Figure 7.16 is the same image, but overlaid with locations of strong chlorine spectra. It is seen that many of the $\sim 5 \mu\text{m}$ particles of medium contrast may be residual salt which was not removed during washing. Figure 7.17 is similar except overlaid for oxygen.

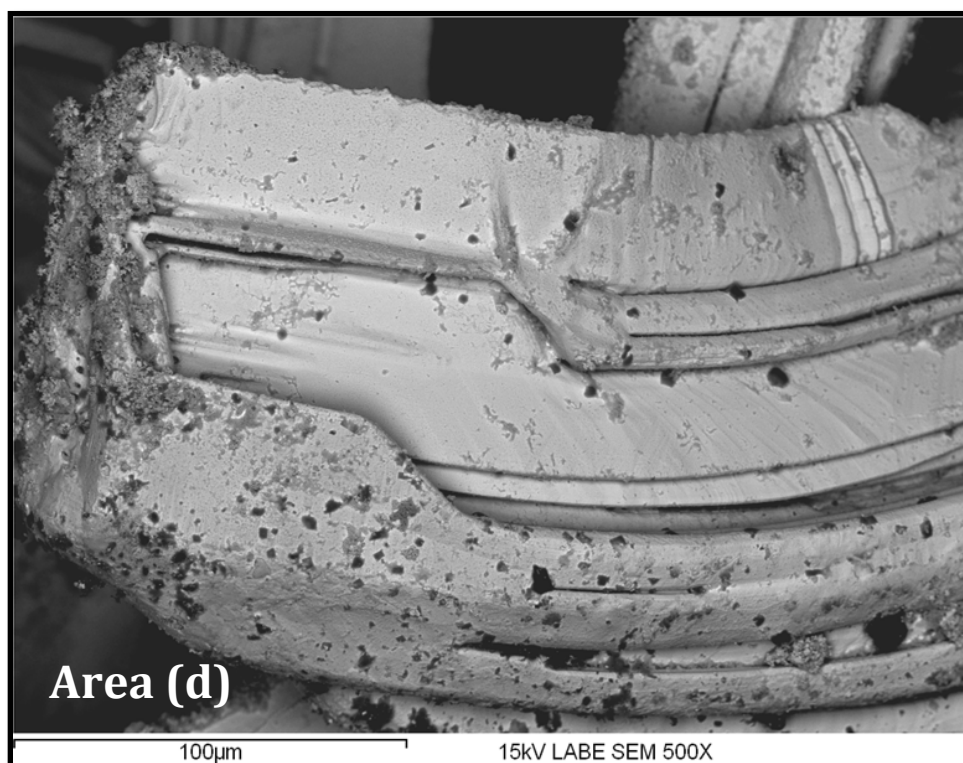


Figure 7.15: BSE image of area (d) from Figure 7.9.

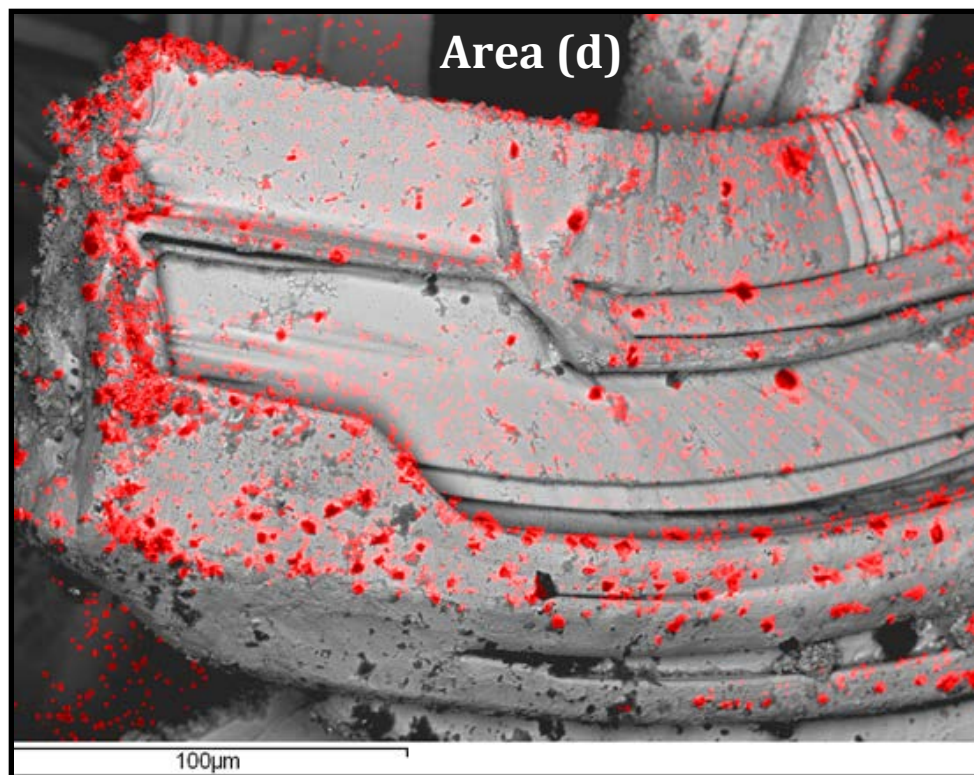


Figure 7.16: Chlorine overlay of BSE image of area **(d)** from Figure 7.9.

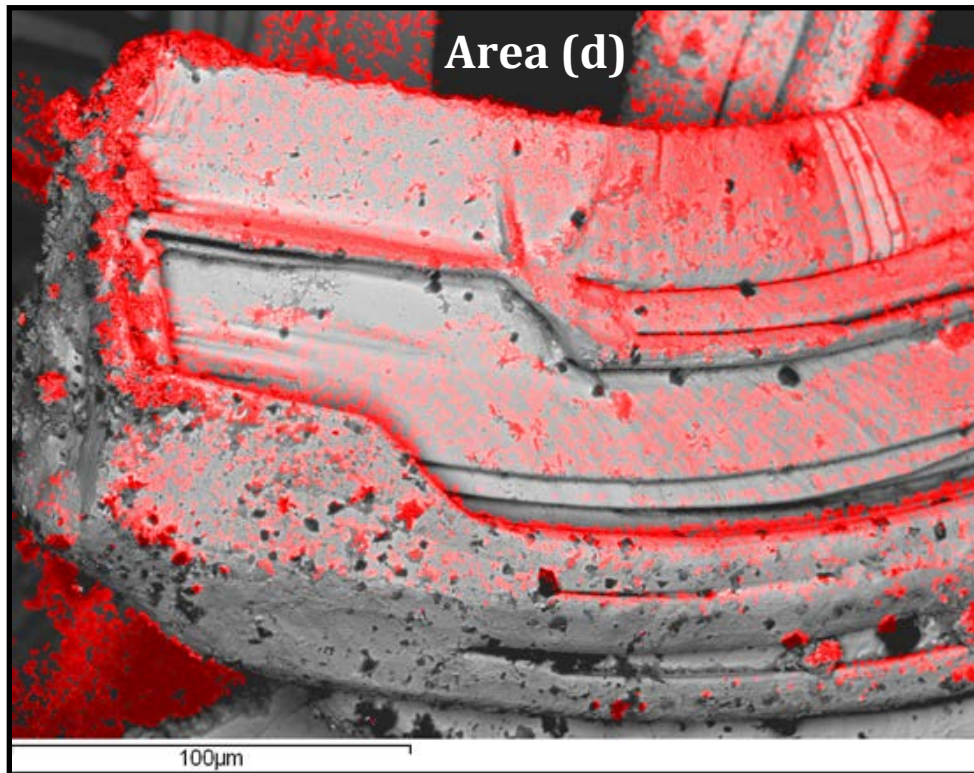


Figure 7.17: Oxygen overlay of BSE image of area **(d)** from Figure 7.9.

Figure 7.18 shows an SE image of area (e) from Figure 7.9. The majority of uranium in this image consists of fibers of individual diameter near 30-50 μm . Some fibers are grouped together as fibers in a larger composite. On the left side of the image, individual fibers have been split and deformed, probably during the harvesting process. In the center of the image under the larger fibers, a mass of smaller fibers can be seen. Figure 7.19 provides a close look at area (e1) from Figure 7.18. It is seen that these fibers are in the range of 20-30 μm diameter. The fibers also appear to be pitted, with fingerprint-like pattern in some places. Figure 7.20 provides a higher resolution inspection of the pitted fiber from area (e1-a). A number of EDS spectra were obtained across this surface and results indicated 4-6 wt% oxygen with balance uranium; no chlorine was detected. These fibers seem to be pitted or corroded by an unknown mechanism, possibly during the water washing process. The fibers seen in Figures 7.18 through 7.21 generally appear to be columnar, being of similar thickness to width. While a few tips are pointed, most are square or blocky. Figure 7.21 provides another SE image of area (e2) from Figure 7.18. Extensive pitting is evident in some of these fibers, as well as small irregular dendritic structures underneath.

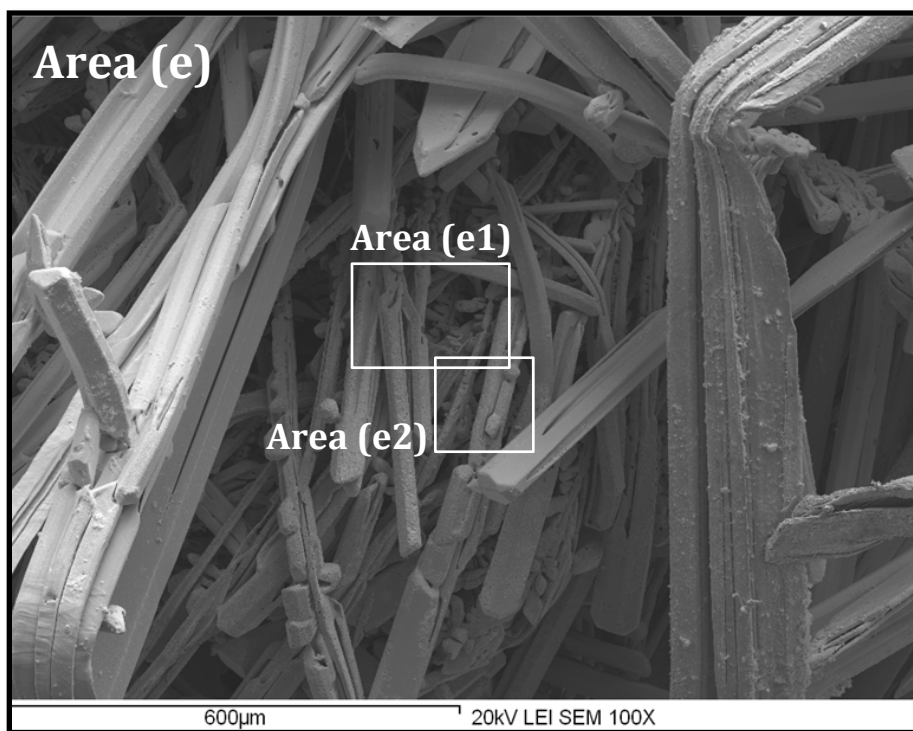


Figure 7.18: SE image of area (e) from Figure 7.9.

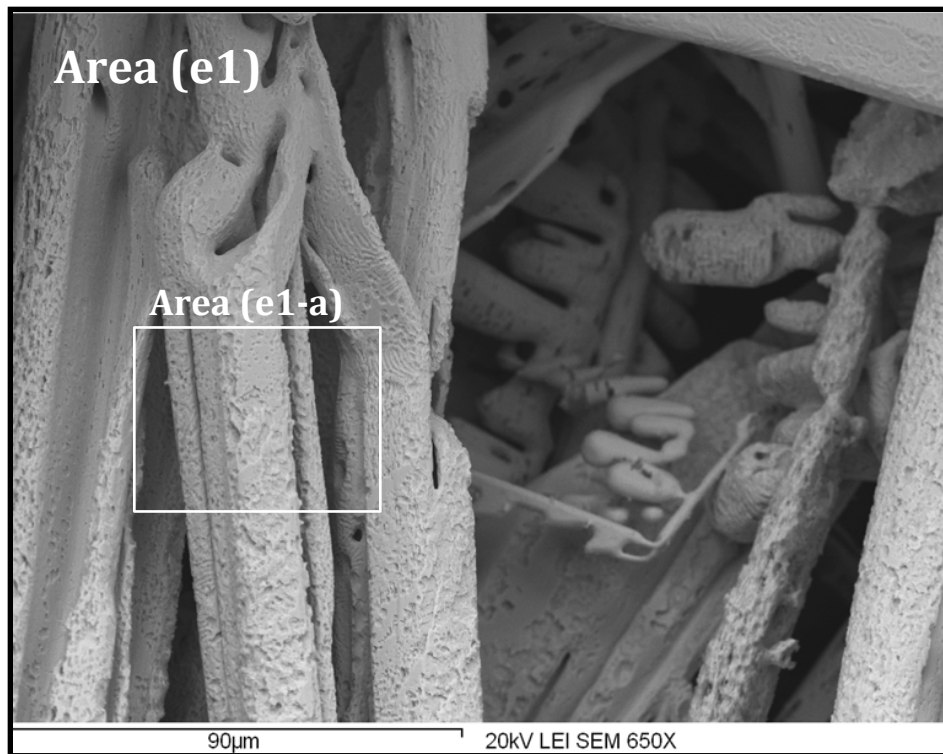


Figure 7.19: SE image of area **(e1)** from Figure 7.18.

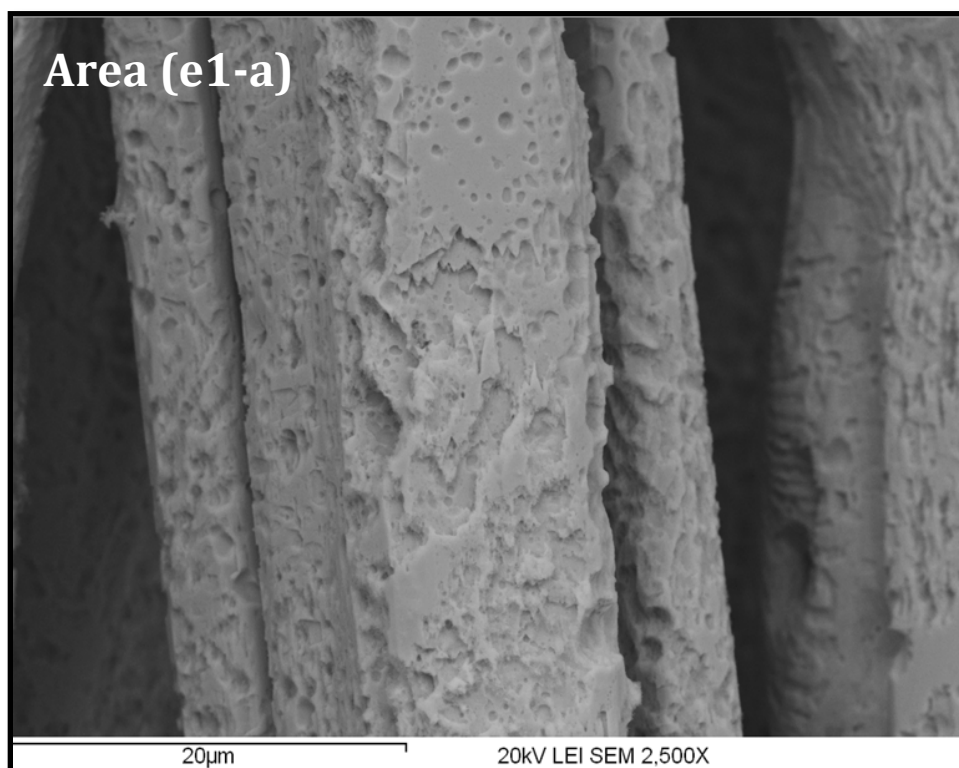


Figure 7.20: SE image of area **(e1-a)** from Figure 7.19.

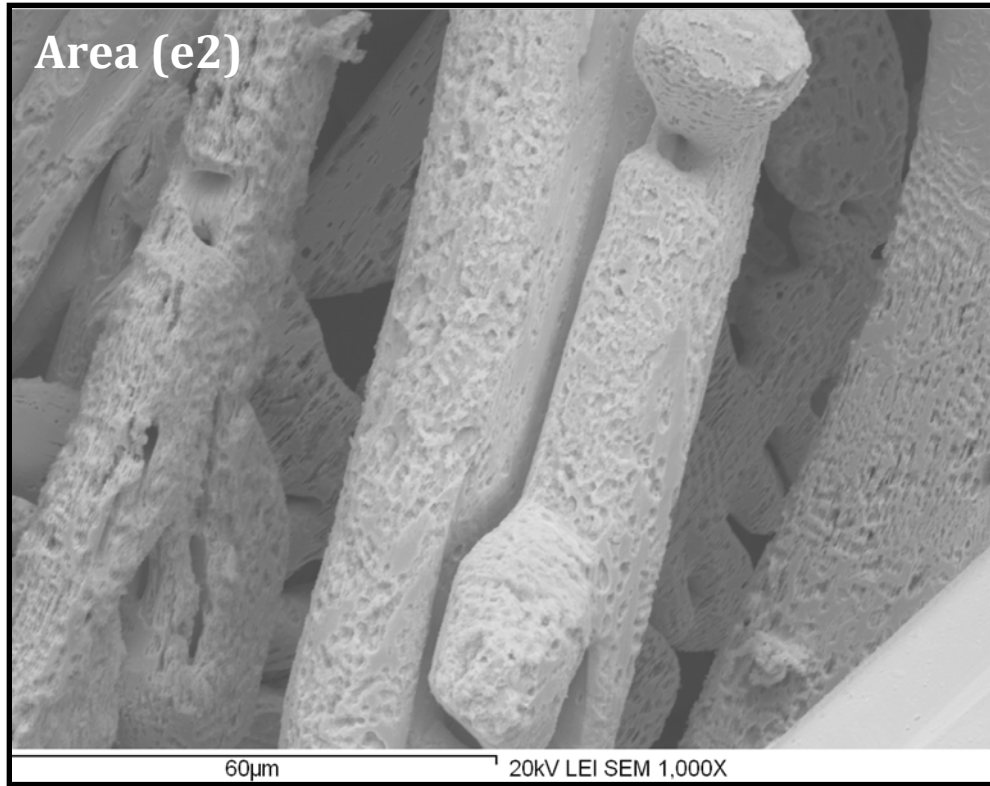


Figure 7.21: SE image of area **(e2)** from Figure 7.18.

Figure 7.22 provides an SE image of a regular dendritic structure, which is labeled as area (f) located in the bottom of Figure 7.9. A chain of side dendrites at nearly regular intervals has grown along one side at an angle of 90 degrees to the parent dendrite. A swirling pattern of etching is apparent in some dendrite surfaces. Figure 7.23 provides a high magnification of area (f1). A single small pore of 1-2 μm diameter is apparent. The etching seems to be occurring in zones of 1-2 μm width. Figure 7.24 provides an image of a zone of very fine fibers of diameters of 1-3 μm . The nature of the surrounding particles has been obscured by oxidation.

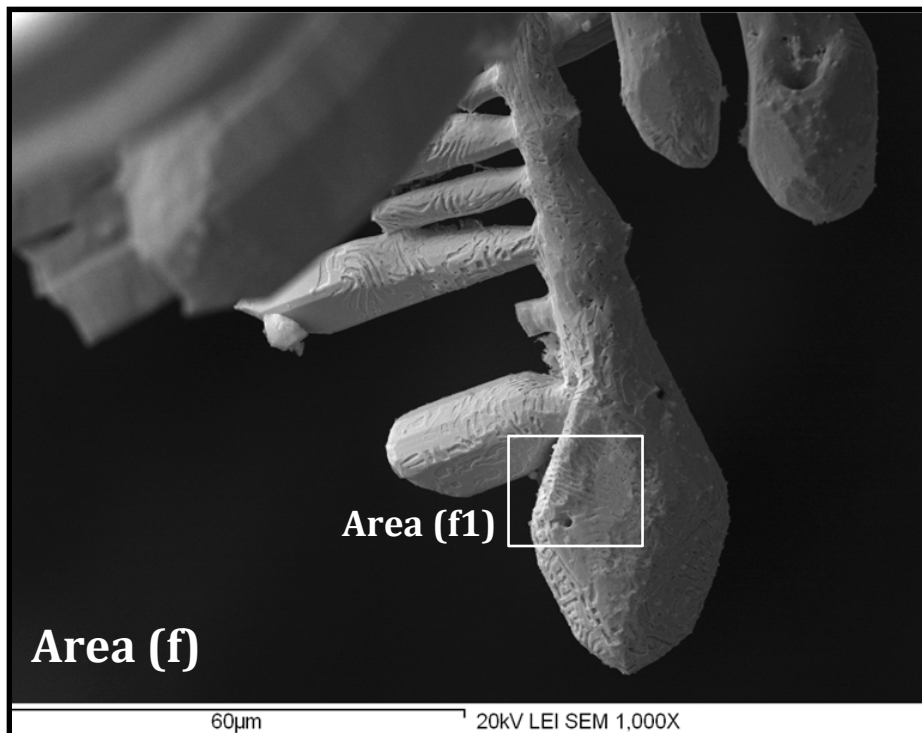


Figure 7.22: SE image of dendrite with regular side branches, from lower layer of deposit below bottom of image presented in Figure 7.9 (not seen in the image).

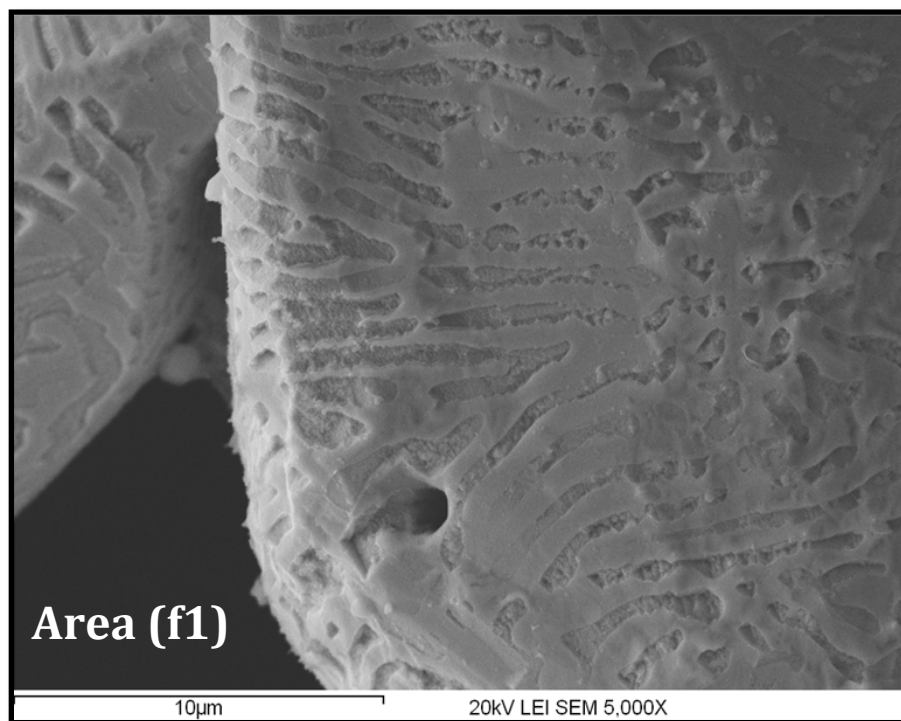


Figure 7.23: Area (f1) from Figure 7.22.

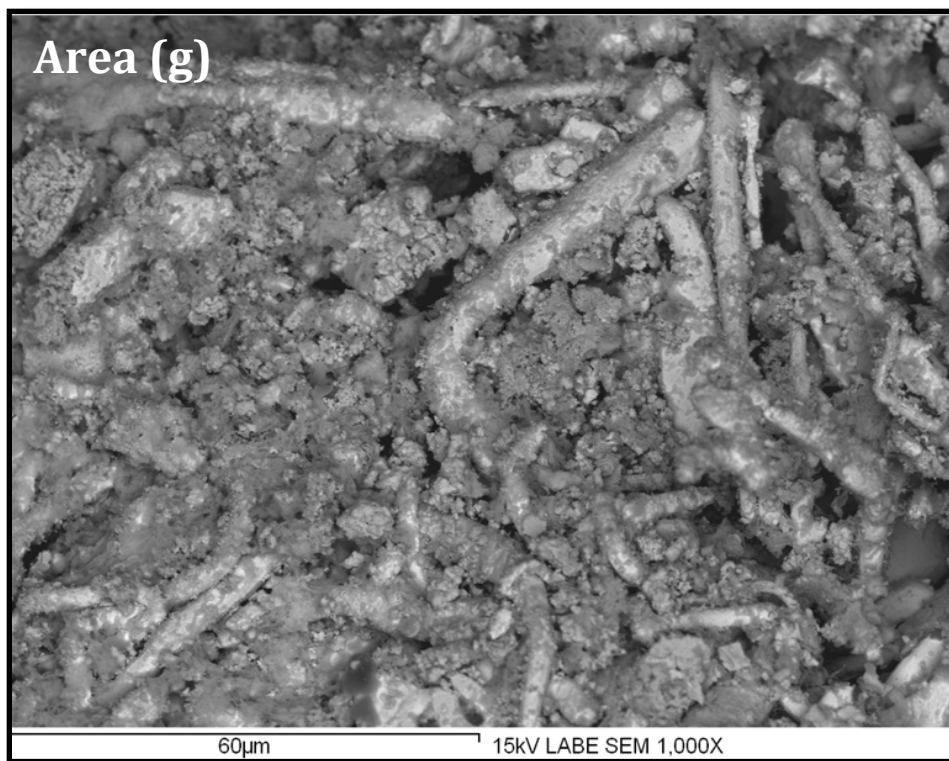


Figure 7.24: Oxidized mass of very fine fibers, from surface of deposit near top of image in Figure 7.9 (not seen in image).

7.2.2 Microscopy of Uranium Deposit from 150 mV Overpotential

Figure 7.25 provides an overview image of a cluster of dendrites produced at 150 mV potential relative to a uranium rod. This dendrite sample was immediately transferred to the SEM vacuum chamber following salt removal by water wash. This image also provides a key to following images. Figure 7.26 is a BSE image of a thin platelet comprised of regular dendritic structures which were likely mechanically deformed during harvesting. Very thin gaps can be seen between dendrite branches and in branches that appear to have merged. The overall structure appears to be very thin, possibly on the order of 5 μm . EDS spectra (Figure 7.27) were obtained for several locations in Figure 7.26 and show one particle of medium contrast to be residual salt. Unlike images of the previous section, little oxidation is seen. Figure 7.28 shows area (b), and the uranium is primarily fibers of 40-50 μm diameter. However, unlike fibers produced at 450 mV overpotential, nearly every one of these has visible rows of pores down the length. A number of fiber tips can be seen, and these tips merely taper to a point without any

dendritic features. Several bubbled blobs appear in this image and will be further examined later in this section. Near the top of the image, one large bent fiber appears to be formed by a number of smaller bundled fibers. Some fibers in the center of the image have blocky, non-uniform side dendrites.

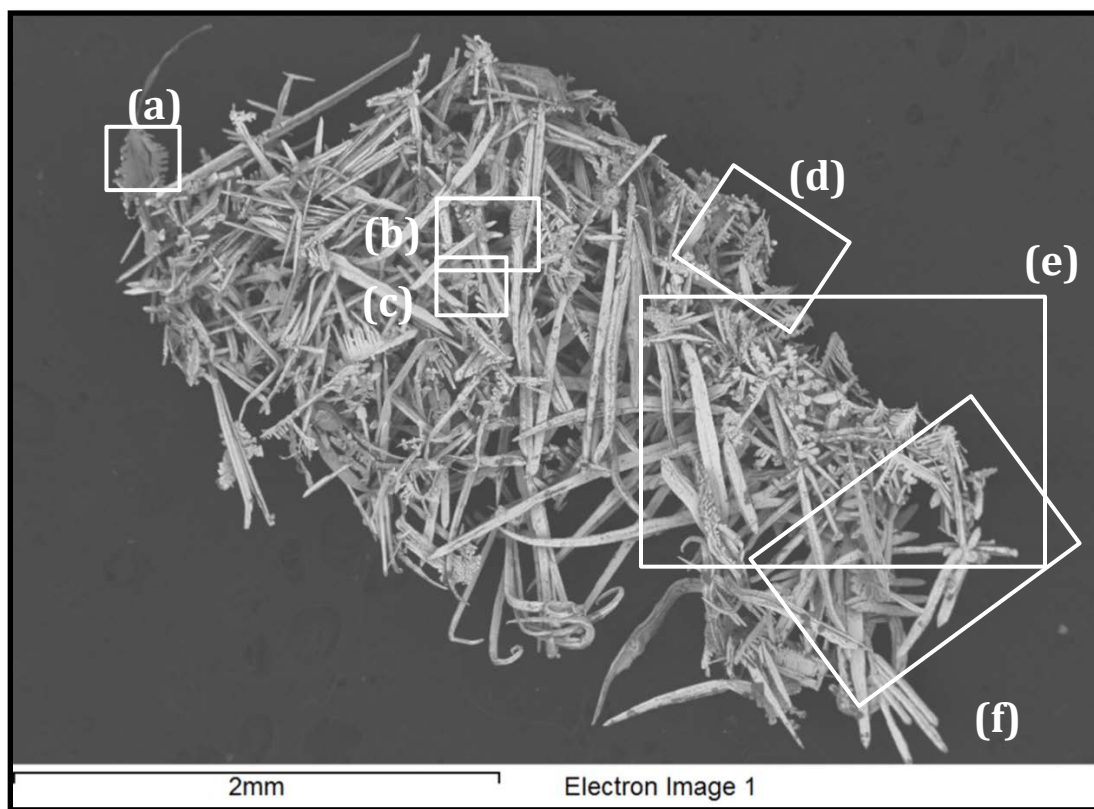


Figure 7.25: SE image of a cluster of fiber-like dendrites produced at 150 mV overpotential from 1 mol% UCl_3 in LiCl-KCl eutectic, with key to location for additional images.

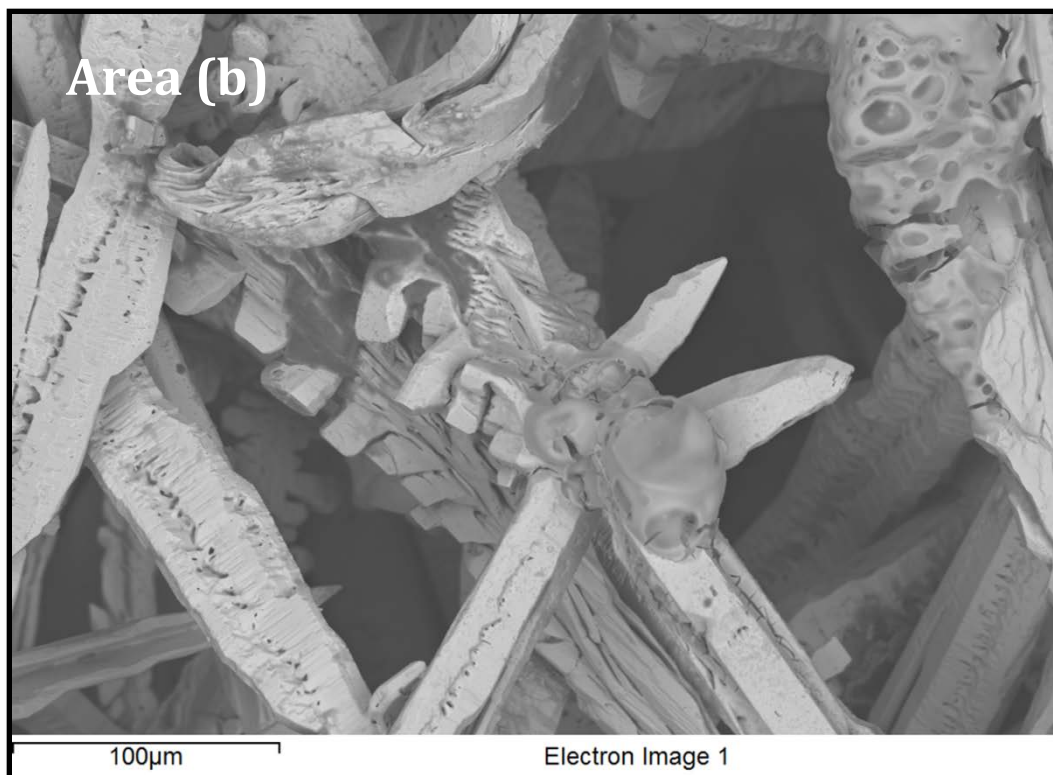


Figure 7.28: BSE image of area **(b)** from Figure 7.25.

Figure 7.29 shows an SE image from area (c) of Figure 7.25. More fibers of 30-50 μm diameter with rows of irregular pores down their length can be seen. In the center of the image is what appears to be a planar dendritic structure of maple-leaf like morphology. It appears to have originated at the tip of a fiber point up from the bottom of the image. Adjacent to this is a bubbled blob of material. EDS spectra for this blob and a nearby point on the dendrite are provided as Figure 7.30; it is seen that the blob is composed of salt. It was likely wet when it entered the SEM vacuum chamber and was rapidly dried and solidified during the chamber evacuation. Figure 7.31 focuses on area (c1) from Figure 7.29 displaying the tip of one of the fibers; here, it can be seen that there are no dendritic structures. The particle seen on the fiber near the center has high concentrations of aluminum and chlorine, and is likely a small piece of debris from the ceramics used in the experimental system. Otherwise the fibers are uranium with very small oxygen signature.

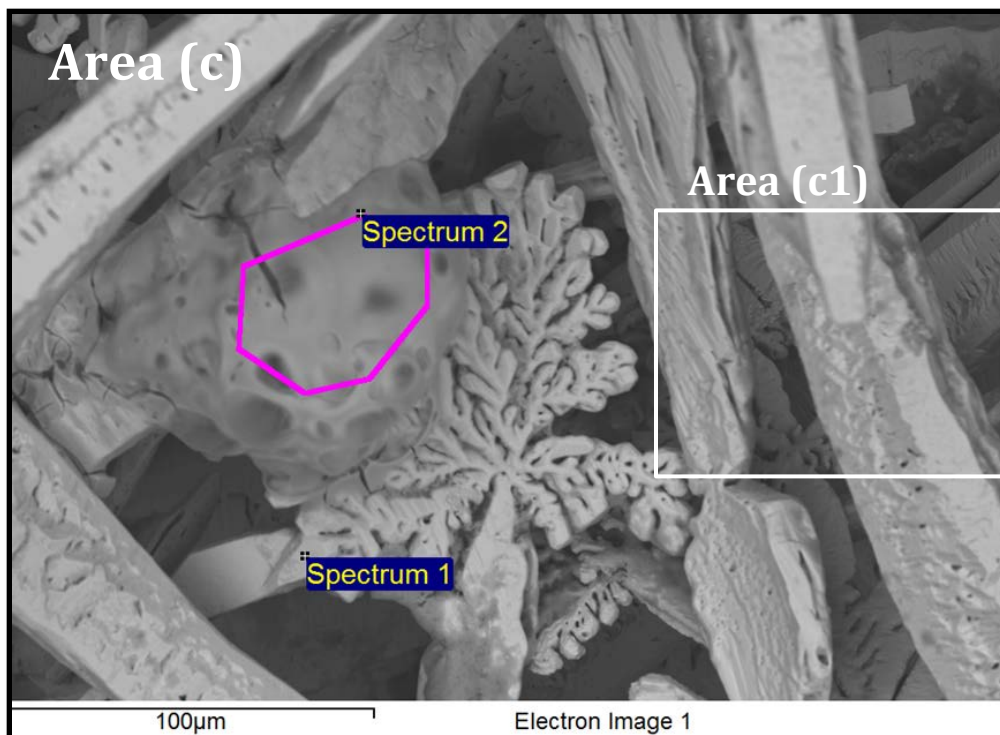


Figure 7.29: SE image of area (c) from Figure 7.25.

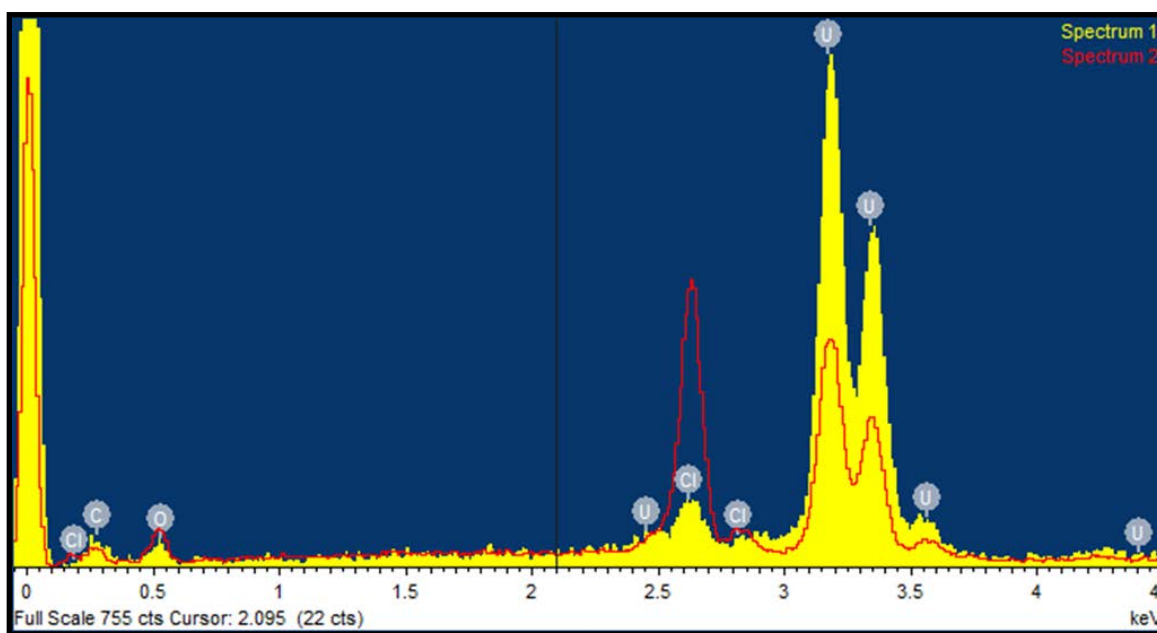


Figure 7.30: EDS Spectra from Figure 7.29, showing spectrum 2 to be residual chloride salt.

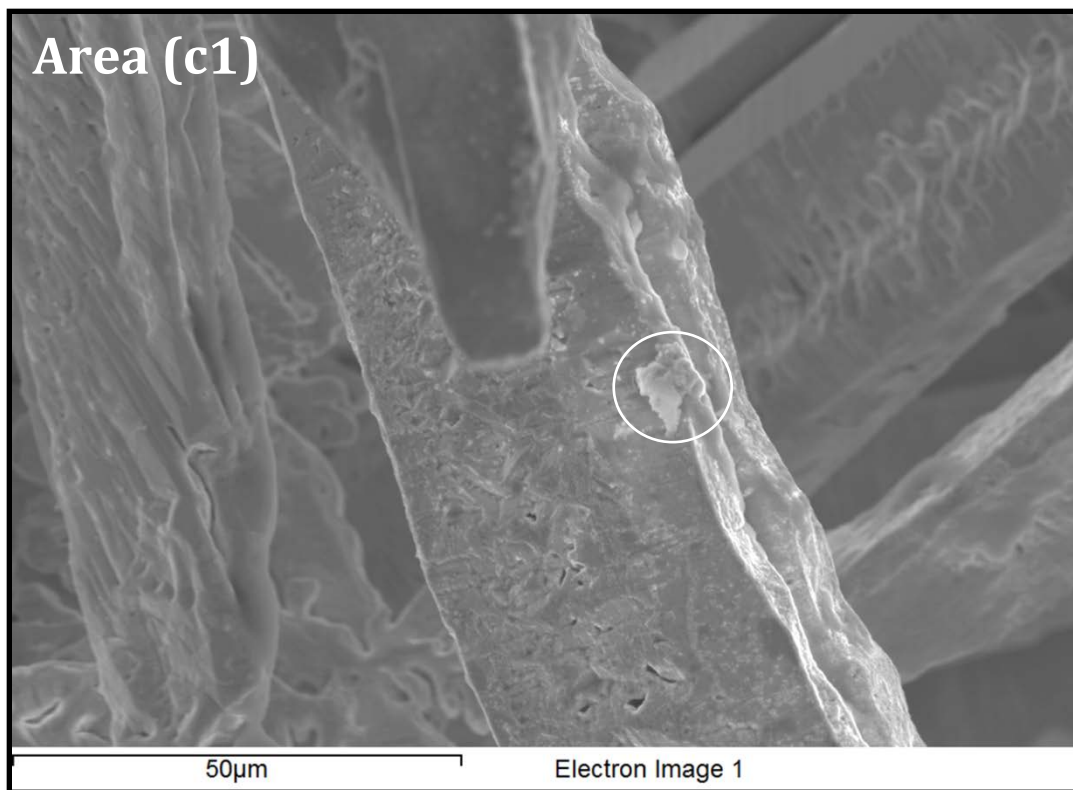


Figure 7.31: SE image of area **(c1)** from Figure 7.29.

Figure 7.32 is a BSE image from area (d) of Figure 7.25, showing a variety of planar, regularly-branched 45° dendrite groups. Figure 7.33 shows a BSE image of area (e) from Figure 7.25. The majority of uranium is comprised of fibers, although the right edge has a number of regular dendritic structures with regular side chains at a 45° angle to the parent dendrite. Figure 7.34 provides a closer view of one of these (area (e1), but carriage was rotated). The structure appears planar and has been damaged during the harvesting. Along the edge of the parent dendrite, narrow slots or pores can be seen where side dendrites appear to have merged. At the ends of the side dendrites, near the top of the image, the morphology appears to have changed to blocky 3-dimensional structures. Several small cubic structures can be seen near the top of the image. Figure 7.35 is a similar view using BSE, and it is seen that the cubic structures have lower atomic mass. EDS analysis indicates high chloride content, and they are likely salt crystals. It is not clear how these survived the washing process with this cubic morphology. Figure 7.36 shows another region of 30-50 μm diameter fibers, including roughly a dozen fiber tips. No dendritic structure is seen at the tips; each fiber simply has an angular

taper to a point. In this image, it can also be seen that the fibers have a sword-like 3-dimensional morphology, with thickness of only 10-20% of the width. Near the bottom of the image, a regular dendritic structure is seen. Unlike the earlier dendrites in this group this appears to have side chains at 90° to the parent dendrite. A planar maple-leaf dendrite group can also be seen near the center of the image.

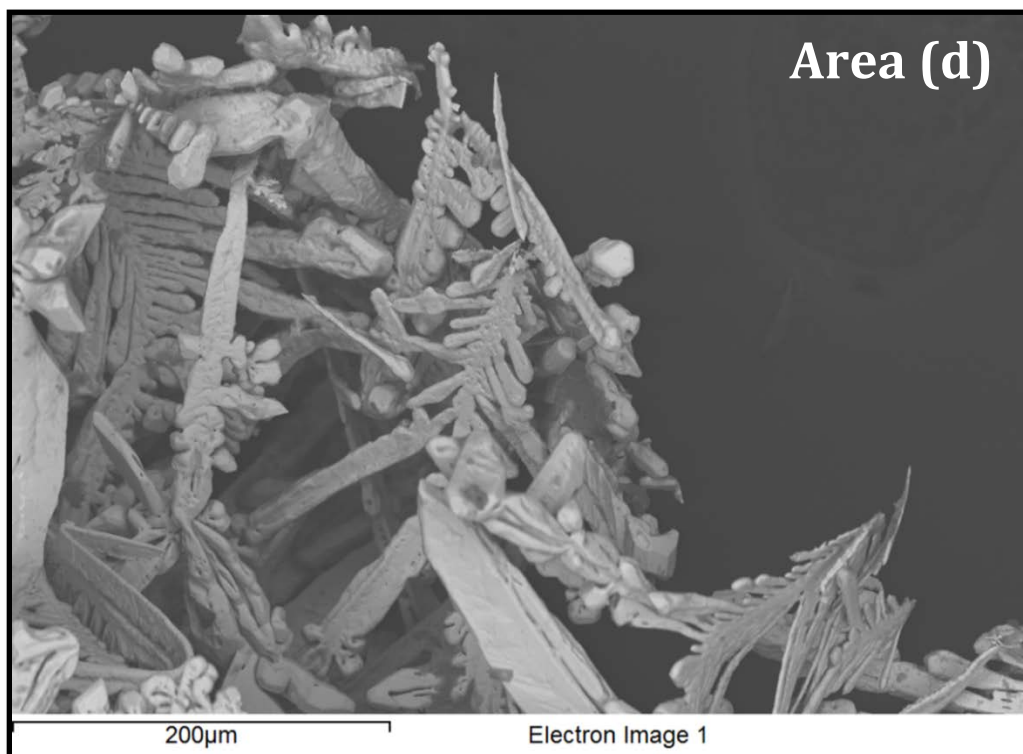


Figure 7.32: BSE image of area **(d)** from Figure 7.25 showing regularly-branched 45° dendrite groups.

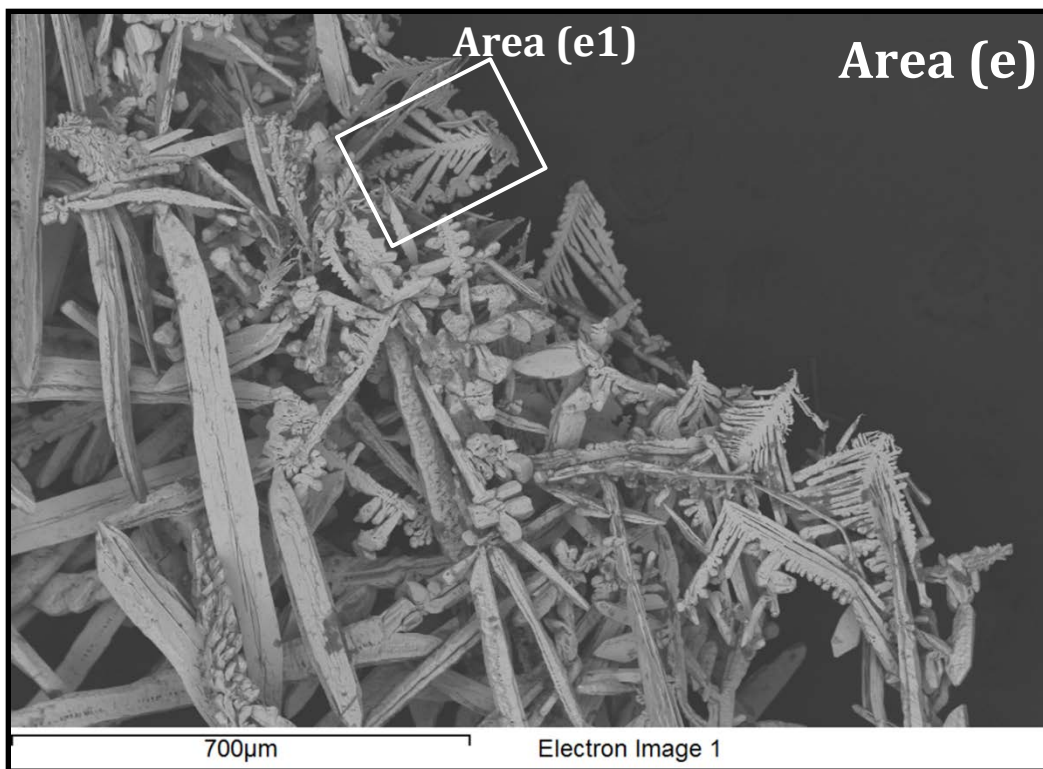


Figure 7.33: BSE image of area **(e)** from Figure 7.25.

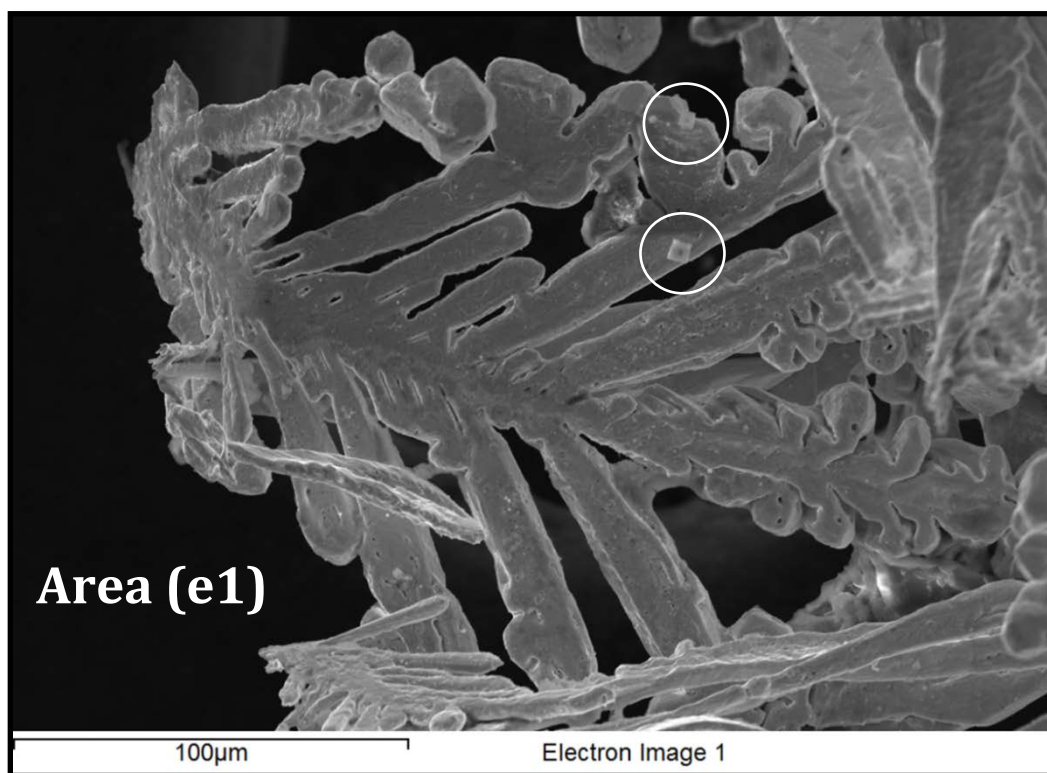


Figure 7.34: SE image of area **(e1)** from Figure 7.33 showing a regularly-branched dendrite.

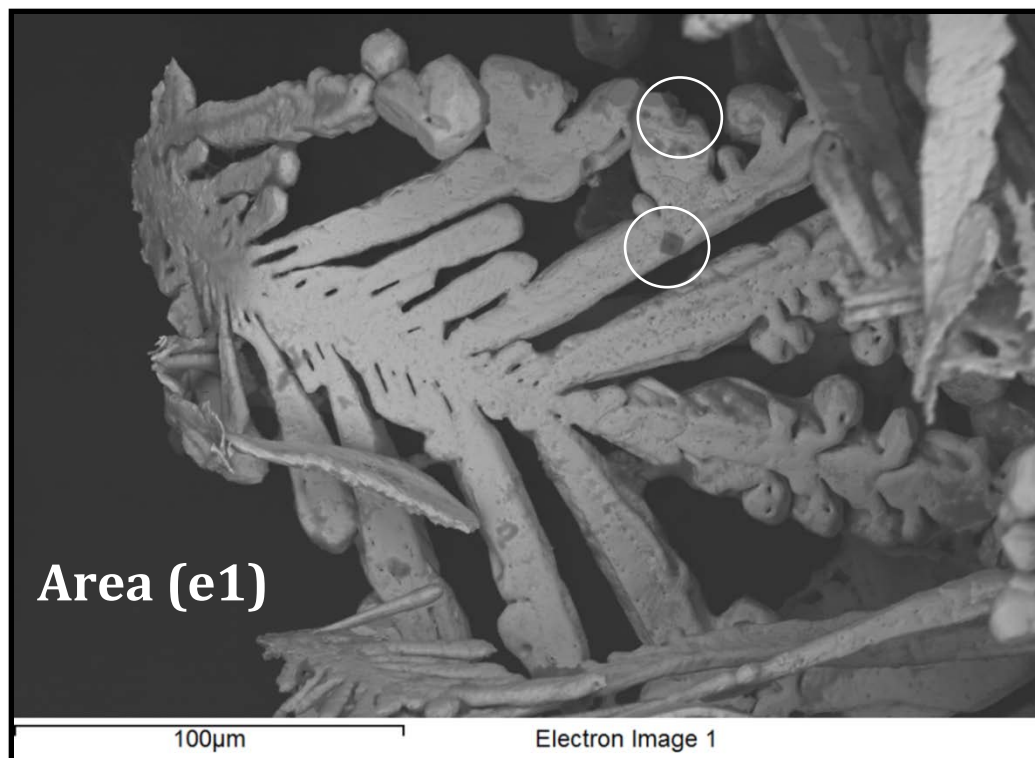


Figure 7.35: BSE image of area **(e1)** from Figure 7.33 showing a regularly-branched dendrite.

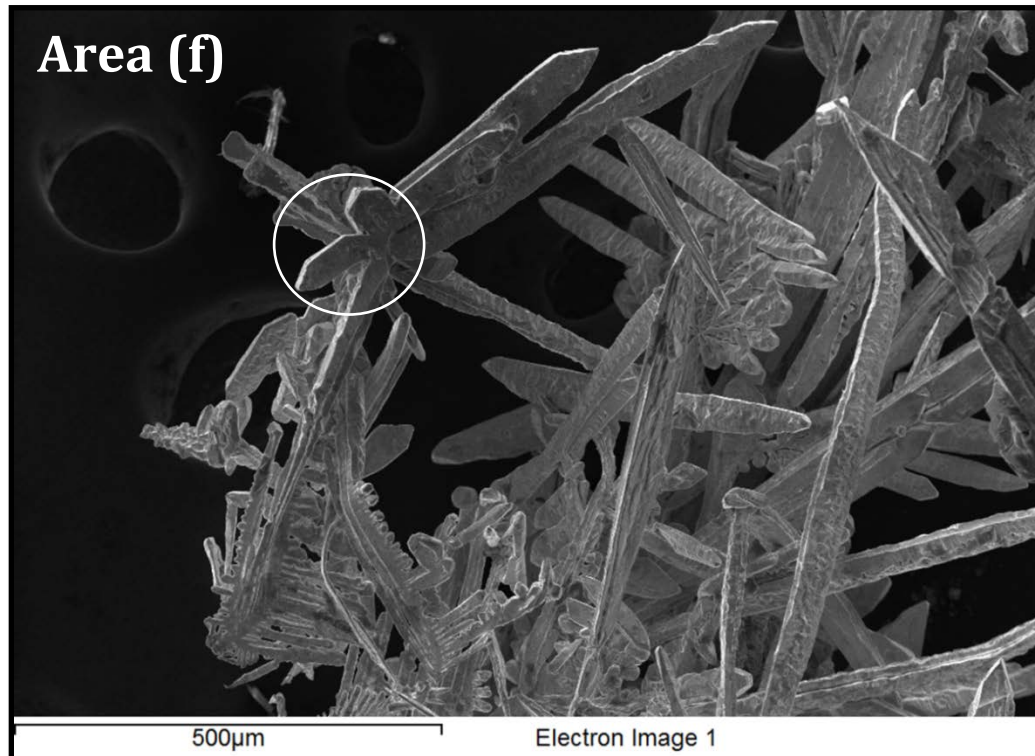


Figure 7.36: SE image of area **(f)** from Figure 7.25 comprised primarily of 50 µm fibers, but also showing 90° regularly-branched dendrite groups and an irregular maple-leaf.

7.2.3 Microscopy of Uranium Deposit from 25 mV Overpotential

The final dendrite sample was produced at an electrochemical overpotential of 25 mV. Figure 7.37 provides a low resolution overview of the deposits on the carbon sticky dot. The morphology is clearly different than that found in the previous two dendrite groups. Most uranium is present as angular rhomboidal platelet dendrites, with a few irregular clusters of blocky crystals. This image also provides a key to later figures. Figure 7.38 is an SE image of a classic rhomboidal crystal, just over a mm in length which appears to be comprised of 4 or more thin stacked plates. A similar curl and lip are seen at the corner of both large platelets. Figure 7.39 provides an SE image of area (b) from Figure 7.37. The crystals in the center of the image are similar stacked rhomboidal platelets. Figure 7.40 is a BSE image from which EDS was performed for several features. The analysis spectra are provided and shown in Figure 7.41; the large particle on the surface film appears to be oxide debris, and the adjacent crystal appears to have a thin residual film of salt. Figure 7.42 shows a higher-magnification SE image of area (b1). The crystal surfaces appear to be smooth and very angular. Furthermore, it appears that regularly-spaced ribs are growing in the cavity between platelets. A light etching, similar to that observed in the 450 mV dendrites is apparent on portions of the surface. Also, the corner of the large platelet has a similar curl to those observed in Figure 7.38. Figure 7.43 provides a clearer image of the ribs with a straight and consistent wall thickness of approximately 5 μm and a gap spacing of approximately 20 μm .

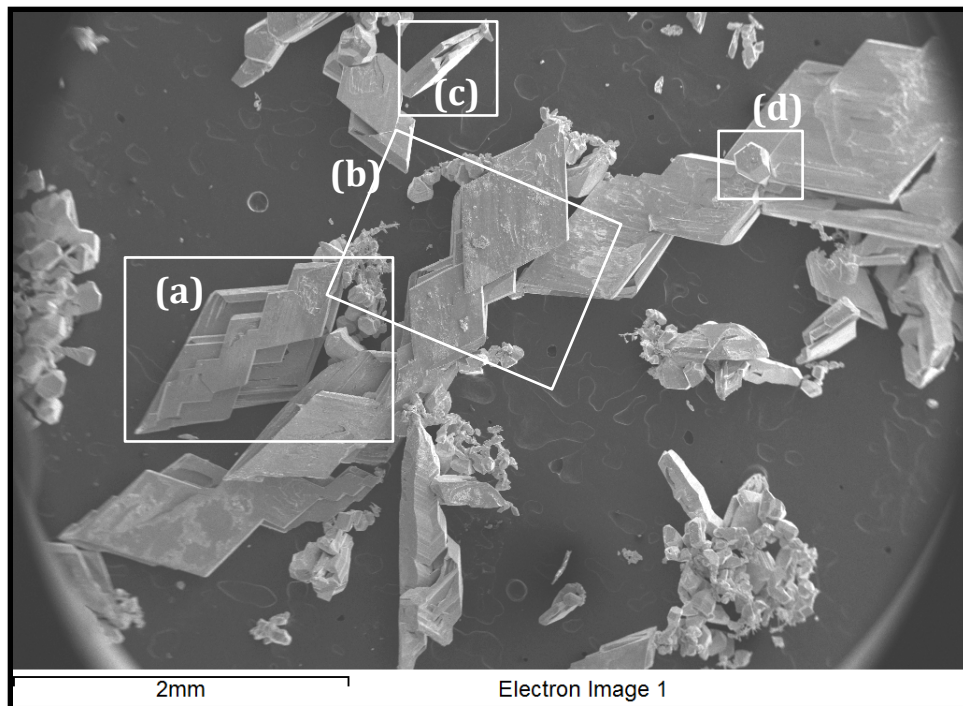


Figure 7.37: Low resolution overview of uranium dendrites from 25 mV overpotential and key to location of additional images **(a)** through **(d)**.

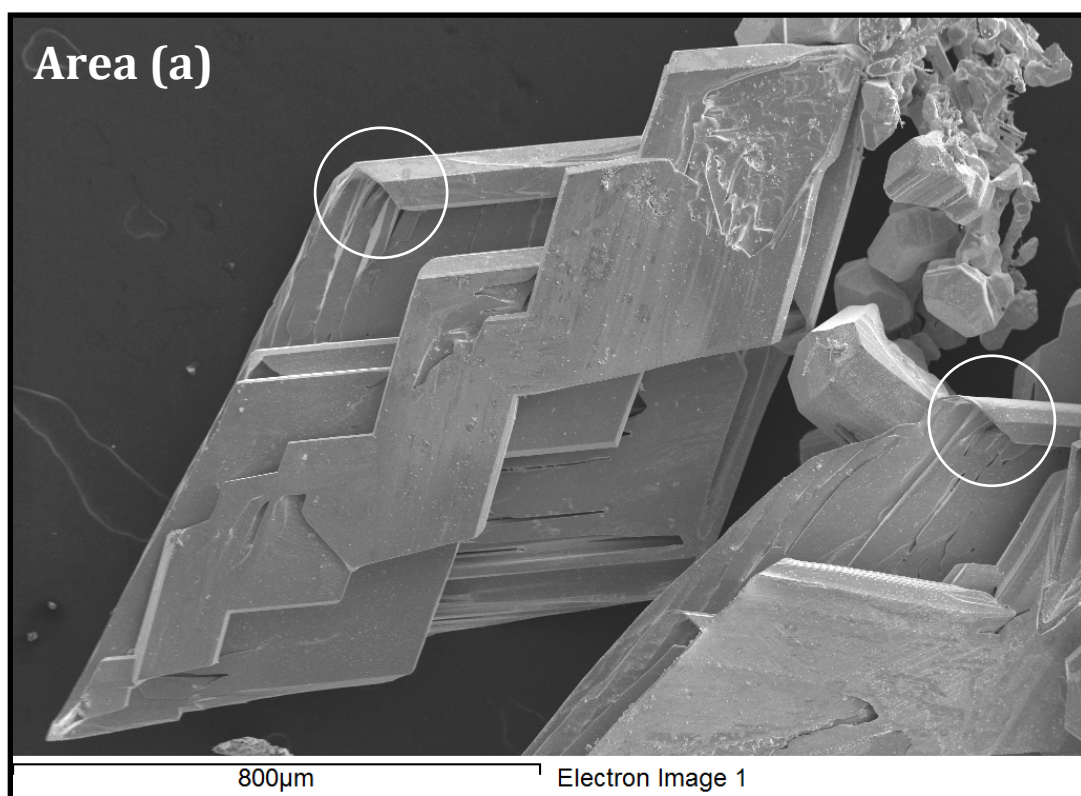


Figure 7.38: SE image of area **(a)** from Figure 7.37.

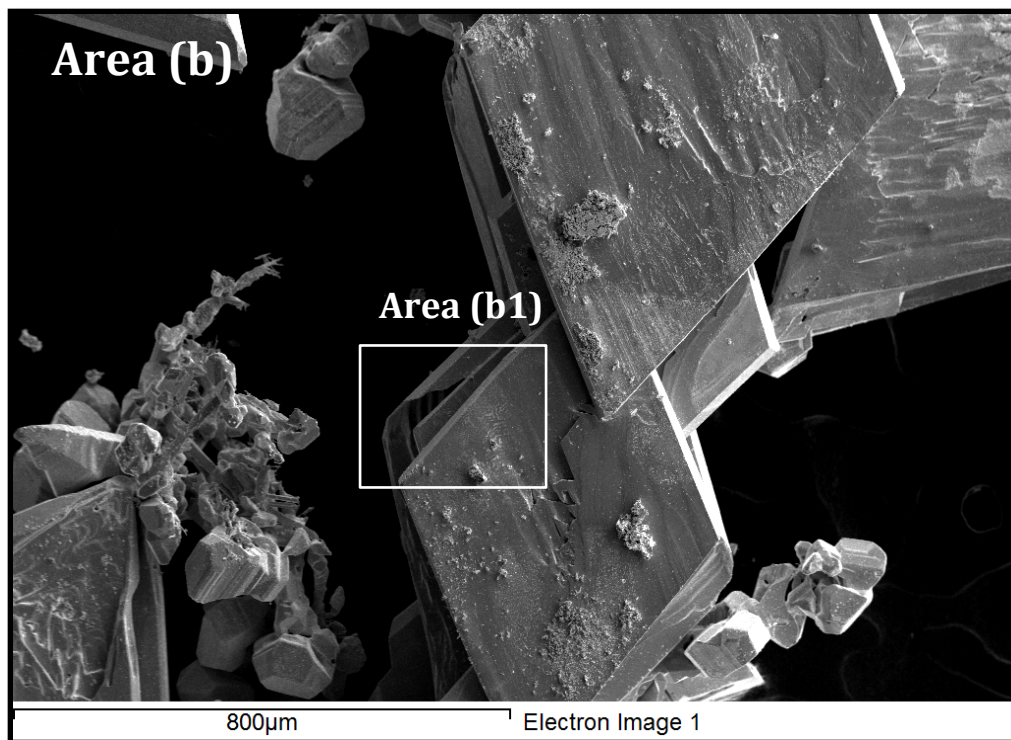


Figure 7.39: SE image of area (b) from Figure 7.37.

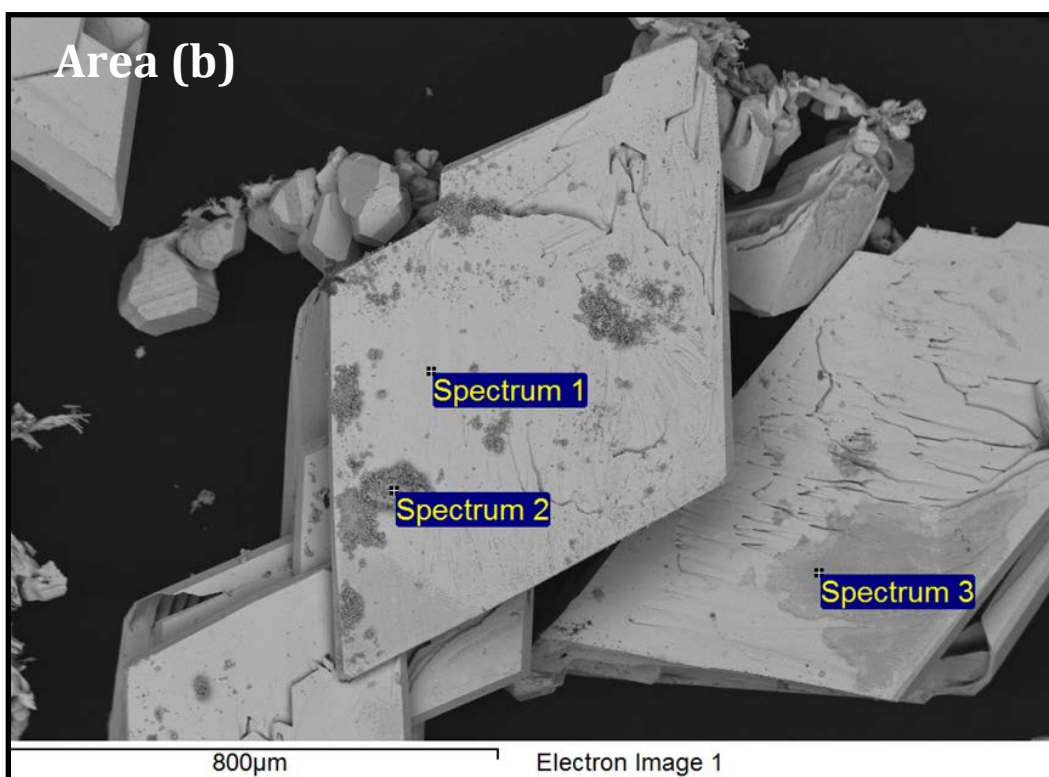


Figure 7.40: BSE image of area (b) from Figure 7.39 for EDS analysis.

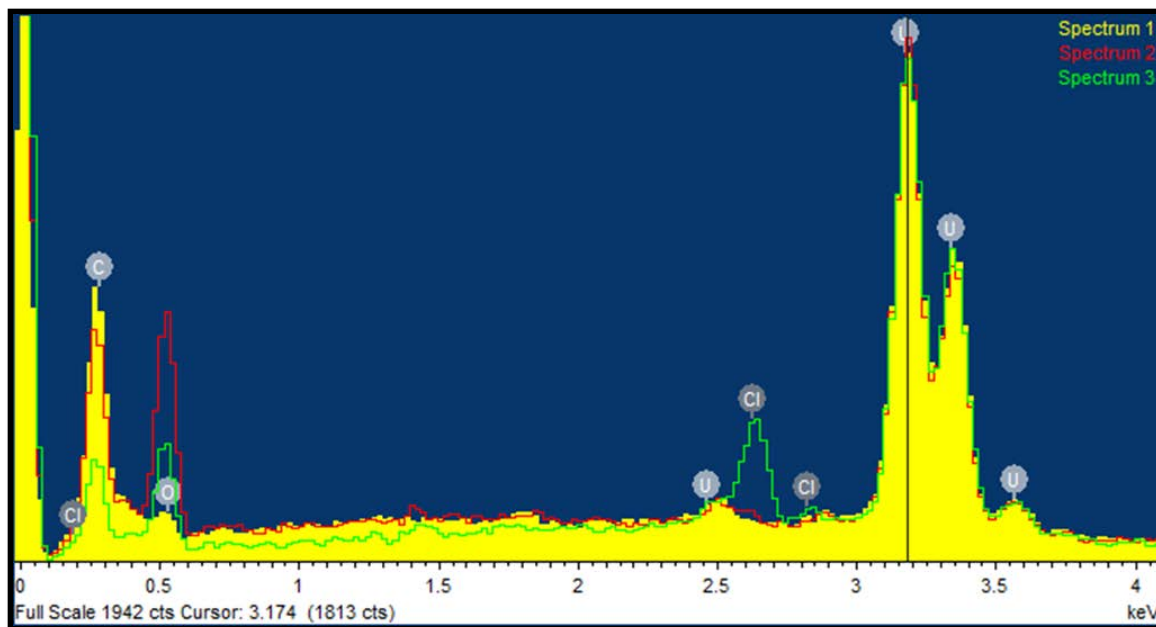


Figure 7.41: EDS spectra of points from Figure 7.40.

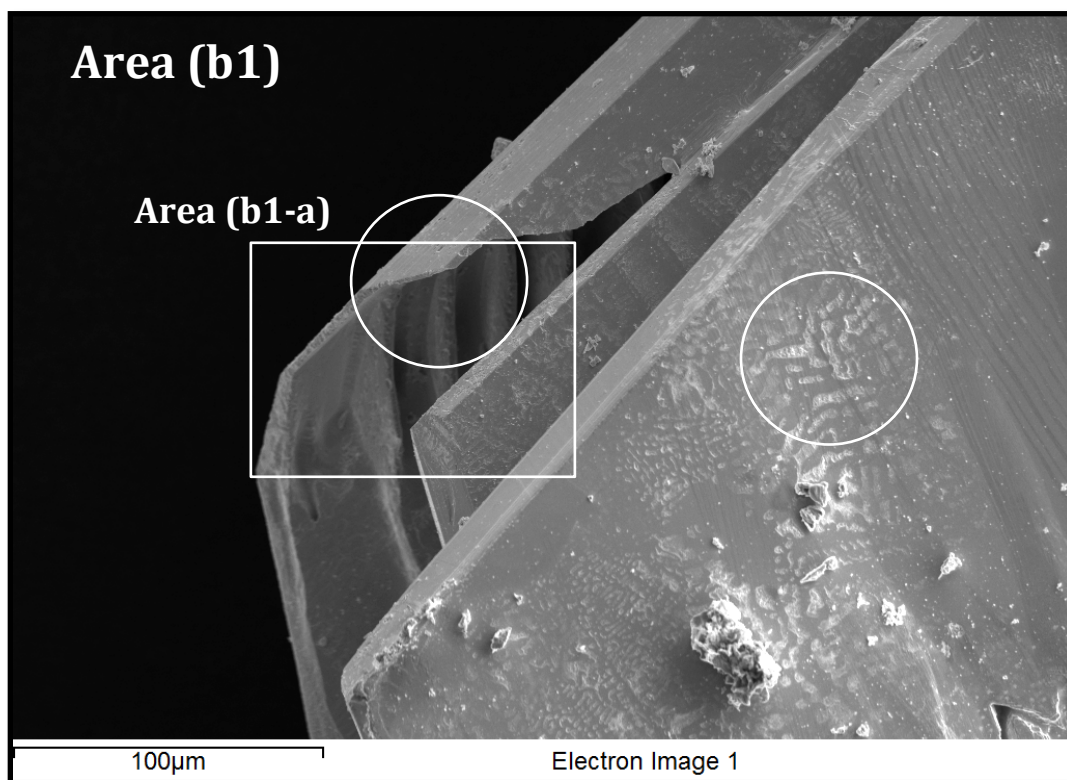


Figure 7.42: SE image of area (b1) from Figure 7.39.

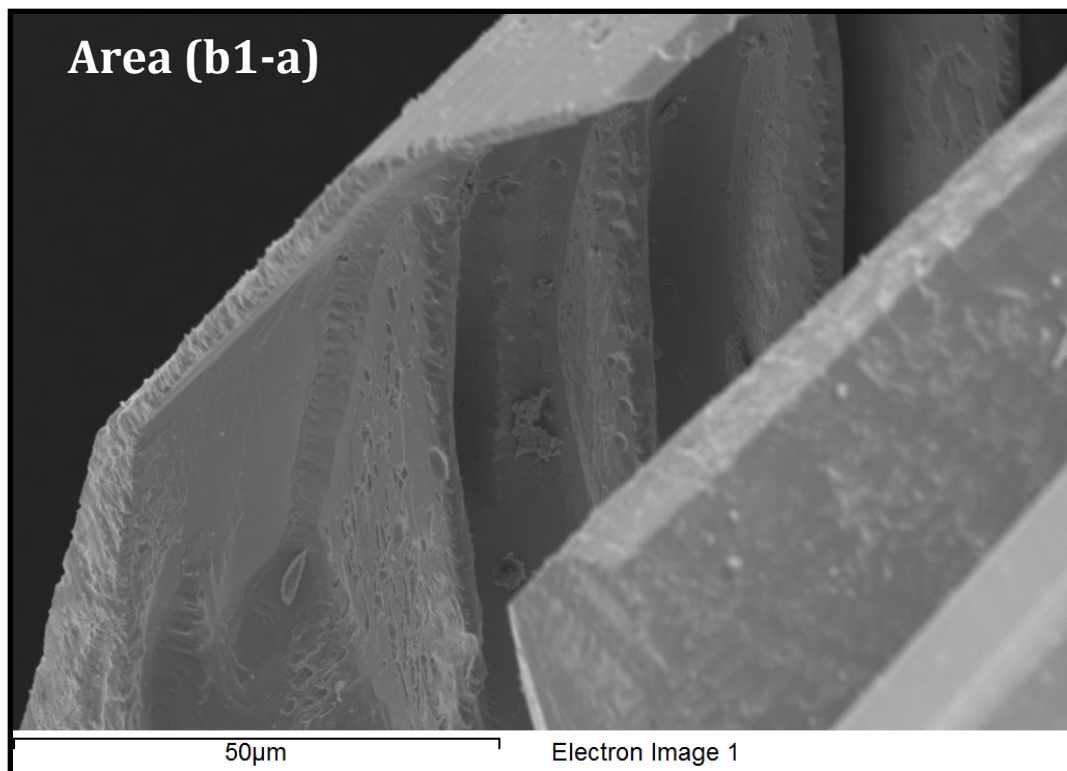


Figure 7.43: SE image of area **(b1-a)** from Figure 7.42.

Figure 7.44 provides an image of area (c), showing the edge of a group of connected platelets. Figure 7.45 provides a closer view of area (c1) from 7.44, and light surface etching is visible. Figure 7.46 provides a high resolution SE image of area (c1-1), and the etching is very shallow, on the order of $\sim 1 \mu\text{m}$. Several EDS spectra were obtained (Figures 7.47) and the surfaces are essentially pure uranium, speckled with tiny particles which are possibly oxidized uranium. Very shallow ridges are apparent in the edge of the crystal, and visible in Figures 7.44 through 7.46. Figure 7.48 shows a blocky, pentagonal crystal from area (d) of Figure 7.37. This crystal appears to be growing at a right angle to the rhomboidal platelets below it. A shallow cavity is visible in the top surface. Based on the planar appearance of the cavity, and the other features observed in this sample, it could be hypothesized that this seemingly-solid uranium crystal may also contain significant internal cavities.

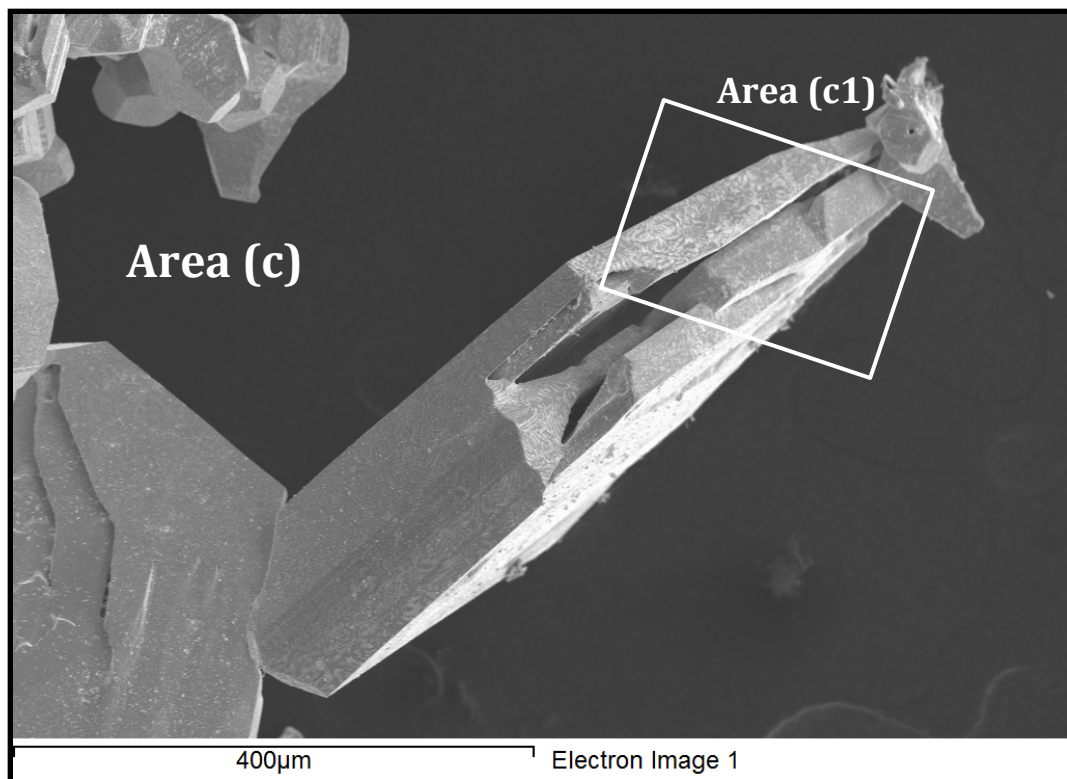


Figure 7.44: SE image of area (c) from Figure 7.37.

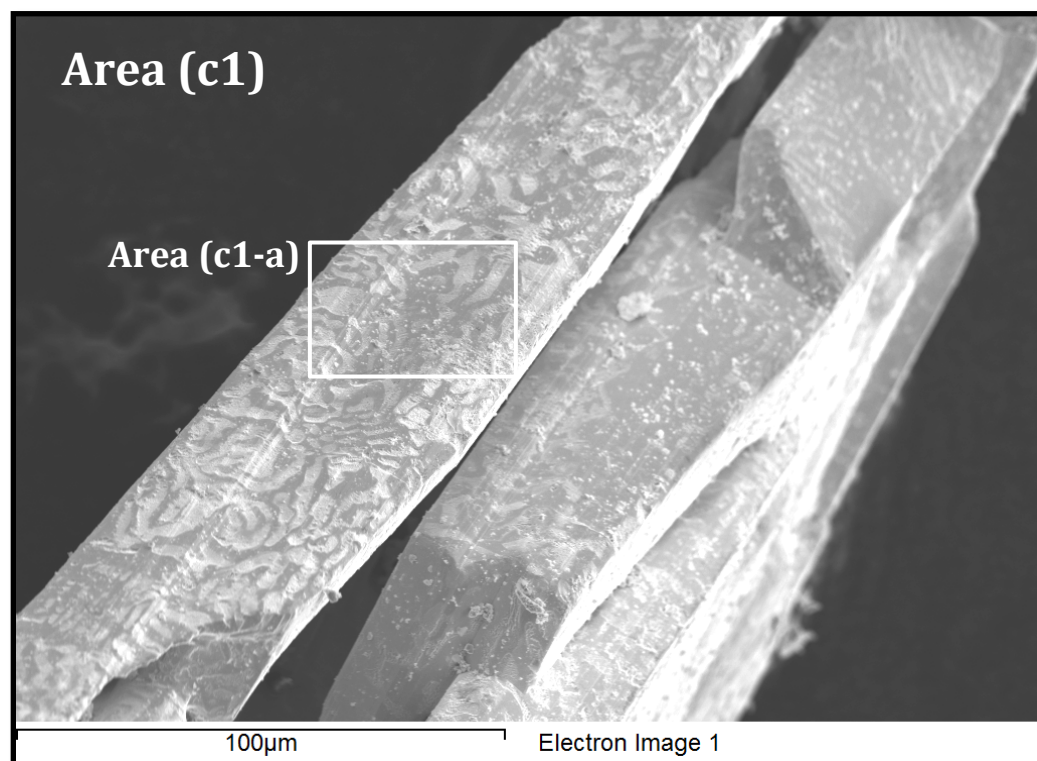


Figure 7.45: SE image of area (c1) from Figure 7.44.

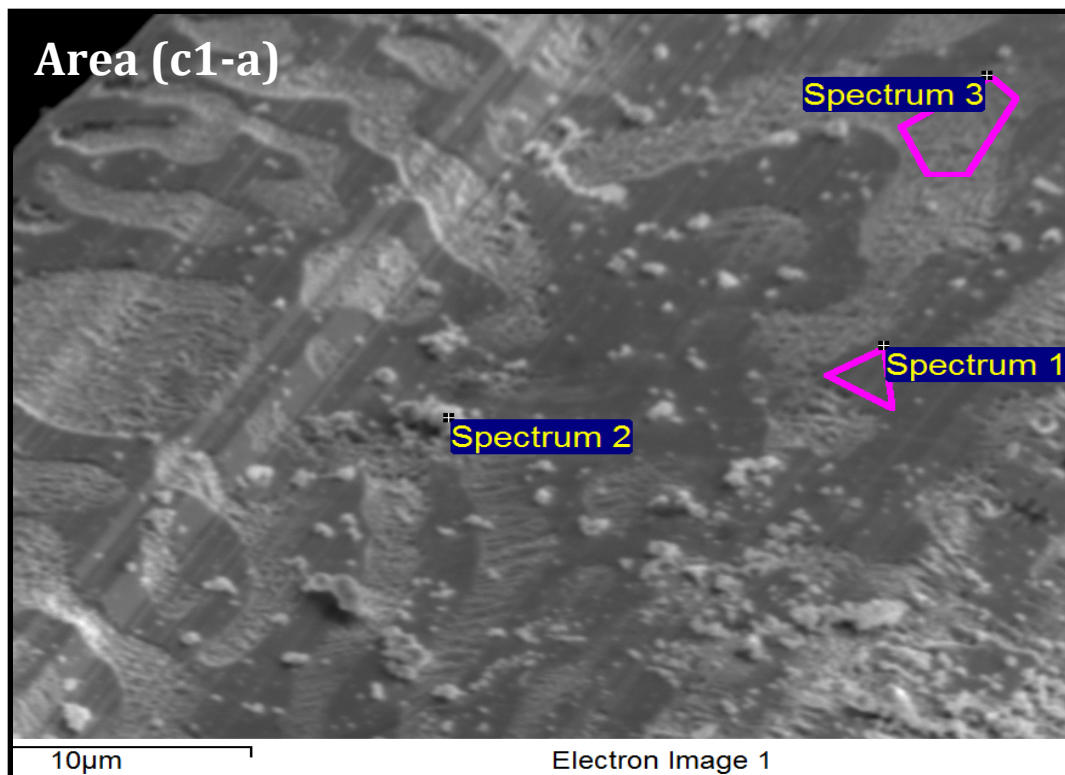


Figure 7.46: SE image of area (c1-a) from Figure 7.45 of uranium dendrite from 25mV overpotential.

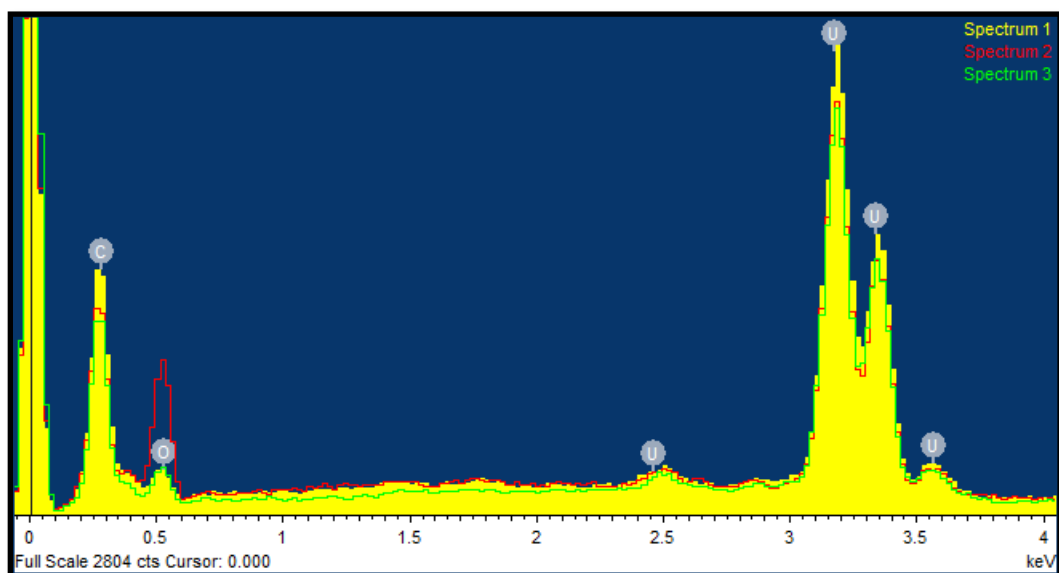


Figure 7.47: EDS spectrum of points from Figure 7.46.

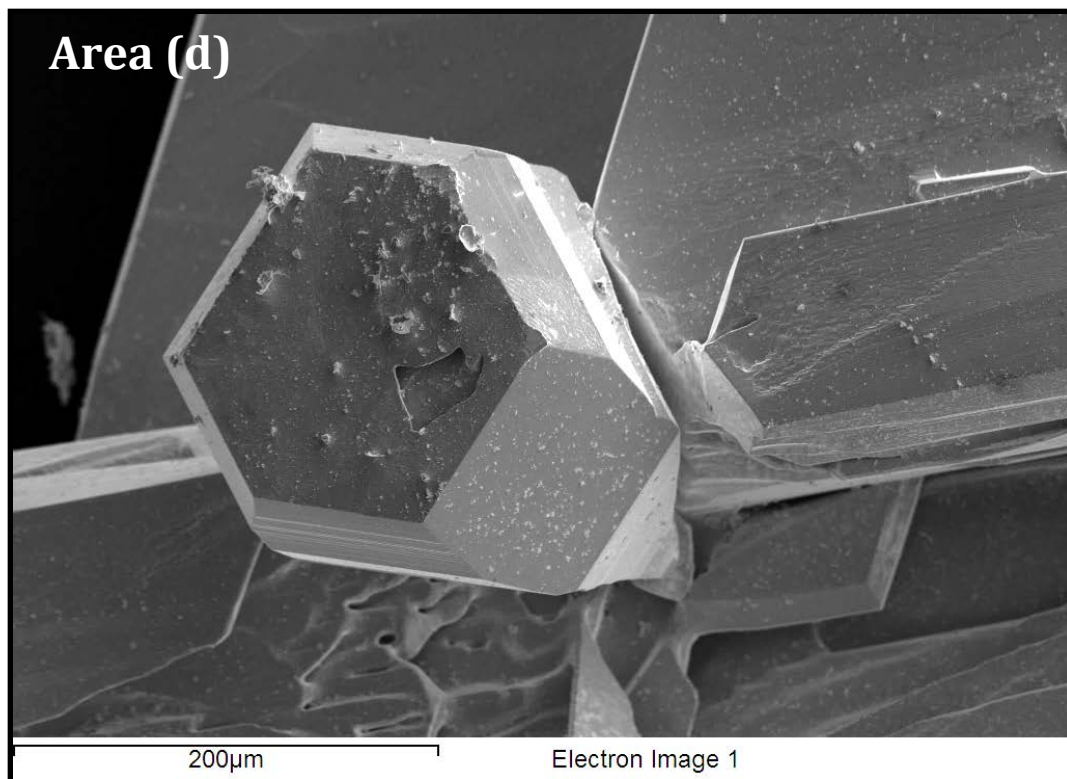


Figure 7.48: SE image of area **(d)** from 7.37 of uranium dendrite from 25 mV overpotential.

Figure 7.49 provides another overview image from the far edge of Figure 7.37. More crystals comprised of rhomboidal platelets and a few blocky clusters can be seen. Figure 7.50 is an SE image of area (e); shallow, thin, and straight ribs can be seen growing out of the lower platelet. Figure 7.51 provides a similar view using BSE; only a few lower-atomic weight particles are evident on the surface. Figure 7.52 is another area on the metallurgical mount, showing familiar rhomboidal platelets and a few clusters of blocky crystals. Areas (f) and (g) are being labeled as a key on the image. Figure 7.53 is an SE image of area (f) showing a cluster of small, blocky crystals while Figure 7.54 displays an SE image of area (g) showing another example of thin, straight, and regularly-spaced internal structure.

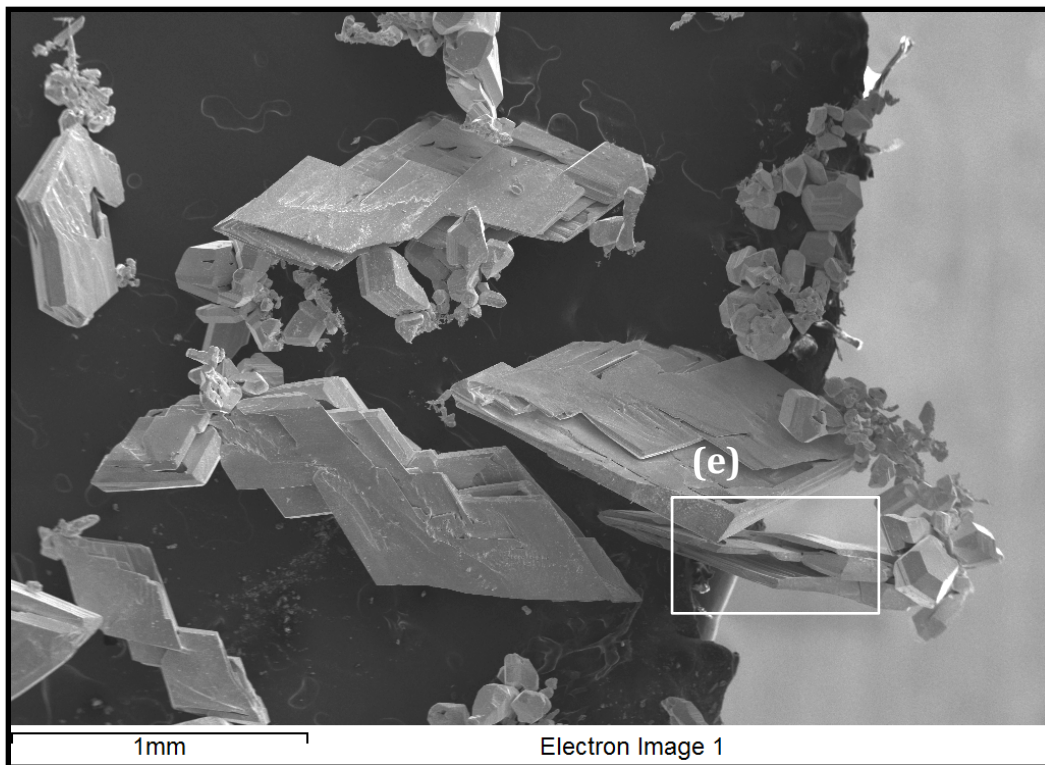


Figure 7.49: SE image of 25 mV uranium dendrites.

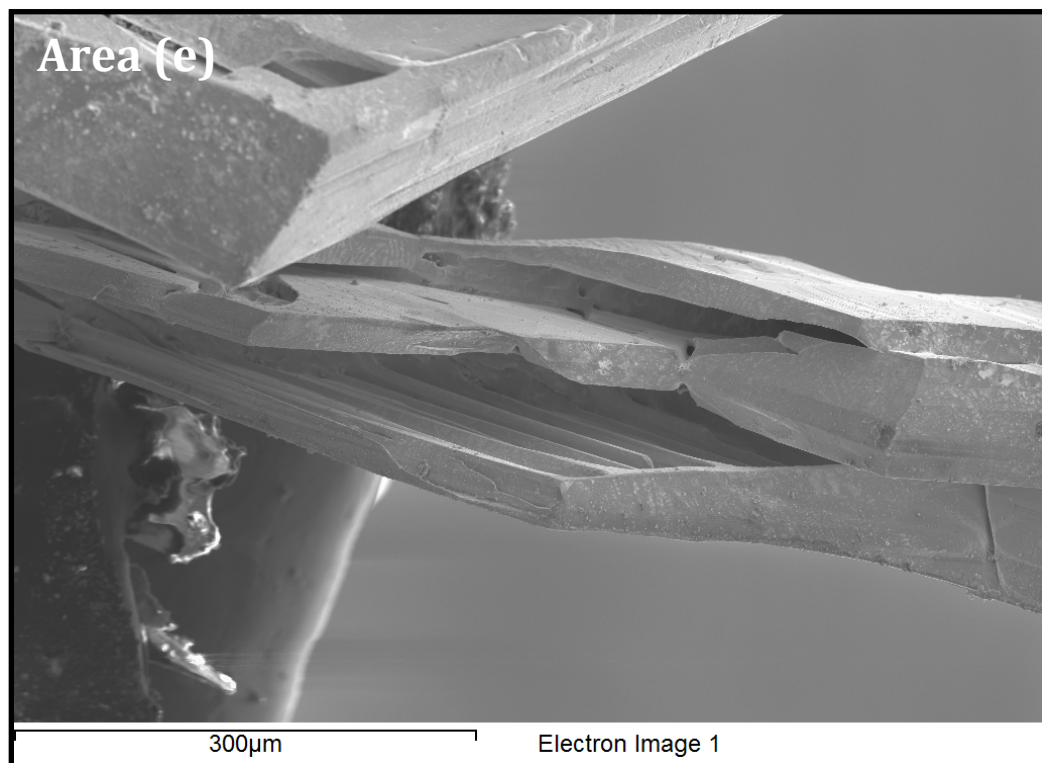


Figure 7.50: SE image of area (e) from Figure 7.49.

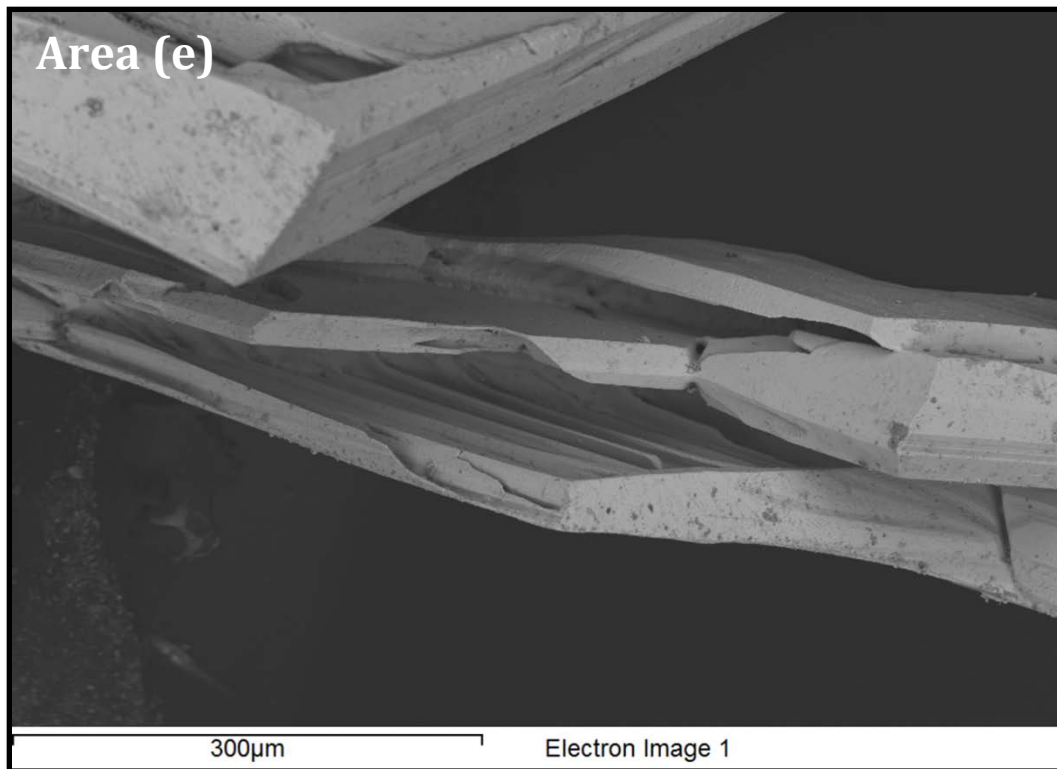


Figure 7.51: BSE image of area (e) from Figure 7.50.

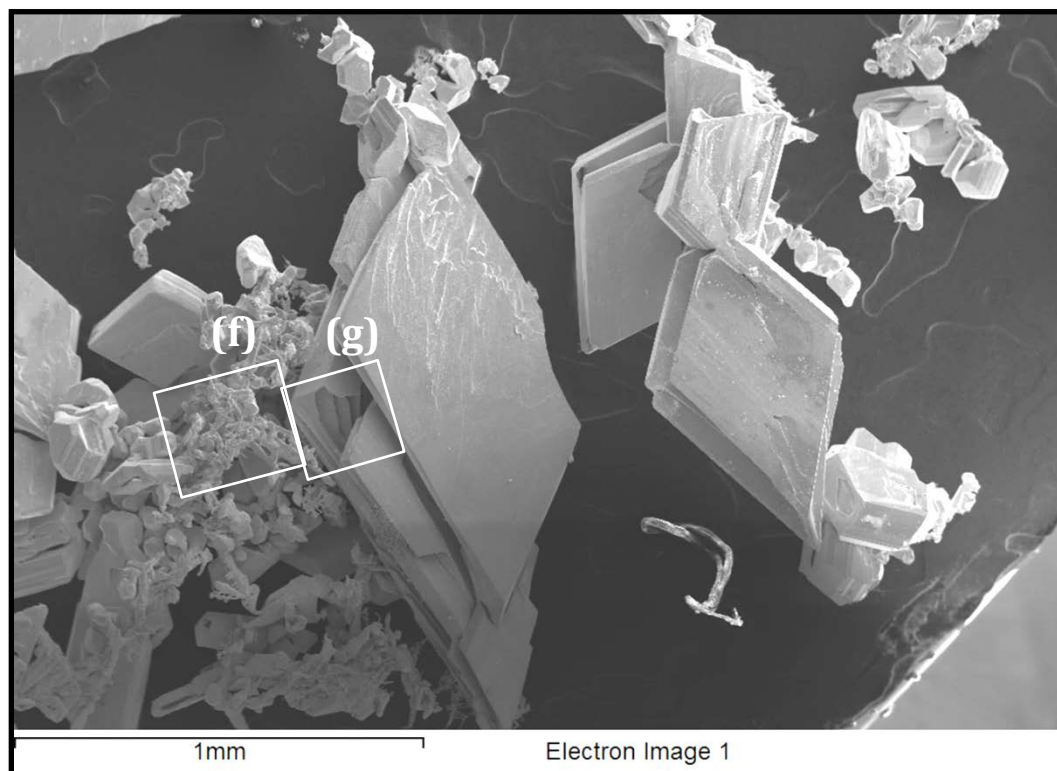


Figure 7.52: SE image of 25 mV uranium dendrites and key to areas (f) and (g).

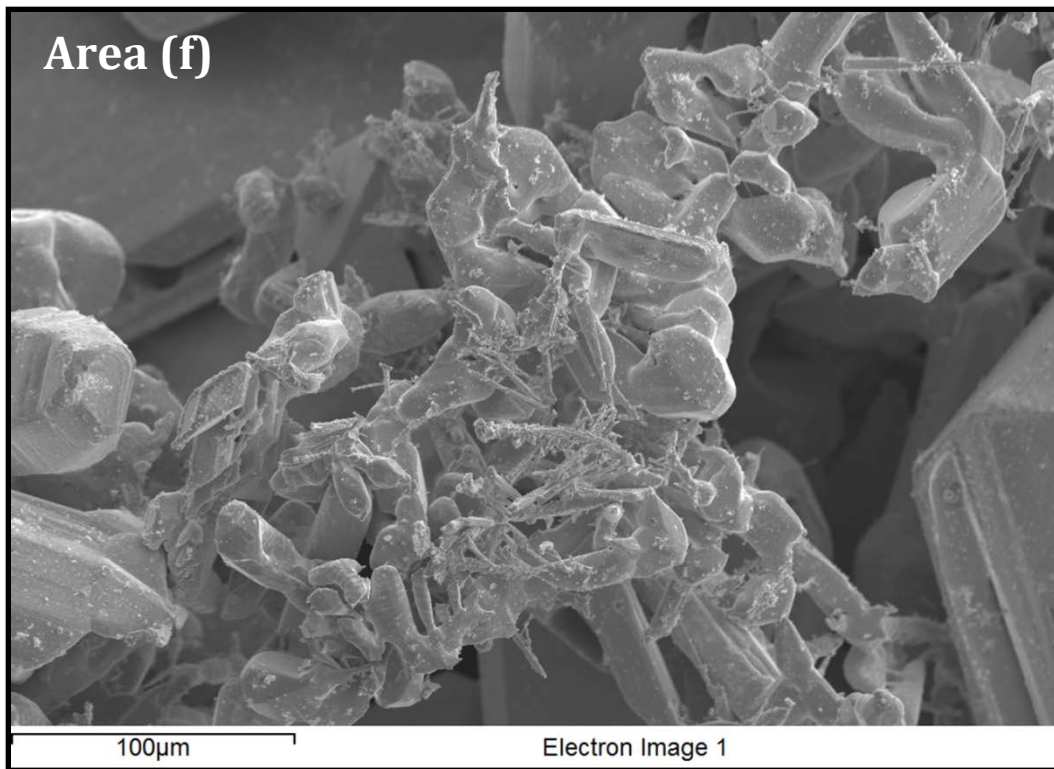


Figure 7.53: SE image of area **(f)** from Figure 7.52.

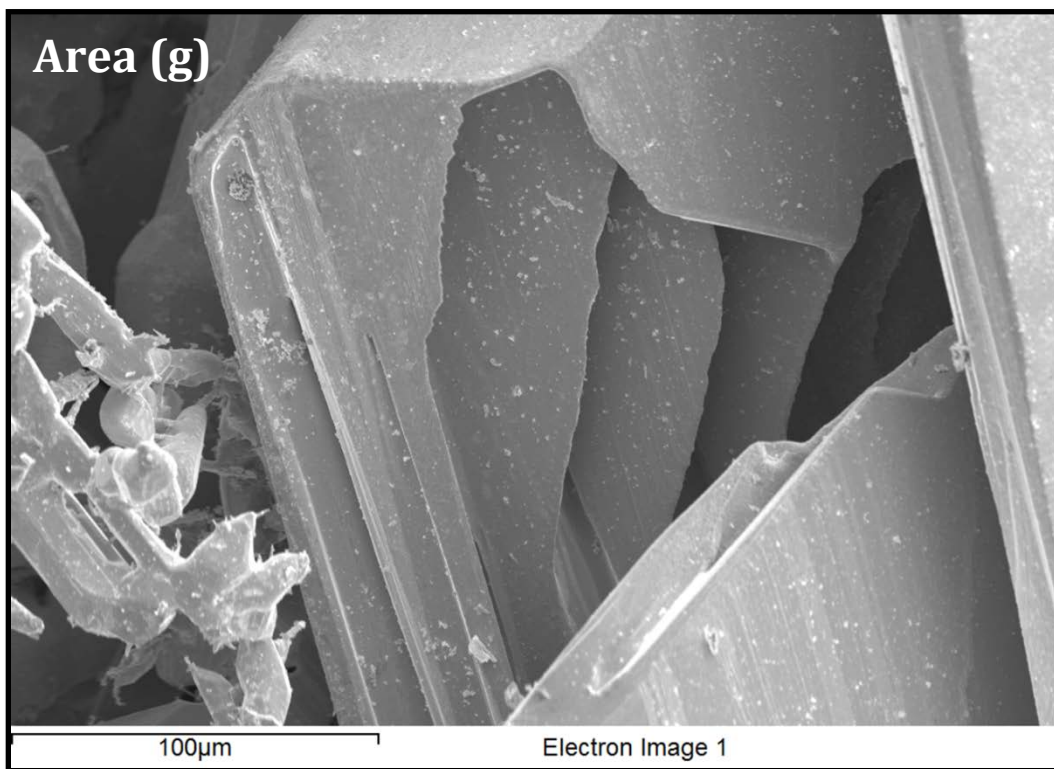


Figure 7.54: SE image of area **(g)** from Figure 7.52.

7.2.4 Discussion of the Electrochemistry of Uranium

An evaluation of the uranium electrochemistry was performed. Equilibrium potential, cyclic voltammetry, and diffusion coefficients were comparable with similar studies. Here, exchange current density, i_0 , was measured with a uranium rod and found to be identical for 1 mol% UCl_3 and 1 mol% UCl_3 - 1 mol% CeCl_3 solutions in LiCl-KCl eutectic at 773 K. However, i_0 was observed to increase nearly linearly with uranium concentration. The measured i_0 values were comparable to those measured by some researchers, but lower than some studies.

Dendrite samples were produced from a LiCl-KCl - 1 mol% UCl_3 solution at three overpotentials relative to open circuit potential for a uranium rod. These samples were washed, mounted, and inspected via SEM. Challenges with uranium corrosion from the water wash solution were observed, and may be a consequence of a hydrolysis reaction. The corrosion seemed to be reduced with a larger water volume, gentle mixing, and a careful decision when to terminate water wash. Oxidation of the washed uranium dendrites was also observed. This seems to have been resolved by careful preparations to allow immediate transfer of the washed dendrites out of the glovebox and into the SEM vacuum chamber.

Previous studies have not explored the link between deposition potential and deposit morphology. In this study, little or no evidence of porosity was observed in uranium produced at the higher overpotential conditions, whereas considerable internal structure was observed in uranium deposits produced at low overpotentials. The low overpotential condition generated deposits similar to those observed in previous studies of uranium electrorefining.

The uranium deposited at 450 mV overpotential largely formed as columnar fibers, with blunt blocky tips, often with several adjacent fibers lying adjacent in a larger composite column. Surface texture was difficult to discern due to a surface oxidation and pitting. The uranium deposited at 150 mV overpotential was largely composed of sword-like fibers with angled, pointed tips and rows of porosity down the length. A smaller quantity of regularly-branched planar dendrites and irregular, planar maple-leaf dendrites were also observed. The uranium deposited at 25 mV overpotential was primarily composed of stacks of rhomboidal platelets whose volume may be largely hollow cavities.

7.3 Uranium Dendrite Samples in the Presence of Cerium

7.3.1 Overview of Sampling and Analysis

Uranium deposits were produced in molten LiCl-KCl eutectic at a range of electrochemical overpotentials relative to the open circuit potential of the uranium rod anode, at a series of salt concentrations. Samples were harvested and analyzed for salt and cerium concentrations. Table 7.3 summarizes the 50 samples that were produced and analyzed. The four samples obtained at 0.01 mole fraction UCl_3 and 0.01 mole fraction CeCl_3 were the first sample set obtained; following these analyses, it was decided to take the time to obtain duplicate samples for most, as well as very low overpotential samples to increase the clarity of the total data set.

Table 7.3: Dendrite samples obtained for this study.

Uranium Concentration (X)	Deposition overpotential, η^1 (vs $E^*_{\text{U(III)/U}}$)	Cerium Concentration (X)	
		0.01	0.06
0.0033	-25 mV	X	X
	-150 mV	X, X	X, X
	-300 mV	X, X	X, X
	-450 mV	X, X	X, X
	-525 mV	X, X	X, X
0.01	-25 mV		X, X
	-150 mV	X	X, X
	-300 mV	X	X, X
	-450 mV	X	X, X
	-525 mV	X	X, X
0.06	-25 mV	X	X
	-150 mV	X, X	X, X
	-300 mV	X, X	X, X
	-450 mV	X, X	X, X
	-525 mV	X, X	X, X

¹ Apparent standard potential of U is -2.514 vs Cl_2/Cl^- . The apparent standard potential of Ce is -3.08 vs Cl_2/Cl^- .

Samples were produced as described in Chapter 4 on window electrodes shown in Figure 4.8, with a typical sample seen previously in Figure 4.12. Samples harvested for analysis were

generally between 0.25 and 1.0 grams of material. Two samples of sufficient mass were sometimes harvested from a single deposition, while in other cases (especially depositions at low overpotentials) duplicate samples were obtained from two consecutive deposits at the same condition. The samples were analyzed as previously described in Chapter 4. Figure 7.55 shows the sample set for condition 0.33 mol% UCl_3 and 6 mol% CeCl_3 at the stages of the process. Image (c) of Figure 7.55 is a sample produced at 450 mV overpotential; the long metallic fibers seen in Section 7.2 are evident.

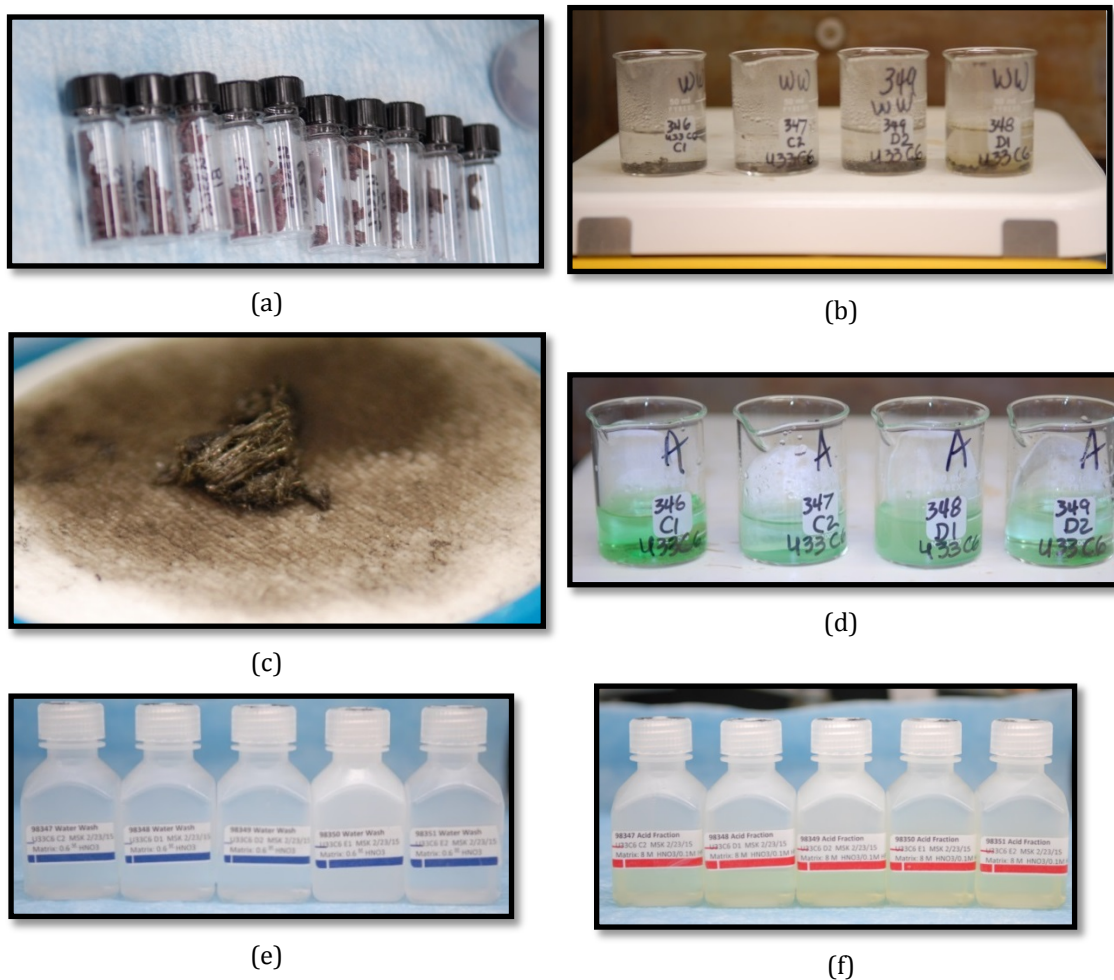


Figure 7.55: Photographs of uranium dendrite samples from 0.33 mol% UCl_3 and 6 mol% CeCl_3 (a) harvested samples, (b) salt removal by water wash, (c) filtering of solids from water wash for 450mV sample, (d) acid dissolution of solids, (e) water wash solution for mass spectrometry, (f) acid fraction for mass spectrometry.

7.3.2 Results and Discussion

Table 7.4 provides data on the target concentrations for the test conditions. The test conditions are defined in molar concentrations, due to the potential importance of species activity to influence contamination. Table 7.4 provides a crosswalk from the molar concentrations to wt% for each electrolyte solution. It also provides calculated values of Ce/Li ratio and K/Li ratio for comparison with experimental data.

Table 7.4: Target test conditions, in mol% and wt%.

	0.33m% UCl ₃ 1.0m% CeCl ₃	0.33m% UCl ₃ 6.0m% CeCl ₃	1.0m% UCl ₃ 1.0m% CeCl ₃	1.0m% UCl ₃ 6.0m% CeCl ₃	6.0m% UCl ₃ 1.0m% CeCl ₃	6.0m% UCl ₃ 6.0m% CeCl ₃
Target [U], mol%	0.33	0.33	1.0	1.0	6.0	6.0
Target [Ce], mol%	1.0	6.0	1.0	6.0	1.0	6.0
Target [U], wt%	1.94	1.67	5.68	4.91	27.53	24.43
Target [Ce], wt%	4.20	21.67	4.07	21.08	3.28	17.48
Calc. Ce/Li (g/g)	0.352	2.222	0.354	2.238	0.373	2.365
Calc. K/Li (g/g)	4.05					

Table 7.5 and Figure 7.56 provide representative information regarding current observed during the growth of dendrite sample from each overpotential for one of the electrolyte conditions. It can be seen that current increases with applied overpotential and with increasing time of deposition as the electrode surface area increases.

Table 7.5: Average observed current during uranium dendrite growth.

Over-potential, η	1.0m% UCl ₃ 6.0m% CeCl ₃
25 mV	-0.048 A
150 mV	-0.317 A
300 mV	-0.506 A
450 mV	-1.138 A
525 mV	-1.424 A

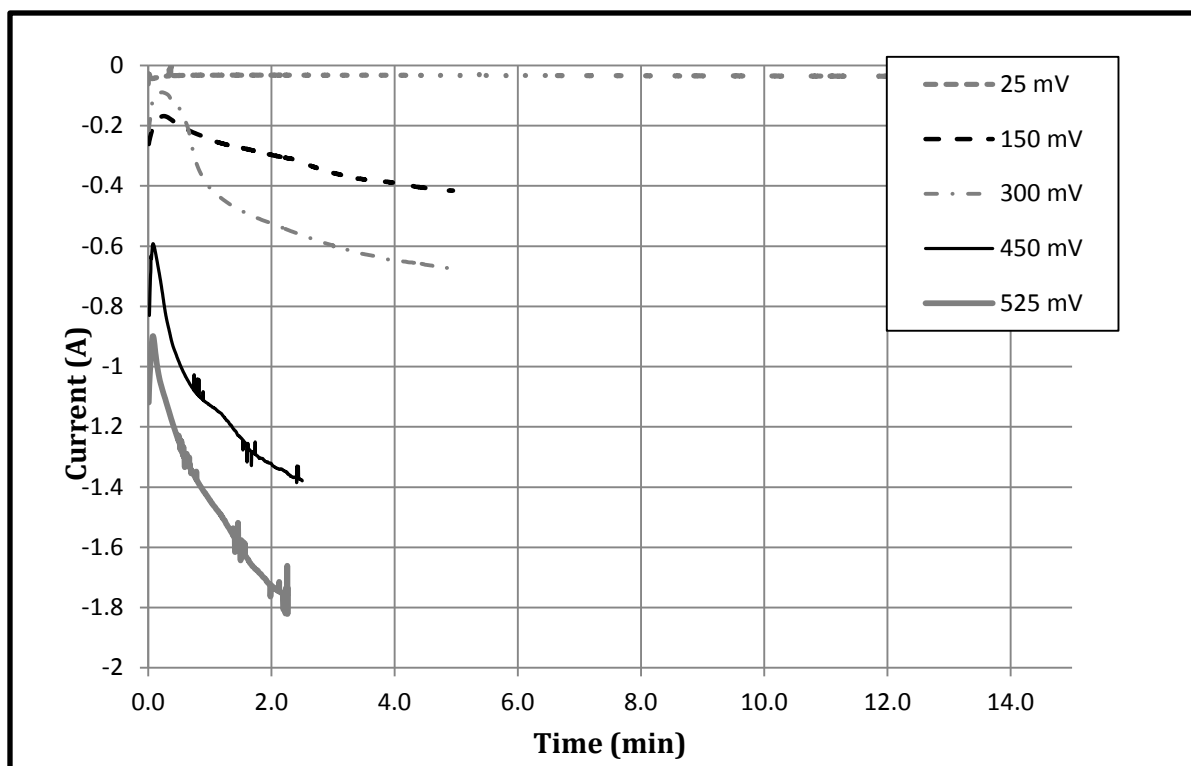


Figure 7.56: Observed currents during uranium dendrite growth for the electrolyte condition of 1.0 and 6.0 mol% UCl_3 and CeCl_3 , respectively.

Table 7.6 summarizes analytical results for electrolyte samples of the tested conditions. Analytical data is typically reported in units of μg per gram of sample by convention. While uranium and cerium were measured by two methods, the ICP-MS measurement is generally considered to be higher accuracy. Measured cerium/lithium ratios are generally within about 10% of target values, with the exception of analysis 97130 and 97573. Analysis 97130 had a target of 1 mol% UCl_3 and 1 mol% CeCl_3 . The data for salt from the dendrite water wash seems (Analysis 97131) is more believable. Analysis 97573 had a target salt of 1 mol% UCl_3 and 6 mol% CeCl_3 . In this case, the measured Ce/Li ratio is only $\sim 30\%$ of target value, whereas again the multiple analyses from the water wash are consistent with expected values. This sample series was impacted by a laboratory shutdown while the samples were in the water wash step. Samples remained in contact with water for ~ 48 hours instead of the desired ~ 1 hour duration. This may be the cause for outlying data from this test series.

Table 7.6: Measured composition of electrolyte samples, $\mu\text{g/g}$ with error at 2σ reported as 5% unless noted.

	0.33m% UCl_3 1.0m% CeCl_3	0.33m% UCl_3 6.0m% CeCl_3	1.0m% UCl_3 1.0m% CeCl_3	1.0m% UCl_3 6.0m% CeCl_3	6.0m% UCl_3 1.0m% CeCl_3	6.0m% UCl_3 6.0m% CeCl_3
Sample ID	98332	98342	97130	97573	98312	98322
Sample Mass	0.7500 g	1.1208 g	0.5056 g	0.7269 g	1.3053 g	0.9620 g
ICP-MS						
Uranium	12300	16600	94700	20906	154000	150000
Cerium	16400	124000	24000	45800	14100	86400
ICP-AES						
Uranium*	11300 \dagger	16300 \dagger	89600	23500	159000 \dagger	150000 \dagger
Cerium*	15400 \dagger	119000 \dagger	26400	44600	13500 \dagger	83200 \dagger
Lithium	71800	58300	59500	65400	59600	52100
Potassium	260000	205000	240000	237000	203000	170000
Ce/Li (g/g)	0.228	2.127	0.403	0.700	0.237	1.658
Ce/K (g/g)	0.06	0.60	0.10	0.19	0.07	0.51
K/Li (g/g)	3.62	3.52	4.03	3.62	3.41	3.26

* Uranium and Cerium analysis by ICP-MS have lower uncertainty, ICP-AES values obtained only for measurement QA

$\dagger \pm 10\%$

Tables A1, A2, and A3 in the Appendix provide the raw analytical data for the dendrite samples. Relevant data has been harvested and analyzed to produce the following Tables 7.7 through 7.12. Table 7.7 provides a summary of cerium/lithium ratios from the salt that was removed during the water wash. As with Table 7.6, the average ratios for each electrolyte condition are generally within about 10% of target values, with a standard deviation between 5 and 10%.

Table 7.7: Summary of cerium/lithium ratio from dendrite water washes.

Over-potential, η	0.33m% UCl_3 1.0m% CeCl_3		0.33m% UCl_3 6.0m% CeCl_3		1.0m% UCl_3 1.0m% CeCl_3		1.0m% UCl_3 6.0m% CeCl_3		6.0m% UCl_3 1.0m% CeCl_3		6.0m% UCl_3 6.0m% CeCl_3	
	25 mV	0.366	n/a	2.502	n/a	n/a	2.277	2.310	0.318	n/a	1.955	n/a
150 mV	0.370	0.363	1.940	2.057	0.242	1.577	1.459	0.315	0.356	2.193	2.250	
300 mV	0.389	0.376	2.332	2.127	n/a	1.794	1.921	0.350	0.352	2.359	2.219	
450 mV	0.418	0.400	1.946	2.186	n/a	2.237	2.288	0.291	0.335	2.256	2.351	
525 mV	0.378	0.384	2.442	2.791	n/a	2.324	2.335	0.312	0.316	2.154	2.205	
Avg	0.383		2.258		0.242	2.052		0.327		2.216		
Std Dev	0.018		0.284		n/a	0.337		0.022		0.119		

As a tool to evaluate the value of the water wash data, the measured ratios of potassium/lithium are summarized in Table 7.8. It is seen that in all cases, the potassium/lithium ratios are within 10% of both the theoretical and measured values (as seen in Tables 7.4 and 7.6) with standard deviations of the data set at 5% or lower.

Table 7.8: Summary of potassium/lithium ratio from dendrite water washes.

Over-potential, η	0.33m% UCl ₃ 1.0m% CeCl ₃		0.33m% UCl ₃ 6.0m% CeCl ₃		1.0m% UCl ₃ 1.0m% CeCl ₃		1.0m% UCl ₃ 6.0m% CeCl ₃		6.0m% UCl ₃ 1.0m% CeCl ₃		6.0m% UCl ₃ 6.0m% CeCl ₃	
	25 mV	3.808		3.788		n/a	4.108	4.139	3.423		3.397	
150 mV	3.791	3.767	3.582	3.662	4.017	3.759	3.668	3.543	3.646	3.622	3.791	
300 mV	3.833	3.761	3.778	3.696	n/a	3.821	4.142	3.642	3.568	3.771	3.656	
450 mV	3.886	3.826	3.612	3.647	n/a	4.118	4.080	3.524	3.551	3.645	3.789	
525 mV	3.750	3.835	3.743	3.767	n/a	4.304	4.278	3.581	3.515	3.600	3.657	
Avg	3.806		3.697		4.017	4.042		3.555		3.659		
Std Dev	0.044		0.076		n/a	0.217		0.068		0.123		

Table 7.9 provides a summary of cerium content normalized to uranium, measured in the dissolved uranium dendrite samples following removal of external salt by the water wash. The values are seen to range from a few hundred μg Ce per g U to nearly two weight percent (1.79 wt% from the 525 mV condition of 1 mol% UCl₃-6 mol% CeCl₃). It is again noticeable that the tests with electrolyte condition of 1 mol% UCl₃-6 mol% CeCl₃ appear to not fit well with other data. Table 7.10 lists the estimated salt-based cerium content for each dendrite sample. The quantity of salt-based cerium was computed by multiplication of the average cerium/lithium ratio for each tested electrolyte condition (from Table 7.7) with the measured normalized quantity of lithium in the dissolved dendrite (acid fraction of the analyses). From inspection of Table 7.9 and Table 7.10, it is seen that generally a significant fraction of measured cerium is the result of encapsulated salt. The average values for each electrolyte condition are presented in Table 7.11. For many test conditions, about half of the cerium present is estimated to be salt species, and with essentially all cerium present as salt for test conditions with 6 mol% uranium. Table 7.12 shows the fraction of the dendrite weight what was estimated to be residual salt, based on the lithium and potassium analysis numbers. The fraction of mass attributed to salt is significant, and noticeably greater than that observed in the Mk-IV dendrites discussed in Chapter 6. However, the typical sample size for these dendrites was approximately an order of magnitude smaller than those harvested from the electrorefiner cathodes.

Table 7.9: Total cerium content in dendrite samples, data normalized to $\mu\text{g Ce}$ per gram U.

Over-potential, η	0.33m% UCl_3 1.0m% CeCl_3		0.33m% UCl_3 6.0m% CeCl_3		1.0m% UCl_3 1.0m% CeCl_3		1.0m% UCl_3 6.0m% CeCl_3		6.0m% UCl_3 1.0m% CeCl_3		6.0m% UCl_3 6.0m% CeCl_3	
	25 mV	355	n/a	1733	n/a	n/a	1770	1922	79	n/a	734	n/a
150 mV	1300	1696	1846	1495	171	8127	4781	147	565	400	515	
300 mV	1212	1274	1412	1263	160	12686	7555	190	310	3690	463	
450 mV	1045	723	1412	1852	182	17251	9356	145	92	795	746	
525 mV	809	527	2580	3061	79	17941	12826	103	133	668	825	

Table 7.10: Salt-based cerium content in dendrite samples, derived from measured lithium content. Data normalized to $\mu\text{g Ce}$ per gram U.

Over-potential, η	0.33m% UCl_3 1.0m% CeCl_3		0.33m% UCl_3 6.0m% CeCl_3		1.0m% UCl_3 1.0m% CeCl_3		1.0m% UCl_3 6.0m% CeCl_3		6.0m% UCl_3 1.0m% CeCl_3		6.0m% UCl_3 6.0m% CeCl_3	
	25 mV	245	n/a	988	n/a	n/a	unkn	135	65	n/a	779	n/a
150 mV	317	581	1051	1235	76	3872	546	160	620	397	214	
300 mV	445	422	299	433	64	7825	4646	191	333	4031	484	
450 mV	339	224	339	801	70	8795	4920	130	78	860	741	
525 mV	332	unkn	1707	1587	unkn	16237	7447	107	156	613	850	

Table 7.11: Average fraction of salt-based cerium for each electrolyte test condition.

0.33m% UCl_3 1.0m% CeCl_3	0.33m% UCl_3 6.0m% CeCl_3	1.0m% UCl_3 1.0m% CeCl_3	1.0m% UCl_3 6.0m% CeCl_3	6.0m% UCl_3 1.0m% CeCl_3	6.0m% UCl_3 6.0m% CeCl_3
38%	49%	41%	49%	100%	96%

Table 7.12: Estimated mass of occluded salt in dendrites, units of wt% of dendrite.

Over-potential, η	0.33m% UCl_3 1.0m% CeCl_3		0.33m% UCl_3 6.0m% CeCl_3		1.0m% UCl_3 1.0m% CeCl_3		1.0m% UCl_3 6.0m% CeCl_3		6.0m% UCl_3 1.0m% CeCl_3		6.0m% UCl_3 6.0m% CeCl_3	
	25 mV	1.9	n/a	2.3	n/a	n/a	0.1	0.1	0.8	n/a	2.3	n/a
150 mV	4.0	6.6	3.2	2.1	0.6	2.7	0.7	1.5	4.0	1.3	1.4	
300 mV	4.7	4.3	3.1	6.4	0.4	4.9	2.9	2.1	2.9	5.1	1.3	
450 mV	3.6	2.4	5.1	4.0	0.5	6.3	3.3	1.7	2.1	1.9	2.3	
525 mV	7.5	1.3	2.6	3.9	0.7	10.6	5.2	1.7	1.6	2.2	1.9	
Avg	4.0		3.6		0.5	4.1		2.0		2.2		
Std Dev	2.1		1.4		0.1	3.2		0.9		1.2		

Table 7.13 presents the final estimated cerium content in the uranium dendrite samples. Cerium contents ranging from a few hundred to a thousand $\mu\text{g Ce}$ per g U are found for the test conditions with 0.33 mol% UCl_3 ; roughly 100 $\mu\text{g Ce}$ per g U is found for 1.0 mol% uranium, and essentially zero cerium content is found in samples produced with 6.0 mol% uranium. Table 7.14 presents the average cerium content found in each test condition. It is seen that the average cerium content approaches 1000 ppm for the electrolyte condition with the widest disparity between uranium and cerium activity (0.33 mol% UCl_3 -6 mol% CeCl_3).

Table 7.13: Final estimated cerium content in dendrite samples. Data normalized to μg Ce per gram U. Compounded error estimates derived from reported 2σ error of analyses.

Over potential, η	0.33m% UCl_3 1.0m% CeCl_3		0.33m% UCl_3 6.0m% CeCl_3		1.0m% UCl_3 1.0m% CeCl_3	1.0m% UCl_3 6.0m% CeCl_3		6.0m% UCl_3 1.0m% CeCl_3		6.0m% UCl_3 6.0m% CeCl_3	
	25 mV	110 ± 35	n/a	745 ± 157	n/a	n/a	unkwn	1787 ± 137	14 ± 9	n/a	-44 ± 94
150 mV	983 ± 97	1115 ± 133	795 ± 168	260 ± 162	95 ± 14	4255 ± 693	4234 ± 342	-13 ± 19	-55 ± 74	3 ± 49	300 ± 42
300 mV	768 ± 97	853 ± 99	1113 ± 104	830 ± 99	96 ± 13	4861 ± 1190	2909 ± 708	-1 ± 23	-23 ± 40	-341 ± 480	-21 ± 58
450 mV	706 ± 81	498 ± 56	1073 ± 105	1051 ± 154	112 ± 15	8455 ± 1504	4436 ± 824	15 ± 17	14 ± 10	-64 ± 103	5 ± 91
525 mV	476 ± 66	unkwn	873 ± 250	1474 ± 268	unkwn	1704 ± 2060	5379 ± 1173	-5 ± 13	-23 ± 18	55 ± 77	-25 ± 103

n/a – Sample was not taken

unkwn – Sample was obtained but unable to calculate, usually due to on quantity being below detection limits

Table 7.14: Average cerium content for each electrolyte test condition, units $\mu\text{g Ce per g U}$.

0.33m% UCl_3 1.0m% CeCl_3	0.33m% UCl_3 6.0m% CeCl_3	1.0m% UCl_3 1.0m% CeCl_3	1.0m% UCl_3 6.0m% CeCl_3	6.0m% UCl_3 1.0m% CeCl_3	6.0m% UCl_3 6.0m% CeCl_3
689	913	101	4225	-9	-15

Figures 7.57 through 7.61 provide a graphic summary of the residual cerium content in the samples from each electrolyte condition. While trends of cerium content with deposition potential may seem possible for some of the electrolyte conditions, there is no clear pattern when the graphic data from all test conditions are considered.

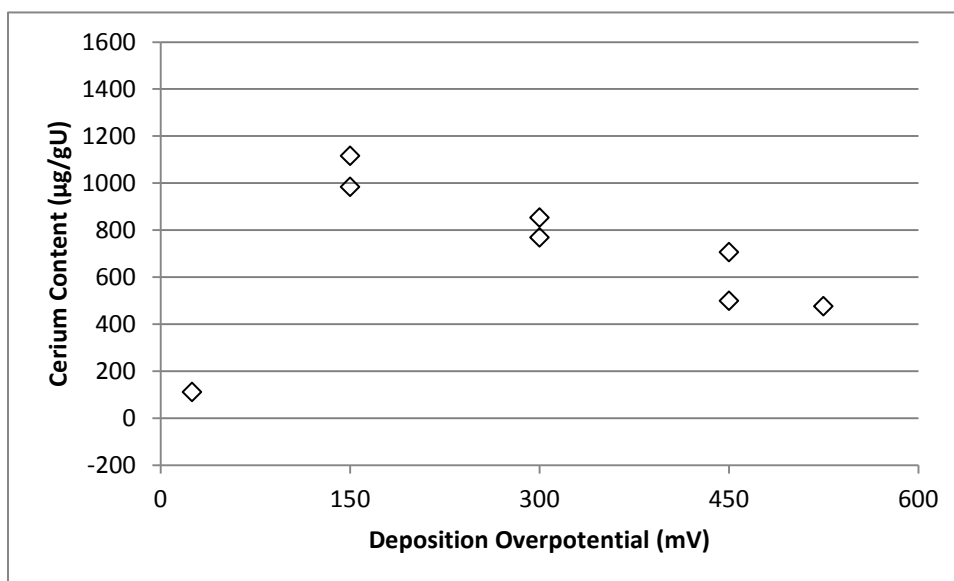


Figure 7.57: Residual cerium content ($\mu\text{g Ce/g U}$) found in uranium dendrites produced from electrolyte of 0.33 mol% UCl_3 and 1.0 mol% CeCl_3 in LiCl-KCl eutectic at 773 K.

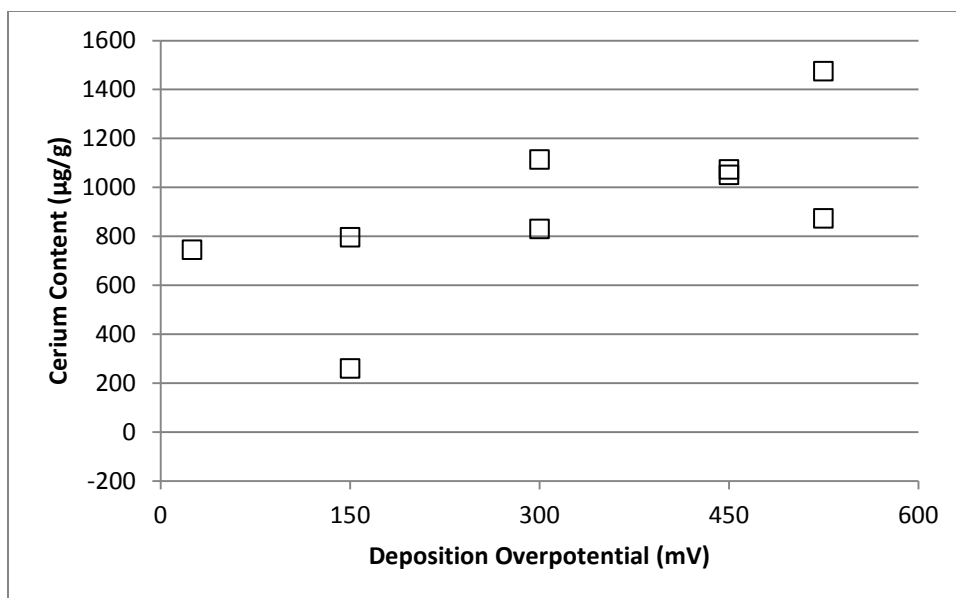


Figure 7.58: Residual cerium content ($\mu\text{g/g}$ U) found in uranium dendrites produced from electrolyte of 0.33 mol% UCl_3 and 6.0 mol% CeCl_3 in LiCl-KCl eutectic at 773 K.

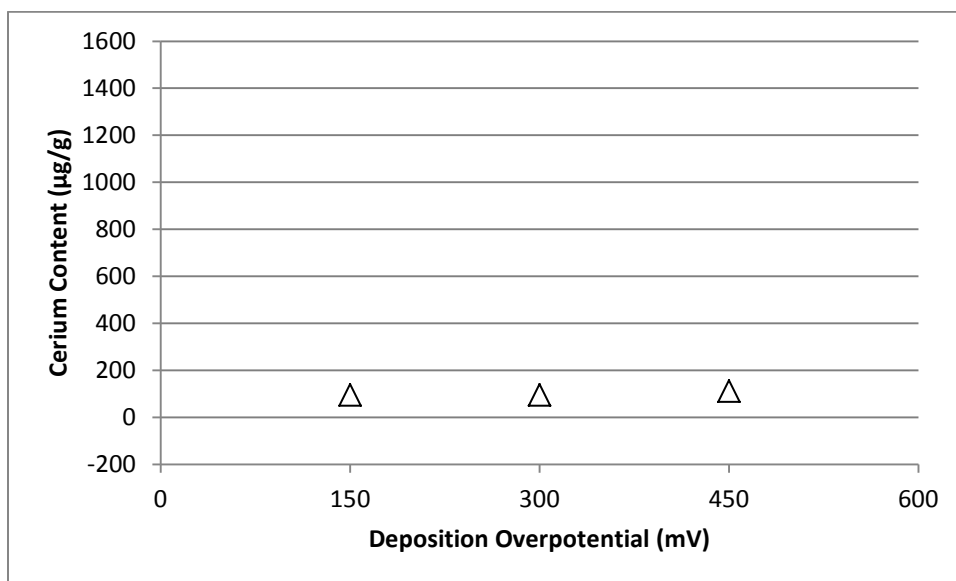


Figure 7.59: Residual cerium content ($\mu\text{g/g}$ U) found in uranium dendrites produced from electrolyte of 1.0 mol% UCl_3 and 1.0 mol% CeCl_3 in LiCl-KCl eutectic at 773 K.

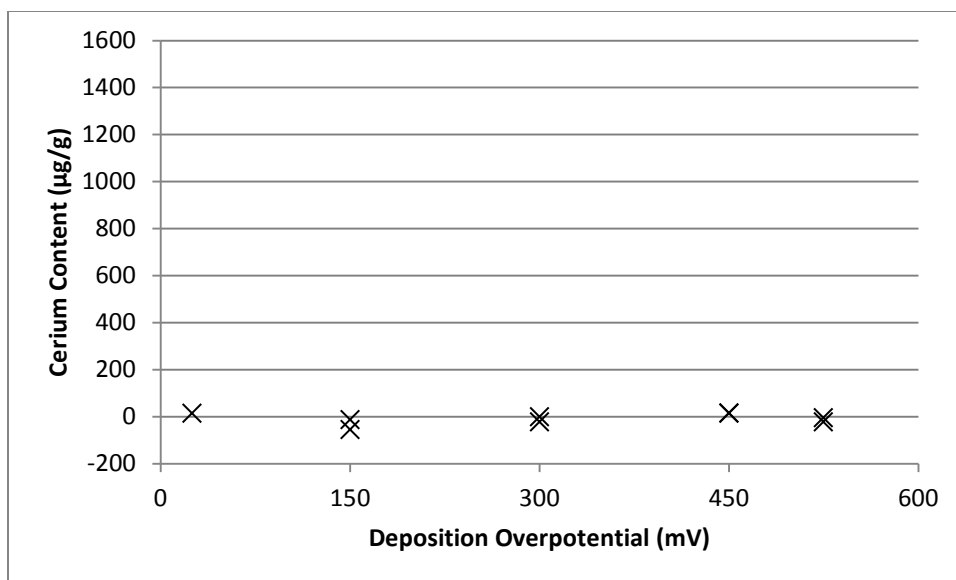


Figure 7.60: Residual cerium content ($\mu\text{g/g U}$) found in uranium dendrites produced from electrolyte of 6.0 mol% UCl_3 and 1.0 mol% CeCl_3 in LiCl-KCl eutectic at 773 K.

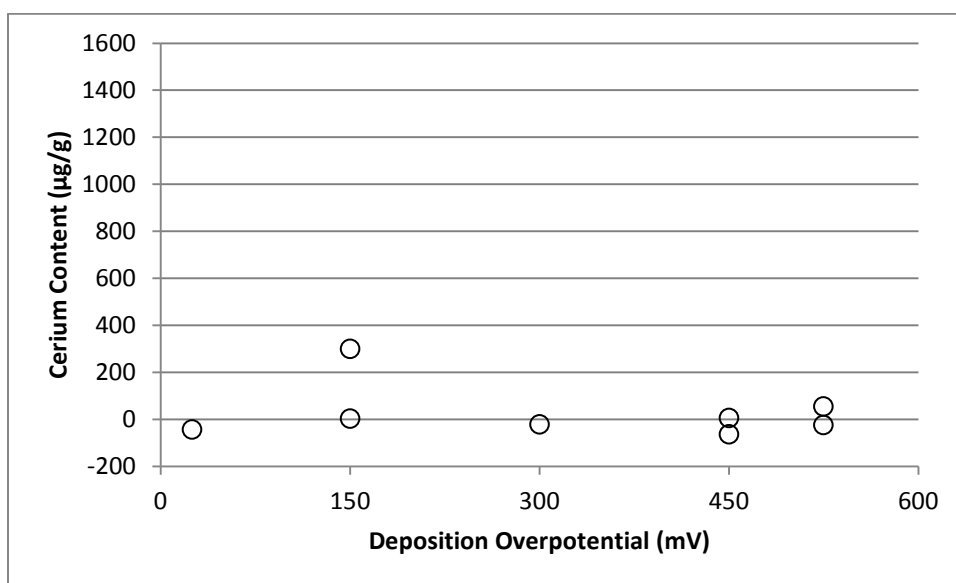


Figure 7.61: Residual cerium content ($\mu\text{g/gU}$) found in uranium dendrites produced from electrolyte of 6.0 mol% UCl_3 and 6.0 mol% CeCl_3 in LiCl-KCl eutectic at 773 K.

During the evaluation of the large set of experimental data, it was noted that potassium/lithium ratios of the salt occluded within dendrites were sometimes significantly different than the theoretical ratio for LiCl-KCl eutectic, and that measured in salt removed by water washing. Table 7.15 shows the potassium/lithium ratios found from salt within the dendrites. When compared with potassium/lithium ratios listed in the bottom row of Table 7.3

and Table 7.4 for theoretical and electrolyte samples, as well as those shown in Table 7.5 for water removed salt, the ratio are consistently very high. The solubility of each species is presented in Table 7.16. It is recommended that future investigations evaluate if the observed ratios are simply the impact of wash duration or the result of electrochemical processes.

Table 7.15: Summary of potassium/lithium ratios from dendrites.

	0.33m% UCl ₃ 1.0m% CeCl ₃		0.33m% UCl ₃ 6.0m% CeCl ₃		1.0m% UCl ₃ 1.0m% CeCl ₃		1.0m% UCl ₃ 6.0m% CeCl ₃		6.0m% UCl ₃ 1.0m% CeCl ₃		6.0m% UCl ₃ 6.0m% CeCl ₃	
	25 mV	12.2	n/a	24.3	n/a	n/a	unkn	unkn	18.2	n/a	30.7	n/a
150 mV	21.8	19.6	33.1	16.5	6.6	4.2	10.5	13.2	7.9	36.0	70.6	
300 mV	18.2	17.4	117.8	171.0	4.6	3.6	3.6	15.6	11.7	11.5	27.9	
450 mV	18.0	18.1	174.5	56.0	unkn	4.5	4.0	19.8	43.1	22.9	33.0	
525 mV	42.2	unkn	14.6	25.7	unkn	3.8	4.3	23.3	14.3	39.0	23.4	
Avg	20.9		76.0		5.6	4.8		18.6		32.8		
Std Dev	9.0		66.1		1.4	2.3		10.3		16.4		

Table 7.16: Solubility of LiCl and KCl in water, units of g/100g H₂O (230).

Species	20 °C	40 °C	60 °C
KCl	34.0	40.0	45.8
LiCl	73.8	89.8	94.1

7.3.3 Summary

The analyses of uranium dendrites produced from mixtures of LiCl-KCl-UCl₃-CeCl₃ electrolytes showed no clear trend of cerium contamination of the uranium with deposition overpotential. It also showed little or no correlation of the cerium contamination with cerium concentration. Considering that the overpotential varied from 25 mV to 525 mV (nearly the deposition potential of Ce(III/0)), and the CeCl₃ concentration varied by a factor of six, an impact from each of these parameters might be expected. Instead, the dominant observed effect was the concentration of uranium in the electrolyte.

A significant fraction of occluded salt was observed in the samples, typically in the range of 2-4 wt% of the dendrite. This was larger than that observed for the uranium dendrites produced in the electrorefiner and seems inconsistent with the minimal amount of residual salt observed in the morphology samples. One potential explanation is the macroscopic encapsulation of salt within the dendrite mass which may have been minimized with the individually-prepared samples for morphology study.

CHAPTER 8. SUMMARY AND FUTURE WORK

8.1. Overview

Molten salt electrorefining of uranium is an important recycling option to potentially reduce the environmental impact of the nuclear fuel cycle. The purity of the recovered uranium product is one of many important considerations which impacts the value of the effort. Two primary groups of contaminants that have been most widely considered are (1) actinoid species, such as plutonium and neptunium, and (2) lanthanoid species, such as cerium, lanthanum and praseodymium. The motivation for the present study was to investigate factors and mechanisms which may contribute to contamination of electrorefined uranium.

8.2 Review of Principles

Chapter 2 presented theory and methods used to analyze the data obtained from electrochemical studies of CeCl_3 and UCl_3 in fused LiCl-KCl . This included methods associated with Nernst, Butler-Volmer, and the Randles-Sevcik relationships as applied to cyclic voltammetry, square wave voltammetry, and chronopotentiometry. The techniques outlined routes to determine fundamental parameters such as reversibility, oxidation states, equilibrium potential, diffusion coefficients, exchange current density, and nucleation mode.

8.3 Summary of Literature Review

Chapter 3 presented a literature survey of a range of important issues to fused salt electrorefining and electrochemistry. A review is provided of studies of the Ag/AgCl reference electrode including a discussion of the importance of understanding the concentration scale in which a work is performed. A discussion was presented regarding the importance of electrolyte purity and potential interactions of reactive chloride species with ceramic crucible materials. Evidence was presented regarding the existence of ionic-bonded complex molecules surrounding high valence state species such as lanthanoids and actinoids in the molten salt, and the existence of disproportionation reactions observed with multivalent species. Prior studies of electrochemistry and exchange current density for cerium and uranium were presented. The purity of products from molten electrorefining processes were presented and discussed.

Finally, surveys of oxidation states, diffusion coefficients, apparent standard potential, and nucleation properties of the lanthanoid and actinoid species were summarized.

8.4 Experimental methods

The present work was comprised of several distinct components, such as cerium electrochemistry, evaluation of products from electrometallurgical treatment, and uranium and uranium/cerium electrochemistry. Chapter 4 presented the experimental methods and setup for each of these components, including the furnace systems, crucibles, electrodes, experiment control, and methods of collecting samples. Analyses of raw materials for some custom materials such as uranium rods and UCl_3 feedstock were also provided. Due to the potential importance of consistent analytical techniques, procedures followed for washing, dissolution, and analysis of samples by ICP-MS were presented.

8.5 Results of Ce Electrochemistry

Chapter 5 presented detailed electrochemical studies of cerium in LiCl-KCl eutectic. The following observations were made.

- $CeCl_3$ reduces to Ce metal as a quasi-reversible reaction.
- Square wave voltammetry measurements determined the reaction to be a simple 3-electron reduction.
- Diffusion coefficients were measured using the Randles-Sevcik equation for data from cyclic voltammetry and the Sand equation for chronopotentiometry. The Diffusion coefficient of $CeCl_3$ was described by the expression

$$\log D_{Ce(III)} = -2.43 - 1952/T \quad (D_{Ce(III)}: cm^2s^{-1}). \quad [5.1]$$

- Based on a range of measurements of open circuit potential of cerium metal, the apparent standard potential of cerium was found to be described by

$$E_{CeCl_3}^* = -3.5338 + 5.923 \times 10^{-4}T \quad (V). \quad [5.4]$$

- The activity coefficient for $CeCl_3$ in fused LiCl-KCl eutectic was found to be approximately 1.5×10^{-2} and 1.2×10^{-2} at 723 and 773 K, respectively.

- Using the methods developed by Allongue and Souteyrand, and Scharifker and Hills, the nucleation mode of cerium was found to be instantaneous with 3-dimensional growth of nuclei.
- The exchange current density of cerium was measured using the linear polarization technique at very low overpotentials during a very slow voltammetric scan. The exchange current density was found to be approximately 10-30, 40-100, and 60-200 mA/cm² at 653, 773, and 973 K, respectively.

8.6 Results of Process Samples from Electrometallurgical Treatment

Chapter 6 provided results of the investigation of purity of uranium dendrites produced under plant conditions in the presence of fission and transmutation products, and compared this information against purity of the final uranium product. The following observations were obtained:

- The intrinsic purity of the uranium crystals is near 99.95% (for recent concentrations of contaminants in the Mk-IV ER).
- Evaluated samples contained an average of approximately 35 ± 5 $\mu\text{g/g}$ Pu contamination following correction for residual salt content within the dendrites. However, reasonable scatter was observed, with one sample containing approximately 150 $\mu\text{g/g}$, and four samples containing essentially zero residual plutonium.
- The presence of significantly greater levels of impurities in final cast uranium products is very likely a consequence of following process operations, such as those where salt is in contact with molten metal at high temperatures.
- An average of approximately 0.25 wt% of the dendrite was measured to be salt resistant to removal by washing and likely to be present as occlusions inside cavities of the metal dendrite. This quantity could introduce an additional 25 $\mu\text{g/g}$ of plutonium contamination into the final product. The majority of contaminants are still a consequence of other processes unrelated to electrorefining.

- A modest reduction in occluded salt content was observed for crushed dendrites, but very thorough pulverization is likely necessary for significant reduction in occluded salt fraction.

8.7 Results of U-Ce Electrochemistry and Morphology

Chapter 7 presented the results from laboratory studies with UCl_3 and UCl_3 - CeCl_3 mixtures in LiCl - KCl mixtures. In Section 7.1, behavior of the salt solutions was examined to confirm similar characteristics with other studies. A limited study of UCl_3 in fused LiCl - KCl was performed with the following observations:

- The U(III)/U(0) couple appeared quasi-reversible.
- The exchange current density of uranium was measured with four uranium rods in different electrolyte solutions. The measured values are similar to those from some studies, and lower than those reported in others. Additional work to elucidate the impact of different computational methods upon estimates of i_0 , and the effects of concentration would be valuable.

Table 7.1: Estimates of i_0 from metallic uranium rods at 773 K.

Rod	Salt constituents	i_0 (A/cm ²)
Solid uranium A, $S= 2.13 \text{ cm}^2$	0.33 mol% UCl_3 and 1 mol% CeCl_3	0.002 – 0.004
Annular uranium, $S= 3.09 \text{ cm}^2$	1 mol% UCl_3	0.009 – 0.017
Solid uranium B, $S= 1.81 \text{ cm}^2$	1 mol% UCl_3 and 6 mol% CeCl_3	0.009 – 0.017
Solid uranium C, $S= 1.71 \text{ cm}^2$	6 mol% UCl_3 and 1 mol% CeCl_3	0.022 – 0.043

In Section 7.2, results were presented from microscopy studies of uranium crystals. Uranium crystals were produced under electrochemical potentials to improve understanding of morphology, with specific interest regarding cavities or voids formed in the crystals. All samples were produced from a solution of 1 mol% UCl_3 in LiCl - KCl eutectic at 773 K onto a 1-mm Ta wire. Three deposits were produced at overpotentials of 450, 150, and 25 mV relative to the open circuit potential of a uranium rod. The following observations were made.

- Great care must be taken during water washing of the residual salt to avoid a potential hydrolysis between the salt and water wash, and to limit oxidation of the exposed uranium metal surface.
- The uranium deposited at 450 mV overpotential largely formed as columnar whiskers and/or fibers, with blunt blocky tips, often with several adjacent fibers lying adjacent in a larger composite column.
- The uranium deposited at 150 mV overpotential was largely composed of sword-like fibers with angled, pointed tips and rows of porosity down the length. A smaller quantity of regularly-branched planar dendrites and irregular, planar maple-leaf dendrites were also observed.

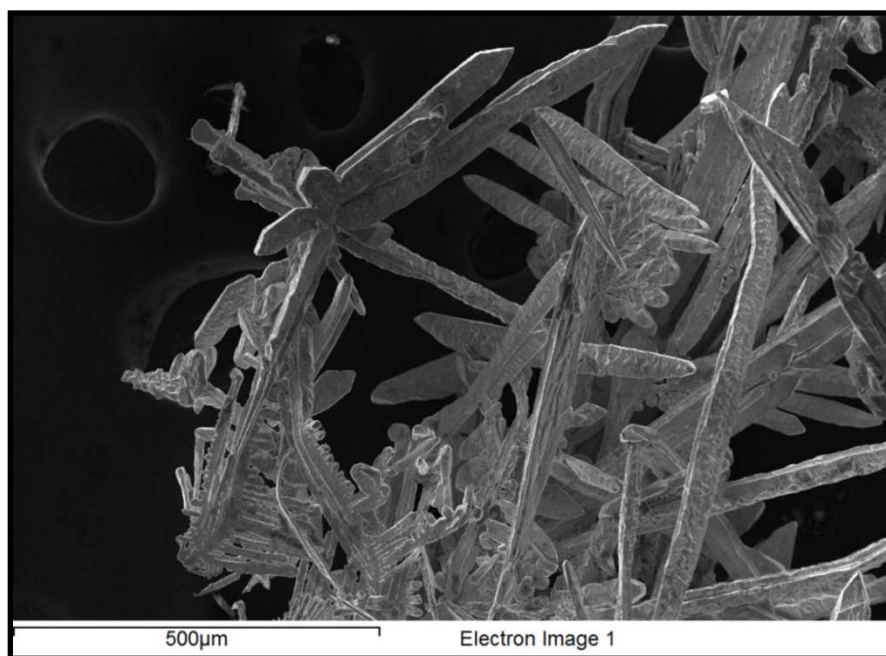


Figure 7.36: SE image of area (f) from Figure 7.25 comprised primarily of 50 μm fibers, but also showing 90° regularly-branched dendrite groups and an irregular maple-leaf.

- The uranium deposited at 25 mV overpotential was primarily composed of stacks of rhomboidal platelets whose interior volume may be largely hollow cavities portioned by thin straight ribs.

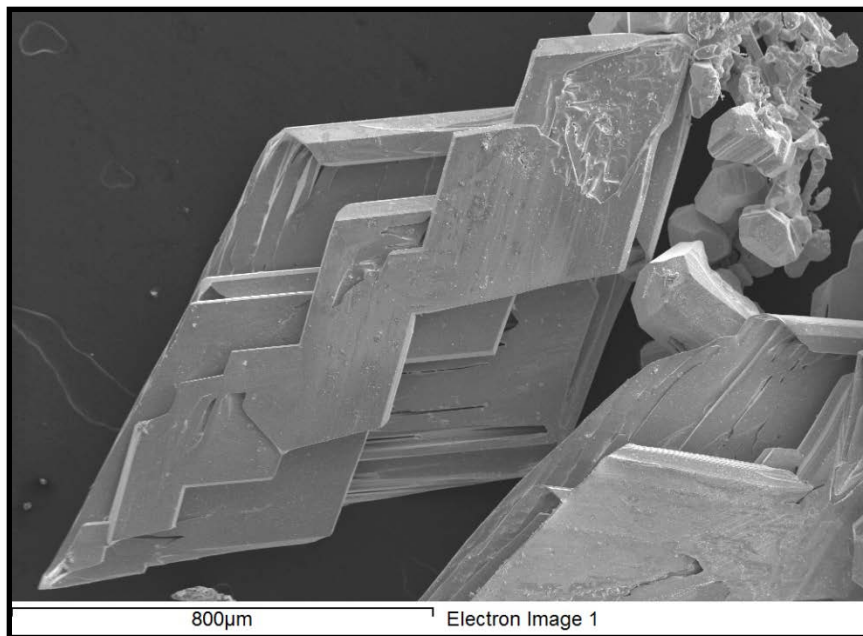


Figure 7.38: SE image of area **(a)** from Figure 7.37 of uranium dendrite from 25mV overpotential.

- While there were commonalities, each sample was dominated by different uranium morphologies. Notably, the crystals produced at low overpotentials were observed to have significantly greater evidence of internal cavities which would be expected to contain occluded salt.
- The uranium structures produced at the highest overpotential appeared to have the least evidence of porosity.

Section 7.3 presented a large collection of data from uranium dendrite samples produced under laboratory conditions in the presence of a CeCl_3 contaminant. Several conclusions can be described as follows:

- Uranium dendrites were produced across a range of electrochemical overpotentials for a series of six electrolyte conditions.
- No clear relationship was found between cerium contamination of the uranium and the deposition overpotential.
- Although one set of data appears to have been compromised by a work shutdown during analysis, the cerium contamination was found to rise significantly at all

deposition potentials in uranium dendrites produced from an electrolyte of low uranium activity. The transition appeared between 1.0 mol% and 0.33 mol% uranium solutions. It appears likely that uranium activity has a greater impact than deposition potential upon the purity of uranium crystals produced in LiCl-KCl eutectic at 773 K.

Table 7.14: Average cerium content for each electrolyte test condition, units $\mu\text{g Ce per g U}$.

0.33m% UCl_3 1.0m% CeCl_3	0.33m% UCl_3 6.0m% CeCl_3	1.0m% UCl_3 1.0m% CeCl_3	1.0m% UCl_3 6.0m% CeCl_3	6.0m% UCl_3 1.0m% CeCl_3	6.0m% UCl_3 6.0m% CeCl_3
689	913	101	4225	-9	-15

8.8 Future work

The reported exchange current density of uranium still has some scatter in values reported between similar studies. In some cases, it appears the root data is very similar, yet different application of Tafel and/or linear polarization technique lead to a divergence of reported exchange current density. A study to more clearly elucidate the impact of literature techniques for this application may be useful.

Data indicate that despite the highly contaminated electrolyte, the intrinsic purity of uranium dendrites in electrorefining is very high. Contamination of uranium by plutonium in electrometallurgical processing is likely dominated by the effects of process operations following electrorefining. Greatest benefit may be obtained by future focus upon contamination mechanisms in these processes.

In some processing conditions, uranium crystallization appears to be dominated by a morphology which favors planar rhomboidal crystals with significant internal cavities. This dominant morphology switched to uranium fibers with a modest increase in electrochemical overpotential. These uranium fibers display only very limited evidence of internal porosity. Investigation of the ability to produce more fibrous morphology in electrorefining would provide some benefit. Physical crushing or grinding of electrorefined uranium may also provide some benefit to open microscopic and macroscopically-occluded salt.

In the case of deposition of uranium in the presence of cerium, no clear increase in cerium contamination was observed for uranium deposition at high overpotentials, even near the

equilibrium potential of cerium. Value may be found if such benefits could also be demonstrated for the uranium-plutonium pair under plant processing conditions. However, contamination of the uranium with cerium was observed to increase at all test conditions for electrolytes with low uranium activity. Uranium concentration in the electrolyte appears to be the dominant parameter impacting purity in these conditions. Future studies to elucidate this observation for a broader group of salt contaminants such as plutonium may be productive.

The morphology of uranium crystals is clearly both a complicated and important factor in electrorefining, yet has received only very limited study. The uranium crystals produced and examined by SEM in this work were all derived from a single bulk uranium concentration (1 mol% UCl_3). It is possible some of the complexity of the observed crystallization within a sample result from depositions at slightly different conditions within the deposit. It is possible that shifts in the salt composition near the cathodic surface could play a role in deposit morphology. Future studies which could provide increased ability to tailor deposit morphology would be a valuable contribution to existing and future electrorefining applications.

REFERENCES

1. Yoo J-H, Seo CS, Kim E-H, Lee H-S. A Conceptual Study of Pyroprocessing for Recovering Actinides from Spent Oxide Fuels. *Nuclear Engineering and Technology*. 2008;40(7).
2. P. Soucek RM. Pyrochemical processes for recovery of actinides from spent nuclear fuels. In: Taylor R, editor. *Reprocessing and Recycling of Spent Nuclear Fuel*: Elsevier Ltd.; 2015.
3. Cassayre L, Caravaca C, Jardin R, Malmbeck R, Masset P, Mendes E, et al. On the formation of U-Al alloys in the molten LiCl-KCl eutectic. *Journal of Nuclear Materials*. 2008;378(1):79-85.
4. Serp J, Chamelot P, Fourcaudot S, Konings RJM, Malmbeck R, Pernel C, et al. Electrochemical behaviour of americium ions in LiCl-KCl eutectic melt. *Electrochimica Acta*. 2006;51(19):4024-32.
5. Pernel C, Ougier M, Glatz JP, Koch L, Koyama T, editors. Partitioning of Americium Metal from Rare Earth Fission Product by Electrorefining. *Workshop on Pyrochemical Separations; 2000 14-16 March 2000; Avignon, France: OECD NEA*.
6. Gao F, Wang C, Liu L, Guo J, Chang S, Chang L, et al. Electrode processes of uranium ions and electrodeposition of uranium in molten LiCl-KCl. *Journal of Radioanalytical and Nuclear Chemistry*. 2009;280(1):207-18.
7. Gao F, Wang C, Liu L, Guo J, Chang S, Chang L, et al. Electrode process of La(III) in molten LiCl-KCl. *Journal of Rare Earths*. 2009;27(6):986-90.
8. Dong W, Yang X, Zhang J, Sheng J. Thermodynamic investigations of liquid cerium–bismuth alloys. *Journal of Materials Science*. 2008;43(9):3240-4.
9. Ohmura H, Mizuguchi K, Kanamura S, Ohsato T, Fujita R, Omori T, et al. Development of hybrid reprocessing technology based on solvent extraction and pyro-chemical electrolysis. *Progress in Nuclear Energy*. 2011;53(7):940-3.
10. Iizuka M, Uozumi K, Inoue T, Iwai T, Shirai O, Arai Y. Behavior of plutonium and americium at liquid cadmium cathode in molten LiCl–KCl electrolyte. *Journal of Nuclear Materials*. 2001;299(1):32-42.
11. Kato T, Inoue T, Iwai T, Arai Y. Separation behaviors of actinides from rare-earths in molten salt electrorefining using saturated liquid cadmium cathode. *Journal of Nuclear Materials*. 2006;357(1-3):105-14.
12. Lee JH, Kang YH, Hwang SC, Shim JB, Ahn BG, Kim EH, et al. Electrodeposition Characteristics of Uranium in Molten LiCl-KCl Eutectic and its Salt Distillation Behavior. *Journal of Nuclear Science and Technology*. 2006;43(3):263-9.
13. Cho Y-H, Kim T-J, Park Y-J, Im H-J, Song K. Electronic absorption spectra of Sm(II) and Yb(II) ions in a LiCl-KCl eutectic melt at 450 °C. *Journal of Luminescence*. 2010;130(2):280-2.
14. Kang YH, Hwang SC, Lee HS, Kim EH, Park SW, Lee JH. Effects of neodymium oxide on an electrorefining process of uranium. *Journal of Materials Processing Technology*. 2009;209(11):5008-13.
15. Ghosh S, Vandarkuzhali S, Gogoi N, Venkatesh P, Seenivasan G, Reddy BP, et al. Anodic dissolution of U, Zr and U-Zr alloy and convolution voltammetry of Zr couple in molten LiCl-KCl eutectic. *Electrochimica Acta*. 2011;56:8204-18.

16. Prabhakara Reddy B, Vandarkuzhali S, Subramanian T, Venkatesh P. Electrochemical studies on the redox mechanism of uranium chloride in molten LiCl–KCl eutectic. *Electrochimica Acta*. 2004;49(15):2471-8.
17. Ghosh S, Vandarkuzhali S, Venkatesh P, Seenivasan G, Subramanian T, Prabhakara Reddy B, et al. Electrochemical studies on the redox behaviour of zirconium in molten LiCl–KCl eutectic. *Journal of Electroanalytical Chemistry*. 2009;627(1-2):15-27.
18. Marsden KC, Pesic B. Evaluation of the Electrochemical Behavior of CeCl₃ in Molten LiCl-KCl Eutectic Utilizing Metallic Ce as an Anode. *Journal of the Electrochemical Society*. 2011;158(6):F111-F20.
19. Goff KM, Wass JC, Marsden KC, Teske GM. Electrochemical processing of used nuclear fuel. *Nuclear Engineering and Technology*. 2011;43(4):335-42.
20. Benedict RW, Solbrig C, Westphal B, Johnson TA, Li SX, Marsden K, et al., editors. *Pyroprocessing Progress at Idaho National Laboratory*. Global 2007; 2007 Sept 9-13; Boise, Idaho.
21. Fusselman SP, Gay RL, Grimmatt DL, Roy JJ, Krueger CL, Nabelek CR, et al., editors. *Dry separation process for actinide removal from PUREX waste*. GLOBAL '97, International Conference on Future Nuclear Systems 1997; Yokohama, Japan.
22. Figueroa J, Williamson MA, Kleeck MAV, Blaskovitz RJ, Vandegrift GF, editors. *Pyrochemical Scrap Recovery in the Fabrication of LEU Monolithic U-Mo Fuel for High-Performance Research Reactors*. RERTR 2010 - 32nd International Meeting on Reduced Enrichment for Research and Test Reactors; 2010 Oct 10-14; Lisbon, Portugal.
23. *Standard Specification for Uranium Hexafluoride Enriched to less than 5% U-235*. ASTM C996-04.
24. Cohen ER, Cvitas T, Frey JG, Holmstrom B, Kuchitsu K, Marquardt R, et al. *Quantities, Units and Symbols in Physical Chemistry*. 2nd Printing, 3rd ed. Cambridge: IUPAC & RSC Publishing; 2008.
25. IUPAC. *Recommendations for Sign Conventions and Plotting of Electrochemical Data*. 1976.
26. G.J. Janz CBA, N.P. Bansal, R.M. Murphy, and R.P.T. Tomkins. II. *Molten Salts: Data on Single and Multi-Component Salt Systems*. National Bureau of Standards, 1979 April 1979. Report No.: Contract No.: NSRDS-NBS 61, Part II.
27. Yang L, Hudson RG. Equilibrium Electrode Potentials of Some Metal-Chlorine Galvanic Cells and Activities of Some Metal Chlorides in LiCl-KCl Eutectic Melt. *Transactions of the Metallurgical Society of AIME*. 1959;215:589-601.
28. Yang L, Hudson RG. Some Investigations of the Ag/AgCl in LiCl-KCl Eutectic Reference Electrode. *Journal of the Electrochemical Society*. 1959;106(11):986-90.
29. Laitinen HA, Liu CH. An Electromotive Force Series in Molten Lithium Chloride-Potassium Chloride Eutectic. *Journal American Chemical Society*. 1958;80(5):1015-20.
30. Salstrom EJ. Thermodynamic Properties of Fused Salt Solutions. VIII. Lead Chloride in Silver Chloride. *Journal American Chemical Society*. 1934;56.
31. Salstrom EJ. The Free Energy of Reactions Involving the Fused Chlorides and Bromides of Lead, Zinc and Silver. *Journal American Chemical Society*. 1933;55(6):2426-8.
32. Takahashi M, Amada Y. Anodic Polarization of Metals in Fused Salt of Lithium Chloride-Potassium Chloride Eutectic. *Denki Kagaku*. 1964;32(2):140-5.

33. Osteryoung J, Osteryoung RA. Square Wave Voltammetry. *Analytical Chemistry*. 1985;57:101A-10A.
34. Bard A, Faulkner L. *Electrochemical Methods: Fundamentals and Applications*. 2nd ed: John Wiley & Sons; 2001.
35. Pletcher D, Greef R, Peat R, Peter L, Robinson J. *Instrumental Methods in Electrochemistry*. Chichester: Horwood Publishing; 1985.
36. Scholz F, editor. *Electroanalytical Methods: Guide to Experiments and Applications*: Springer; 2005.
37. Matsuda H, Ayabe Y. *Z Electrochem*. 1955;59.
38. Berzins T, Delahay P. Oscillographic Polarographic Waves for the Reversible Deposition of Metals on Solid Electrodes. *J Am Chem Soc*. 1953;75(3):555-9.
39. Ramaley L, Krause MS. Theory of Square Wave Voltammetry. *Analytical Chemistry*. 1969;41((11)):1362-5.
40. Krause MS, Ramaley L. Analytical application of square wave voltammetry. *Analytical Chemistry*. 1969;41(11):1365-9.
41. Barker GC. Square wave polarography and some related techniques. *Analytica Chimica Acta*. 1958;18:118-31.
42. Bermejo MR, Barrado E, Martinez AM, Castrillejo Y. Electrodeposition of Lu on W and Al electrodes: Electrochemical formation of Lu-Al alloys and oxoacidity reactions of Lu(III) in the eutectic LiCl-KCl. *Journal of Electroanalytical Chemistry*. 2008;617:85-100.
43. Kuznetsov SA, Hayashi H, Minato K, Gaune-Escard M. Electrochemical behavior and some thermodynamic properties of UCl_4 and UCl_3 dissolved in a LiCl-KCl eutectic melt. *Journal of the Electrochemical Society*. 2005;152(4):C203-C12.
44. Delahay P. *New Instrumental Methods in Electrochemistry: Theory, Instrumentation, and Applications to Analytical and Physical Chemistry*. New York: Interscience Publishers; 1954.
45. Adams RN. *Electrochemistry at solid electrodes*. New York: Marcel Dekker; 1969. 402 p.
46. Delahay P, Mamantov G. Voltammetry at Constant Current: Review of Theoretical Principles. *Analytical Chemistry*. 1955;27(4):478-83.
47. Serrano K, Taxil P. Electrochemical reduction of trivalent uranium ions in molten chlorides. *Journal of Applied Electrochemistry*. 1999;29:497-503.
48. Christensen CR, Anson FC. Chronopotentiometry in Thin Layers of Solution. *Analytical Chemistry*. 1963;35(2):205-9.
49. Sand HJS. III. On the concentration at the electrodes in a solution, with special reference to the liberation of hydrogen by electrolysis of a mixture of copper sulphate and sulphuric acid. *Philosophical Magazine Series 6*. 1901;1(1):45-79.
50. Stern M. A Method for Determining Corrosion Rates from Linear Polarization Data. *Corrosion*. 1958;14.
51. Stern M. The Electrochemical Behavior, Including Hydrogen Overvoltage, of Iron in Acid Environments. *Journal of the Electrochemical Society*. 1955;102(11):609-16.
52. Stern M, Geary AL. Electrochemical Polarization I. A Theoretical Analysis of the Shape of Polarization Curves. *Journal of the Electrochemical Society*. 1957;104(1):56-63.

53. Scharifker B, Hills G. Theoretical and experimental studies of multiple nucleation. *Electrochimica Acta*. 1983;28(7):879-89.
54. G. Gunawardena GH, I. Montenegro, B. Scharifker. Electrochemical Nucleation Part I. General Considerations. *J Electroanal Chem*. 1982;138:225-39.
55. G.J. Hills DJS, J. Thompson. Electrochemical Nucleation from Molten Salts I. Diffusion Controlled Electrodeposition of Silver from Alkali Molten Nitrates. *Electrochimica Acta*. 1974;19:657-70.
56. B.R. Scharifker JM. Three-Dimensional Nucleation with Diffusion Controlled Growth, Part I. Number Density of Active Sites and Nucleation Rates Per Site. *J Electroanal Chem*. 1984;177:13-23.
57. Allongue P, Souteyrand E, Allemand L. Charge Transfer Process at Illuminated Semiconductor/Electrolyte Junctions Modified by Electrodeposition of Microscopic Metal Grain. *Journal of the Electrochemical Society*. 1989;136(4):1027-33.
58. Allongue P, Souteyrand E. Metal electrodeposition on semiconductors: Part I. Comparison with glassy carbon in the case of platinum deposition. *Journal of Electroanalytical Chemistry and Interfacial Electrochemistry*. 1990;286(1-2):217-37.
59. Chamelot P, Lafage B, Taxil P. Studies of Niobium Electrocrystallization Phenomena in Molten Fluorides. *Journal of the Electrochemical Society*. 1996;143(5):1570-6.
60. Gruner AC, Thompson WT. The Activity of AgCl in AgCl-LiCl-KCl Melts. *Canadian Journal of Chemistry*. 1975;53:1084-92.
61. Roy JJ, Grantham LF, McCoy LR, Krueger C, Storvick TS, Inoue T, et al. Standard Potentials of Lanthanide and Actinide Trichlorides in Molten Eutectic LiCl-KCl Electrolyte. *Materials Science Forum*. 1991;73-75:547-54.
62. Caravaca C, de Córdoba G, Tomás MJ, Rosado M. Electrochemical behaviour of gadolinium ion in molten LiCl-KCl eutectic. *Journal of Nuclear Materials*. 2007;360(1):25-31.
63. Mottot Y. Doctoral Thesis. Paris VI: Pierre et Marie Curie; 1986.
64. Roy JJ, Grantham LF, Grimmitt DL, Fusselman SP, Krueger CL, Storvick TS, et al. Thermodynamic Properties of U, Np, Pu, and Am in Molten LiCl-KCl Eutectic and Liquid Cadmium. *Journal of the Electrochemical Society*. 1996;143(8):2487-92.
65. Fusselman SP, Roy JJ, Grimmitt DL, Grantham LF, Krueger CL, Nabelek CR, et al. Thermodynamic properties for rare earths and americium in pyropartitioning process solvents. *Journal of the Electrochemical Society*. 1999;146(7):2573-80.
66. Smirnov MV. *Electrode Potentials in Molten Chlorides*. Moscow 1973. 45 p.
67. Pankratz LB. *Thermodynamic Properties of Halides*. United States Department of the Interior, Bureau of Mines, 1984 Contract No.: Bulletin 674.
68. Barin I. *Thermochemical Data of Pure Substances*, 3rd Edition. New York: VCH; 1995.
69. *Thermochemical Properties of Inorganic Substances*. Barin I, Knacke O, editors. New York: Springer Verlag; 1973.
70. Fuger J, Parker VB, Hubbard WN, Oetting FL. Part 8, *The Actinide Halides*. Vienna: IAEA, 1983.
71. Roine A, Kotiranta T, Lamberg P, Ahlberg R. *HSC Chemistry Software*. Espoo, Finland: Outotec Research Oy.

72. Burkhard WJ, Corbett JD. The Solubility of Water in Molten Mixtures of LiCl and KCl. *J Am Chem Soc.* 1957;79(24):6361-3.
73. Maricle DL, Hume DN. A New Method for Preparing Hydroxide-Free Alkali Chloride Melts. *Journal of the Electrochemical Society.* 1960;107(4):354-6.
74. Laitinen HA, Ferguson WS, Osteryoung RA. Preparation of Pure Fused Lithium-Chloride-Potassium Chloride Eutectic Solvent. *Journal of the Electrochemical Society.* 1957;104(8):516-20.
75. Cao P, Zhang M, Han W, Yan Y, Wei S, Zheng T. Electrochemical behavior of erbium and the preparation of Mg-Li-Er alloys by codeposition. *Journal of Rare Earths.* 2011;29(8):763-7.
76. Yoon SY, Flint JH, Kipouros GJ, Sadoway DR. Raman Scattering Studies of Molten Salt Electrolysis of Light Metals. Bautista RG, Wesely R, editors. Warrendal PA: TMS-AIME; 1985.
77. Konishi H, Nohira T, Ito Y. Formation and phase control of Dy alloy films by electrochemical implantation and displantation. *Journal of the Electrochemical Society.* 2001;148(7):C506-C11.
78. Gardner HJ, Brown CT, Janz GJ. The Preparation of Dry Alkali Chlorides for Solutes and Solvents in Conductance Studies. *J Phys Chem.* 1956;60(10):1458-60.
79. Johnson KE, Mackenzie JR. Samarium, Europium, and Ytterbium Electrode Potentials in LiCl-KCl Eutectic Melt. *Journal of the Electrochemical Society.* 1969;116(12):1697-703.
80. Kuznetsov SA, Hayashi H, Minato K, Gaune-Escard M. The Influence of Oxide Ions on the Electrochemical Behavior of UCl_4 and UCl_3 in a LiCl-KCl Eutectic Melt. *Electrochemistry.* 2005;73(8):630-2.
81. Kvam KR, Bratland D, Øye HA. The solubility of neodymium in the systems $NdCl_3$ -LiCl and $NdCl_3$ -LiCl-KCl. *Journal of Molecular Liquids.* 1999;83(1-3):111-8.
82. Novikov GI, Polyachenok OG. Halides of Rare Earth Elements in a Lower State of Oxidation. *Russian Chemical Reviews.* 1964;33(6):342-50.
83. Castrillejo Y, Fernández P, Bermejo MR, Barrado E, Martínez AM. Electrochemistry of thulium on inert electrodes and electrochemical formation of a Tm-Al alloy from molten chlorides. *Electrochimica Acta.* 2009;54(26):6212-22.
84. Cho YZ, Yang HC, Lee HS, Kim IT, editors. Investigation of Various LiCl Waste Salt Purification Technologies. Atalante 2008, May 19-22; 2008; Montpellier, France.
85. Zakiryanova I, Salyulev A. Raman Spectra of Crystalline and Molten $GdCl_3$. *Russian Metallurgy.* 2010(2):87-93.
86. Papatheodorou GN. Raman Spectrum of the $LaCl_6^{-3}$ Octahedron in Molten and Solid $Cs_2NaLaCl_6$, Cs_3LaCl_6 , and K_3LaCl_6 . *Inorganic Nuclear Chemistry Letters.* 1975;11:483-90.
87. Mulcahy M, Heymann E. On the Nature of Molten Salts and Their Mixtures. *J Phys Chem.* 1943;47(7):485-96.
88. Lantelme F, Turq P. The Role of Coulomb Forces in the Properties of Ionic Liquids. *Journal of Chemical Physics.* 1984;81(11):5046-52.
89. Kovalevskii AV, Shishalov VI. Electroconductivity of Molten Mixtures of LiCl-KCl Eutectics with Chlorides of Rare-Earth Elements. *Russian journal of Physical Chemistry A.* 2011;85(1):136-40.

90. Akdeniz Z, Tosi M. Correlations Between Entropy and Volume of Melting in Halide Salts. *Proc R Soc Lond A*. 1992;437:85-96.
91. Maroni VA, Hathaway EJ, Papatheodorou GN. On the Existence of Associated Species in Lanthanum(III) Chloride-Potassium Chloride Melts. *J Phys Chem*. 1974;78(11):1134-5.
92. Zissi GD, Chrissanthopoulos A, Papatheodorou GN. Vibrational modes and structure of the LaCl_3CsCl melts. *Vibrational Spectroscopy*. 2006;40(1):110-7.
93. Chrissanthopoulos A, Papatheodorou GN. Temperature dependence of the $f \leftarrow f$ hypersensitive transitions of Ho^{3+} and Nd^{3+} in molten salt solvents and the structure of the $\text{LaCl}_3\text{-KCl}$ melts. *Journal of Molecular Structure*. 2006;782(2-3):130-42.
94. Chrissanthopoulos A, Papatheodorou G. Probing the Structure of $\text{GdCl}_3\text{-KCl}$ melt mixtures by electronic absorption spectroscopy of the hypersensitive $f \leftarrow f$ transitions. *Physical Chemistry Chemical Physics*. 2000;2(16):3709-14.
95. Matsuura H, Adya AK, Bowron DT. Phase transitions in rare earth chlorides observed by XAFS. *J Synchrotron Radiat*. 2001;8:779-81.
96. Wasse JC, Salmon PS. Structure of molten lanthanum and cerium tri-halides by the method of isomorphic substitution in neutron diffraction. *Journal of Physics-Condensed Matter*. 1999;11(6):1381-96.
97. Tosi M, Price D, Saboungi M. Ordering in Metal Halide Melts. *Ann Rev Phys Chem*. 1993;44:173-211.
98. Takagi R, Hutchinson F, Madden PA, Adya AK, Gaune-Escard M. The structure of molten DyCl_3 and DyNa_3Cl_6 simulated with polarizable- and rigid-ion models. *Journal of Physics-Condensed Matter*. 1999;11(3):645-58.
99. Anonymous A, editor. The structure of molten rare earth chlorides. Denmark2000.
100. Fukushima K, Yamoto H, Iwadate Y. Raman spectroscopic study of molten $\text{SmCl}_3\text{-AlCl}$ systems *Journal of Alloys and Compounds*. 1999;290:114-8.
101. Iwadate Y, Okako N, Koyama Y, Kubo H, Fukushima K. Melting behaviour in hexagonal CeCl_3 and monoclinic ErCl_3 crystals. In: Hiroyasu Nomura FK, Jack Y, editors. *Studies in Physical and Theoretical Chemistry*. Volume 83: Elsevier; 1995. p. 369-72.
102. Okamoto Y, Shiwaku H, Yaita T, Narita H, Tanida H. Local structure of molten LaCl_3 by K-absorption edge XAFS. *Journal of Molecular Structure*. 2002;641(1):71-6.
103. Matsuura H, Watanabe S, Sakamoto T, Kanuma T, Naoi K, Hatcho M, et al. Short-range structure of molten CeCl_3 and NdCl_3 determined by XAFS. *Journal of Alloys and Compounds*. 2006;408-412:80-3.
104. Wasse J, Salmon P. Structure of molten trivalent metal chlorides. *Physica B: Condensed Matter*. 1997;241-243:967-9.
105. Hutchinson F, Rowley AJ, Walters MK, Wilson M, Madden PA, Wasse JC, et al. Structure of molten MCl_3 systems from a polarizable ion simulation model. *Journal of Chemical Physics*. 1999;111(5):2028-37.
106. Hutchinson F, Wilson M, Madden P. A Unified description of MCl_3 Systems with a Polarizable Ion Simulation Model. *Molecular Physics*. 2001;99(10):811-24.
107. Okamoto Y, Suzuki S, Shiwaku H, Ohno A, Taita T, Madden P. Local Coordination about La^{3+} in Molten LaCl_3 and Its mixtures with Alkali Chlorides. *J Phys Chem A*. 2010;114:4664-71.

108. Adya A, Matsuura H, Takagi R, Rycerz L, Gaune-Escard M, editors. Structural and Thermodynamic Properties of Molten UCl_3 and $\text{UCl}_3\text{-MCl}$ Systems. Electrochemical Society; 1999.
109. Okamoto Y, Akabori M, Itoh A, Ogawa T. X-ray absorption study of molten uranium chloride system. *J Nucl Sci Tech.* 2002;Supplement 3:638-41.
110. Okamoto Y, Yaita T, Shiwaku H, Suzuki S. Behavior of trivalent metal ion in LiCl-KCl eutectic melt. 2006.
111. Zissi G, Papatheodorou G. Changes of vibrational modes upon melting solid $\text{Cs}_2\text{NaScCl}_6$, Cs_3ScCl_6 , $\text{Cs}_3\text{Sc}_2\text{Cl}_9$ and ScCl_3 . *Chemical Physics Letters.* 1999;308:51-7.
112. Wasse J, Salmon P. Structure of molten ScCl_3 and ScI_3 studied by using neutron diffraction. *Journal of Physics: Condensed Matter.* 1999;11(10):2171-7.
113. Kuznetsov S, Gaune-Escard M. Kinetics of electrode processes and thermodynamic properties of europium chlorides dissolved in alkali chloride melts. *Journal of Electroanalytical Chemistry.* 2006;595:11-22.
114. Kuznetsov SA, Gaune-Escard M. Redox electrochemistry and formal standard redox potentials of the Eu(III)/Eu(II) redox couple in an equimolar mixture of molten NaCl-KCl . *Electrochimica Acta.* 2001;46(8):1101-11.
115. Janz G, Bansal N. Molten Salts Data: Diffusion Coefficients in Single and Multi-Component Salt Systems. *J Phys Chem Ref Data.* 1982;11(3):505.
116. Koyama Y, Takagi R, Y. Iwadate KF. Phase diagram and Raman spectroscopy of $\text{EuCl}_2\text{-NaCl}$ binary mixtures. *Journal of Alloys and Compounds.* 1997;260(1-2):75-9.
117. Bermejo MR, Rosa Fdl, Barrado E, Castrillejo Y. Cathodic behavior of europium(III) on glassy carbon, electrochemical formation of Al_4Eu , and oxoacidity reactions in the eutectic LiCl-KCl . *Journal of Electroanalytical Chemistry.* 2007;603:81-95.
118. Castrillejo Y, Fernández P, Medina J, Vega M, Barrado E. Chemical and Electrochemical Extraction of Ytterbium from Molten Chlorides in Pyrochemical Processes. *Electroanalysis.* 2011;23(1):222-36.
119. Biggins S, Enderby J. The structure of molten calcium chloride. *J Phys C: Solid State Phys.* 1981;14:3577-83.
120. Kuznetsov SA, Rycerz L, Gaune-Escard M. Electrochemical and calorimetric investigations of some thermodynamic properties of EuCl_3 and EuCl_2 dissolved in alkali chloride melts. *Journal of Nuclear Materials.* 2005;344(1-3):152-7.
121. Kuznetsov SA, Gaune-Escard M. Kinetics of electrode processes and thermodynamic properties of europium chlorides dissolved in alkali chloride melts. *Journal of Electroanalytical Chemistry.* 2006;595(1):11-22.
122. Papatheodorou GN, Ostvold T. Thermodynamic Studies of Binary Charge Unsymmetrical Fused Salt Systems - Calorimetric and Electromotive-Force Measurements of Liquid Lanthanum(III) Chloride alkali Chloride Mixtures. *J Phys Chem.* 1974;78(2):181-5.
123. Iizuka M. Diffusion Coefficients of Cerium and Gadolinium in Molten LiCl-KCl . *Journal of the Electrochemical Society.* 1998;145(1):84-8.
124. Lantelme F, Berghoute Y. Electrochemical studies of LaCl_3 and GdCl_3 dissolved in fused LiCl-KCl . *Journal of the Electrochemical Society.* 1999;146(11):4137-44.

125. Lantelme F, Cartailier T, Berghoute Y, Hamdani M. Physicochemical properties of lanthanide and yttrium solutions in fused salts and alloy formation with nickel. *Journal of the Electrochemical Society*. 2001;148(9):C604-C13.
126. Castrillejo Y, Bermejo MR, Barrado E, MartInez AM, Diaz Arocas P. Solubilization of rare earth oxides in the eutectic LiCl-KCl mixture at 450 °C and in the equimolar CaCl₂-NaCl melt at 550 °C. *Journal of Electroanalytical Chemistry*. 2003;545:141-57.
127. Inman D, Jovanovic D, White SH. Interdiffusion Coefficients in Molten Li₂SO₄-K₂SO₄. *Journal of Electroanalytical Chemistry*. 1973;43.
128. Bouteillon B. Grenoble, France: University of Grenoble; 1969.
129. Bouteillon J, Barbier MJ. Mecanisme d'Echange Electrochimique DU systeme Ni/Ni (II) DANS L'Eutectique LiCl-KCl Fondu. *Electrochimica Acta*. 1976;21:817-21.
130. Laitinen H, Tisher R, Roe D. Exchange Current Measurements in KCl-LiCl Eutectic Melt *Journal of the Electrochemical Society*. 1960;107:546-55.
131. Driscoll KJ, Fray DJ. Fundamental aspects of fused-salt electrorefining of zinc. *Transactions of the Institution of Mining and Metallurgy, Section C (England)*. 1993;102:C99-C108.
132. Settle JL, Nagy Z. Metal Deposition-Dissolution in Molten Halides: On the Question of Measurability of Very Fast Electrode Reaction Rates. *Journal of the Electrochemical Society*. 1985;132(7):1619-27.
133. Choi I, Serrano B, Li S, Herrmann S, Phongikaroon S, editors. Determination of Exchange Current Density of U³⁺/U Couple in LiCl-KCl Eutectic Mixture. *Global 2009*; 2009 September 6-11; Paris, France.
134. Ghosh S, Vandarkuzhali S, Gogoi N, Venkatesh P, Seenivasan G, Reddy BP, et al. Anodic dissolution of U, Zr and U-Zr alloy and convolution voltammetry of Zr⁴⁺|Zr²⁺ couple in molten LiCl-KCl eutectic. *Electrochimica Acta*. 2011;56(24):8204-18.
135. Rose MA, Williamson MA, Willit J. Determining the Exchange Current Density and Tafel Constant for Uranium in LiCl/KCl Eutectic. *ECS Electrochemistry Letters*. 2015;4(1):C5-C7.
136. Cumberland RM, Yim M-S. A Computational Meta-Analysis of UCl₃ Cyclic Voltammograms in LiCl-KCl Electrolyte. *Journal of The Electrochemical Society*. 2014;161(4):D147-D9.
137. Rodriguez-Betancourt VM, Natland D. Raman spectroscopic study of mixed valence neodymium and cerium chloride solutions in eutectic LiCl-KCl melts. *Phys Chem Chem Phys*. 2005;7:173-9.
138. Castrillejo Y, Bermejo MR, Millan RS, Martinez AM, Barrado E, Caravaca C, et al. Chemical and Electrochemical Behavior of Cerium in Molten LiCl-KCl and CaCl₂ and NaCl. Berg RW, Hjuler HA, editors: Elsevier; 2000.
139. Castrillejo Y, Bermejo MR, Pardo R, MartInez AM. Use of electrochemical techniques for the study of solubilization processes of cerium-oxide compounds and recovery of the metal from molten chlorides. *Journal of Electroanalytical Chemistry*. 2002;522(2):124-40.
140. Yoon D, Phongikaroon S. Electrochemical Properties and Analyses of CeCl₃ in LiCl-KCl Eutectic Salt. *Journal of The Electrochemical Society*. 2015;162(10):E237-E43.
141. Masset P, Konings RJM, Malmbeck R, Serp J, Glatz J-P. Thermochemical properties of lanthanides (Ln = La, Nd) and actinides (An = U, Np, Pu, Am) in the molten LiCl-KCl eutectic. *Journal of Nuclear Materials*. 2005;344(1-3):173-9.

142. Shirai O, Iwai T, Suzuki Y, Sakamura Y, Tanaka H. Electrochemical behavior of actinide ions in LiCl–KCl eutectic melts. *Journal of Alloys and Compounds*. 1998;271–273(0):685-8.
143. Sakamura Y, Hijikata T, Kinoshita K, Inoue T, Storvick TS, Krueger CL, et al. Measurement of standard potentials of actinides (U,Np,Pu,Am) in LiCl–KCl eutectic salt and separation of actinides from rare earths by electrorefining. *Journal of Alloys and Compounds*. 1998;271-273(0):592-6.
144. Martinot L. Some Thermodynamic Properties of Dilute Solutions of Actinide Chlorides in (Li-K)Cl and in (Na-K)Cl Eutectics. *J Inorg Nucl Chem*. 1974;37:2525-8.
145. Hoover RO, Shaltry MR, Martin S, Sridharan K, Phongikaroon S. Electrochemical studies and analysis of 1–10wt% UCl₃ concentrations in molten LiCl–KCl eutectic. *Journal of Nuclear Materials*. 2014;452(1):389-96.
146. Polovov IB, Sharrad CA, May I, Vasin BD, Volkovich VA, Griffiths TR. Spectroelectrochemical study of uranium and neptunium in LiCl-KCl eutectic melt. *ECS Transactions*. 2007;3(35):503-11.
147. Masset P, Apostolidis C, Konings RJM, Malmbeck R, Rebizant J, Serp J, et al. Electrochemical behaviour of neptunium in the molten LiCl–KCl eutectic. *Journal of Electroanalytical Chemistry*. 2007;603(2):166-74.
148. Serp J, Konings RJM, Malmbeck R, Rebizant J, Scheppler C, Glatz JP. Electrochemical behaviour of plutonium ion in LiCl–KCl eutectic melts. *Journal of Electroanalytical Chemistry*. 2004;561(0):143-8.
149. Frank WB, editor. *Aluminum*: Wiley-VCH; 2009.
150. Totten GE, Mackenzie DS. *Handbook of Aluminum*: Marcel Dekker; 2003.
151. Kononov A, Kuznetsov S, Polyakov E. Electrorefining in molten salts - an effective method of high purity tantalum, hafnium and scandium metal production. *Journal of Alloys and Compounds*. 1995;218(2):173-6.
152. Nagai H, Beaudry BJ, Gschneidner KA. Purification of Gadolinium by Electrorefining. *Metallurgical Transactions B-Process Metallurgy*. 1978;9(1):25-8.
153. Sharma IG, Mukherjee TK. A study on purification of metallurgical grade silicon by molten salt electrorefining. *Metallurgical Transactions B*. 1986;17(2):395-7.
154. Lai Y-Q, Jia M, Tian Z-L, Li J, Yan J-F, Yi J-G, et al. Study on the Morphology Evolution and Purification of Electrorefined Silicon. *Metallurgical and Materials Transactions A*. 2010;41(4):929-35.
155. Lei KP, Sullivan TA. Report of Investigation—7484. US Bureau of Mines, 1971.
156. Lei KP, Campbell RE, Sullivan TA. Electrolytic Preparation of Vanadium from Vanadium Carbide. *Journal of the Electrochemical Society*. 1973;120(2):211-5.
157. Tripathy PK, Rakhasia RH, Hubli RC, Suri AK. Electrorefining of carbothermic and carbonitrothermic vanadium: a comparative study. *Materials Research Bulletin*. 2003;38(7):1175-82.
158. McCawley FX, inventor Electrorefining of Molybdenum. United States 1961.
159. Mullins LJ, Leary JA. Fused-Salt Electrorefining of Molten Plutonium and Its Alloys by LAMEX Process. *Industrial & Engineering Chemistry Process Design and Development*. 1965;4(4):394-400.

160. Marzano C, Noland R. The Electrolytic Refining of Uranium. Argonne National Laboratory, 1953 August 2, 1953. Report No.: Contract No.: ANL-5102.
161. Pernel C, Serp J, Ougier M, Malmbeck R, Glatz JP, editors. Electrochemical Investigations of La, Nd and Am in Molten Chloride Salts in View of Am/Ln Partitioning. Proceedings of Global 2001; 2001; Paris, France.
162. Yamana H, Park BG, Shirai O, Fujii T, Uehara A, Moriyama H. Electrochemically produced divalent neodymium in chloride melt. *Journal of Alloys and Compounds*. 2006;408-412:66-70.
163. Bronstein HR. Electromotive Force Measurements on Solutions of Rare Earth Metals in Their Molten Halides. I. The Cerium-Cerium chloride, Praseodymium-Praseodymium Chloride, and Neodymium-Neodymium Chloride Solutions. *The Journal of Physical Chemistry*. 1969;73:1320-6.
164. Panchenko ID, Penkalo II, Delimarksi YD. A Polarographic Study of the Cerium Group of Rare Earth Elements, with base Electrolyte consisting of a Fused LiCl-KCl Eutectic. *Soviet Electrochemistry*. 1966;2(5):485-90.
165. Salyulev A, Tkatcheva O, Shishkin V, Red'kin A, Khokhlov V. Charge Transfer in Molten Chloride Systems Containing Cerium Ions. *Progress in Molten Salt Chemistry*. 2000;1.
166. Bronstein HR, Dworkin AS, Bredig MA. *J Phys Chem*. 1962;66.
167. Dworkin AS, Bronstein HR, Bredig MA. *J Phys Chem*. 1962;66.
168. Druding LF, Corbett JD. *Journal American Chemical Society*. 1961;83:2462-7.
169. Lu QT, Li SX, Yu RL, Chen SG. *Kiyou Jinshu*. 1988;7(1):13-6.
170. Wu I, Zhu H, Sato Y, Yamamura T, Sugimoto K, editors. The Mechanism of the dissolution of Nd and the Electrode Reaction in Eutectic LiCl-KCl, NdCl₃ melts. 9th International Symposium Molten Salts, May 22-27; 1994; San Francisco, CA.
171. Castrillejo Y, Bermejo MR, Martinez AM, Diaz Arocas P. Electrochemical Behavior of Lanthanum and Yttrium Ions in Two Molten Chlorides with Different Oxoacidic Properties: The Eutectic LiCl-KCl and the Equimolar Mixture CaCl₂-NaCl. *Journal of Mining and Metallurgy*. 2003;39(1-2 B):109-35.
172. Picard GS, Mottot YE, Tremillon BL. Acidic and Redox Properties of Some lanthanide ions in molten LiCl-KCl Eutectic. *Proceedings of the Electrochemical Society*. 1986;86-1(Molten Salts):189-204.
173. Baptiste J, Lesourd PF, Plambeck JA. Electrochemical Studies of lanthanum and lanthanum-zinc alloys in fused LiCl-KCl eutectic. *Canadian Journal of Chemistry*. 1969;47:3387-91.
174. Sridharan K. Thermal Properties of LiCl-KCl Molten Salt for Nuclear Waste Separation. U.S. Department of Energy, 2012 NEUP Final Report, Project 09-780.
175. Castrillejo Y, Bermejo MR, Díaz Arocas P, Martínez AM, Barrado E. Electrochemical behaviour of praseodymium (III) in molten chlorides. *Journal of Electroanalytical Chemistry*. 2005;575(1):61-74.
176. Qiao ZY, Duan S, Inman D. Electrochemical reduction of praseodymium chloride in LiCl-KCl melt. *Journal of Applied Electrochemistry*. 1989;19:937-9.
177. Zhao M, Lu X, Jin L. Electrochemical Behavior of Nd³⁺ and Ho³⁺ in LiCl-KCl Melt. *Journal of Rare Earths*. 1997;15(2):103-6.

178. Fukasawa K, Uehara A, Nagai T, Fujii T, Yamana H. Electrochemical Study of Neodymium Ions in Molten Chlorides. Yao T, editor: Springer; 2010.
179. Cordoba G, Caravaca C. An electrochemical study of samarium ions in the molten eutectic LiCl+KCl. *Journal of Electroanalytical Chemistry*. 2004;572(1):145-51.
180. Bermejo MR, Barrado E, Herguedas M, Castrillejo Y, editors. Chemical and Electrochemical Behaviour of Eu(III) and Yb(III) in the Eutectic LiCl-KCl. EUCHEM Conference on Molten Salts and Ionic Liquids; 2006; Hammamet, Tunisia.
181. Bermejo MR, Gómez J, Medina J, Martínez AM, Castrillejo Y. The electrochemistry of gadolinium in the eutectic LiCl-KCl on W and Al electrodes. *Journal of Electroanalytical Chemistry*. 2006;588(2):253-66.
182. Shubin AB, Yamshchikov LF, Raspopin SP, Brettser-Portnov IV. Equilibrium potentials of scandium in a eutectic melt of potassium and lithium chlorides. *Rasplavy*. 1991;6:102-4.
183. Duan SZ, Zhao LZ, Wei SK. Electrochemical Reduction of Yttrium Ions. *Journal of Rare Earths*. 1992;10(3):183-8.
184. Bermejo MR, Gómez J, Martínez AM, Barrado E, Castrillejo Y. Electrochemistry of terbium in the eutectic LiCl-KCl. *Electrochimica Acta*. 2008;53(16):5106-12.
185. Chang KG, Lu XP, Du YY, Zhao MS. Determination of the apparent standard potential of the Dy/Dy(III) system in the LiCl-KCl eutectic. *Chinese Journal of Chemistry*. 1994;12(6).
186. Franklin K, Kobayashi F, Akabori M, Takano M, Itho A, Ogawa T, editors. A study on the electrode potential of dysprosium metal and dysprosium nitride in LiCl-KCl eutectic salt. 31st Symposium on Molten Salt Chemistry; 11-12 November 1999; Sendai, Japan.
187. Sheng J, Tamana H, Moriyama H. *Journal of Nuclear Materials*. 2002;301.
188. Castrillejo Y, Bermejo MR, Barrado AI, Pardo R, Barrado E, Martínez AM. Electrochemical behaviour of dysprosium in the eutectic LiCl-KCl at W and Al electrodes. *Electrochimica Acta*. 2005;50(10):2047-57.
189. Castrillejo Y, Bermejo MR, Barrado E, medina J, Martinez AM. Electrodeposition of Ho and Electrochemical Formation of Ho-Al Alloys from the Eutectic LiCl-KCl. *Journal of the Electrochemical Society*. 2006;153(10):C713-C21.
190. Castrillejo Y, Bermejo MR, Barrado E, Martínez AM. Electrochemical behaviour of erbium in the eutectic LiCl-KCl at W and Al electrodes. *Electrochimica Acta*. 2006;51(10):1941-51.
191. Smolenski V, Novoselova A, Osipenko A, Caravaca C, de Córdoba G. Electrochemistry of ytterbium (III) in molten alkali metal chlorides. *Electrochimica Acta*. 2008;54(2):382-7.
192. Chen Y, Ye K, Zhang M. Preparation of Mg-Yb alloy film by electrolysis in the molten LiCl-KCl-YbCl₃ system at low temperature. *Journal of Rare Earths*. 2010;28(1):128-33.
193. De Córdoba G, Laplace A, Lacquement J, Caravaca C. Electrochemical Behavior of Np in the Molten LiCl - KCl Eutectic. *Journal of The Electrochemical Society*. 2007;154(1):F16-F24.
194. Smirnov MV, Sokolovskii YS, Krasnov YN. Equilibrium between cerium(II) and cerium (III) ions in the molten eutectic of potassium and lithium chlorides. *Nauk SSSR, Ural'sk Filial*. 1964;5:7-16.
195. Vnuchkova LA, Bayanov AP, Degtyar VA, Serebrennikov VV. Reaction of metallic praseodymium with its trichloride in the melt of an equimolar potassium and lithium chloride mixture. *Izv Vyssh Ucheb Zaved, Tsvet Met*. 1972;15(3):115-9.

196. Usov PM, Bel'skaya NN, editors. V All Union conference on Physical Chemistry and Electrochem of Fused Salts, Oxide Melts, and Solid Electrolytes; 1973; Sverdlovsk.
197. Lebedev VA. Standard and Quasi-Standard Potentials of Lanthanides and Their Alloys in Fused Chlorides. *Russian Journal of Electrochemistry*. 1995;31(1):36-45.
198. Lebedev VA. *Dokl Akad Nauk*. 1993;330.
199. Eastman ED, Fontana BJ, Thurmond CD, Wilmarth WK. The Preparation of Cerium by Electrolysis of Molten Salts. US AEC, 1955 Contract No.: TID-5212.
200. Guo C, Feng L, Yang Z, Tang D. Dissolution of La in KCl-NaCl and LaCl₃-KCl-NaCl Melts. *Acta Metallurgica Sinica*. 1991;B, 4(1):18-21.
201. Feng L, Guo C, Tang D. Relationship between the dissolution behaviours and current efficiencies of La, Ce, Pr and Nd in their chloride molten salts. *Journal of Alloys and Compounds*. 1996;234(2):183-6.
202. Park YJ, Kim TJ, Cho YH, Jung YJ, Im HJ, Song K, et al. EPR investigation on a quantitative analysis of Eu(II) and Eu(III) in LiCl/KCl eutectic molten salt. *Bull Korean Chem Soc*. 2008;29(1):127-9.
203. Kiselev YM, Brandt A, Martynenko LI, Spizin VI. *Dokl AN SSSR*. 1979;246:879-82.
204. Smirnov MV, Krasnov YN, Komarov VE, Alekseev VN. Diffusion Coefficients of Trivalent Lanthanum in Molten LiCl-KCl and LiCl-KCl+LiF Mixtures. *Transactions of the Institute of Electrochemistry, Urals Academy of Sciences*. 1968;6:47-50.
205. Glatz JP, Malmbeck R, Pernel C, Scheppler C, Serp J. Electrochemical Behavior of Lanthanides in LiCl-KCl Eutectic Melts. 2003 September 2003. Report No.: FIS5-1999-00199.
206. Picard GS, Mottot YE, Tremillon BL, editors. Study on Electrowinning of Solid Lanthanum-Nickel Alloys in LiCl-KCl Eutectic Melt. Fourth International Symposium on Molten Salts; 1984; Pennington, NJ: The Electrochemical Society.
207. Matsumiya M, Matsumoto S, Matsuura H. Diffusion Coefficient of La(III) and Nd(III) Measured by Chronopotentiometry in Molten LiCl-KCl Eutectic. *Electrochemistry*. 2005;73(8):570-2.
208. Vandarkuzhali S, Gogoi N, Ghosh S, Reddy BP, Nagarajan K. Electrochemical behavior of LaCl₃ at tungsten and aluminum cathodes in LiCl-KCl eutectic melt. *Electrochimica Acta*. 2012;59:245-55.
209. Smolenskii VV, Novoselova AV, Osipenko AG. Electrochemical Study of the Redox Reaction Yb(III) + e = Yb(II) in a Molten LiCl-KCl Eutectic. *Russian Journal of Electrochemistry*. 2008;81(10):1768-73.
210. Shirai O, Iizuka M, Iwai T, Arai Y. Electrode Reaction of Pu³⁺/Pu Couple in LiCl-KCl Eutectic Melts: Comparison of the Electrode Reaction at the Surface of Liquid Bi with That at a Solid Mo Electrode. *Analytical Sciences*. 2001;17(1):51-7.
211. Plambeck JA. Beryllium and scandium electrode potentials in fused LiCl-KCl eutectic. *Canadian Journal of Chemistry*. 1968;46(6):929-31.
212. Hoshino Y, Plambeck JA. Electrochemical Studies of yttrium and yttrium-zinc alloys in fused LiCl-KCl eutectic. *Canadian Journal of Chemistry*. 1970;48:685-7.
213. Chang KG, X.P.Lu, F.Y.Du, Zhao MS. Determination of the apparent standard potential of the Dy/Dy(III) system in the LiCl-KCl eutectic. *Chinese Journal of Chemistry*. 1994;12(6):509-15.

214. Ogawa T, Minato K. Dissolution and formation of nuclear materials in molten media. *Pure and Applied Chemistry*. 2001;73(5):799-806.
215. Smolenskii VV, Novoselova AV, Bove AL. *Rasplavy*. 2007(6):66-72.
216. Smolenskii VV, Novoselova AV, Bove AL. *Zh Prikl Khim*. 2007;80(10):1632-7.
217. Serrano K, Taxil P. Electrochemical nucleation of uranium in molten chlorides. *Journal of Applied Electrochemistry*. 1999;29(4):505-10.
218. Okamoto H. Ce-U (Cerium-Uranium). *Binary Alloy Phase Diagrams*, II Ed, Ed TB Massalski, Vol 2 1990:1126-7.
219. Totemeier TC, Mariani RD. Morphologies of uranium and uranium–zirconium electrodeposits. *Journal of Nuclear Materials*. 1997;250(2–3):131-46.
220. Diagram Number 900674. ASM International; 2006.
221. Copper AS. Precise Lattice Constants of Germanium, Aluminum, Gallium Arsenide, Uranium, Sulphur, Quartz and Sapphire. *Acta Crystallogr*. 1962;15:578-82.
222. Yangzhong L, Tzu-Ray S, Tao L, Susan BS, Simon RP. Classical interatomic potential for orthorhombic uranium. *Journal of Physics: Condensed Matter*. 2012;24(23):235403.
223. Thomas RK, Penfold J. *Simple Solids and Diffraction*. Available from: <http://rkt.chem.ox.ac.uk/lectures/liqsolns/solids/solids.html>.
224. Littlewood R. *Electrochimica Acta*. 1961;3:270-8.
225. Hamel C, Chamelot P, Taxil P. Neodymium (III) cathodic processes in molten fluorides. *Electrochimica Acta*. 2004;49(25):4467-76.
226. Peters D, Ligane J. Theory of chronopotentiometry with cylindrical electrodes. I. The quinone-hydroquinone reaction at platinum and gold wire electrodes. *J Electroanal Chem*. 1961;2:1-16.
227. Evans DH, Price JE. An aid to the interpretation of data in chronopotentiometry with cylindrical electrodes. *Journal of Electroanalytical Chemistry* (1959). 1963;5(1):77-80.
228. Oldham KB. Diffusive transport to planar, cylindrical and spherical electrodes. *Journal of Electroanalytical Chemistry and Interfacial Electrochemistry*. 1973;41(3):351-8.
229. Kuznetsov SA, Gaune-Escard M. Electrochemical transient techniques for study of the electrochemistry and thermodynamics of nuclear materials in molten salts. *Journal of Nuclear Materials*. 2009;389(1):108-14.
230. *Solubility Data Series*, International Union of Pure and Applied Chemistry. 1994; 47.

APPENDIX A. RAW ANALYTICAL DATA FROM U-CE DENDRITE SAMPLES

Table A.1: Received Analytical results from 0.33 mol% UCl₃ dendrite samples, units of $\mu\text{g}/\text{sample}$ with 2σ at $\pm 5\%$ unless noted.

	0.33 mol% UCl ₃ 1.0 mol% CeCl ₃	0.33 mol% UCl ₃ 6.0 mol% CeCl ₃		
Test	25 mV			
Sample	98333 0.6022 g	n/a	98343 0.5910 g	n/a
ID	wash		wash	
Ce (MS)	8570		61300	
U (MS)	2400		3050	
Li (AES)	23400		24500	
K (AES)	89100		92800	
ID	acid		acid	
Ce (MS)	86		227	
U (MS)	242000		131000	
Li (AES)	155		57.3	
K (AES)	1890		1390	
Test	150 mV			
ID	98334	98335	98344	98345
Smpl M.	0.6041 g	0.4999 g	0.5711 g	0.7424 g
ID	wash	wash	wash	wash
Ce (MS)	12400	10900	54700	64600
U (MS)	1560	1830	1400	2410
Li (AES)	33500	30000	28200	31400
K (AES)	127000	113000	101000	115000
ID	acid	acid	acid	acid
Ce (MS)	156	115	163	272
U (MS)	120000	67800	88300	182000
Li (AES)	99.5	103	41.1	99.5
K (AES)	2170	2020	1360	1640
Test	300 mV			
ID	98336	98337	98346	98347
Smpl M.	0.6027 g	0.5916 g	0.7417 g	0.5345 g
ID	wash	wash	wash	wash
Ce (MS)	13500	13200	82100	58700
U (MS)	1370	1520	909	2680
Li (AES)	34700	35100	35200	27600
K (AES)	133000	132000	133000	102000
ID	acid	acid	acid	acid
Ce (MS)	121	105	144	65.8
U (MS)	99800	82400	102000	52100
Li (AES)	116	90.8	13.5	10
K (AES)	2110	1580	1590	1710
Test	450 mV			
ID	98338	98339	98348	98349
Smpl M.	0.7635 g	1.0415 g	0.5755 g	0.4670 g
ID	wash	wash	wash	wash
Ce (MS)	16900	21100	58200	47000
U (MS)	1350	879	2140	1400

Li (AES)	40400	52800	29900	21500
K (AES)	157000	202000	108000	78400
ID	acid	acid	acid	acid
Ce (MS)	163	185	92.2	153
U (MS)	156000	256000	65300	82600
Li (AES)	138	150	9.8	29.3
K (AES)	2480	2720	1710	1640
Test	525 mV			
ID	98340	98341	98350	98351
Smpl M.	0.5272 g	0.8056 g	0.4804 g	0.3537 g
ID	wash	wash	wash	wash
Ce (MS)	10900	16300	50300	36000
U (MS)	3370	3530	1850	1910
Li (AES)	28800	42500	20600	12900
K (AES)	108000	163000	77100	48600
ID	acid	acid	acid	acid
Ce (MS)	92.2	89.1	258	176
U (MS)	114000	169000	100000	57500
Li (AES)	99	<10	75.6	40.4
K (AES)	4180	1140	1100	1040

Table A.2: Received Analytical results from 1.0 mol% UCl₃ dendrite samples, **units of μg** with 2σ at $\pm 5\%$ unless noted.

	1.0 mol% UCl ₃ 1.0 mol% CeCl ₃	1.0 mol% UCl ₃ 6.0 mol% CeCl ₃	
25 mV			
ID		97574	97575
Smpl Mass	n/a	0.7829 g	0.6103 g
Wash Water			
Ce (AES)	n/a	71500	43200
U (AES)		15600	7920
Li (AES)		31400	18700
K (AES)		129000	77400
Metal Fraction			
Ce (AES)	n/a	308	467‡
U (AES)		174000	243000
Li (AES)		<3.7	16
K (AES)		<120	<88
150 mV			
ID	97131	97576	97577
Smpl Mass	0.4199 g	0.5116 g	0.6982 g
Water Wash			
Ce (MS, AES)	11200*	39900	53700
U (MS, AES)	23200*	4370	13300
Li (AES)	46300*	25300	36800
K (AES)	186000*	95100	135000
Metal Fraction			
Ce (MS, AES)	34.5*	616	316
U (MS, AES)	202000*	75800	66100
Li (AES)	63.3*	143	17.6†
K (AES)	415*	602	184†
300 mV			
ID	97132	97578	97579
Smpl Mass	0.8154 g	0.5888 g	1.0083
Water Wash			
Ce (AES)	n/a	54000	97400
U (AES)		6900	16400
Li (AES)		30100	50700
K (AES)		115000	210000
Metal Fraction			
Ce (MS, AES)	35.6*	732	831
U (MS, AES)	223000*	57700	110000
Li (AES)	59.1*	220	249
K (AES)	273*‡‡	787	885
450 mV			
ID	97133	97580	97581
Smpl Mass	0.7371 g	0.4702 g	0.7004 g
Water Wash			
Ce (AES)	n/a	51000	74600
U (AES)		10600	17600
Li (AES)		22800	32600
K (AES)		93900	133000
Metal Fraction			

Ce (AES)	29.8*	640	683
U (AES)	164000*	37100	73000
Li (AES)	47.5*	159	175
K (AES)	<280*	720‡	694
525 mV			
ID	97134	97582	97583
Smpl Mass	0.7590 g	0.7139 g	0.8070 g
Water Wash			
Ce (AES)	n/a	71800	90600
U (AES)		14000	18000
Li (AES)		30900	38800
K (AES)		133000	166000
Metal Fraction			
Ce (AES)	11*	1830	767
U (AES)	139000*	102000	59800
Li (AES)	<23	807	217
K (AES)	<420	3060	930

* units of $\mu\text{g/g}$ of received sample weight

† $\pm 10\%$

‡ $\pm 15\%$

‡‡ $\pm 25\%$

Table A.3: Received Analytical results from 6.0 mol% UCl₃ dendrite samples, units of µg/sample with 2σ at ±5% unless noted.

	6.0 mol% UCl ₃ 1.0 mol% CeCl ₃		6.0 mol% UCl ₃ 6.0 mol% CeCl ₃	
25 mV				
ID	98313		98323	
Smpl Mass	0.5178 g		0.4460 g	
Wash Water				
Ce (MS)	3530		35000	
U (MS)	20800		39600	
Li (AES)	11100		17900	
K (AES)	38000		60800	
Metal Fraction				
Ce (MS)	23.3		130	
U (MS)	294000		177000	
Li (AES)	58.3		62.2	
K (AES)	1060†		1910	
150 mV				
ID	98314	98315	98324	98325
Smpl Mass	0.5949 g	0.7414 g	0.5101 g	0.5156 g
Wash Water				
Ce (MS)	7250	9850	26100	20000
U (MS)	45400	62000	25900	17700
Li (AES)	23000	27700	11900	8890
K (AES)	81500	101000	43100	33700
Metal Fraction				
Ce (MS)	27.1	118	114	159
U (MS)	184000	209000	285000	309000
Li (AES)	90.2	396	51.1	29.9
K (AES)	1190	3120	1840	2110
300 mV				
ID	98316	98317	98326	98327
Smpl Mass	0.6308 g	0.5413 g	0.5451 g	0.7711 g
Wash Water				
Ce (MS)	7130	6190	45300	40600
U (MS)	31400	34500	59800	45000
Li (AES)	20400	17600	19200	18300
K (AES)	74300	62800	72400	66900
Metal Fraction				
Ce (MS)	48.8	65.4	572	174
U (MS)	257000	211000	155000	376000
Li (AES)	150	215	282	82.1
K (AES)	2340	2520	3240	2290
450 mV				
ID	98318	98319	98328	98329
Smpl Mass	0.5271 g	0.5217 g	0.6445 g	0.8743 g
Wash Water				
Ce (MS)	4830	5220	45800	59000
U (MS)	19700	24700	45400	72300
Li (AES)	16600	15600	20300	25100
K (AES)	58500	55400	74000	95100
Metal Fraction				

Ce (MS)	32.9	20.3	171	252
U (MS)	227000	220000	215000	338000
Li (AES)	90.1	52.7	83.4	113
K (AES)	1780	2270	1910	3730
525 mV				
ID	98320	98321	98330	98331
Smpl Mass	0.6616 g	1.0332 g	0.5634 g	0.6131
Wash Water				
Ce (MS)	6340	11600	37700	36600
U (MS)	40500	74100	27200	38400
Li (AES)	20300	36700	17500	16600
K (AES)	72700	129000	63000	60700
Metal Fraction				
Ce (MS)	27.6	50.6	141	174
U (MS)	269000	380000	211000	236000
Li (AES)	88.4	181	58.4	90.5
K (AES)	2060	2590	2280	2120

† ±10%